Design and Control of Piezoelectric Actuation for Hydraulic Valves

Persson, Johan

Award date:
2017

Awarding institution:
University of Bath

Design and Control of Piezoelectric Actuation for Hydraulic Valves

Submitted by
Lars Johan Persson

A thesis submitted for the degree of Doctor of Philosophy

Mechanical Engineering

University of Bath

October 2017.

Johan Persson

ABSTRACT

Servohydraulic systems are widely used for actuation where high force and fast response are needed, and the servovalve is the type of control valve which provides the highest performance for such systems. In aerospace, servovalves are used for many safety critical systems, such as flight control, steering and braking. However, during the last fifty years the conventional two stage servovalve design for aerospace applications has hardly changed. Due to the desire for increased energy efficiency, there is a need to make valves more efficient and lighter. A new type of servovalve for aerospace applications is therefore investigated. Increased efficiency implies that leakage should be small, and other key requirements are reliability, robustness and low manufacturing cost. The aim of this research is to provide background knowledge so that in the future an improved two stage servovalve can be manufactured. The prototype valve in this research will not be lightweight, but will provide knowledge for a future researcher or manufacturer to create a light weight servovalve.

A two stage servovalve was designed with a multi-layer piezoelectric ring bender actuating a low leakage small spool as a first stage to control a second stage spool with electrical position feedback. The valve body was manufactured through Additive Manufacturing.

A dynamic model of the complete valve was developed and correlated with experimental data. The model included the drive amplifier for the piezoelectric ring bender, the ring bender with hysteresis, first stage spool with overlap and the second stage spool. This showed that hysteresis and overlap had a significant effect on valve behaviour.

A second stage spool position controller was developed to counteract the non-linear behaviour due to the piezoelectric hysteresis and the dead-band due to the first stage overlap. The controller also includes a feed forward path to increase the bandwidth of the valve. This controller outperforms a conventional Proportional-Integral controller and is also less sensitive to amplitude change.

Mounting a ring bender sufficiently stiffly so that it can generate a high blocking force, but also in such a way that the deformation and hence the free displacement of the ring bender is not constrained, is a significant challenge. An analytical model to optimize the ring bender mount has been developed. This model can be used to find the optimum mount overlap at the outer edge of the ring bender, and the optimum thickness of the mount.

An extensive investigation of the durability of the ring bender in Hyjet has been completed. Hyjet is a tradename for a fire-resistant phosphate-ester hydraulic fluid commonly used in civil aerospace. The ring bender will quickly start to break down if the Hyjet reaches the electrical connections. The Hyjet will penetrate the ceramic and create an electrical circuit between the electrical connection, the Hyjet and the outermost internal electrode. The breakdown of the ring bender can probably be eliminated by

protecting the ceramic with an impermeable layer of material. In this research a metallic foil applied to the surface of the ring bender was investigated.

ACKNOWLEDGMENT

Firstly, I would like to express my utmost gratitude to my principal supervisor Prof. Andrew Plummer and my co-supervisor Prof. Chris Bowen at the University of Bath for their help and support during this PhD project. Andrew for his guidance, advice, knowledge and patience throughout the project. Chris for always keeping his 'door open', motivation and always happy to help.

I am thankful to Moog Controls Ltd. in Tewkesbury for their commitment towards the project and their support and guidance, but also for providing me with this opportunity. A special acknowledgment goes to Chris Pagett at Moog for his time, dedication, technical assistant, discussions of ideas and help with creating some of the CAD drawings of the valve presented in this thesis. Murray Yeomans for his practical knowledge and help with the valve and Dr Phil Elliott for his technical advice. I would also like to thank Dr Paul Guerrier and Ian Brooks for believing in my potential and for their support.

I would also like to thank all my friends in Bath, London and Sweden, and especially to my dear friend George Clack who has always been there to talk to and always managed to put a smile on my face, even during hard times.

Finally, I must express my very profound gratitude to my parents Ulf Persson and Eva Strömberg Persson for their unshakable support and dedication to everything I have been undertaking, but also for helping me become the person I am today. My younger brother David Persson for his support, motivation and just being my brother who is always there when needed. My younger sister Ingrid Persson and for her support and motivation. Last, but definitely not least, a massive thank you to my lovely girlfriend Camilla Kirk-Reynolds for providing me with unfailing love, support and continuous encouragement throughout this PhD, through the process of researching and writing this thesis.

This accomplishment would not have been possible without any of these people mentioned.

Thank you!

Table of Contents

List of Figures

List of Tables

ABBREVIATIONS

AM	Additive Manufacturing
ASTM	American Society for Testing and Materials
BSA	Bushing Spool Assembly
CFD	Computational Fluid Dynamics
DDV	Direct Drive Valve
DJ	Deflector Jet
EPDM	Ethylene Propylene Diene Monomer
FEA	Finite Element Analysis
FSO	First Stage Overlap
LVDT	Linear Variable Differential Transformer
PI	Proportional-Integral
PTFE	Polytetrafluoroethylene
PVD	Physical Vapour Deposition
PZT	Lead Zirconate Titanate
USD	United States Dollar
VITAL	Valve Integration Through Additive Layer Manufacturing

NOMENCLATURE

Parameter	Explanation
α	Hystereis tuning parameter
β	Hystereis tuning parameter
γ	Hystereis tuning parameter
μ	Poisson's ratio of the mount
μ_i	Normalised inner edge stiffness
μ_o	Normalised outer edge stiffness
μ_{pr}	Poisson's ratio of the piezoelectric ring bender
ξ	Damping factor or the amplifier
θ	Jet angle
ρ	Fluid Density
σ	Stress in piezoelectric element
ϕ	Angle of the deflected surface at a specific point
ϕ_o	Angle of the outer edge of the piezoelectric ring bender
ϕ_i	Angle of the inner edge of the piezoelectric ring bender
δ	Compression of the mount
τ_{FF}	Feedforward lag term
τ_{ref}	Reference model lag
υ	Kinematic viscosity
ω_n	Natural frequency of the amplifier
a_f	First stage open flow slot area
A_m	Area of the ring bender mount
A_s	Second stage spool end area
B	Bulk modulus
c	Piezoelectric ring bender damping ratio
C	Damping coefficient of the piezoelectric ring bender
C_d	Discharge coefficient
C_1, C_2, C_3, C_4	Boundary conditions of the mounting
C_0	Null offset compensation
C_q	Flow coefficient
C_{rb}	Capacitance of piezoelectric ring bender
d_{31}	Piezoelectric strain coefficient

D	Flexural rigidity of a plate
e	Electric field
E	Young's Modulus of the piezoelectric ring bender
E_m	Young's modulus of the ring bender mount
f_q	Non-linear function representing the first stage spool overlap region
F_e	In-plane blocking force per unit length of half of the piezoelectric ring bender
F_f	Flow forces acting on the first stage spool
F_{bf}	Blocking force of the piezoelectric ring bender
F_m	Force applied to the ring bender mount
F_{rb}	Force provided by the piezoelectric ring bender
h	Thickness of the piezoelectric ring bender
h_a	Active thickness of the piezoelectric ring bender
it	Polyfit coefficient for the thickness
io	Polyfit coefficient for the overlap
I_{max}	Maximum current of the amplifier
k_1	Fluid stiffness in control port 1
k_2	Fluid stiffness in control port 2
k_a	Axial stiffess of the mounting
k_i	Stiffness on the inner edge of the ring bender
k_q	Ratio of the total piezoelectric ring bender stroke
k_{rb}	Spring konstant of the piezoelectric ring bender
k_t	Torsional stiffness of the mounting
k_o	Stiffness of the outer edge of the piezoelectric ring bender due to the mounting
k_{I+}	Maximum displacement ratio of the ring bender
k_{I-}	Minimum displacement ratio of the ring bender
k_{IO+}	Input of the start of the overlap region on the positive side
k_{IO-}	Input of the start of the overlap region on the negative side
k_{O+}	Maximum output flow
k_{O-}	Minimum output flow
k_{OO+}	Output of the start of the overlap region on the positive side
k_{OO-}	Output of the start of the overlap region on the negative side
k_v	Volumetric flow rate
K_a	Amplifier scaling factor
K_{dv}	Ring bender blocking force versus applied voltage relationship

K_{FF}	Feedforward gain term
K_h	Hysteresis scaling factor
K_i	Integral gain for the non-linear controller
K_{i1}	Integral gain for control loop PI1
K_{i2}	Integral gain for control loop PI2
K_p	Proportional gain for the non-linear controller
K_{pc}	Pressure loss coefficient
K_{p1}	Proportional gain for control loop PI1
K_{p2}	Proportional gain for control loop PI2
K_{ref}	Reference gain model
m_{add}	Added mass
m_s	Mass of first stage spool
M_1	Bending moment per unit length on the cylindrical section of the ring bender
M_{1i}	Bending moment per unit length on the cylindrical section of the ring bender on the inner edge
M_2	Bending moment per unit length on the dimetrical section of the ring bender
M_e	Piezoelectric bending moment
M_s	Mass of second stage spool
n	Hysteresis non-linear term
n_f	Number of lands on the first stage
n_l	Number of active layers of the piezoelectric ring bender
n_s	Number of lands on the second stage
o	Overlap of the mounting over the piezoelectric ring bender
O_+	Positive overlap compensation output
O_-	Negative overlap compensation output
p	Total pressure loss
P	Blocking force of the piezoelectric ring bender
P_1	Pressure in control port 1
ΔP_1	Pressure losses in control port 1
P_2	Pressure in control port 2
ΔP_2	Pressure losses in control port 2
P_b	Maximum force provided by the piezoelectric ring bender due to the mounting
P_{ef}	Effective force output of the piezoelectric ring bender due to the mounting
P_s	Supply pressure of the system

P_{s1}	Pressure on end of second stage spool in control port 1
P_{s2}	Pressure on end of second stage spool in control port 2
P_r	Return pressure of the system
q	First stage flow rate
Q	Flow
Q_1	Flow in control port 1
Q_2	Flow in control port 2
r	Radius of the piezoelectric ring bender.
r_i	Inner radius of the piezoelectric ring bender
r_m	Ring bender mounting stiffness factor
r_o	Outer radius of the piezoelectric ring bender
R	Ratio of the inner to outer radii of the piezoelectric ring bender
S	Maximum stroke of the piezoelectric ring bender
t	Thickness of the mounting
t_m	Thickness of experimental ring bender mount
u_+	Positive overlap compensation input
u_-	Negative overlap compensation input
v_1	Fluid velocity in control port1
v_2	Fluid velocity in control port 2
v_{vol1}	Trapt fluid volume between the first and second stage spool in control port 1
v_{vol2}	Trapt fluid volume between the first and second stage spool in control port 2
V	Applied voltage
V_{amp}	Amplifier voltage to the piezoelectric ring bender
V_c	Control voltage to the amplifier
V_{max}	Maximum operating voltage of the piezoelectric ring bender
V_s	Shear force per unit length acting on the sides of a element of the piezoelectric ring bender
V_h	Voltage minus the hysteresis term
w	Deflection of the piezoelectric ring bender
w_i	Inner edge ring bender displacement
w_{if}	Maximum displacement of the piezoelectric ring bender
w_s	First stage flow slot width
W_{rb}	Work output of the piezoelectric ring bender
x	Displacement of the first stage

x_s	Second stage position

1 INTRODUCTION

This chapter gives an overview of the research project, an introduction to servovalves and torque motors, motivation for the research, aim and objectives, the original contribution and the structure or the thesis.

1.1 OVERVIEW AND MOTIVATION

The conventional two stage servo valve layout for aerospace applications has not changed considerably in the last fifty years. However, it is believed that due to a desire for reduced energy usage there is a need to make valves more efficient and lighter. A new type of servovalve for aerospace applications is therefore needed.

Key drivers for aerospace hydraulic servovalve designs are to reduce weight, reduce manufacturing costs and improve efficiency. The efficiency can be improved by reducing the internal leakage. By reducing the internal leakage the airline companies can save up to 2000 USD per valve per year of fuel cost [1][2]. In a typical single-aisle airliner there are approximately 40 hydraulic servovalves, which are the key control components in electrohydraulic actuation for primary flight control, landing gear deployment, on-ground braking and steering [2].

In conventional two-stage servovalves a torque motor is used for the pilot stage. The torque motor, however, is relatively heavy, can be time-consuming and expensive to set-up, and may require significant manual intervention [3]. If not adjusted precisely, the first stage amplifier may not provide stable operation, and there is a continual flow loss (and power loss) through the nozzles or jet. An alternative approach is required, providing a more cost-effective design, being both more efficient and lighter, and which is amenable to automated manufacture.

In regards to reducing the weight of a servovalve the amount of material used needs to be reduced. Additive Manufacturing (AM) is becoming mature enough to be able to produce parts of a standard that can be used in an aerospace environment. A good enough standard would be to obtain material properties of the AM part that are close to wrought material properties or obtain enough knowledge of the material properties that any differences could be taken into account during the design process. AM is a relatively new manufacturing method providing new possibilities when it comes to design and since material is only added where needed the finished part will be lighter.

The internal leakage of the valve is another area where energy can be saved. Conventional valves have a quiescent first stage internal leakage, as hydraulic fluid is constantly pumped through the jet or nozzle. This implies significant energy loss. Consequently, a new first stage has been designed to reduce the

internal leakage. By using a small first stage spool with significant overlap, the internal leakage is reduced.

The control of the first stage in a conventional valve is done by a torque motor. A torque motor is a complex, heavy and expensive device, due to winding of the coils, and the fine manufacturing tolerances of the flexure tube. Additionally, it requires a significant amount of manual work to install and to set up properly. Piezoelectric actuators are in comparison relatively light and simple. Piezoelectric actuators have previously been tested successfully for several servovalve applications. In this research, a piezoelectric ring bender was used to control the first stage. A ring bender is a small annular disc that can dome in a convex and concave fashion in response to an applied voltage. Its weight is a fraction of a conventional torque motor and it is less complex, since it is one part made from multiple layers of piezoelectric ceramic and electrodes.

Since the complexity and precision manufacturing of valve parts make them expensive and more time-consuming to set up, future valves need to be simple and easy to assemble. To further mechanically simplify the valve and to provide a greater flexibility of the controller design, the second stage feedback could be done by an electrical signal instead of the conventional feedback wire used in mechanical feedback valve.

The following section provides background on different hydraulic servovalve designs.

1.2 HYDRAULIC SERVOVALVE BACKGROUND

Hydraulic control systems are widely used in the industry. Servovalves are used within hydraulic control systems when high force, fast response, high power to weight ratios and greater position control accuracy are demanded [3][4]. Servovalve is usually a two-stage device where the first stage works as an amplifier to the second stage, and the second stage is typically a sliding spool. Servovalves amplify a low electrical input signal to a high hydraulic force [5]. The second stage positioning feedback is conventionally made through mechanical feedback using a ‘feedback wire’. In traditional two stage servovalves with mechanical feedback and a torque motor, the steady state spool position is proportional to the electrical input current to the torque motor [6][7]. This is achieved by a feedback spring exerting a feedback torque on the torque motor proportional to spool position. Most servovalves used in industrial and aerospace use this mechanical second stage positioning feedback [8].

A conventional two stage servovalve can be seen in Figure 1-1, where the torque motor, flexure sleeve, feedback spring (feedback wire) and the second stage spool and bushing can be seen.

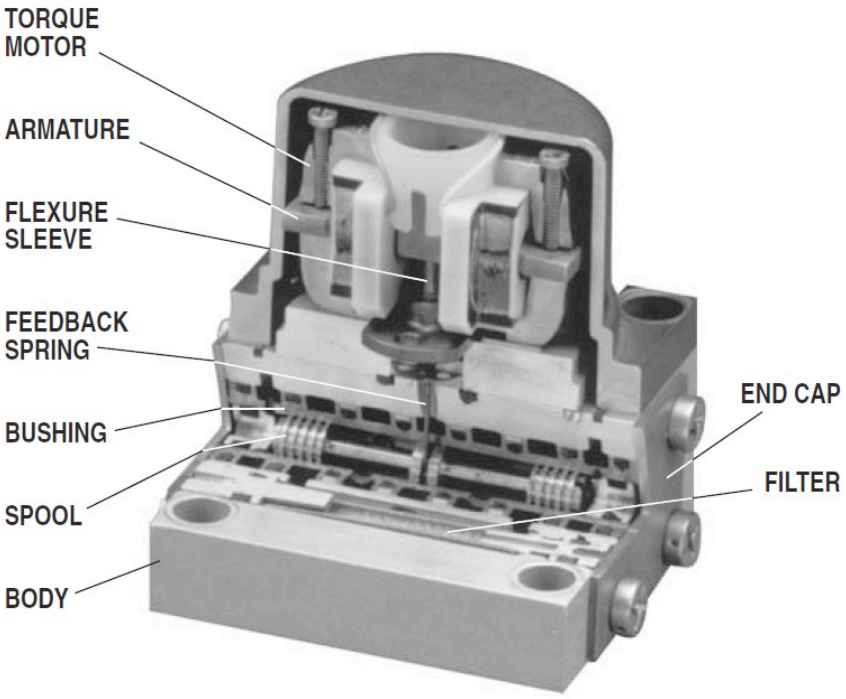

Figure 1-1. Cross section of Moog 264 series servovalve [7].

Typically, the first stage is controlled by a torque motor that is then coupled with a hydraulic amplifier. There are several types of hydraulic amplification. The most common types are a nozzle flapper, a jet pipe or a deflector jet. All these hydraulic amplifier arrangements will create a pressure difference in the two control ports that will act on the different sides of the second stage spool. This will make the second stage spool move, which in turn then directs flow to move an actuator.

The nozzle flapper arrangement is described in multiple sources [9][10][11] and a nozzle flapper valve can be seen in Figure 1-2. In a nozzle flapper valve, the torque motor will move the flapper and will restrict the exit flow from one of the nozzles, in this case on the right side. This will create a pressure increase in that control port and create a pressure difference between the two ends of the second stage spool. This pressure difference will force the second stage spool to move, which can be observed in Figure 1-2, where the pressure increase will be on the right side and force the second stage spool to move to the left.

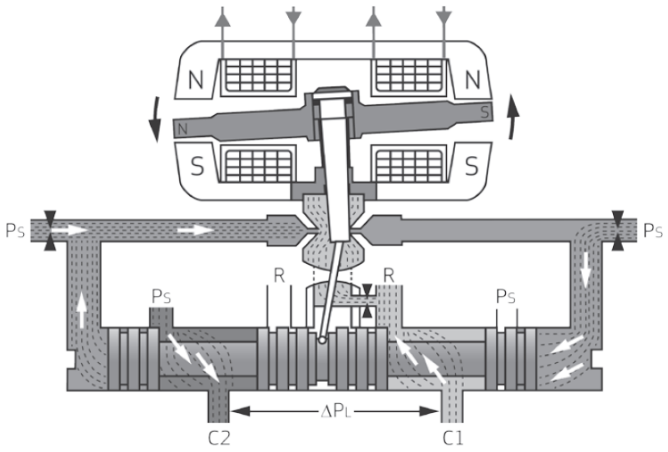

Figure 1-2. Cross section illustration of a nozzle flapper valve arrangement, including the torque motor and the second stage spool. Ps is supply pressure and R is return pressure [10].

In the jet pipe arrangement, the torque motor moves a nozzle (jet pipe) from which a jet of fluid is directed into two control ports, C_1 and C_2. At the null position the jet is directed in the middle of the two control ports, hence there is no pressure difference. As the nozzle is moved away from the null position more of the jet will enter one of the control ports, which will increase the pressure in that control port and move the second stage spool [11]. A schematic diagram of jet pipe hydraulic amplifier arrangement can be seen in Figure 1-3, where the movable nozzle, with supply pressure P_s, and the two control ports ($C_1$and C_2) can be observed.

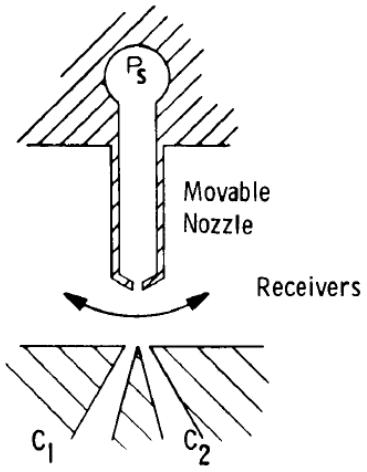

Figure 1-3. Schematic diagram of a jet pipe hydraulic amplifier [11].

The Deflector Jet (DJ) hydraulic amplifier arrangement is similar to the jet pipe in the sense that a jet is directed into two receivers. In the DJ arrangement, the root of the feedback wire has a slot through which a jet of hydraulic fluid is be forced. The slot has a 'V-shape' design, and is called a deflector, to be able to direct the jet, as can be seen in Figure 1-4. As the deflector is moved away from its null

position, the jet is deflected into one of the two control ports, to create a pressure difference to move the main stage spool. In Figure 1-4 the deflector is moved to the right to direct the flow and increase the pressure in control port B.

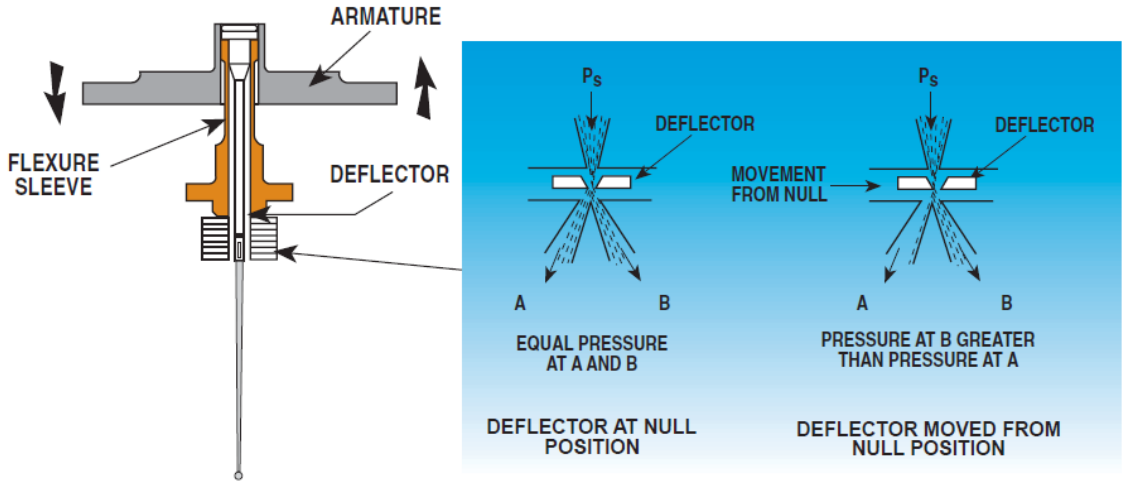

Figure 1-4. Deflector jet arrangement. The left side shown the armature flexure sleeve and deflector. The right side shows the deflector and the pressure increase in control port B as the deflector is moved to the right [7].

The next section will describe the torque motor used to control the first stage arrangements described in this section.

1.3 Torque Motor

A conventional first stage module with the torque motor can be seen in Figure 1-5. The torque motor is a limited rotation electromagnetic actuator and made up of an armature, two coils and two pole pieces. It also consists of a flexure tube and flapper. An illustration of a torque motor can be seen in see Figure 1-6. The pole pieces are permanent magnets with opposite polarisation. The armature is fitted in between the upper and lower pole piece. The two sides of the armature polarity will change due to the direction of the current flowing through the coils around the armature. Depending on the current supplied to the coils the armature will rotate in a clockwise or counter clockwise direction [12].

Figure 1-5. First stage module of Moog 264 series servovalve including the torque motor assembly and the amplifier segment [7].

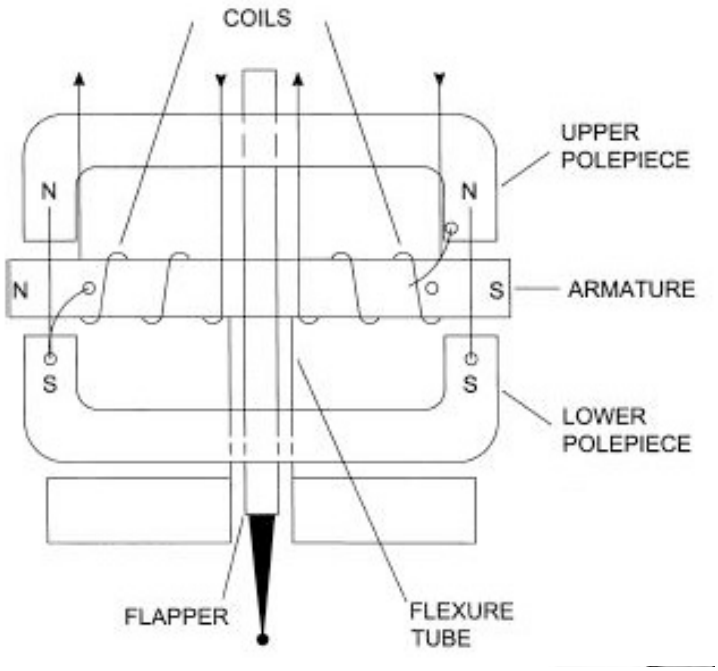

Figure 1-6. Illustration of a torque motor showing the poling pieces, armature, coils, flapper and flexure tube [12].

There are limitations and concerns with torque motors. Torque motors are usually divided into two categories, wet and dry [3]. For the wet application, the torque motor is submerged in the hydraulic fluid, which over time can attract and accumulate unwanted metallic particles that are in the hydraulic fluid, which could eventually cause a failure [13]. The dry application is more commonly used, where the torque motor is isolated from the hydraulic fluid. This is achieved by introducing a 'flexure tube' which acts as a frictionless seal [14]. This will eliminate the issues with metallic particles accumulating on the torque motor. However, the flexure tube introduces design challenges. The flexure tube needs to be frictionless seal and needs to be manufactured to fine tolerances to provide the desired mechanical characteristics. The flexure tube makes the manufacturing and assembly of the first stage both expensive and time consuming.

Due to its fine mechanical tolerances of the flexure tube, the winding of coil wire, a torque motor is relatively complex and expensive. It is also time consuming to implement and to set up into the valve due to the extensive manual intervention needed to be appropriately installed on to the valve.

The next section will highlight the aim and objectives for this PhD research.

1.4 AIM AND OBJECTIVES

The aim of this project is to design and investigate a new type of aerospace servovalve. The servovalve should have the potential to be lightweight, reliable, robust and more efficient.

This research started with a project called Valve Integration Through Additive Layer Manufacturing or in short VITAL. This was a collaborative project between the University of Bath, Moog and Renishaw. There were several outcomes from the initial phase of the VITAL project:

i. Understanding the material properties through extensive fatigue testing.
ii. Understanding how the laser settings and parameters affect the material microstructure.
iii. Work was conducted to decide on the material for the AM valve body.
iv. Deciding on design concept of the valve. Work was conducted to investigate different possible low leakage designs using a piezoelectric actuator. The design of the valve used in this research is an outcome of this work.

When the initial phase of the VITAL project came to an end there were still areas that needed to be further investigated, which leads to this PhD research.

The key objectives of the PhD are:

i. To design, manufacture and test a practical piezoelectric actuated servovalve suitable for aerospace use.
ii. To create an analytical dynamic model of the prototype valve. This is to be able to gain more understanding about the valve characteristics.
iii. Create a main spool position control algorithm, which uses electrical position feedback, to compensate for the first stage non-linearities caused by overlap and piezoelectric hysteresis.
iv. Investigate durability of piezoelectric ring benders operating in phosphate ester based hydraulic fluid and to test possible encapsulation methods. This is the type of fluid used in civil aerospace applications.
v. Analytical investigation to obtain an optimum mounting arrangement for the piezoelectric ring bender and to create a mounting design guideline.

The valve(s) and test equipment developed during the VITAL project are used as the basis for the subsequent investigations.

AM was chosen as it only adds material where material is needed, with the hope of making it lighter than conventional manufactured valve bodies. This manufacturing method will also provide new design possibilities.

A final design for a valve is not created as a part of this research, instead the research is to provide the knowledge base and to test the principles concerning piezoelectric ring benders and AM so that a light weight low leakage valve can be produced in the future.

The following section will highlight the original contributions described in this thesis.

1.5 ORIGINAL CONTRIBUTION

The original contribution of this PhD research is the following:

i. Detail design of a novel two-stage additive manufactured valve body.
ii. Understanding the characteristics of the piezoelectric actuated valve, through validation of an analytical model against experimental results.
iii. Creating and experimentally validating a controller algorithm to compensate for the piezoelectric hysteresis and the first stage spool overlap. The controller also includes a feed-forward path to increase the bandwidth.
iv. Analytical investigation to optimize the ring bender mounting and to create a guide line for design of the mounting. Create a method to optimise the thickness-overlap combination and the Young's modulus of the mounting material.
v. Understanding of failure modes of the piezoelectric ring benders in a phosphate ester based hydraulic fluid called Hyjet and test possible encapsulation to protect the ring bender.

The structure of this thesis will be described in the following section.

1.6 STRUCTURE OF THESIS

This thesis has been separated into eight chapters describing the investigation and development of a piezoelectric ring bender actuated two stage servovalve.

Chapter 2 presents a literature review of the piezoelectric ceramic, the ring bender, piezoelectric actuated valves, durability and encapsulation, piezoelectric hysteresis compensation, mounting of the ring bender and additive manufacturing for aerospace.

Chapter 3 presents the design of two-stage piezoelectric actuated servovalve that was investigated in this research. This includes an Additive Manufactured valve body, piezoelectric ring bender, first stage spool with significant overlap and the controller platform.

Chapter 4 explains the analytical modelling of the valve. This includes the amplifier, the piezoelectric ring bender with hysteresis, first stage flow and the second stage spool motion.

Chapter 5 presents a proposed controller design for second stage spool position control. The controller includes compensation for the piezoelectric hysteresis, compensation for the first stage spool overlap and a feed-forward loop to increase the bandwidth of the valve.

Chapter 6 analyses the ring bender mounting to create guidelines to obtain a good overlap-thickness ratio. This includes a FEA investigation to obtain the axial and torsional stiffness of the mounting for different overlap and thickness levels. This is incorporated into an analytical model based on the Timoshenko plate bending equations, but incorporates the mounting stiffness models.

Chapter 7 presents an investigation of the durability of a piezoelectric ring bender submerged in a phosphate ester based hydraulic fluid called Hyjet. This investigation includes an examination of how failures could occur, and presents a possible encapsulation method.

Chapter 8 the final chapter presents the conclusions from the research and describes possible avenues of future research that still could to be investigated.

1.7 LIST OF PUBLICATIONS

This section presents a list of publications that the author has written and been involved with percentage contribution in brackets.

List of publications where the author of this thesis has been the main author:

i. "Design and Modelling of a Novel Servovalve Actuated by a Piezoelectric Ring Bender" [15]. An analytical model of the first stage was described in this paper. It included the amplifier, the piezoelectric ring bender, hysteresis model and flow curve. The model was validated against experimental data. (80%)
ii. "Dynamic Modelling and Performance of a Two Stage Piezoelectric Servovalve" [16]. The paper describes an analytical model and validated against experimental data. It includes the amplifier, first stage piezoelectric ring bender and spool and second stage behaviour. (80%)
iii. "Non-linear Control of a Piezoelectric Two Stage Servovalve" [2]. This paper describe a novel controller to compensate for the overlap on the first stage spool, compensate for the hysteresis of the piezoelectric ring bender and incorporated a velocity feed forward loop to increase the bandwidth. (80%)

List of publications where the author of this thesis has been a co-author:

i. "Mechanical Properties of titanium-based Ti–6Al–4V Alloys Manufactured by Powder Bed Additive Manufacture" [17]. This paper is a literature review of the mechanical properties of

the of the titanium Ti-6Al-4V alloy that was used to manufacture the valve body in this research. (25%)

ii. "Non-linear Control of a hydraulic piezo-valve using a generalised Prandtl–Ishlinskii hysteresis model" [18]. This paper uses the Prandtl-Ishinskii hysteresis model to compensate for the hysteresis in a piezoelectric ring bender. The author of this thesis wrote parts of the paper, helped to control the ring bender and was involved in discussions throughout the work. (25%)

iii. "A Lightweight, Low Leakage Piezoelectric Servovalve" [19], [20]. This paper was written to present the prototype valve in this research for the aerospace industry in Toulouse. This paper is based in the work of the author of this thesis and the author has written large parts of the paper, but the paper was composed by Professor Andrew Plummer. (65%)

2 LITERATURE REVIEW

In this project a piezoelectric ring bender actuator is chosen to control a servovalve, therefore this section presents a literature review covering piezoelectric ceramics, piezoelectric ring benders, piezoelectric controlled valves, durability and encapsulation of piezoelectric actuators, piezoelectric hysteresis control and mounting of ring benders. Additive manufacturing is used for the prototype valve manufacturing so this is also briefly reviewed.

2.1 PIEZOELECTRIC CERAMIC

Piezoelectricity is the name of the phenomenon of a crystalline material to develop an electrical charge from a mechanical applied stress [21][22]. This piezoelectric effect was discovered by Jacques and Pierre Curie in the year 1880 [21][22][23]. The word piezo stands for pressure [24]. Nowadays piezoelectric ceramics are used in a wide range of applications like diesel injection pumps, submarine sonar, micro pumps, ultrasonic cleaning, medical applications and energy harvesting [25].

A piezoelectric ceramic will produce an electrical charge or voltage, when a mechanical stress is applied to the piezoelectric ceramic. This process is called the direct piezoelectric effect. The direct piezoelectric process is reversible, where a voltage or charge is applied to a piezoelectric material, resulting in stress created in the material that will force the ceramic to change shape. This is called the converse piezoelectric phenomenon. For sensing technology the direct piezoelectric effect is used while the converse piezoelectric effect is used for actuators [23].

One of the most common piezoelectric material is lead zirconate titanate (PZT) [26]. The piezoelectric effect arises from the non-centrosymmetric crystal lattice structure of the dipoles, see Figure 2-1 (b) where the Ti or Zr ion is not centred (the Ti and Zr are positively charged). The crystal structure is symmetric and cubic at temperatures above a certain critical temperature called curing temperature. The symmetrical crystal structure of the PZT ceramic above the curie temperature can be seen in Figure 2-1 (a). Due to the symmetric lattice structure above the curie temperature no piezoelectric effect can be obtained. At temperatures lower than the curie temperature the lattice structure deforms into a tetragonal or rhombohedral structure, which can be seen in Figure 2-1 (b) [3][26]. The positive charged Ti or Zr ion will displace away from the centre, in this case upwards, which will have the effect that the upper region of the dipole will be more positively charged compared to the bottom part that will be negatively charged.

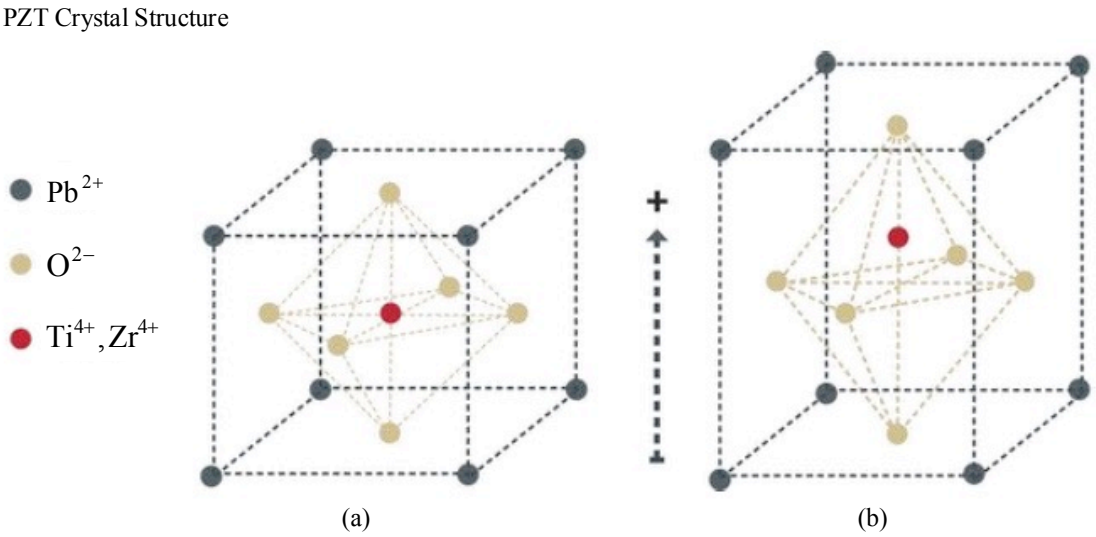

Figure 2-1. PZT crystal structure (a) symmetric state above curie temperature resulting in no piezoelectric effect (b) unsymmetrical state below curie temperature where the Ti, Zr is offset from the centre introducing piezoelectric effect [26].

A cluster of dipoles, with their positively charged side in the same direction, is called a domain. Before the so-called poling process, the grains and domains in a piezoelectric material are randomly orientated, see Figure 2-2 (a). The material is isotropic, which results in that the net polarisation of the material is zero. This implies that the material exhibits no piezoelectric properties. During the poling process, the material exhibits a high electrical field under which the domains in the material align in the field direction, as can be seen in Figure 2-2 (b). The poling process is usually done at a relatively high temperature, but below the curie temperature, to make it easier for the domains to align. The material will be cooled down while the high electric field is still applied. After the high electric field has been removed, the domains 'freeze' into the current alignment and will permanently remain aligned, see Figure 2-2 (c). This process is called the 'poling' process, which will induce piezoelectric properties to the ceramic [26][3][23].

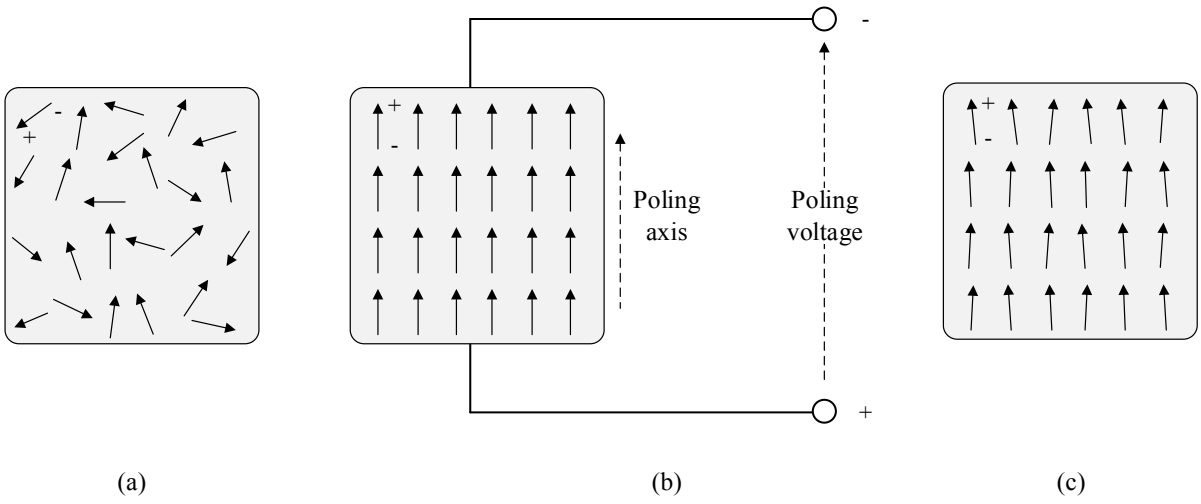

Figure 2-2. (a) Randomly orientated domains before the poling process (b) poling process with a voltage applied (c) as the voltage is removed domains remain permanently aligned.

The domains will not remain perfectly aligned, but will shift slightly when the electric field is removed, see Figure 2-2 (c). This slight shift of the domains will cause creep. Creep is the effect that the domains start to align with the electric field as the final voltage is reached. Creep will occur over time and thus is usually a low frequency issue [27]. Due to creep, the piezoelectric material might change displacement over time under the same voltage.

Hysteresis is another phenomenon of piezoelectric actuators. Hysteresis implies that for the same applied voltage, different displacements can be obtained, which is due to movements of ferroelectric domains. As a voltage is applied, the domains will start to rotate, and as the voltage is reduced the domains will not return to their initial position.

The following section will describe the piezoelectric ring bender used for this research project.

2.2 PIEZOELECTRIC RING BENDER

There are multiple different types of piezoelectric actuators: ring stacks, plate stacks, rectangular benders, shear stacks and amplified actuators with several piezoelectric actuators combined. However, for the research completed in this PhD investigation an actuator manufactured by Noliac called a 'ring bender' was used.

Considerable work has been undertaken on stack and bending actuators [28]. The ring bender developed by Noliac has become available relatively recently, which is an annular disk that domes in a concave or convex fashion depending on the applied voltage, as can be seen in Figure 2-3 [28][29][30]. A Ring bender can provide a stroke and force output similar to that of a torque motor, so it is a good candidate for a servovalve first stage actuation. A ring bender is a bipolar multilayer three wire device that can bend in both directions depending on the sign of the applied voltage [30]. There are specific advantages

with this type of arrangement: an increase in displacement in relationship with its size compared to stack actuators and an increase in its stiffness in comparison to rectangular bending actuators of similar size [28][30], see Table 2-1 [31][32][33]. A comparison between free stroke and blocking force between different kinds of piezoelectric actuators manufactured by Noliac can be observed in Figure 2-4, where it can be seen that the piezoelectric ring bender provides a good compromise between force and stroke.

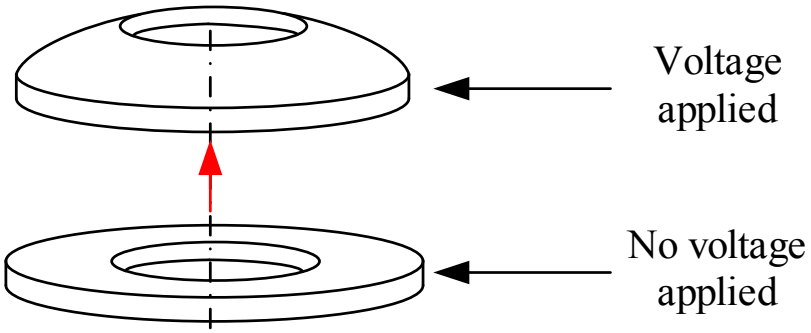

Figure 2-3. Doming effect of the piezoelectric ring bender when no voltage is applied and when voltage is applied.

Table 2-1. Piezoelectric actuator, manufactured by Noliac, comparison between a ring stack, a plate bender and a ring bender of similar size. Comparing stiffness, displacement and blocking force.

Actuator	**Dimensions (mm)**	**Stiffness (N/µm)**	**Displacement (µm)**		**Blocking force (N)**
			Min	**Max**	
Ring stack (HAC2125-Hxx)	Outer diameter: 20 Inner diameter: 12 Height: 4	2817	0	3	8450
Plate bender (CMBP08)	Length: 50 Width: 7.8 Thickness: 1.3	0.0019	-850	850	1.6
Ring bender (CMBR08)	Outer diameter: 40 Inner diameter: 8 Height: 1.25	0.34	-115	115	39

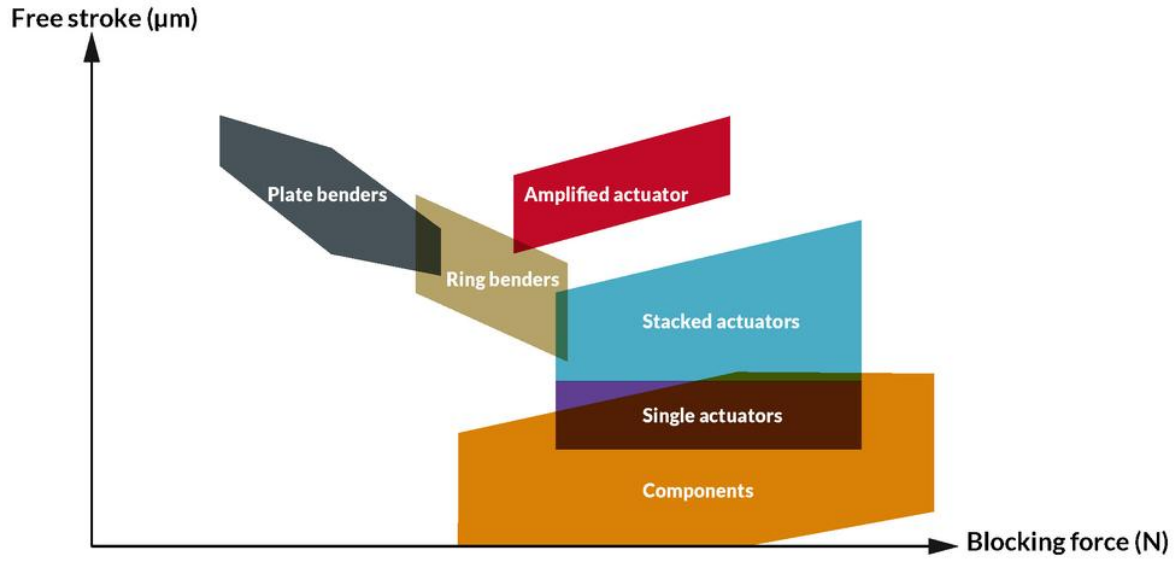

Figure 2-4. Comparison between different kind of piezoelectric actuators in regards to free stroke and blocking force [29].

Figure 2-5 (a) shows a Noliac ring bender with the wires attached. The Noliac piezoelectric ring benders are made up of 67µm thick piezoelectric ceramic layers. Between the piezoelectric ceramic layers there are silver palladium electrodes. For the piezoelectric ceramic material to deflect, an electrical field needs to be applied. Therefore, the electrodes are combined into three groups, see Figure 2-5 (b). One third of the electrodes are maintained at low voltage (-100V, black wire), one third are maintained at high voltage (+100V, red wire) and the voltage is varied on the remaining electrodes (control electrodes, blue wire). The variable voltage (control voltage) varies between -100V to +100V. As a result of this electrode configuration, half of the piezoelectric ceramic layers will force the ring bender to bend in one direction and the other half in the other. As the voltage is varied the electric field between the electrodes changes, and as a result the ring bender changes shape. At zero control voltage, the action of the electric fields will cancel each other out, resulting in zero displacement of the piezoelectric ring bender. With non-zero control voltage, the electric field in one set of layers will be larger than in the other, resulting in a movement of the piezoelectric ring bender.

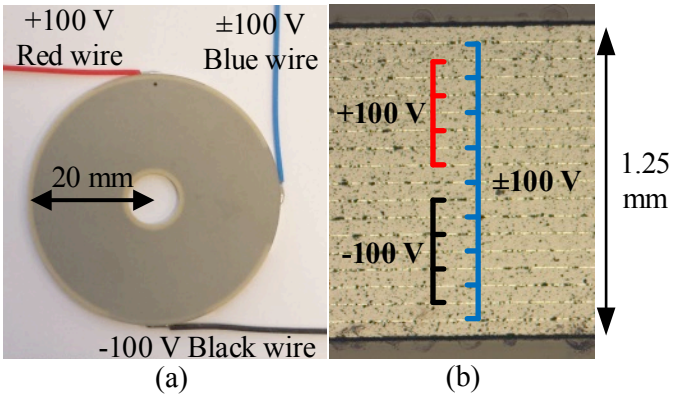

Figure 2-5. (a) Photograph of a Noliac ring bender with the three wires attached (b) Microscopic section of a piezoelectric ring bender where the internal electrodes (lighter colour horizontal lines) can be seen.

There are multiple alternative piezoelectric actuated valve designs investigated in the literature and the next section will present some of these.

2.3 PIEZOELECTRIC ACTUATED VALVES

Sangiah [3] developed a two stage piezoelectric bimorph actuated servovalve. It was based on a Moog 26 series DJ valve. However, instead of the conventional first stage torque motor, a piezoelectric bimorph bender was used to control the first stage. The valve still had a mechanical second stage feedback, where the feedback wire was attached to the rectangular piezoelectric bimorph bender. The piezoelectric bender bends and deflects the fluid jet into one of the control ports that move the second stage spool, as described in section 1.2. A schematic cross section of the valve developed by Sangiah can be seen in Figure 2-6, where the rectangular bimorph actuator, deflector, feedback wire, control ports and the second stage spool can be seen. This arrangement could potentially make the valve lighter due to the weight difference of the piezoelectric bender in comparison with a torque motor. However, a conventional DJ arrangement is used, which have a constant internal leakage. It also still uses a mechanical feedback using a feedback wire. It can be difficult to attach the feedback wire to the bender without damaging the actuator.

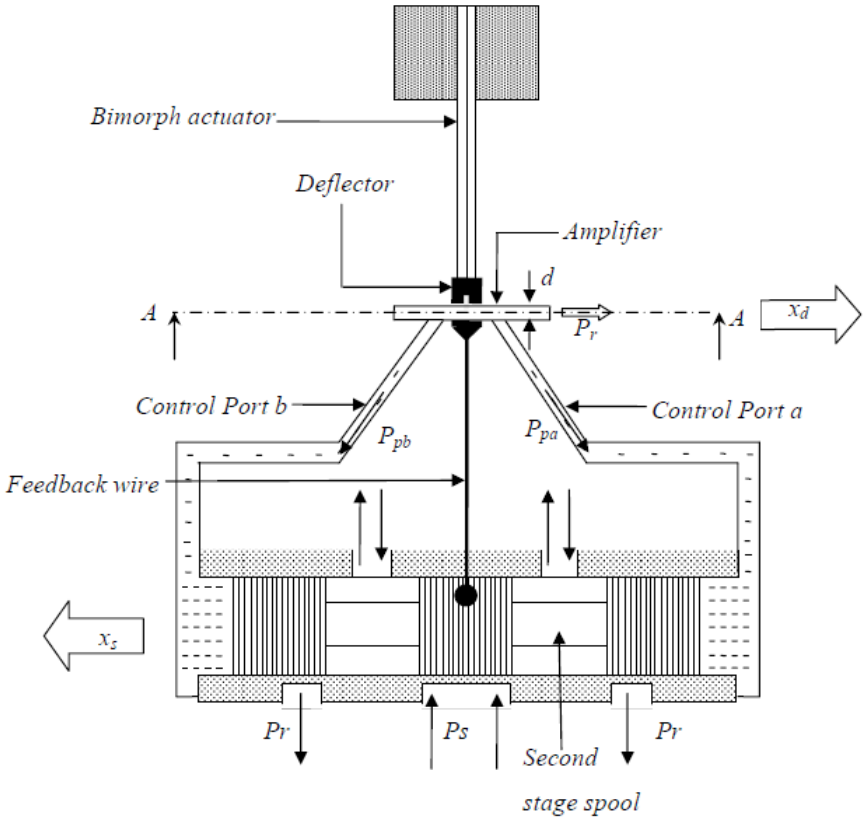

Figure 2-6. Cross section illustration of rectangular piezoelectric bender controlling a deflector jet valve developed by Sangiah [3].

Lihui et al. [34] developed a piezoelectric valve, replacing the torque motor with a rectangular piezoelectric bender to control a nozzle flapper valve, which in turn controls a second stage spool. Additionally, an electrical second stage positioning feedback was used for control, which meant that no feedback wire was used. A schematic cross section of the piezoelectric nozzle flapper valve can be seen in Figure 2-7, where the piezoelectric bender, the spool and the electrical sensor can be seen. Similar to Sangiah, Lihui replaces the torque motor with a piezoelectric bender, but is using a conventional nozzle flapper arrangement, but with an electrical second stage position feedback.

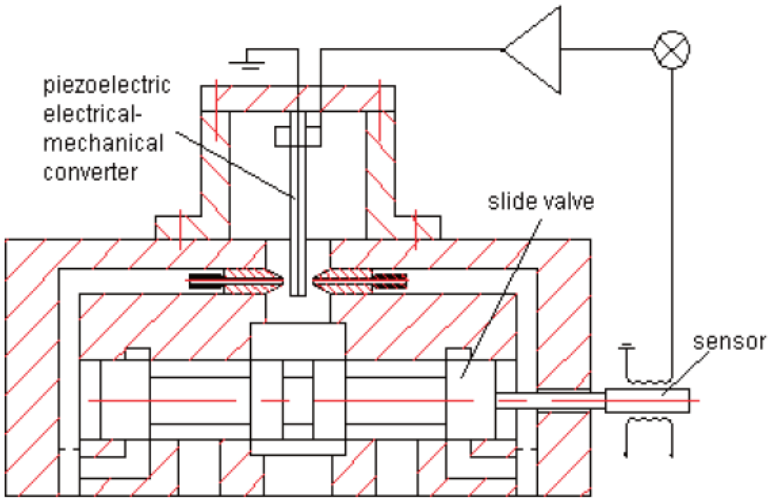

Figure 2-7. Cross section illustration of rectangular piezoelectric bender controlling a nozzle flapper valve [34].

Piezoelectric Direct Drive Valves (DDV) have been investigated as a way of obtaining high bandwidth. The main feature of a DDV is that the 'main' spool is directly controlled without a hydraulic first stage amplification. Jeon et al. [35][36] have created a DDV using a piezoelectric stack actuator with a mechanical amplification to control the spool. Due to the limited stroke relative to the length of the piezoelectric stack actuator, an amplification device is needed. Jeon et al. applied a flexible beam mechanism to transfer the force and amplify the displacement of the piezoelectric stack to the spool. A return spring is used to force the spool back to its initial position as the voltage to the piezoelectric stack is decreased. A schematic cross section of the valve developed by Jeon et al. can be seen in Figure 2-8. This valve is essentially controlling the flow rate from one port to another and not controlling the spool into different control ports. This arrangement could potentially be adjusted to control the flow into different control ports, but to eliminate any asymmetry the amplification device and the spring needed to be manufactured with very tight tolerances.

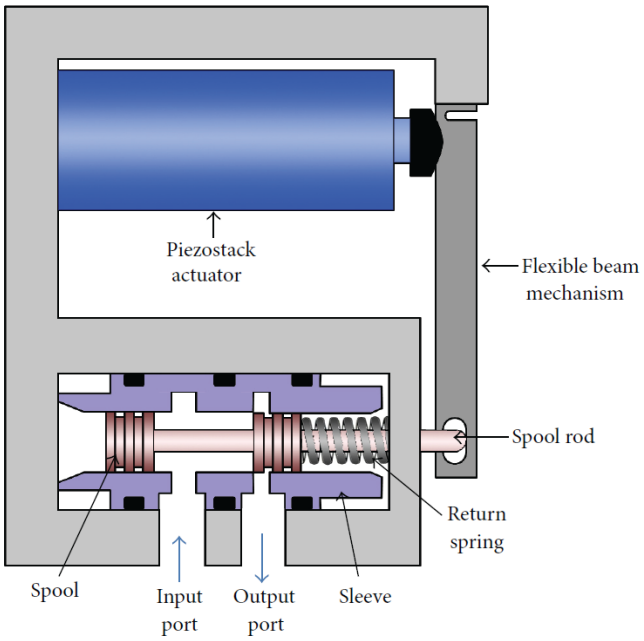

Figure 2-8. Illustration of a DDV actuated by a piezoelectric stack with a flexible beam [35].

Johnston et al. [37] describe a piezoelectric valve where a piezoelectric stack actuator is controlling the flow through a Hörbiger plate, see Figure 2-9. The piezoelectric stack will control the upper plate and at full applied voltage will provide minimum flow and as the voltage is reduced the plates will move further apart and increase flow rate. This valve design provides a high flow valve at a high frequency. However, it can only regulate flow between the ports and not directing the flow into different control ports. This valve does address the internal leakage, however to be able to control a second stage spool two of these valves would be needed to control the flow to either side of the spool. This could be useful in applications where low leakage and fast response are needed.

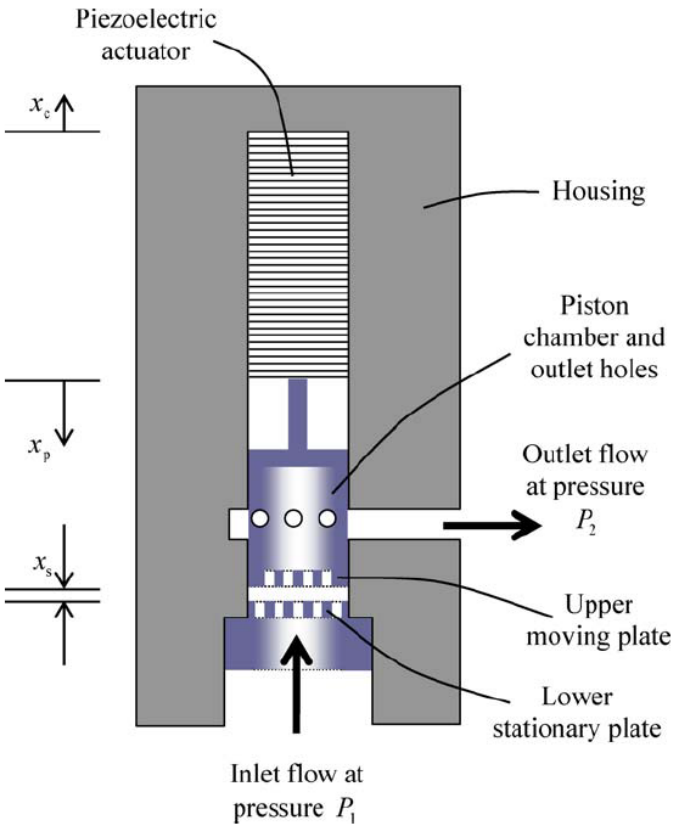

Figure 2-9. Illustration of a piezoelectric stack actuated Hörbiger plate valve [37].

In in the 1980's a piezoelectric actuated nozzle flapper valve were developed, where a piezoelectric double-layer plate was used to control the two nozzles that in return controls the main stage spool movement [38]. This valve arrangement can be seen in Figure 2-10, where number 12 shows the piezoelectric plate. This valve uses the same principle as Lihui using a nozzle flapper arrangement, but is using a piezoelectric plate instead of a rectangular bender.

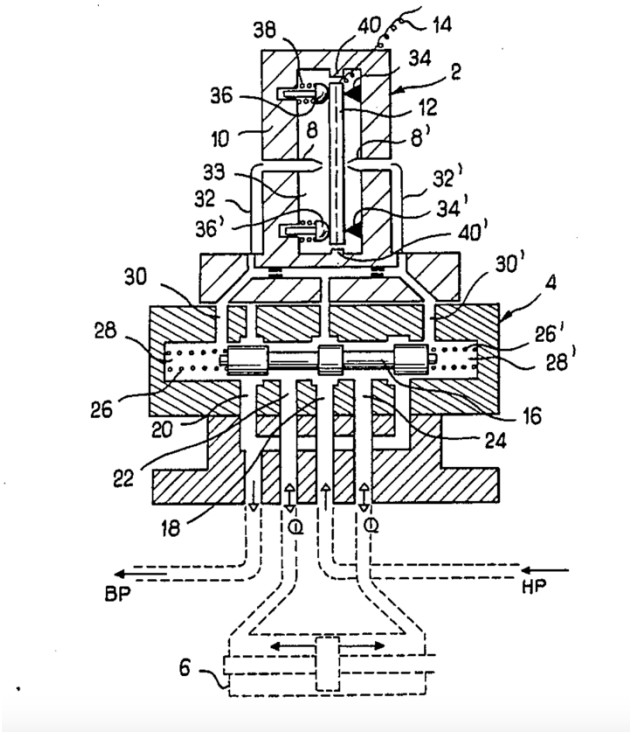

Figure 2-10. Piezoelectric double-layer plate actuating a nozzle flapper valve [38].

There is limited work examining the potential of piezoelectric ring benders. Bertin developed a two-stage fuel metering control valve for gas turbine aero engines controlled by a piezoelectric ring bender. The pilot stage is a nozzle flapper controlled by a piezoelectric ring bender and the second stage or main stage of the valve is a spool that regulates the size of the flow pathway through to the combustion chamber [39][28]. A schematic sketch of the first stage ring bender controlled nozzle flapper can be seen Figure 2-11. Bertin has also investigated ring bender mountings using elastomeric O-rings. Similar to previous presented valves, this could potentially make a valve lighter, but uses conventional nozzle flapper design and does not attempt to reduce the internal leakage.

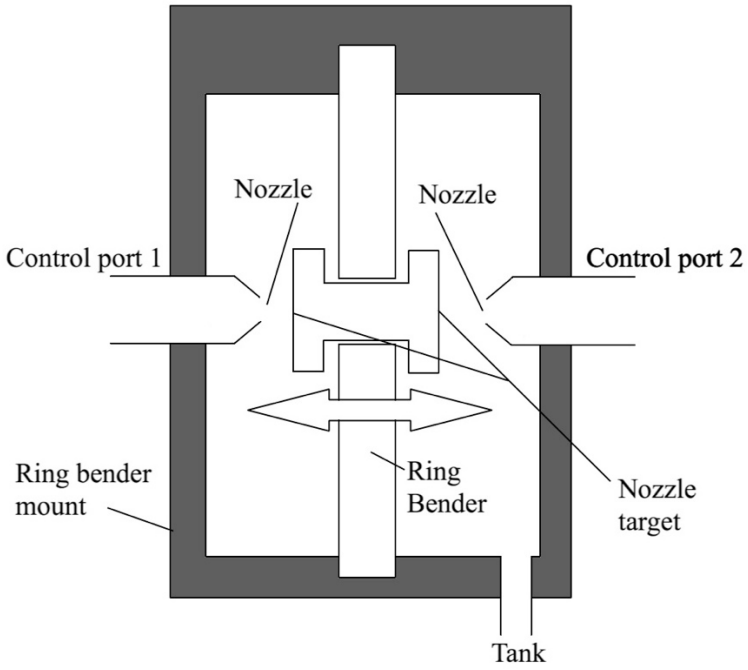

Figure 2-11. Nozzle flapper valve controlled by a piezoelectric ring bender designed by Bertin [39].

Wu [40] has been investigating and testing a microvalve for medical application using a piezoelectric ring bender to control nitrogen gas flow in a real-time blood pressure monitoring system. Ring benders have also been used in micro thrusters on the space probe LISA-Pathfinder [23][35].

For this research work, a Noliac CMBR08 multilayer piezoelectric ring bender was used for first stage actuation of a small spool in a two-stage valve. The piezoelectric ring bender used has a diameter of 40mm and thickness of 1.2mm, a free displacement of ±115µm and a blocking force of ±39N. This ring bender was used since it provides enough force and displacement to control a small hydraulic spool.

2.4 DURABILITY AND ENCAPSULATION

Nowadays the use of piezoelectric components is expanding fast. A concern regarding the use of piezoelectric actuators is durability, especially under high electrical field and in a humid environment or, like in this investigation, while submerged into a hydraulic fluid. Therefore, the durability of the piezoelectric actuator in a fluid needs to be known, and the need for encapsulation should be investigated.

When multilayer piezoelectric actuators are used in an environment containing water, failure can occur over time. Increased temperature and humidity has been reported to greatly decrease the lifetime of piezoelectric devices [42][43]. Degradation can occur when ionized atomic metal from the anode (positively charged electrode) will migrate through the piezoelectric material towards the cathode (negatively charged electrode). The metal is most likely to be have a high silver content, and migration will occur more easily the higher the degree of silver content of the electrodes. The silver will migrate through the grain boundaries or possible fractures within the piezoelectric ceramic [42][43][44][45], as

can be seen in Figure 2-12. As the silver ions get closer to the anode, heat will be produced which accelerates the migration. Eventually, the heat that is generated will melt the electrodes and destroy the actuator. In the case where the silver reaches the anode, it will short circuit and destroy that layer of ceramic. Silver migration can also cause holes in the piezoelectric material, as well as cracks [46].

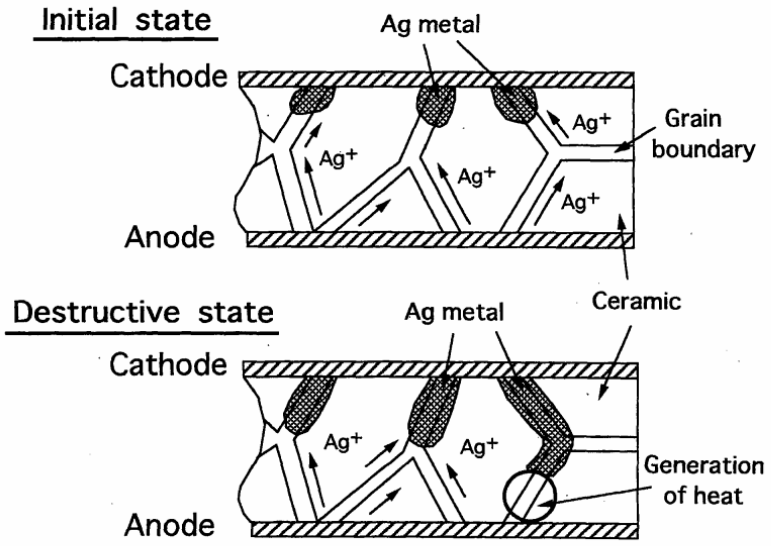

Figure 2-12. Degradation of a piezoelectric actuator due to metallic migration between two internal electrodes [42].

The shape of the piezoelectric actuator will have an impact on the failure rate of the actuator. Thanks to the lack of edges and the symmetric shape of a disc or ring bender, it is less sensitive to failure due to humidity or temperature compared to square shaped actuators. Noliac found that corners are the most common area where breakdown occurs. This is most likely due to the piezoelectric material being attacked from two sides [47]. To reduce this risk, the actuator could also be protected by an inactive protective layer of piezoelectric ceramic [46]. The Noliac ring benders have an inactive outer ceramic layer.

There are several patents for protection of piezoelectric actuators in harsh environments. Most patents propose a multiple layer covering, where an inner layer is of a non-conductive polymeric material and the outer is a metallic layer. The polymeric layer provides electrical insulation and creates a chemical or humidity barrier [48]. However, the polymeric material alone is not enough to prevent humidity reaching the piezoelectric material, since most polymers are semi-permeable. Therefore, the second layer of metal is applied, since metal is impermeable. There are multiple ways in which the polymer and metallic layer can be applied.

Bosch et al. [49] describe a multilayer protection where the first and second layer should be of a insulation polymeric material with an outer conductive metallic sheet wrapped around both the piezoelectric actuator and the polymer layer. Berlemont [48] describes a method where a heat shrink

polymeric sleeve are applied around the actuator with a second layer of metallic film that is held in place by a second layer of heat shrink polymer.

Bayer et al. [50] suggests a similar technique where the piezo actuator is encapsulated with an insulating polymer layer and then an outer metallic layer. However, Beyer et al. are suggesting that the metallic layer can be created by a Physical Vapour Deposition method (PVD) on top of an insulating polymer layer. The polymer layer could be created by methods such as dipping, spraying, injecting, screen printing or lamination of films. To protect the piezoelectric actuator, they are also suggesting that this could be accomplished by cold gas spraying. In cold gas spraying, metallic particles are sprayed onto the piezo actuator surface. The kinetic energy of the individual particle hitting the surface creates a welding/melting zone for each individual particle.

There are also ideas of using a gas as insulation for piezoelectric actuator. Cooke [51] describes an encapsulation approach where a layer of gas is surrounding the piezoelectric actuator. The gas should be at a pressure higher than atmospheric pressure and could be retained with a polymer layer.

2.4.1 Diesel Injector

The diesel injector is a piezoelectric controlled valve to control the flow of diesel in a car diesel engine. The piezoelectric actuator used in a diesel injector is a stack actuator and since it is operating in a fluid it needs to be protected from the environment. The purpose to examine a diesel injector is to investigate how the piezoelectric stack actuator inside a diesel injector is isolated and protected from the diesel. A conventional diesel injector was dissected and investigated.

The main parts of the injection pump, including the piezo actuator, nozzle module, control valve and coupling module can be seen in Figure 2-13 which shows a cross section of a diesel injector. When the piezo actuator expands, it will open the nozzle module to release a desired amount of diesel out. The rapid dynamic response of a piezo actuator, which gives good control over the fuel rate injection [52], combined with the high loading capability, makes a piezo stack actuator ideal for a common rail fuel injector. However, as the piezo actuator will be completely surrounded by the fuel, which is called a “wet design”, a protective envelope needs to be provided for the piezo actuator. This envelope needs to provide electric insulation as well as protection against chemical attack [50].

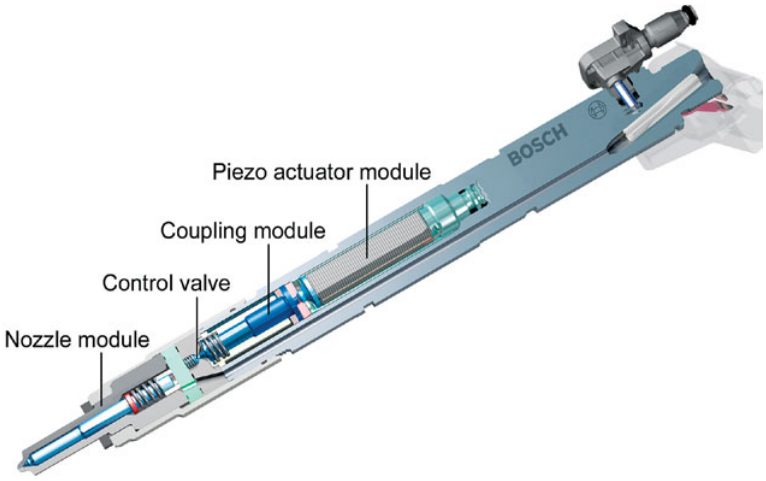

Figure 2-13. Cross section of a piezoelectric diesel injection pump [53]

Figure 2-14 shows the diesel injector before disassembly, and Figure 2-15 shows the location of the piezo along with the other parts in the disassembled pump. The piezo actuator was removed from the main body and can be seen in more detail in Figure 2-16, which shows the piezoelectric actuator and its encapsulation, and Figure 2-17, which shows the piezoelectric actuator and the encapsulation when the metallic layer is removed. As described earlier, the piezo stack was encapsulated in a polymer coating and wrapped in a metallic casing. The metallic encapsulation needed to be cut lengthways and removed in order to see the polymer layer and the piezoelectric actuator.

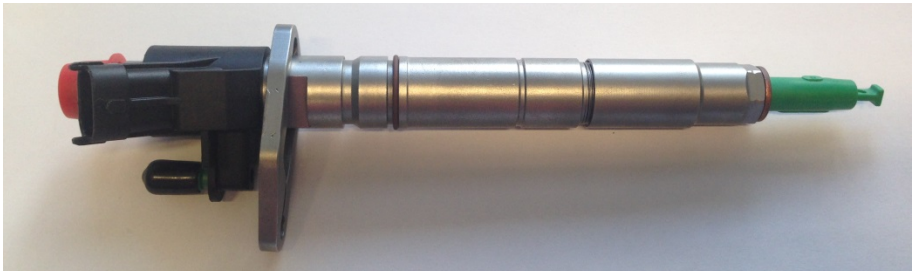

Figure 2-14. Photograph of a complete diesel injector.

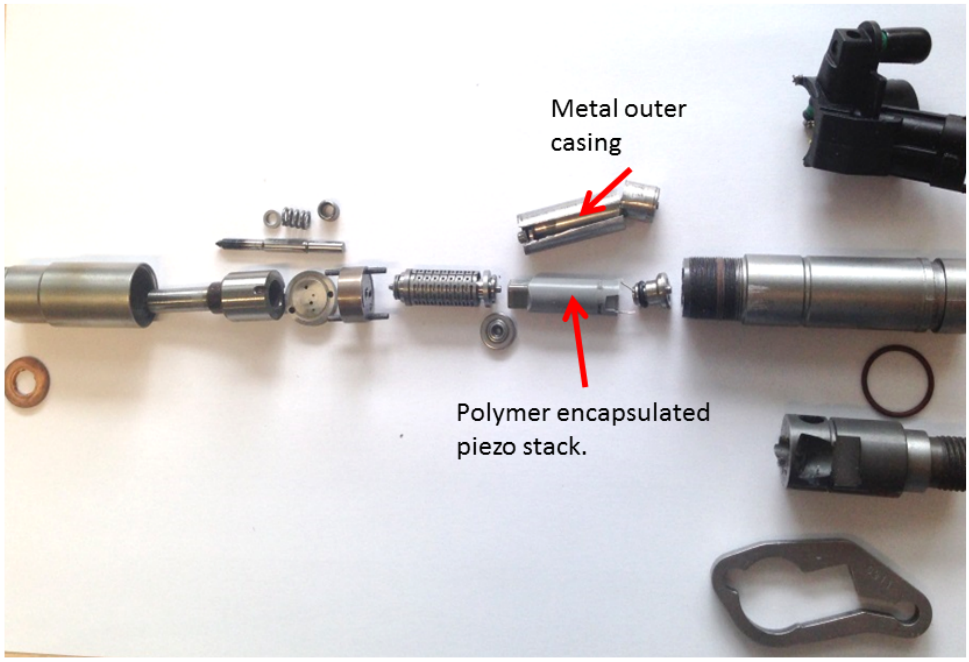

Figure 2-15. Parts inside the injection pump.

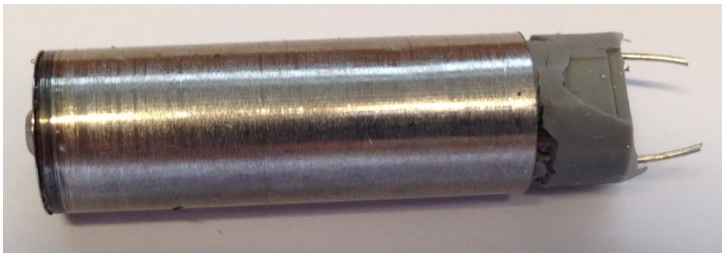

Figure 2-16. The encapsulated piezo actuator used in a diesel injection pump. Top of the metal casing taken off.

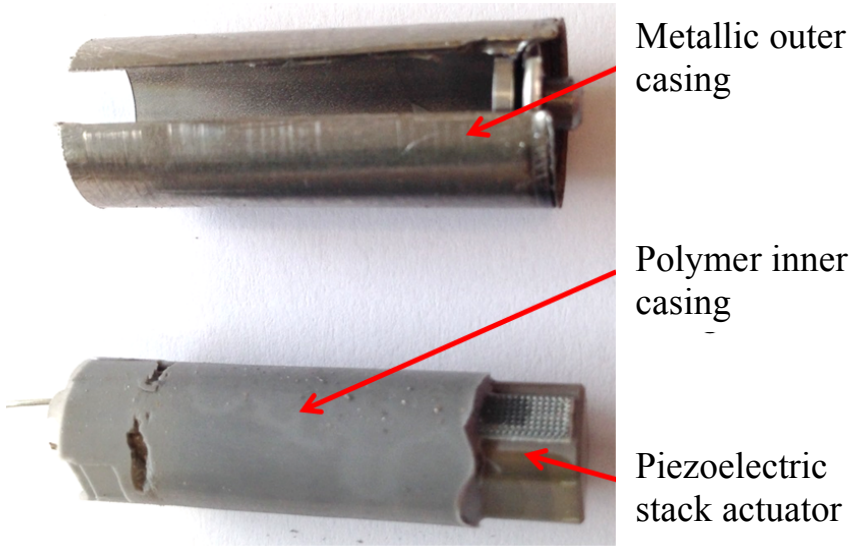

Figure 2-17. Piezoelectric stack actuator encapsulated by a polymer layer and the protective metal sheet.

2.5 PIEZOELECTRIC HYSTERESIS COMPENSATION

It is well known that voltage-driven piezoelectric actuators will exhibit hysteresis, typically of 20% magnitude [54][27]. In a positioning system, hysteresis could reduce the positioning accuracy and effect the control loop. Efforts have been made to eliminate or compensate for the hysteresis, and there are a number of possible solutions. First, is to implement a closed loop control system with actuator position feedback [54]. However, this solution needs a first stage position sensor, which adds complexity, size and weight to the valve, which is undesirable.

Most often piezoelectric actuators are driven by voltage amplifiers. Voltage hysteresis implies that for the same applied voltage, different displacements can be obtained, as can be seen in Figure 2-18 (a). However, by controlling a piezoelectric actuator with a charge amplifier the hysteresis is significantly reduced due to the near linear relationship between charge and displacement [55], see Figure 2-18 (b). However, charge amplifiers exhibit drift, and this problem has no satisfactory solution.

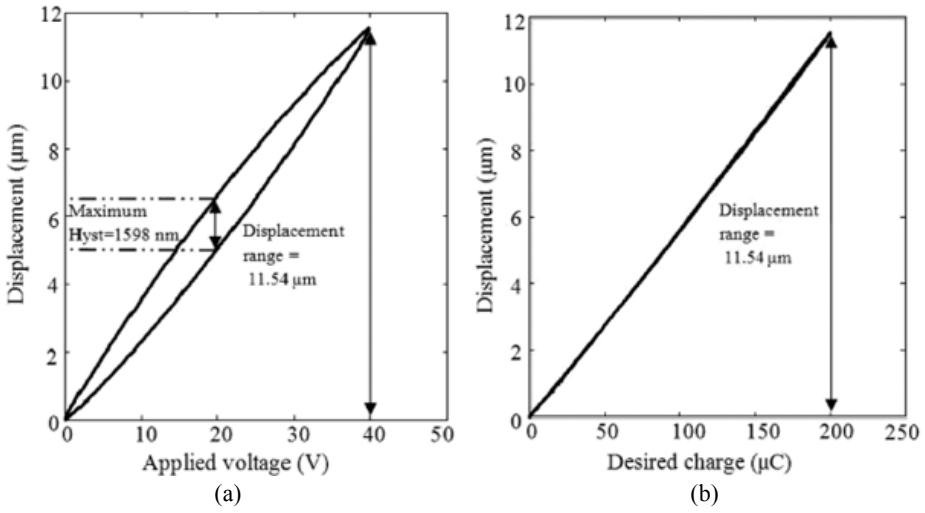

Figure 2-18. Piezoelectric hysteresis loop (a) hysteresis loop using a voltage amplifier (b) hysteresis loop using a charge amplifier [27].

Another approach to reduce the effect of piezoelectric hysteresis is to implement an inverse model of the hysteresis into the control loop, as can be seen in Figure 2-19. This is done by first modelling the hysteresis of a piezoelectric actuator, and incorporating the inverse model into the control algorithm. This solution has been investigated in multiple papers both for piezoelectric and other smart actuators which exhibits hysteresis [56][57][54].

In addition to research presented later in this thesis, the author has been involved in investigating the use of a Prandtl-Ishlinskii model to reduce the hysteresis of a piezoelectric ring bender, as can be seen in the paper in Appendix A.3.1 [18].

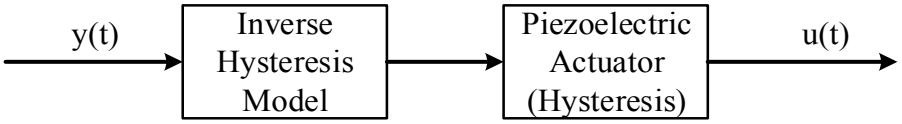

Figure 2-19. Example of how an inverse hysteresis model can be implementation into a control algorithm.

2.6 MOUNTING OF RING BENDER

To be able to extract the maximum force and displacement from the piezoelectric ring bender the mounting design is essential. The mounting needs to be axially stiff enough to overcome forces on the first stage spool and to have minimum torsional stiffness to let the edges of the ring bender rotate [58].

Noliac suggests that piezoelectric ring benders are mounted by either using mechanical clamping or gluing. When using mechanical clamping, a moderate force should be applied close to the outer edge of the piezoelectric ring bender, as can be seen Figure 2-20 (a). The force applied needs to be as low as possible in order not to reduce the maximum displacement. Gluing with epoxy is also a possibility to mount the piezoelectric ring bender, Figure 2-20 (b). The outer edge mounting needs to be flexible enough to allow the outer edge of the piezoelectric ring bender to rotate and deform as well as being stiff enough the obtain the maximum force, hence not to reduce the output of the ring bender [59].

By investigating the deformation model described in Chapter 6 it can be seen that constraining the outer edge has more effect on the work output than constraining the inner edge of the ring bender. Therefore, the focus will be on the mounting of the outer edge.

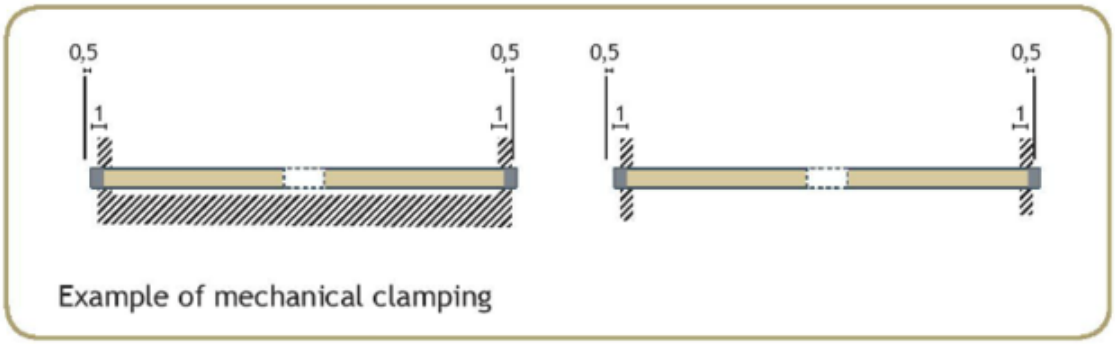

(a)

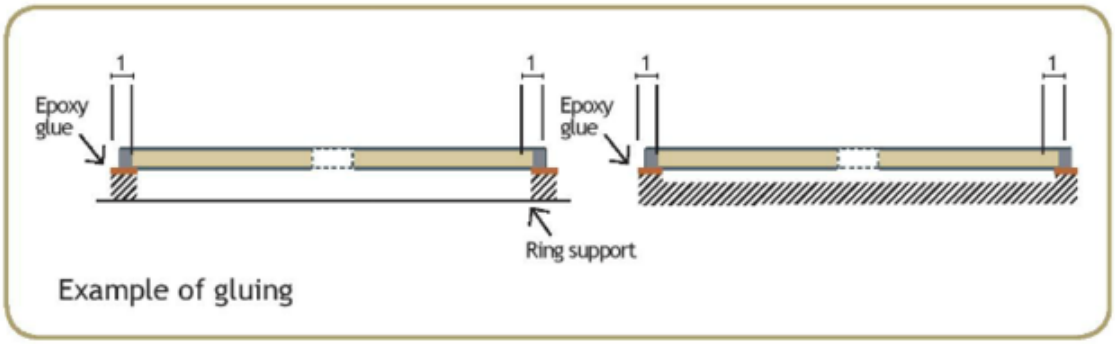

(b)

Figure 2-20. Noliac mounting suggestions for the ring bender (a) mechanical clamping, applying a force on the outer edge to keep the ring bender in place (b) epoxy adhesive, gluing the outer edge [29].

Physik Instrumentete manufactures an annular piezoelectric disc similar to the Nolac piezoelectric ring bender called Round PICMA Multilayer Bender. Physik Instrumentete suggests the bender be attached to a flexible metal structure by using epoxy adhesive, as can be seen in Figure 2-21. The mechanical structure should minimise the rotational stiffness [58]. Physik Instrumentete also suggests using a helical spring to press the bender on to a soft rubber ring, as can be seen in Figure 2-22.

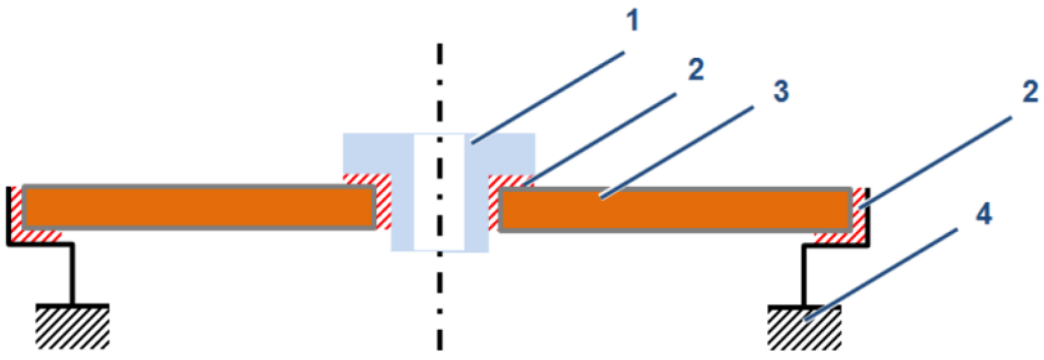

Figure 2-21. Mechanical structure mount for a piezoelectric ring bender [58].

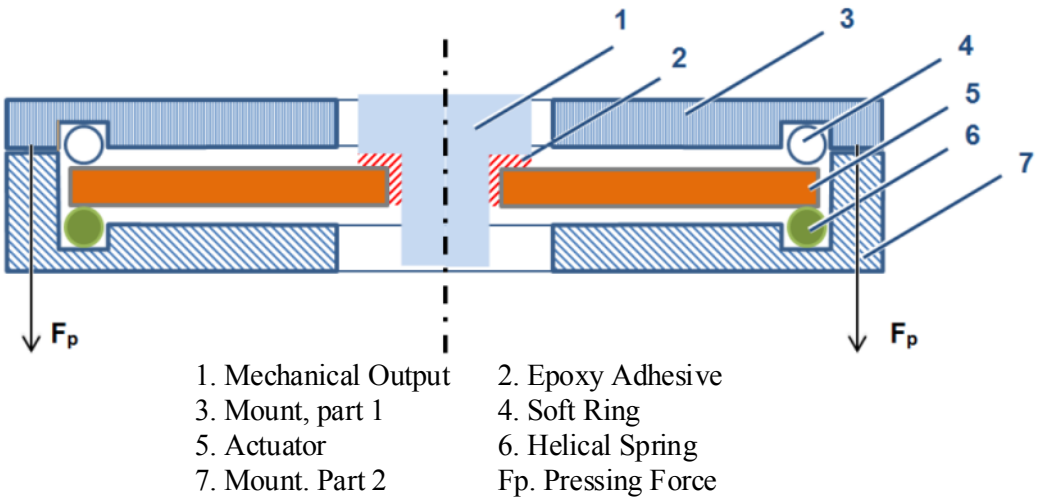

Figure 2-22. Mounting for a piezoelectric ring bender using a helical ring and a soft rubber ring [58].

Bertin et al. [28] have been investigating mounting of the piezoelectric ring bender by clamping the piezoelectric ring bender between two O-rings with two aluminium clamps, see Figure 2-23. Bertin concludes that torsional flexibility at the outer edge is essential not to reduce the movement of the piezoelectric ring bender.

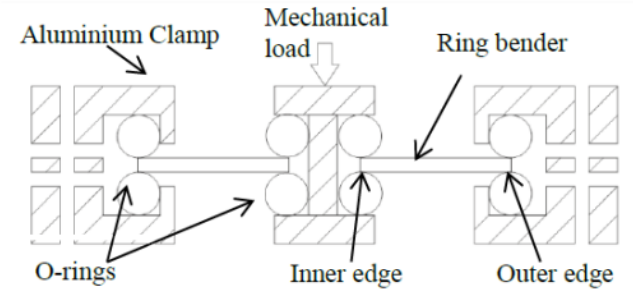

Figure 2-23. Ring bender mounting arrangement using O-rings [28]

In the books by Young et al. [60] and Timoshenko [61] bending equations for an annular disc for different mounting arrangements (built in or pin jointed at inner and outer edges) can be found. These equations could provide a further understanding on how the mounting effects the displacement of the ring bender.

Using a piezoelectric ring bender as actuation for a servovalve can potentially reduce weight and complexity. Additive manufacturing could potentially also reduce both weight and complexity of a servovalve body. The next section describes additive manufacturing for aerospace applications, a technique which will be used for prototype manufacture in this project.

2.7 ADDITIVE MANUFACTURING FOR AEROSPACE

The ASTM standards explain additive manufacturing (AM) as a method which "… fabricates parts by adding material in a layer-by-layer manner" [62]. The origins of modern AM dates back to the late 1960's when 3D parts were created using lasers to bond plastic powder together [63]. However, it has only relatively recently been sufficiently developed to become an important commercial manufacturing technology [64]

AM provides a new way of manufacturing hydraulic components and it is now on the verge of becoming a mainstream production process [65]. There are several benefits to producing a servovalve in AM; this can result in shorter development cycles, reduced inventory costs for material, better hydraulic efficiency, weight saving, new design possibilities and possibly environmental benefits [66]. There are already a few AM parts that are manufactured for aerospace applications; some are AM seat buckles, a bleed air leak detector bracket for the F-35 jet fighter and an air flow measuring probe [67][68]. There are even parts designed for space, such as an antenna bracket for a satellite [69]. However, most of the AM parts designed are not safety critical or not structural parts.

Moog, one of the leading valve manufacturers, started their AM centre in 2013 as a result of the VITAL project. They have now produced many different AM valves and several thousand parts through AM [70]. However, the servovalve in this research was the first AM valve that Moog was involved with.

According to Renishaw, a producer of both AM parts and AM machines, a mass reduction of 79% can be achieved by making a AM valve manifold instead of using a subtractive method [71]. Eos is another manufacturer of AM parts and machines, they believe that around 40-60% weight reduction can be achieved by producing parts in AM instead of conventional subtractive method [72]. A comparison of a manifold block can be seen in Figure 2-24, where (a) shows the manifold block manufactured in the conventional subtracting method and (b) an optimized AM version of the same manifold block produced by Renishaw. It can be seen that in the AM version, most of the 'unnecessary' material has been removed and only the essential material is used. They are also pointing out that that the flow efficiency can be improved up to 60%, by avoiding the use of sharp corners, which is the result of the subtracting method [71].

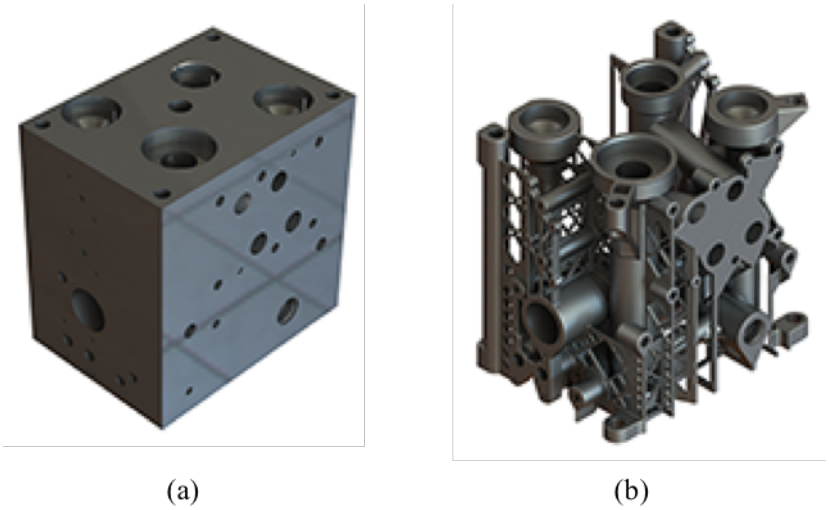

Figure 2-24. Comparison between conventional manufacturing method and AM (a) Original manifold block with flow galleries (b) AM design of the same manifold block with optimized wall thickness [71].

AM can now a days be found in multiple different applications, however, there is limited information about AM parts that are exposed to high pressure, similar to a servovalve, or AM for safety critical parts. There are a few patents that has been published that mention that AM can be used to manufacture servovalves and manifolds [73]. One describes that curved internal flow galleries can be produced by using AM to manufacture valve bodies [74]. It is also mentioned that with AM one single part can be produced, combining parts, where with traditional manufacturing methods several parts needed to be created separately [75].

Additive manufacturing will be further discussed in the 'Valve Design' chapter.

2.8 CONCLUSION

There have been multiple piezoelectric actuated valves using, stacks, rectangular benders and ring benders. Rectangular benders had been used to replace the conventional torque motor in the pilot stage. Stack actuators have been used as direct drive of a main stage spool, and to control a Hörbiger plate. Ring benders has been used in micro-pumps and in a nozzle flapper arrangement. Most valves presented in the literature uses a conventional valve arrangement coupled with piezoelectric actuation. This could potentially make a valve lighter, however they do not attempt to reduce the internal leakage. To reduce the internal leakage a new first stage design is needed. None have used a ring bender together with a small spool to replace the conventional pilot stage to reduce the internal leakage.

Most literature about reliability mention water and humidity, but none mention phosphate ester. Since a phosphate ester based hydraulic fluid is used in aerospace applications it is essential to investigate the reliability of a piezoelectric ring bender in phosphate ester.

Noliac and Physik Instrumente explain some basic mounting arrangement for ring benders and disc actuators. However, they do not provide an optimized mounting arrangement. No literature has been found where the mount needs to work as a mount for the ring bender as well as a seal.

Research has been done into hysteresis compensation. However, combining overlap compensation and hysteresis compensation for a piezoelectric actuator controlling a spool has not been investigated. Previously, hysteresis compensation has primarily been done by a relatively complicated hysteresis model, particularly the Prandtl Ishlinskii model.

Additive manufacturing has been used for aerospace applications, but not for servovalve bodies, safety critical or structural parts.

The next chapter will describe the valve design, which includes as additive manufacturing, first stage piezoelectric ring bender and spool, second stage and the controller platform.

3 VALVE DESIGN

This chapter describes the design of the valve prototype investigated in this research. This includes additive manufacturing, describing the AM method and design rules, first stage low leakage, the design of the valve body and the controller platform used.

3.1 INTRODUCTION

A new two-stage servovalve has been designed incorporating ring bender actuation and electrical spool position feedback, manufactured using Additive Manufacturing (AM). The aim of this valve design is to provide more knowledge of design through AM, and increase efficiency, as well as understand the potential for piezoelectric actuation to reduce manufacturing cost. It is expected that AM will significantly reduce the valve weight, however it needs to be determined if an AM valve body can be designed which functions correctly.

The concept in this research is to use a piezoelectric ring bender for actuation of the first stage. The first stage consists of a small spool with significant amount of overlap between the spool and bushing, to reduce leakage compared to a conventional nozzle-flapper, jet pipe or deflector jet amplifier. This low internal leakage will increase the efficiency of the valve. The first stage controls a conventional second stage spool with electrical position feedback instead of conventional mechanical second stage position feedback. The circuit configuration of the two-stage valve is shown in Figure 3-1, which shows the piezoelectric actuated first stage, second stage, the hydraulic connections between the first and second stage and how it can be connected to an actuator.

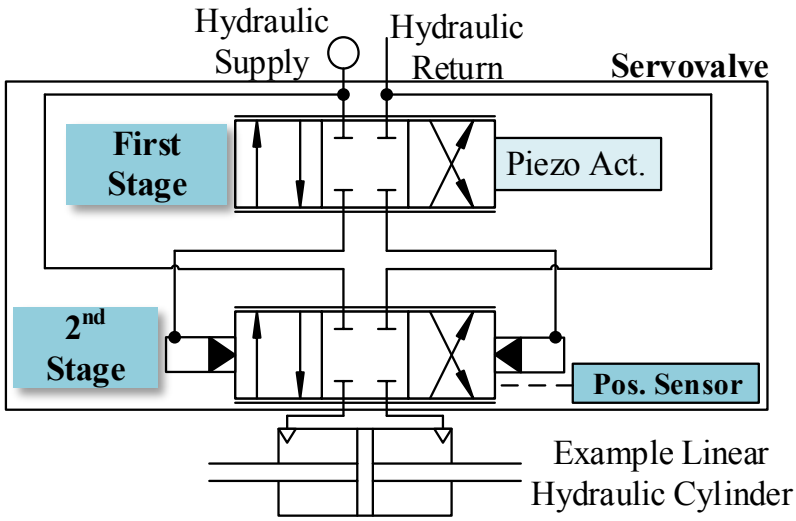

Figure 3-1. Schematic sketch of the internal servovalve circuit.

The valve was designed collaboratively by several people including the author.

The contribution of the author was to investigate several different first stage actuation possibilities, including a direct drive of the second stage spool. Due to the packaging of the actuators, weight and the low leakage requirements, the solution proposed in this research was believed to be the ideal. The author designed the AM valve body with inputs from experts of conventional valves design from Moog and from the AM field from Renishaw. The author was also involved with investigating the AM material properties and how these could be improved. The author was involved in writing a paper about AM, which can be found in Appendix A.3.2.

The valve prototype designed in this initial investigation will not be lighter than a conventional valve of similar size. There are several reasons for this. At the time the AM body was designed, the material properties of AM parts were not fully known, therefore the walls were made thicker than necessary to prevent failure of the valve body, since this research was to provide background knowledge and show that the concept has potential. Therefore, convectional components were used to save time and cost. Consequently, the parts that were used for the valve prototype had the potential of being bigger and heavier than if purposely made to save weight. A list of possible improvements for future valves can be found in section 3.10.

The additive manufacturing method, the AM valve body and a design guide will be explained in the following section.

3.2 ADDITIVE MANUFACTURING

Additive Manufacturing (AM) is a term used for a manufacturing process where layer upon layer of material is selectively laid down or deposited, unlike the conventional 'subtractive manufacturing', where material is removed from a larger block of material. AM allows a greater design freedom, however, there are design constraints that need to be known when designing any AM parts [17]. Nonetheless, many key areas such as weight, cost and reliability can be improved with a AM design [66].

The method used to produce the valve body in this project was a powder bed laser additive manufacturing method. A thin layer of material, in this case titanium powder, is deposited and a laser is used as a heat source to selectively melt the material [64]. Multiple layers will be deposited and melted together to create the final part. Figure 3-2 shows the process of the powder bed laser method. It shows the metal powder, the roller to apply the layers of material, the laser and the finished part. It also shows that the powder needs to be in a protective atmosphere, usually argon, due to the flammability of metallic powder. The build plate could also be heated, to have a more uniform temperature in the part and reduce thermal stresses that could improve the quality of the part.

The benefit is that material is only applied where needed and the unused material can be reused, which reduces the amount of waste material [17]. This manufacturing process could make the parts cheaper, lighter, and also reduces energy consumption, thus having a smaller carbon footprint [64].

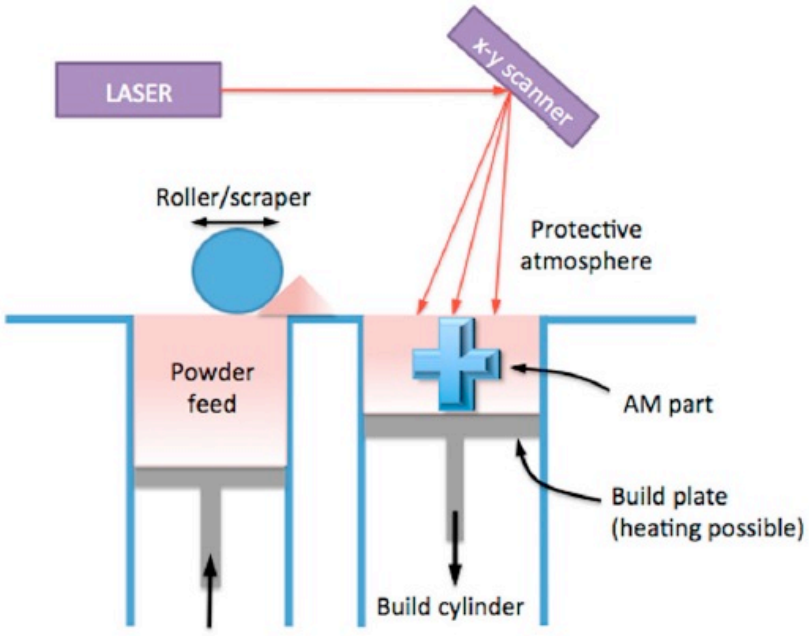

Figure 3-2. Illustration showing the powder bed laser additive manufacturing process, using a laser as heat source to melt the powder layer [17].

Conventional valves are usually made through subtractive manufacturing, in which material is removed from a larger block of material. Using this method only straight flow galleries can be produced and potential unwanted material cannot be machined away.

If acceptable material properties can be obtained, producing servovalve bodies using AM could provide significant benefits in weight, manufacturing cost and labour cost, as well as providing additional design freedom. Acceptable material properties would be similar fatigue and porosity levels as for wrought material. If similar material properties cannot be achieved, enough knowledge needs to be obtained to be able to design the valve for these properties, and the resultant design must be assessed to see if AM still provides an advantage.

Reducing servovalve and actuator weight in aerospace is of course particularly important. The manufacture of complex internal flow galleries which have proven difficult using traditional subtractive manufacturing methods, can be much more straightforward with AM. AM also allows new opportunities for integrating novel sensing and actuation into the valve itself, which could make it lighter, smaller and less complex.

An AM valve body was designed and manufactured for this research project, a photograph of the AM valve body can be seen in Figure 3-3. The valve includes a filter, second stage bore, flow galleries,

second stage LVDT mounting surface and first stage mounting surface. The valve has a length of 82mm, width of 69mm and a height of 37.5mm.

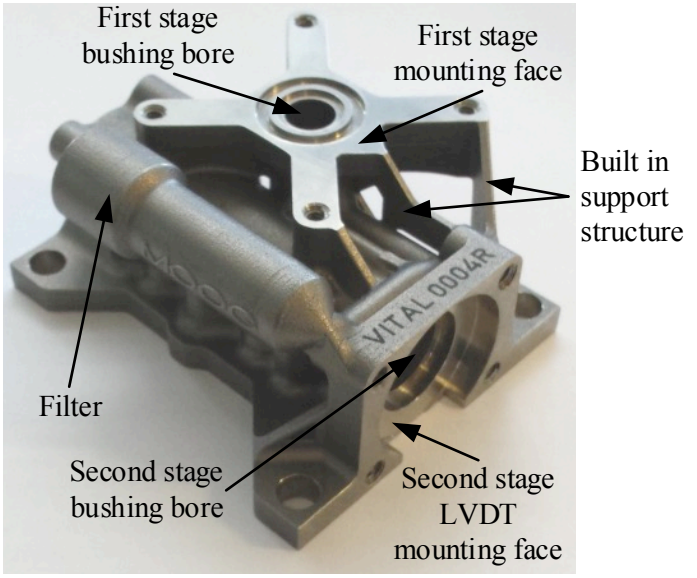

Figure 3-3. Photograph of the additive manufactured valve body prototype.

The material used to manufacture the valve was the titanium alloy Ti-6Al-4V. There are other titanium alloys used for additive manufacturing, but it is one of the most commonly used. This is because it has a good strength-to-weight ratio, and is corrosion resistant, which makes it desirable for aerospace applications [17]. Both the first and second stage spool and bushing are machined using the conventional subtractive method. They are made from 440C steel due to its resistance to wear.

Whilst the AM method provides significant benefits, there are still limitations and areas where further research is needed. Since AM is a relatively new manufacturing method the material properties are not yet fully established.

Several different test samples were designed to investigate the possibilities and limitations of AM. A photograph of some of these test samples can be seen in Figure 3-5, where for example different wall thicknesses, overhangs and a test how close walls can be created to each other can be seen. The build direction is out of page. In Figure 3-5 test samples testing different size and shaped holes were tested a relatively thick beam and a sample can be seen. It can be observed that even a relatively simple design, like a beam in this case, can bend due to internal stresses in the build process. The different holes show some deformation on the top surface due to collapsing of the powder. The remaining test samples were manufactured without issues.

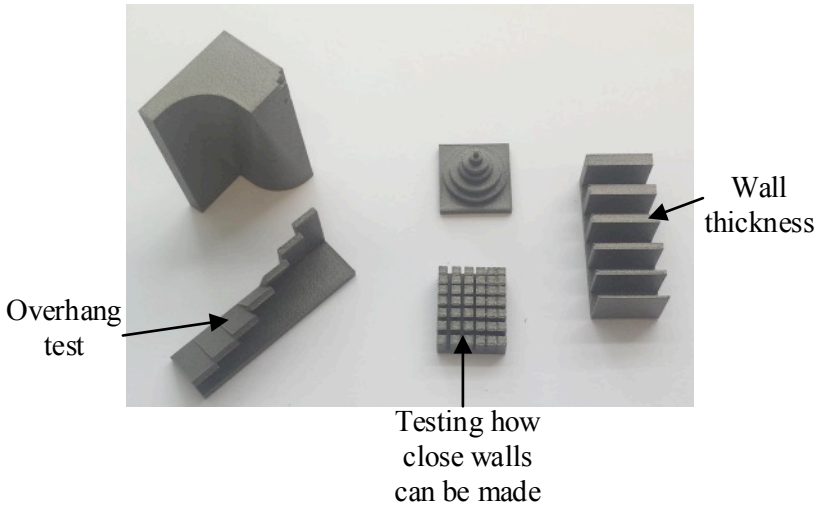

Figure 3-4. Photograph of several different AM test samples to investigate the possibilities and limitation of the AM process. The build direction is out of page.

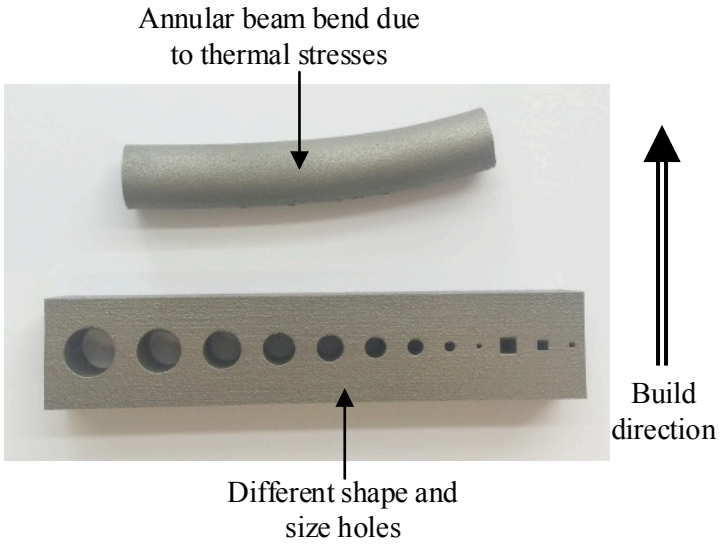

Figure 3-5. Photograph of AM test sample. Top shows a beam bend due to stresses in the build process. The bottom shows different hole sizes for round and square holes.

When designing a complex object e.g. a valve body, there are 'rules' to follow to ensure a successful build process. These are mostly documented in previous work, but have been validated in the current work:

- There is a certain overhang angle that cannot be exceeded, usually around 30-45°. If exceeded the part might deform or even 'collapse'. Overhang means the angle leaning away from the build direction. This can be seen in Figure 3-6, where the overhang angle is represented as θ_{oh}. Overhang areas generally have the highest surface roughness, which could cause an issue in internal flow galleries [17].
- The internal flow galleries need to be designed to allow the powder to be extracted. This both depends on the size of the flow galleries as well as the angle of the bends. If the powder is not

removed before the valve body is stress-relieved (heat treatment to reduce internal stresses created during the build process) the powder can be sintered and cause flow galleries to become blocked.

- Holes or flow galleries that are perpendicular to the build direction need to be ‘tear drop’ shape or rectangular-shaped, due to the overhang rule, see Figure 3-6. ‘Larger’ size holes or flow galleries would be designed using the tear drop shape, and ‘smaller’ would be designed using the rectangular shaped hole. In Figure 3-7 different round and square holes of different sizes can be seen. It can be observed that the overhanging top surface is rougher than the bottom, as the powder is not attached properly and has collapsed. It can also be observed that this is a greater concern with smaller and square holes. For smaller holes a larger proportion of the hole is deformed.
- If the overhang is larger than the allowed angle, support structures will be needed. Support structures can be built into the design, which could also help with the stiffness of the valve. A built-in structure to support the first stage mounting face can be observed in Figure 3-3. By reducing and/or incorporating support structure into the design, the amount of post processing can be reduced.
- Due to the fact that material is only added where needed, a certain amount of work needs to be conducted to ensure that the design is sufficiently stiff. This has previously not been a concern when designing a valve body using the subtractive method. The AM valve needs to be stiff enough that it will not ‘lift off’ from the mounting surface when hydraulic pressure is applied and cause leakage or damage the O-rings. From FEA investigation it was found that the valve used in this investigation will flex and bend, but not to the extent of concern.
- To distribute the stress more evenly, corners and sharp edges can be avoided. This will increase the fatigue life.
- When a AM part is manufactured the surface roughness is high and metal particles can come loose. This is not optimal for flow galleries. Usually AM parts are blasted (similar to sand-blasting) to clean the surface, however, this will not clear the internal flow galleries.

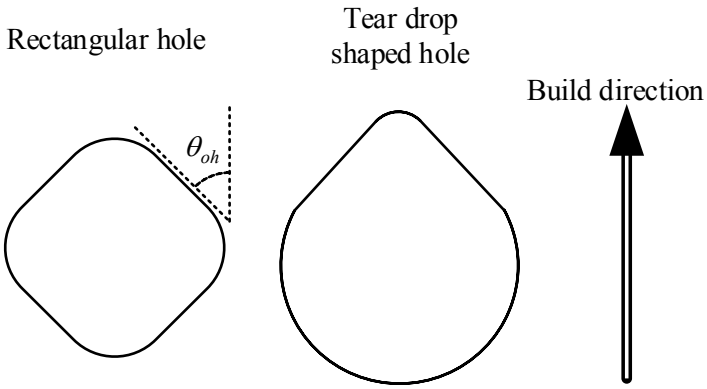

Figure 3-6. Two examples, rectangular and tear drop shaped, of shapes of holes and flow galleries used in an AM model.

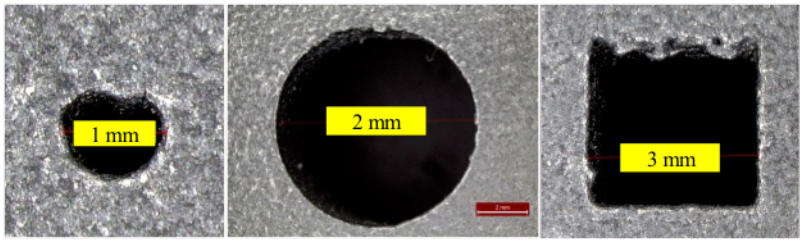

Figure 3-7. Microscopic photograph of different size holes and shape manufactured in AM. (a) shows a round hole with a diameter of 1mm (b) shows a round hole with a diameter of 2mm (c) shows a square hole where the length of the sides are 3mm

3.3 First Stage

In a conventional valve, the first (or pilot) stage refers to the torque motor and either nozzle-flapper, jet pipe or deflector jet amplifier, and it provides the actuation to move the main stage spool (second stage).

Torque motors are complex and can be time-consuming and expensive to set-up, requiring significant manual intervention [76]. If not adjusted precisely, the first stage amplifier may not provide stable operation, and there is a continual flow loss (and power loss) through the nozzles or jet. An alternative approach is required providing a more cost effective, reliable, low leakage solution which is amenable to automated manufacture.

Smart materials, in particular piezoelectric actuators, are a possible alternative to the complex and heavy torque motor, providing high forces and fast response times [2][77]. Considerable research has been undertaken on stack and bending actuators [28]. The relatively new type of bending actuator, the piezoelectric ring bender, exhibits a greater displacement than a stack actuator of the same mass, and an increase in stiffness in comparison to similar size rectangular bimorph type bender.

While the piezoelectric ring bender is providing the actuation of the first stage, the flow is controlled by a small spool with significant overlap, ~20µm, to reduce the internal leakage. A spool overlap arrangement also called closed centre will result in a ‘dead-band’, where very little or zero flow is

passing through the first stage to the second stage while in the overlap region [78], as illustrated in Figure 3-8. There will be no flow through the first stage until the overlap region is cleared.

The piezoelectric ring bender moves the spool to control the flow to the second stage, and thereby gives movement of the second stage spool. It is desirable to have a linear relationship between the input signal and the flow characteristics. However, as overlap is introduced, an undesirable 'dead-band' is introduced, which makes the relationship non-linear [79]. This 'dead-band' could also cause issues when trying to control the second stage due to the non-linear relationship between the flow and position, as can be seen in Figure 3-8. This dead-band could be compensated for within the control loop and make the control more linear by moving the spool through the dead-band rapidly, as will be discussed in Chapter 5 'Controller Design' [79].

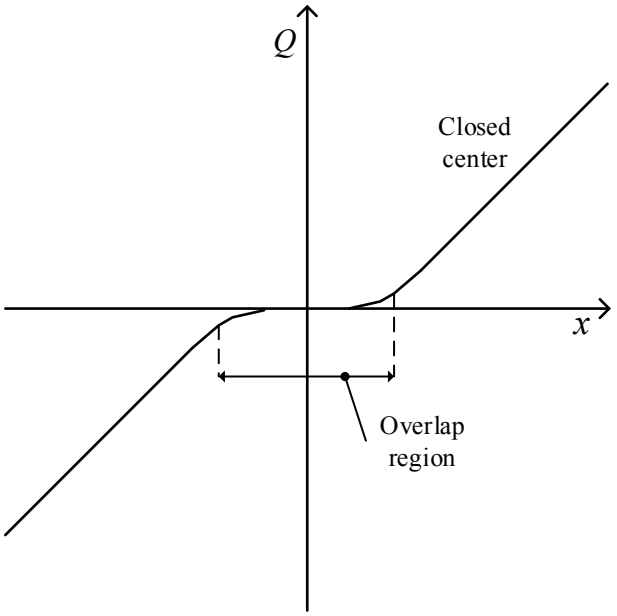

Figure 3-8. Closed port flow characteristics where reduced flow in the overlap region can be seen.

Figure 3-9 illustrates a simplified schematic of the pilot stage, which includes the piezoelectric ring bender and small spool. When a voltage, and associated electric field, is applied to the piezoelectric ring bender, it will bend and thereby force the spool to move. As the spool moves in the positive x direction, this will connect control port 1 (P_1) to the supply pressure (P_s), hence increasing the pressure in P_1 and producing a flow Q_1. Control port 2 (P_2) will then be connected to the return pressure (P_r) and thereby lower the pressure in P_2.

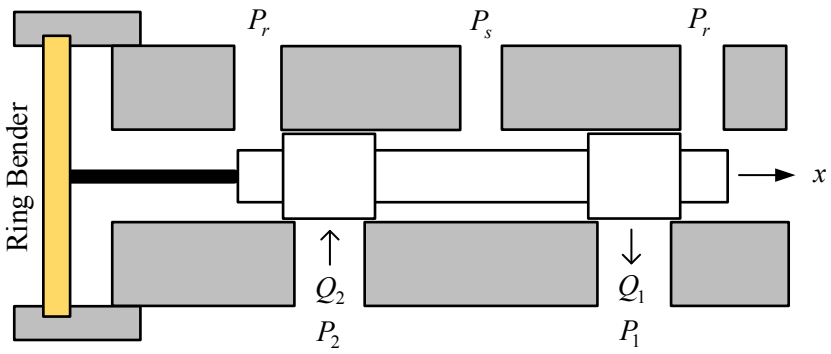

Figure 3-9. Illustration sketch of first stage concept, showing the ring bender and first stage spool.

Figure 3-10 shows a cross section of the first stage assembly where the piezoelectric ring bender and the first stage spool can be seen. The piezoelectric ring bender was submerged in the hydraulic oil when tested and connected to the first stage spool and the LVDT core through a small rod (quill shaft). This LVDT will normally only be used to monitor the behaviour of the ring bender and first stage spool, and not used for control. When the behaviour of the first stage is known and understood, the first stage LVDT will not be needed in later versions. The second stage spool was fitted with an LVDT to provide position feedback to the control loop.

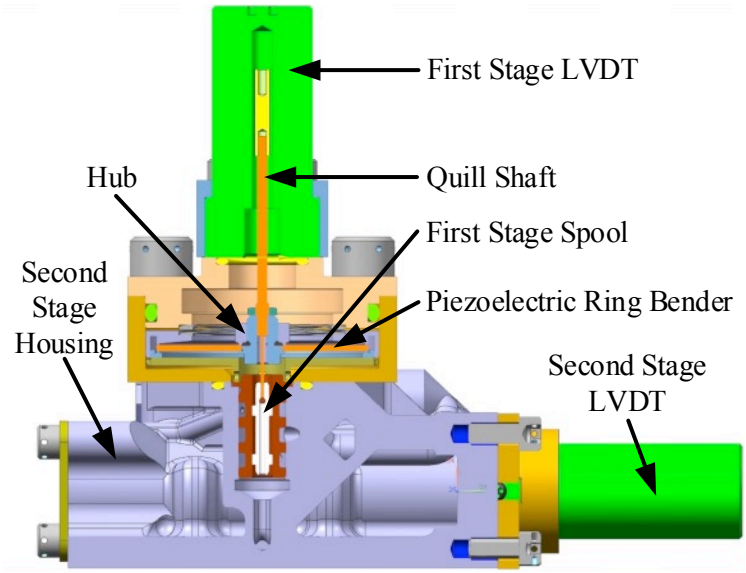

Figure 3-10. Cross section of the pilot stage.

Figure 3-11 shows a cross section of the valve, where the first stage, first stage housing, second stage, flow galleries, filter and glass wire connector can be seen. A glass connector is used, as it needs to ensure no leakage and withstand a large pressure, but still needs to allow electrical signals to pass.

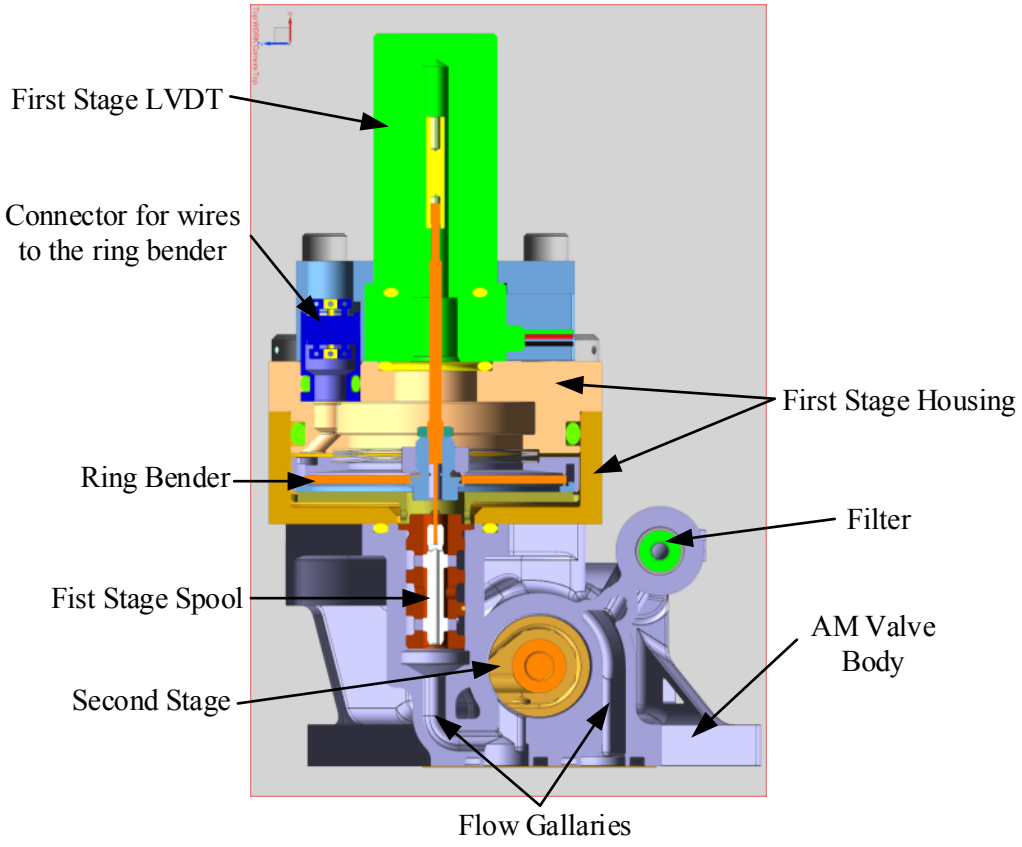

Figure 3-11. Cross section of the valve.

Figure 3-12 shows a cross section of the first stage, which includes the mounting, piezoelectric ring bender, the hub to attach the quill shaft and the rod that connects the piezoelectric ring bender to the spool, the first stage spool and bushing. It also shows the flow slots in the first stage bushing that connects the first stage to the second stage spool.

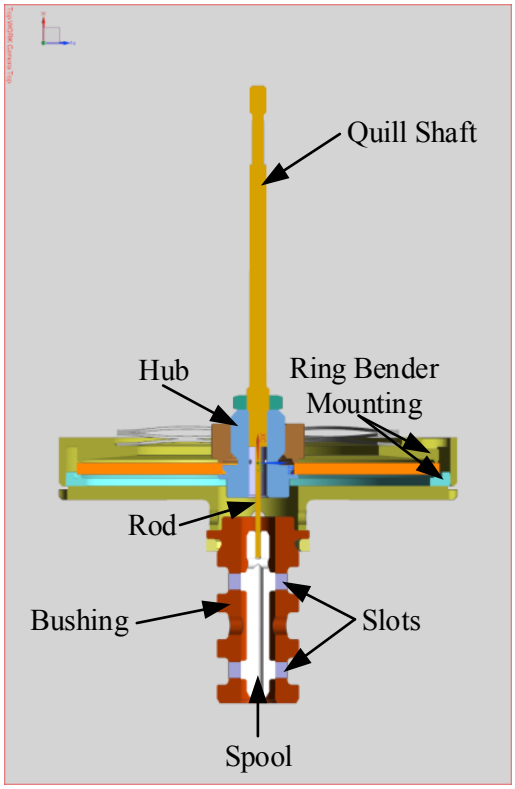

Figure 3-12. Cross section of first stage, showing the first stage spool, bushing, ring bender and the quill shaft.

Figure 3-13 shows a cross section along the length of the first stage spool and bushing. It also shows the flow slots through which the flow galleries are connected to either side of the second stage spool. The pressure and the flow control ports can be seen in Figure 3-14. The first stage spool has a hollow centre to ensure the return pressure is present at both sides of the first stage spool. Figure 3-15 shows a cross section across the first stage spool and bushing, where the spool, bushing and the flow slots can be seen.

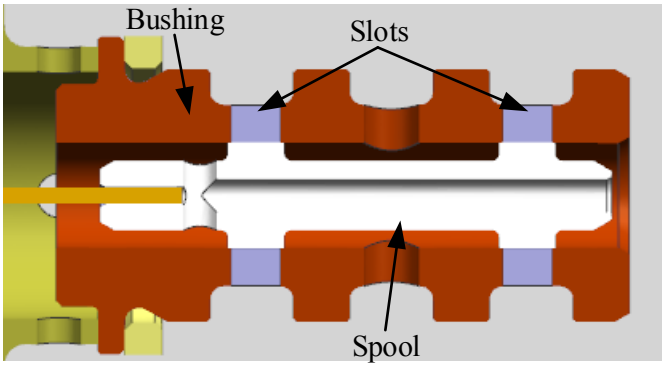

Figure 3-13. Cross section of the spool and bushing, along the spool length.

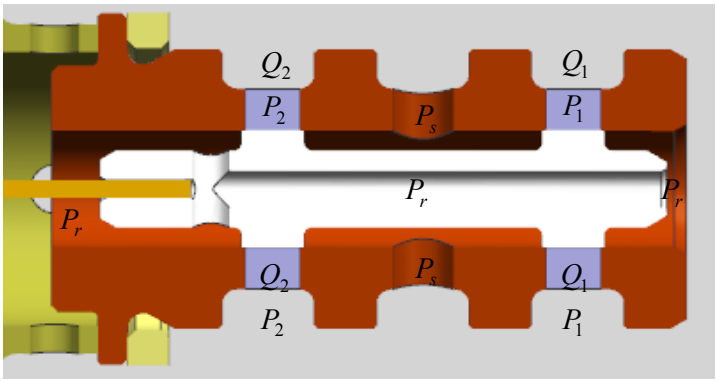

Figure 3-14. Cross section of the first stage spool and bushing, along its length, showing the different pressures subjected to the different areas within the first stage.

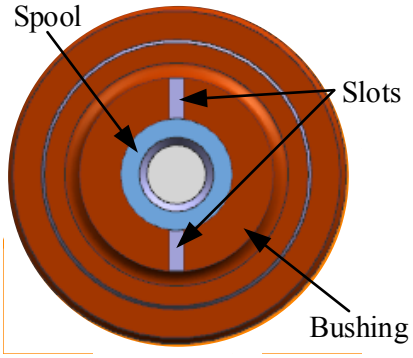

Figure 3-15. Cross section of the first stage spool and bushing and showing the flow slots.

3.4 RING BENDER

The ring bender used in the prototype valve was the Noliac CMBR08 piezoelectric ring bender. There are different versions and sizes of ring benders, but it was decided to use this version of the ring bender because it provides enough displacement and sufficient force. The specifications of the CMBR08 ring bender can be seen in Table 3-1. Figure 3-16 shows a photograph of the Noliac CMBR08 ring bender. Generally, a linear relationship can be assumed between the maximum displacement and the force provided by a piezoelectric ring bender, as shown in Figure 3-17, by the dotted line. The effective work output can be obtained by calculating the area under the line.

Table 3-1. Specifications for the Noliac CMBR08 ring bender [33].

Parameter	Value
Outer diameter	40 mm
Inner diameter	8 mm
Thickness	1.25 mm
Free stroke	± 115 µm
Blocking force	39 N
Capacitance	$2 \cdot 1740$ nF
Stiffness	0.34 N/µm
Material	NCE57

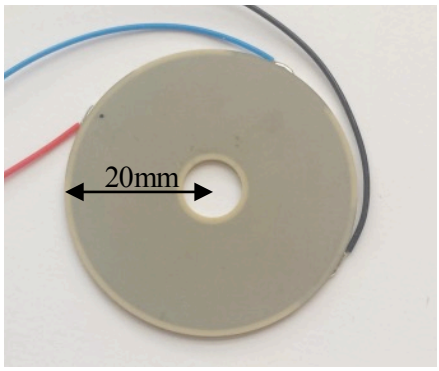

Figure 3-16. Photograph of a Noliac CMBR08 40mm diameter ring bender.

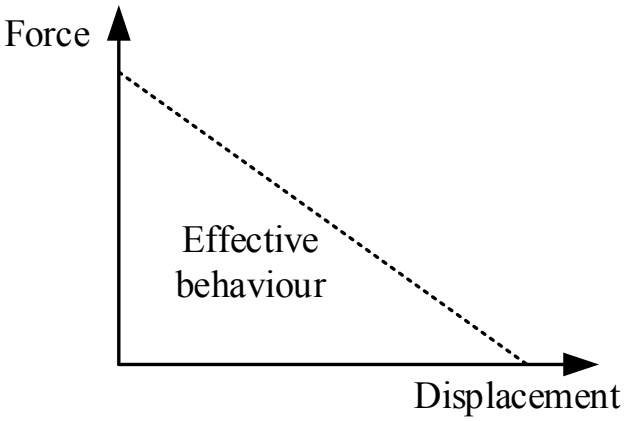

Figure 3-17. The effective output of a piezoelectric ring bender.

3.5 AMPLIFIER

The amplifier used to control the ring bender was a Noliac NDR6220DC. Noliac manufacture two versions of amplifiers that can control a three-wire device like a ring bender. The NDR6220DC was

chosen since it has a higher current output and therefore able to move the ring bender at a higher frequency. The parameters of the Noliac NDR6220DC amplifier can be seen in Table 3-2 and a photograph can be seen in Figure 3-18.

Table 3-2. Noliac NDR6220DC amplifier specifications.

Parameter	**Value**
Output voltage range (for benders)	± 100 V
Maximum current amplitude	1 A
Peak current (<0.5ms impulse)	1.5 A
Input signal	$0 - 10$ V

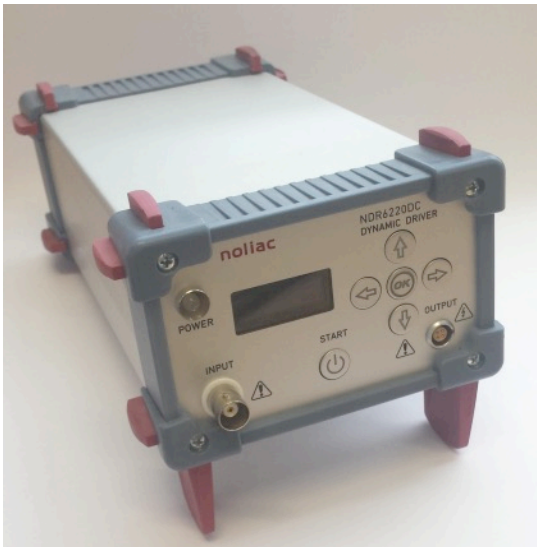

Figure 3-18. Photograph of a Noliac NDR6220DC amplifier.

3.6 ELECTRICAL SECOND STAGE FEEDBACK

Due to the first stage arrangement, no mechanical second stage position feedback is possible, therefore, the second stage had electrical position feedback. By not having a mechanical second stage feedback, the mechanical complexity of the valve is reduced and also gives the possibility, in the future, to reduce the size of the second stage spool and thereby also the size of the valve. The second stage position feedback is provided by an LVDT, as can be seen in Figure 3-10. The LVDT creates a voltage which is representative to a certain spool position. This voltage is feedback to the control algorithm to close the second stage position control loop. The advantages of using an electrical position feedback over the conventional mechanical feedback, is that a higher loop gain and/or a higher order controller that is more effective at reducing any kind of disturbance, like flow forces and contamination can be used [80]. However, if an electrical failure occurs the spool will not return to its 'null' position, whereas using

mechanical feedback it will. This is a disadvantage, as the spool will end up in its maximum flow position. However, if it is designed to move to one specific side, this could be acceptable.

3.7 COMPLETE PROTOTYPE

The complete prototype was assembled and tested on a dedicated test bench. A photo of the complete valve prototype can be seen in Figure 3-19. The ring bender housing is made through conventional subtractive methods and it is a stand-alone unit. The main reason for having a first stage as stand-alone unit is so that the first stage could be tested on its own. In the future, the complete first stage assembly could be incorporated into the AM valve body, which will make it smaller and lighter.

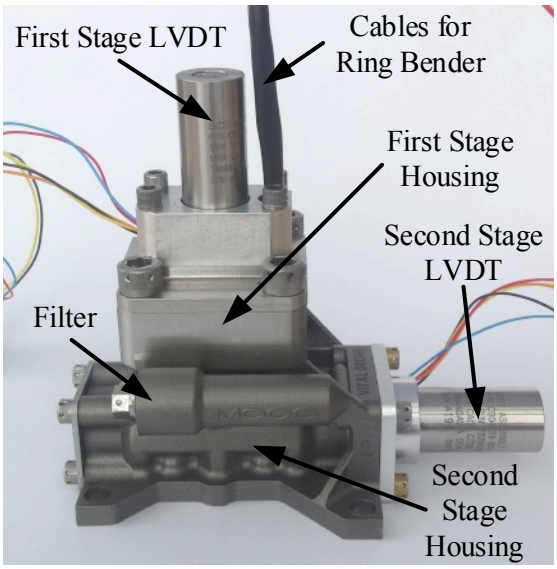

Figure 3-19. Photograph of the complete valve prototype valve tested.

The AM valve body was designed around a Moog 264 series second stage Bushing and Spool Assembly (BSA). The reason for basing the research valve on a Moog 264 series is that it is used for actuation in flight control systems and it is one of the more common valves used in aerospace applications. The first stage BSA has the same diameter as a Moog 264 series made for motorsport, but the spool and bushing is unique for this research due to the large overlap. The LVDT for the first stage will only be used for monitoring purposes and to learn about the behaviour of the first stage movement. The second stage spool and bushing can be seen in Figure 3-20, which shows a cross section of the valve along the length of the second stage spool.

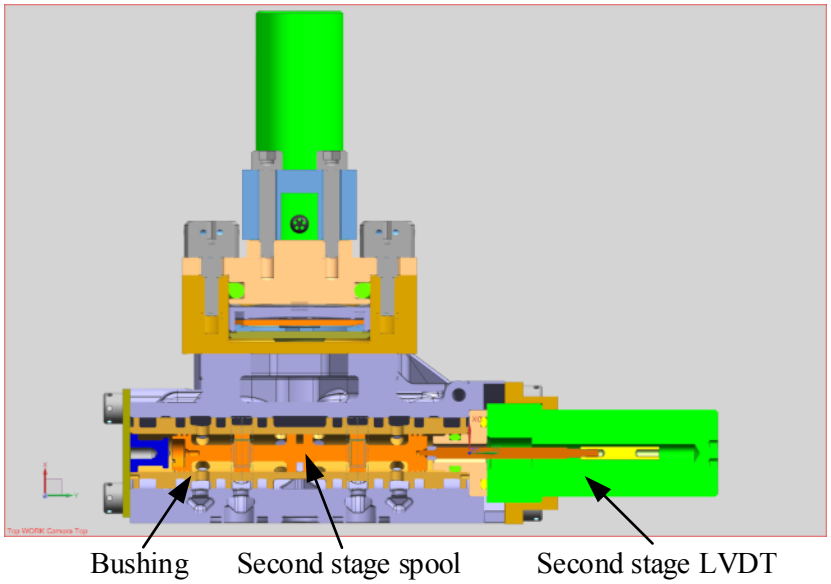

Figure 3-20. Cross section of the second stage, showing the second stage spool and bushing.

Due to the design of first stage, it was challenging to null the first stage electrical null to the first stage hydraulic null. This is because it must be precise to a few micrometres and the nulling is achieved by tightening a screw on the hub and rod. In the test setup, the electrical null of the first stage is approximately 13µm (around 17% of the approximately 75µm maximum stroke) off the hydraulic null of the first stage. This implies that the amplifier needs to always apply a voltage to the ring bender to get it to its hydraulic null position.

3.7.1 Low Leakage First Stage

The first stage was designed to reduce the internal leakage. A leakage test was completed to measure the leakage through the first and second stage. The leakage graph can be seen in Figure 3-21, where the first stage leakage is the leakage on either side of the zero control signal (also called tare leakage) [7]. The peak around zero is the total leakage through the valve. It can be seen that the first stage spool leakage is 0.08L/min, for a 207bar system pressure. A conventional first stage nozzle flapper valve (Moog 264 valve) has according to the data sheet a leakage of up to 0.44 L/min at 207bar [7]. However, according to Moog it usually has a leakage of around 0.38L/min [81]. This shows a significant leakage reduction of 0.3L/min or a reduction of about 80% by using a first stage spool with significant overlap.

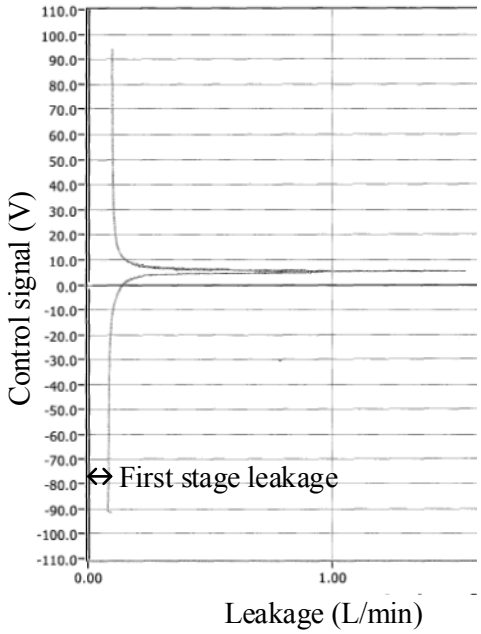

Figure 3-21. Leakage graph of the first stage large overlap small spool.

3.8 CONTROLLER PLATFORM

The controller platform used was an xPC target system. The xPC target system is a high performance real-time prototyping environment, where a Matlab Simulink model is coded in real-time and connected to a physical system and uses standard PC hardware [82]. The reason for using an xPC system is that all components are commercially available, it is easy to use, the control algorithm can be easily setup and changed in real time through Simulink. The University of Bath also has experience with xPC systems.

The Simulink model was designed to control both the first stage in an open loop fashion and the second stage in a closed loop fashion. Within the Simulink model the control algorithm was designed to close the control loop and save data. A circuit diagram of the test system can be seen in Figure 3-22. The Simulink control algorithm provides a signal which is turned to a low voltage through the I/O board that is sent to the amplifier. The amplifier in turn provides a voltage to move the piezoelectric ring bender that moves the first stage spool, which in return controls the flow to move the second stage spool. The position of the second stage spool is feedback into the control model and closes the loop. The system was also designed to monitor and record the voltage from the amplifier, first and second stage spool positions as well as pressures if needed.

The sampling time of the controller platform was 0.1ms.

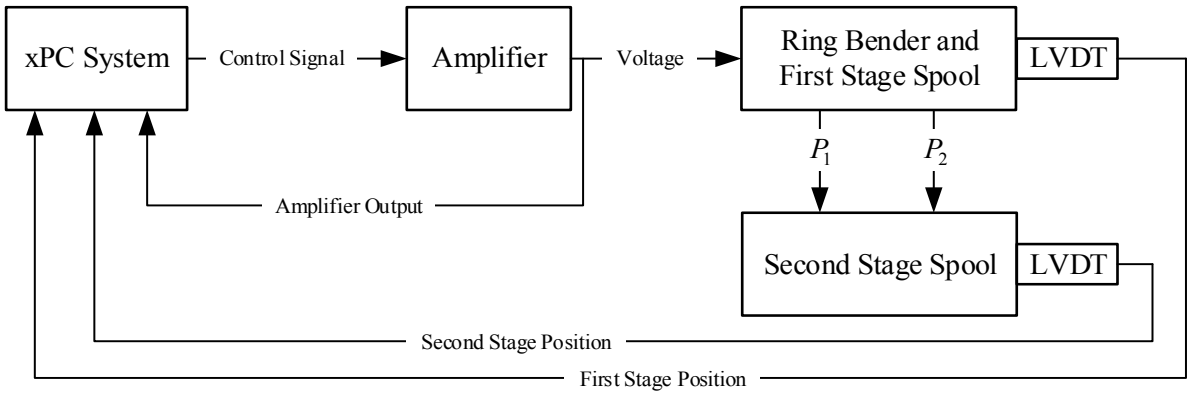

Figure 3-22. Circuit diagram of the controller platform for the prototype valve.

3.9 HYDRAULIC TEST CIRCUIT

The hydraulic test circuit can be seen in Figure 3-23, where the hydraulic connections also can be observed. It also shows how the first and second stage are hydraulically connected, with the first stage directing the flow of hydraulic fluid to either side of the second stage spool. An accumulator was added to reduce pressure fluctuations. The test pressure was 207bar or 3000psi. The hydraulic fluid used for testing the valve prototype was mineral oil.

The second stage control ports were blocked. This was done since only the valve was of interest in this research. This could influence the dynamic response since there are no flow forces present and there could be possible dynamic effects of the fluid. However, open-port tests were simulated using the analytical model where it was observed that the flow forces did not have any significate influence on the second stage dynamics. A second reason the ports were blocked was that no suitable test facilities and appropriate size actuators were available.

When conventional valves are tested the manufacturer often have the possibility to test it for both open and closed ports. The open ports test, which imitates a frictionless and unloaded actuator, was tested to obtain the flow and the effect of the flow on static and dynamic response. The blocked ports represent the opposite scenario, essentially when an actuator has seized. The pressure in the two control ports can then be measured. In practice, with a real actuator it is somewhere between these extremes, due to friction in the actuator and the load [81].

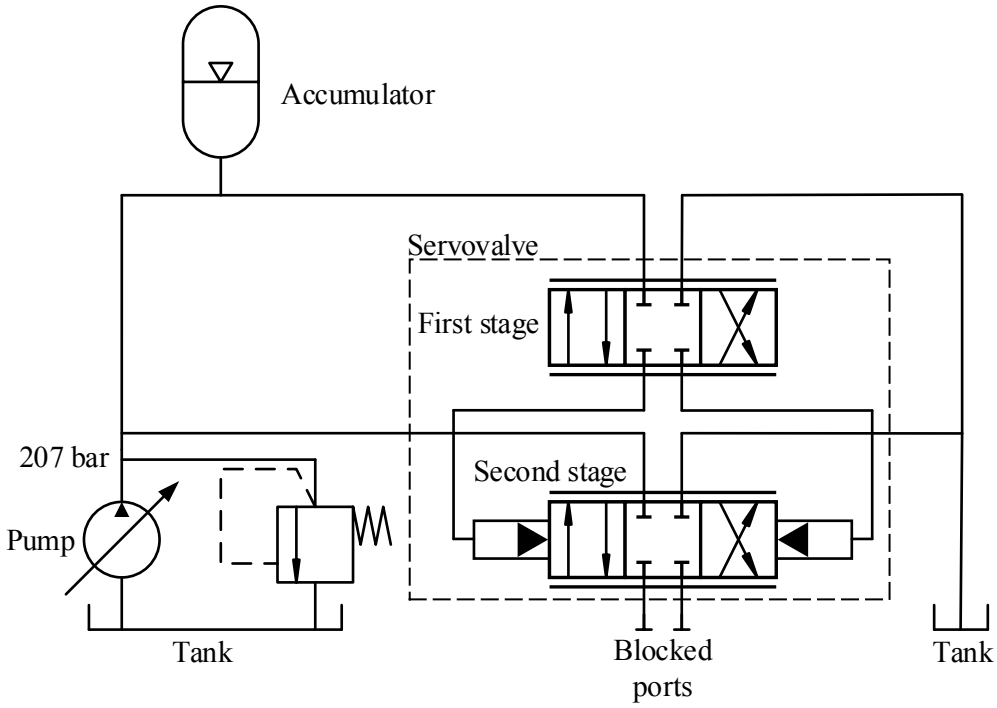

Figure 3-23. Schematic sketch of the hydraulic test circuit for the prototype valve.

3.10 FUTURE DESIGN IMPROVEMENTS

This valve tested in this research project was not optimized for weight. This research was completed to provide the background information and to test the principles of AM, first stage spool with significant overlap and to use a piezoelectric ring bender as an actuation method.

It is believed that the valve prototype can be optimized significantly more for both size and weight. There are several areas where it is known that weight and size can be reduced:

i. As no feedback wire is used as positioning feedback the second stage spool can be made shorter. The second stage spool can be shortened by about a third.
ii. The second stage positioning feedback is completed by a LVDT, which is a relatively big and heavy device. The author was involved with the design and successful testing of a digital encoder that could be used instead of the LVDT. The encoder is roughly a third of the size and weight compared to the LVDT.
iii. The first stage LVDT will not be needed in the future. However, to obtain sufficient knowledge it essential to use it on this first prototype to understand the behaviour of the first stage. This knowledge is essential to be able to design a control algorithm and to understand the piezoelectric hysteresis.
iv. The filter used for the tested prototype can be changed to a smaller design.
v. The first prototype was not optimized for minimum weight.

a. It was designed to obtain understanding of the AM process and to obtain valuable information about the methods for designing AM parts.
b. The valve was designed to ensure that the valve body would withstand the system pressure. Since, the material properties were not fully understood at the time the wall thickness were thicker than needed.
c. The first stage housing could be incorporated into the design, which would save weight.

vi. It is also believed that a smaller version of the first stage piezoelectric ring bender could be used, which would make the valve both smaller and lighter.

3.11 CONCLUSION

For the pilot stage actuation, a piezoelectric ring bender was chosen to control a small first stage spool. The low leakage was achieved by introducing a significant amount of overlap between the spool lands and the bushing. The second stage positioning feedback was achieved by an electrical feedback using an LVDT instead of a conventional mechanical second stage feedback. The valve body was manufactured through AM. This process could make the part lighter and greater design possibilities are obtained, by being able to incorporate actuators and sensors more efficient into the valve. In the complete prototype a LVDT was attached on the first stage, however this was only used for monitoring purposes. The controller platform used was an xPC target system, which is a high performance real-time prototyping environment. A Matlab Simulink model was coded in real-time and connected to a physical system and uses standard PC hardware.

The novel aspects are that a AM valve with low internal leakage using a small first stage spool actuated by a piezoelectric ring bender to control the main stage spool has been designed and manufactured. This is most likely the first time an AM servovalve has been developed and tested for aerospace applications. The ring bender has been used in micropumps and Bertin developed a valve for gas turbines using a ring bender, but combining a ring bender to actuate a small low leakage, large overlap, spool in a first stage application to control a two stage servovalve is novel.

The following chapter will describe an analytical model for the piezoelectric actuated two stage low leakage servovalve described in this chapter.

4 ANALYTICAL MODELLING

This chapter describes an analytical model of the piezoelectric actuated two stage servo valve including validation. It was developed to obtain a better understanding of the valve behaviour and to test the controller.

4.1 INTRODUCTION

To be able to obtain a better understanding of the piezoelectric ring bender behaviour and the complete valve, a mathematical model of the piezoelectric actuated two stage valve was completed. The model is also used to test different control algorithms. The model is made up of several parts; the sub-models include the amplifier, the piezoelectric ring bender with hysteresis, the first stage spool and second stage spool. The models for the first and second stage spools include the flow characteristics of the orifices, flow forces and viscous friction.

4.2 AMPLIFIER

The controller will send a control voltage (V_c) to the amplifier which in turn creates a voltage to control the piezoelectric ring bender (V_{amp}). The amplifier was modelled using the following second order transfer function:

$$V_{amp} = \frac{K_a \omega_n}{s^2 + 2\zeta\omega_n s + {\omega_n}^2} V_c \qquad (4\text{-}1)$$

where K_a is a scaling factor, ω_n is the natural frequency and ζ is the damping factor of the amplifier.

To model the current limit, the rate of change of voltage is limited to this maximum value:

$$\frac{dV_{amp}}{dt} = \frac{I_{max}}{C_{rb}} \qquad (4\text{-}2)$$

where C_{rb} is the capacitance of the ring bender and I_{max} is the current limit of the piezoelectric amplifier.

The control voltage (V_c) that is supplied to the amplifier is in the range ±5 volts and the V_{amp} will be in the range of ± 100 volts.

4.3 FIRST STAGE

4.3.1 Piezoelectric Hysteresis

The Bouc-Wen model shown in Equation (4-3) is used to represent the hysteresis of the ring bender [3][83]. n is the deviation from the linear characteristics. The Bouc-Wen model is a relatively simple hysteresis model with three dimensionless tuning parameters α, β and γ, used to match the model to

experimental data. The n is subtracted from the voltage from the amplifier (V_{amp}) to create the effective voltage (V_h) to which the piezoelectric ring bender responds linearly, see Equation (4-4). The parameters were obtained from matching the analytical model to experimental data.

$$\dot{n} = \alpha \dot{V}_{amp} - \beta \left|\dot{V}_{amp}\right| n - \gamma \dot{V}_{amp} |n| \tag{4-3}$$

$$V_h = V_{amp} - n \tag{4-4}$$

4.3.2 First Stage Spool Dynamics

The dynamic characteristics can be approximated by a spring with damping. The ring bender has certain stiffness, and both the displacement of fluid by the bender and the friction of the close-fitting spool in its bushing will act as damping.

These combine with the spool mass to give Equation (4-5), where C is a damping coefficient, F_f is the flow forces (see Equation (4-20) and m_s is the mass of the first stage spool and hub. F_{rb} is the force provided by the piezoelectric ring bender.

$$F_{rb} - k_{rb} x - F_f = m_s \ddot{x} \tag{4-5}$$

Thus Equation (4-6) is obtained to give the spool displacement, x, where s is the differential operator.

$$x = \frac{1}{m_s s^2 + Cs + k_{rb}} \left(F_{rb} - F_f\right) \tag{4-6}$$

To obtain the spring constant k_{rb} of the piezoelectric actuator Equation (4-7) is used, where F_{rb} is the blocking force of the ring bender and S is its maximum stroke.

$$k_{rb} = \frac{F_{bf}}{S} r_m \tag{4-7}$$

where r_m is a mounting stiffness factor. Due to non-linear mounting stiffness r_m depends on the position of the piezoelectric ring bender and is implemented as a look-up table in the simulation model. The damping is found by matching experimental data.

The blocking force provided by the piezoelectric ring bender at a certain voltage, is obtained by the following equation:

$$F_{rb} = K_{dv} V_h \tag{4-8}$$

where:

$$K_{dv} = \frac{F_{bf}}{V_{max}} \tag{4-9|}$$

where F_{bf} is the maximum ring bender blocking force, at zero displacement, and V_{max} is the maximum operating voltage of the ring bender.

4.3.3 First Stage Flow Model

The flow model consists of several parts. First the ring bender position is converted into a ratio of the total piezoelectric ring bender stroke, see Equation (4-10), thereafter the pilot stage spool overlap model was included by the use of a lookup table

$$k_q = f_q\left(\frac{x}{S}\right) \tag{4-10}$$

where f_q is the non-linear function representing the overlap region as can be seen in Figure 4-1. S is the maximum stroke of the ring bender.

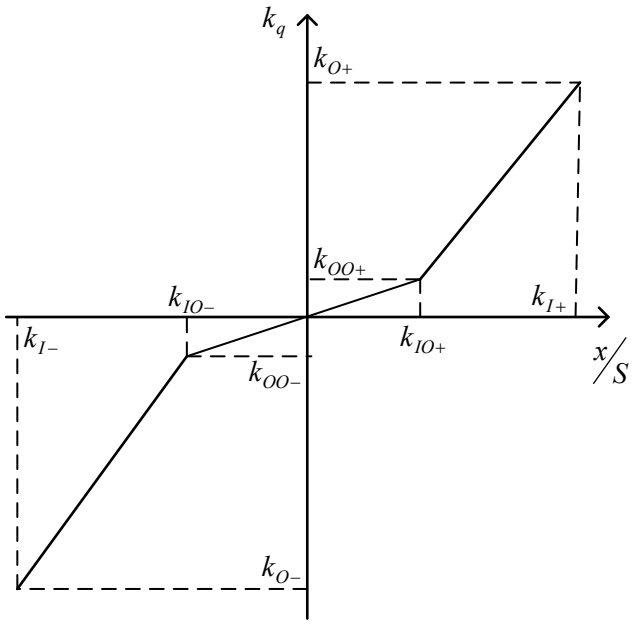

Figure 4-1. Parameters of the non-linear function f_q representing the overlap region.

The spool orifice equation model calculates flow from the first stage to either end of the second stage spool. The flow depends on the first stage spool position. As the first stage spool moves in a negative x direction, control port 2 will be connected to supply pressure (P_s) and create a flow (Q_2) from the first stage to the second stage and thereby move the second stage spool. At the same time the flow in control port 1 will be connected to return pressure (P_r) and the flow will go from the control port to return.

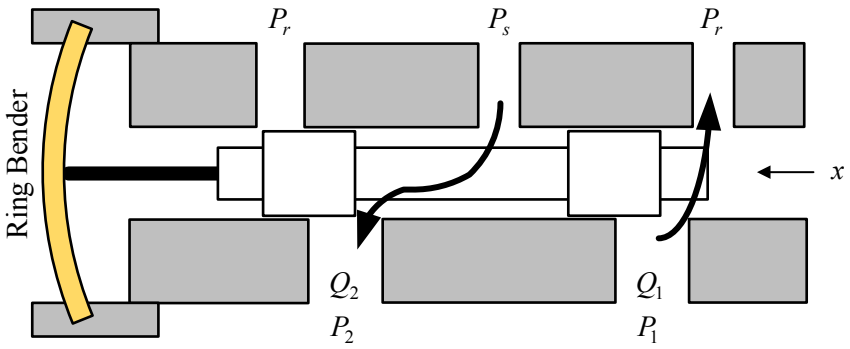

Figure 4-2. First stage illustration of the flow as the first stage spool is moved in the negative x direction.

The orifice equations of the first stage are as follows [4][84][85]:

$$Q_1 = k_v k_q \sqrt{P_s - (P_1 + \Delta P_1)} \text{ for positive } x \tag{4-11}$$

$$Q_2 = k_v k_q \sqrt{(P_2 - \Delta P_2) - P_r} \text{ for positive } x \tag{4-12}$$

$$Q_1 = k_v k_q \sqrt{(P_1 - \Delta P_1) - P_r} \text{ for negative } x \tag{4-13}$$

$$Q_2 = k_v k_q \sqrt{P_s - (P_2 + \Delta P_2)} \text{ for negative } x \tag{4-14}$$

$$k_v = C_q w_s \sqrt{\frac{2}{\rho}} \tag{4-15}$$

where w_s is the first stage flow slot width, which is the width total width of the two slots shown in Figure 3-12. C_q is the flow coefficient, P_s is the supply pressure, P_r is return pressure, P_1 is the pressure is control port 1, P_2 is the pressure is control port 2, ΔP_1 is the pressure losses in control port 1, ΔP_2 is the pressure losses in control port 2 and k_v is the flow rate constant. Q_1 and Q_2 are the flows in the respective control ports.

The additional pressure loss in the valve galleries is modelled as the square of the flow, which is shown in Equations (4-16) and (4-17) [4].

$$\Delta P_1 = K_{pc} Q_1^2 \tag{4-16}$$

$$\Delta P_2 = K_{pc} Q_2^2 \tag{4-17}$$

where K_{pc} is the pressure loss coefficient.

4.3.4 Forces Acting on the First Stage Spool

To accurately simulate the forces acting on the spool the flow forces were included. The flow forces are created by the flow through a valve due to the fluid momentum that acts to close the valve where

a_f is the open slot area of the first stage that depends on the spool displacement, and C_d is the discharge coefficient [4] Values used are $C_d = 0.7$ and $\theta = 69°$ [4]

The fluid velocity through the orifice 1 is given by Equation (4-18) and orifice 2 by Equation (4-19) [4].

$$v_1 = \frac{Q_1}{a_f C_d} \tag{4-18}$$

$$v_2 = \frac{Q_2}{a_f C_d} \tag{4-19}$$

The final equation to obtain the flow force is given by Equation (4-20) [4].

$$F_f = (Q_1 v_1 + Q_2 v_2)\rho \cos\theta \tag{4-20}$$

where ρ is the fluid density.

The flow forces acting on the spool had a negligible effect on the results.

4.4 SECOND STAGE

The flows from the first stage spool are directed to either end of the main stage spool. The force balance is accomplished by Equation (4-21), where M_s is the second stage spool mass, x_s is the second stage position, A_s is the spool end area, P_{s1} and P_{s2} are the pressures on either end of the second stage spool. The force is divided by the mass, to obtain acceleration, integrated twice to obtain the second stage position.

$$(P_1 - P_2)A_s = M_s \ddot{x}_s \tag{4-21}$$

Flows from the first to the second stage are obtained by Equation (4-22) and (4-23) [84].

$$Q_1 = A_s \dot{x}_s + \frac{\dot{P}_1}{k_1} - C_L(P_1 - P_2) \tag{4-22}$$

$$Q_2 = A_s \dot{x}_s + \frac{\dot{P}_2}{k_2} - C_L(P_1 - P_2) \tag{4-23}$$

The fluid stiffness, k_1 and k_2, on each side of the main spool is represented by Equation (4-24) and (4-25), where B is the bulk modulus.

$$k_1 = \frac{B}{v_{vol1}} \tag{4-24}$$

$$k_2 = \frac{B}{v_{vol2}} \tag{4-25}$$

where v_{vol1} and v_{vol2} are the trapped fluid volumes between the first and second stage.

The second stage port was modelled with blocked ports, therefore no flow and no flow forces act on the second stage spool.

4.5 VALIDATION OF MATHEMATICAL MODEL

This section provides a comparison between the experimental data and the analytical model. The model is solved numerically using Matlab Simulink. The parameter values can be seen in Table 4-1.

The piezoelectric amplifier, the piezoelectric ring bender, the hysteresis of the piezoelectric ring bender and the flow curve of the flow from the first stage to the second stage were matched to the experimental data. The second stage movement was not compared in this chapter, since its behaviour depends heavily on the control algorithm, which will be discussed in 'Control Design'.

For all the experimental tests shown in this chapter, the data obtained by using the test arrangement is described in section 3.8 and 3.9. For all the tests the amplifier was connected to the ring bender and hydraulic pressure was applied. The sampling interval of the experimental results is 0.1ms.

4.5.1 Amplifier

An open loop step response was used to investigate the dynamic response of the mathematical model of the amplifier it was compared to experimental results. The amplifier was always connected to the ring bender. It can be seen in Figure 4-3 and Figure 4-4 that the mathematical amplifier model correlates well with the experimental amplifier data in both the positive and negative direction. Figure 4-3, (a) positive direction and (b) negative direction, shows commanded step response with an amplitude of 20 V (20% of maximum voltage) and Figure 4-4, (a) positive direction and (b) negative direction, shows and amplitude of 60 volts (60% of maximum voltage). In Figure 4-3 it can also be seen that the experimental data does not reach the demanded value within the time shown.

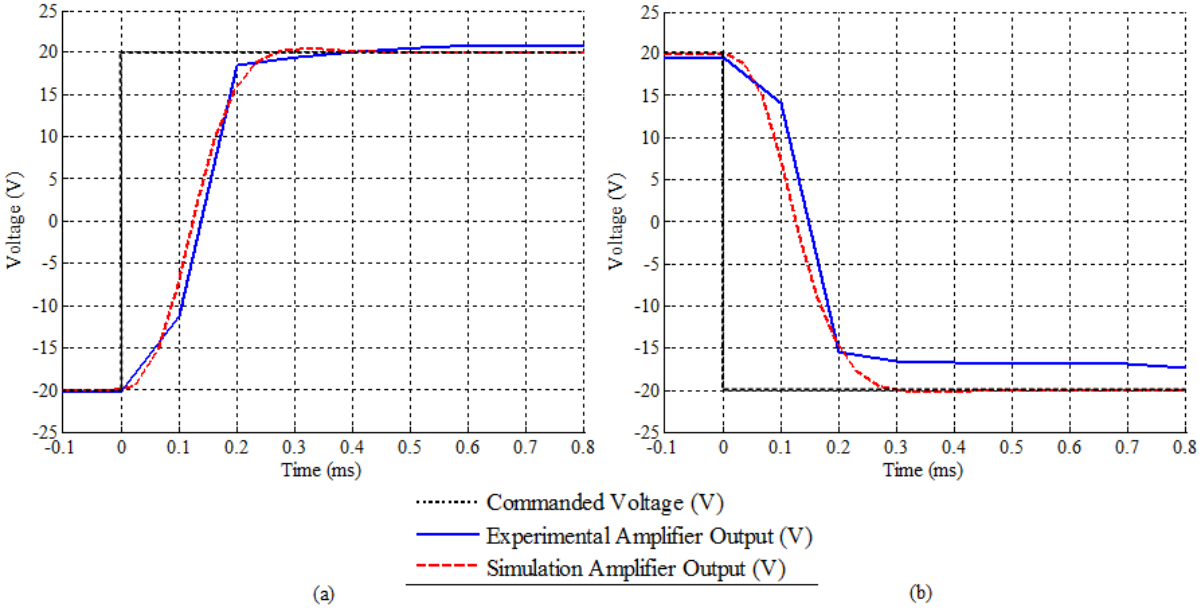

Figure 4-3. Open loop amplifier response with 20 V amplitude square wave (a) Positive direction (b) Negative direction.

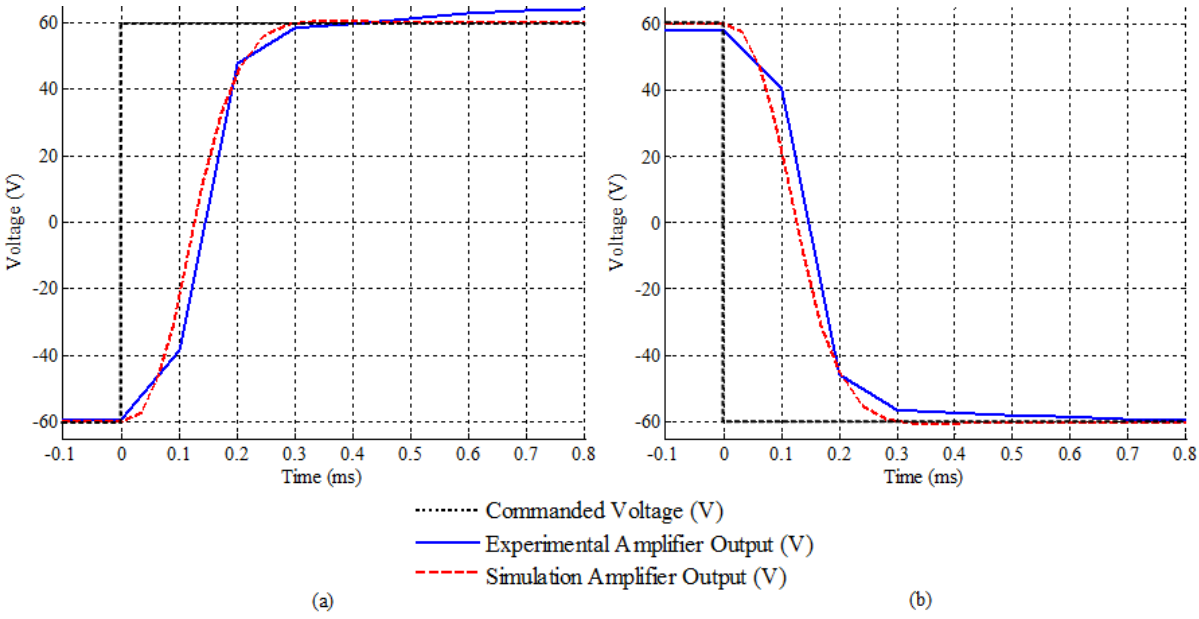

Figure 4-4. Open loop amplifier response with 60 V amplitude square wave (a) Positive direction (b) Negative direction.

4.5.2 Piezoelectric Ring Bender

The voltage from the amplifier is then applied to the piezoelectric ring bender, which bends and moves the spool. An open loop step response comparison between the experimental data and the analytical model of the ring bender movement can be seen in Figure 4-5 (20 volts amplitude, 20% of maximum voltage) and Figure 4-6 (60 volts amplitude, 60% of maximum voltage). It can be observed that the mathematical model compares well with the experimental data in both the positive and negative direction.

A significant amount of damping was introduced in the analytical model. This damping is due to the fluid inside the valve. There is a restriction in the path of fluid movement from one side of the ring bender to the other, hence additionally damping the system. Also, a delay of 0.5ms was required in the model to match the experimental data due to the phase lag of the LVDT.

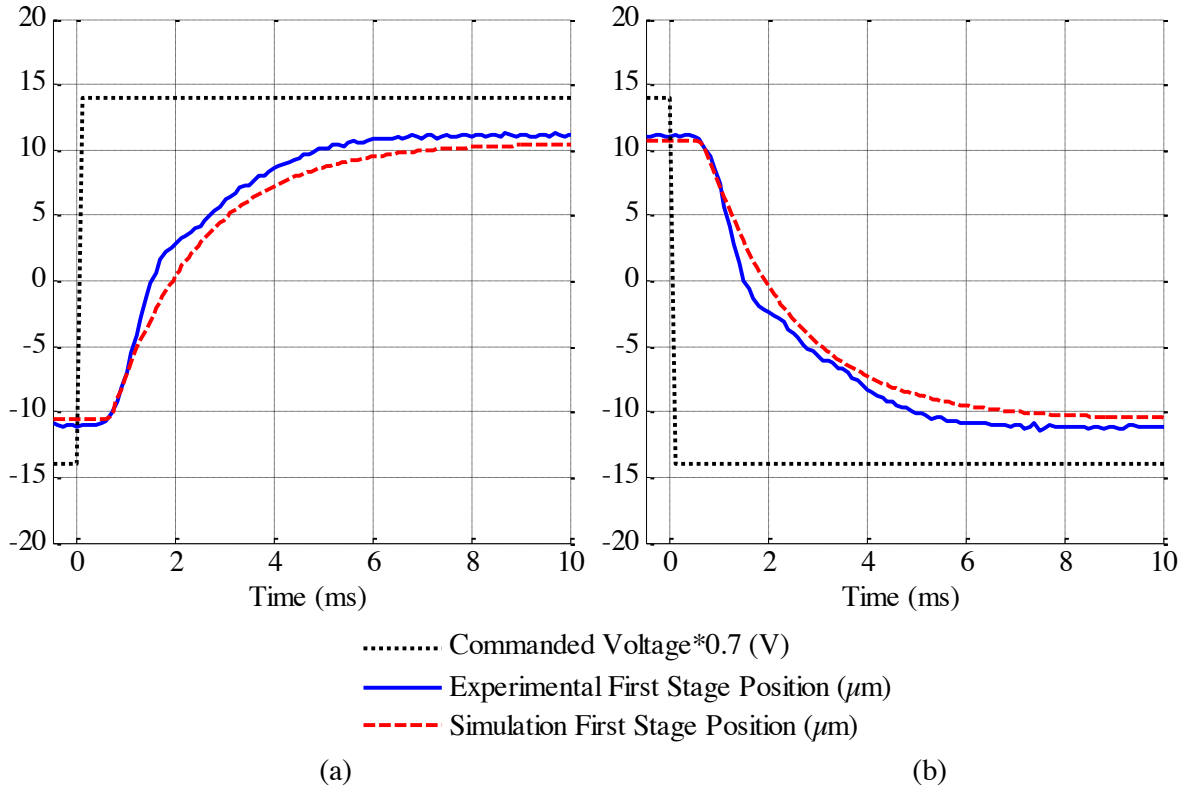

Figure 4-5. Open loop first stage comparison between mathematical model and experimental data with 20 volts amplitude (a) Positive direction (b) Negative direction.

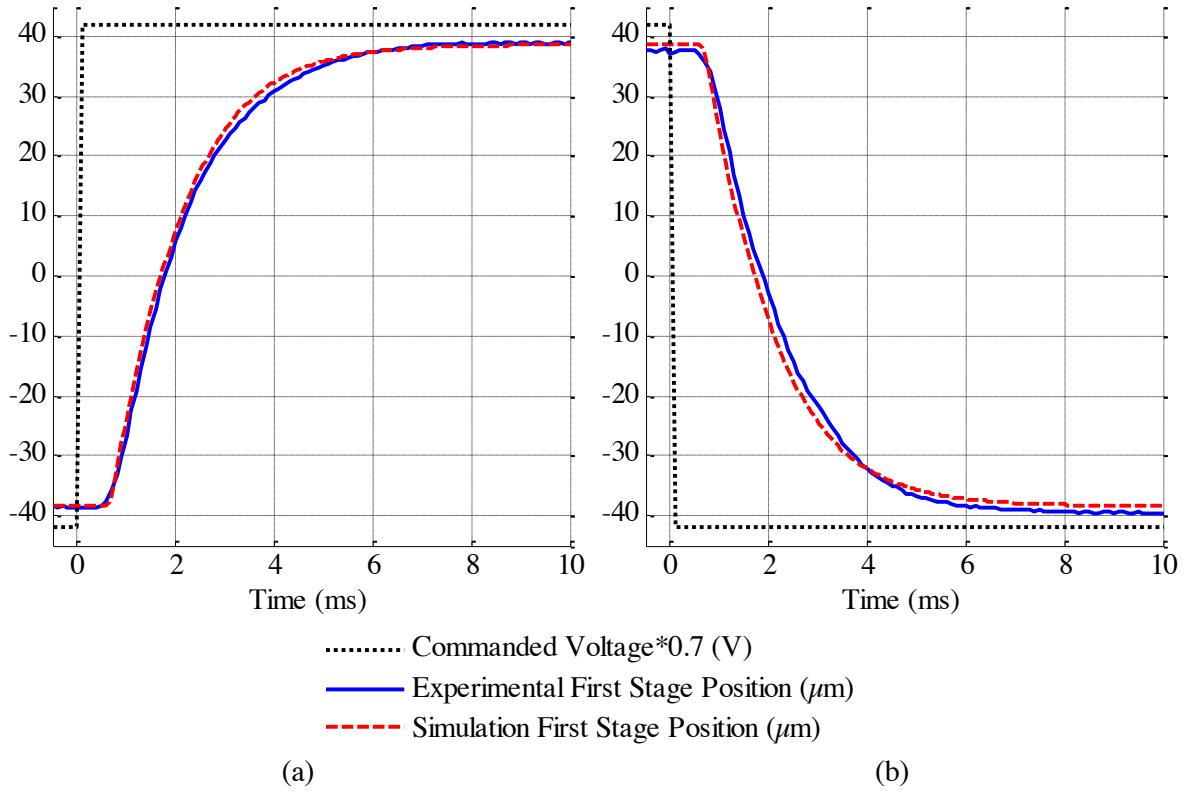

Figure 4-6. Open loop first stage comparison between mathematical model and experimental data with 60 volts amplitude (a) Positive direction (b) Negative direction.

4.5.3 Piezoelectric Hysteresis

The Bouc-Wen mathematical hysteresis model was compared and matched to the experimental results of the piezoelectric ring bender hysteresis. The tuning parameters used in the mathematical models to match the experimental hysteresis loop can be found in Table 4-1. A comparison of the hysteresis loops from the experimental data and the mathematical Bouc-Wen model can be seen in Figure 4-7. The figure shows the displacement of the piezoelectric ring bender against the applied voltage and it can be seen that the analytical model provides realistic results when compared to the experimental results.

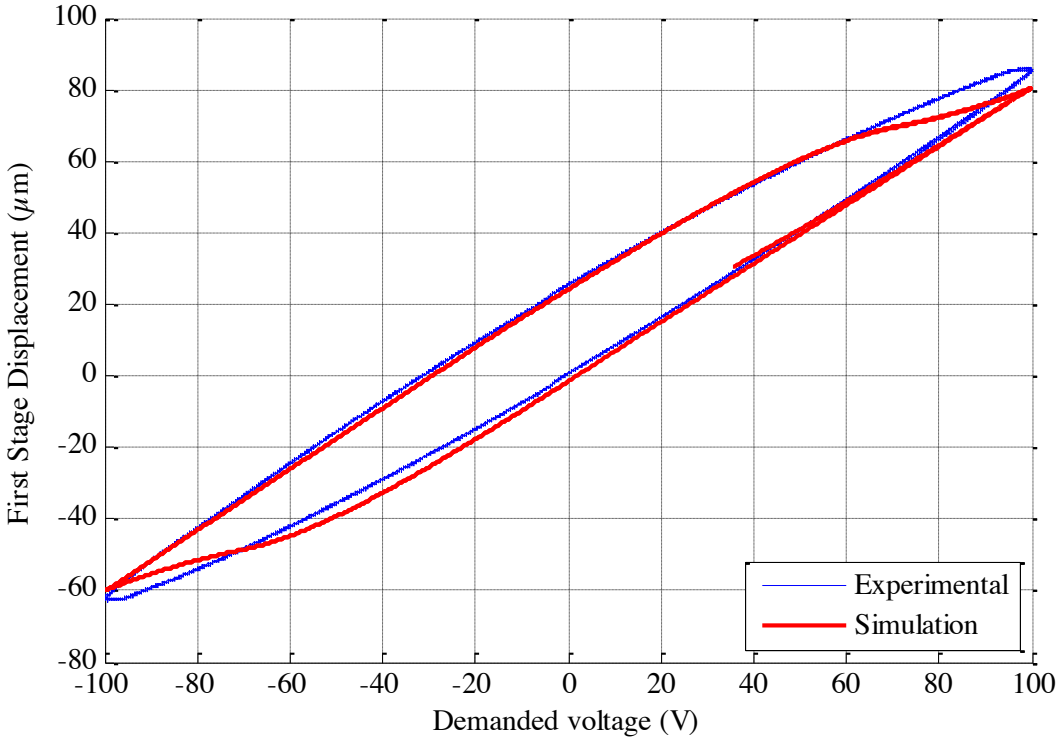

Figure 4-7. Ring bender hysteresis loop comparing the analytical Bouc-Wen model to experimental data.

4.6 Flow Curve

The first stage flow characteristics represents the flow from the first stage to the second stage. This was done by controlling the second stage in closed loop in a sine wave fashion at 20Hz. From the position and velocity of the second stage, the flow could be obtained. This flow will affect behaviour and performance of the second stage spool. It can be seen in Figure 4-8 that the simulation has a similar flow curve to the experimental data, but there are differences. It can be seen that the experimental data has a 'constant' amount of hysteresis. This hysteresis could be due to the hysteresis still present in the first stage piezoelectric ring bender as well as friction in the valve [86]. The analytical model has less hysteresis around zero and more hysteresis further away from zero.

The second stage movement is sensitive to changes in this flow curve, therefore it is difficult to match the analytical model to the experimental data. The simulated flow curve as obtained after correlating the dynamic experimental second stage characteristics with the analytical model, as can be seen in section 5.9. The second stage characteristic is heavily dependent on the controller, therefore this can be seen in the 'Controller Design' chapter.

Another reason for the difference between the experimental flow curve and the analytical could be due to yet unknown characteristics. A possible source of error could be flow reattachment in the spool and bushing assembly. Generally, a free jet passes through an orifice at an angle of 69°, but in some cases

the jet can curve and reattach to the wall. This effect can change the flow coefficient of the flow from the first to the second stage [4].

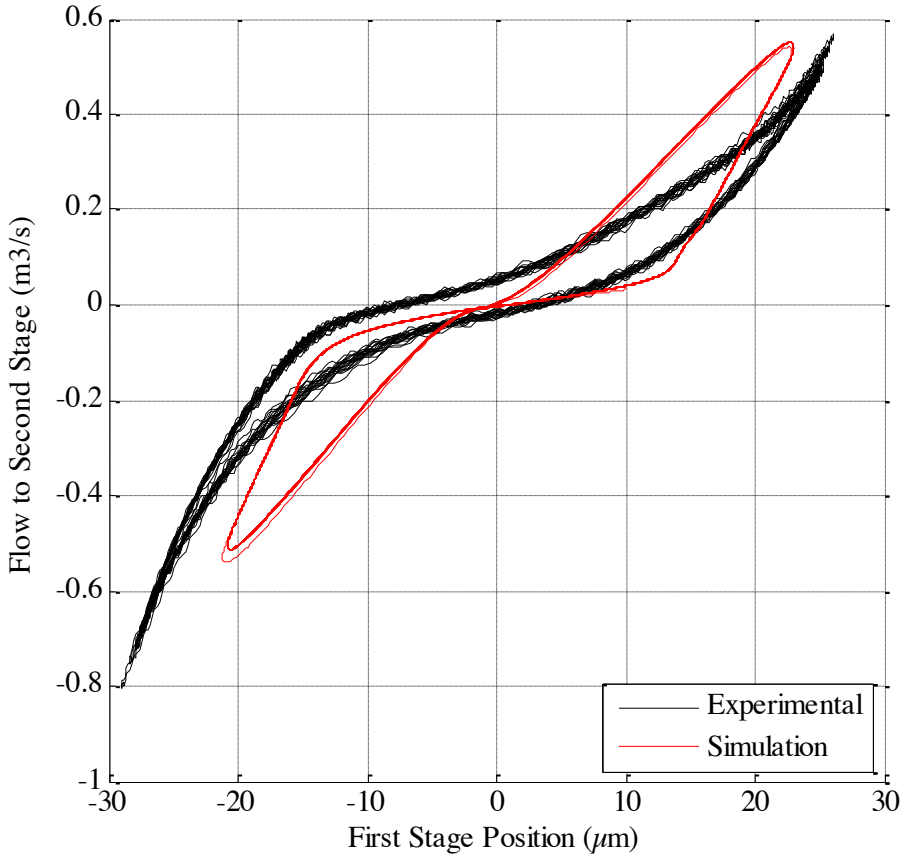

Figure 4-8. Graph showing a comparison between experimental and analytical first stage flow curve.

Table 4-1. Parameters used for the analytical model.

Parameter	**Explanation**	**Value**
α	Hysteresis tuning parameter	0.0017
β	Hysteresis tuning parameter	0.00065
γ	Hysteresis tuning parameter	0.0015
ζ	Damping factor of the amplifier	0.8
θ	Jet angle	69 deg
ρ	Fluid Density	1000 $\mathrm{kg/m^3}$
υ	Kinematic viscosity	0.000011 $\mathrm{m^2/s}$
ω_n	Natural frequency of the amplifier	21000 $\mathrm{rad/s}$
A_s	Second stage piston area	0.5355 $\mathrm{m^2}$
c	Piezoelectric ring bender damping	5.6

C_d	Discharge coefficient	0.7
C_q	Flow coefficient	$1.6667 \text{x} 10^{-5}$
C_{rb}	Capacitance of piezoelectric ring bender	$2 \cdot 1740$ nF
F_{bf}	Blocking force of the piezoelectric ring bender	39 N
I_{max}	Maximum current	1 A
K_a	Amplifier scaling factor	20
k_{I+}	Positive input value in the outside the overlap region	1
k_{I-}	Negative input value in the outside the overlap region	1
k_{IO+}	Positive input value in the overlap region	0.1217
k_{IO-}	Negative input value in the overlap region	-0.1217
k_{O+}	Positive output value in the outside the overlap region	0.87
k_{O-}	Negative output value in the outside the overlap region	1
k_{OO+}	Positive output value in the overlap region	0.007
k_{OO-}	Negative output value in the overlap region	-0.007
m_{add}	Added mass	3 g
m_s	Mass of first stage spool	2.61 g
M_s	Mass of second stage spool	20 g
n_f	Number of lands on the first stage	2
n_s	Number of lands on the second stage	5
p	Total pressure loss	70 bar
P_s	Supply pressure	3000 psi
P_r	Return pressure	50 psi
q	First stage flow rate	0.21 l/min
S	Maximum stroke of the piezoelectric ring bender	115 µm
V_c	Control voltage	± 5 V
V_{max}	Maximum operating voltage	100 V
v_{vol1}	Fluid volume between the first and second stage spool in control port 1	0.818 cm^3
v_{vol2}	Fluid volume between the first and second stage spool in control port 2	0.818 cm^3
w_s	First stage flow slot width	0.508 mm
y_f	Clearance between the first stage spool and bushing	0.001 mm
y_s	Clearance between the second stage spool and bushing	0.004 mm

4.7 CONCLUSION

An analytical model of the two-stage piezoelectric actuated valve with a first stage small spool has been developed to obtain a further understanding of the complete valve. The analytical model included the amplifier for the piezoelectric ring bender, the ring bender with hysteresis, the first stage spool and the flow from the first stage to the second stage. The model shows good correlation with the experimental data. Due to the sensitivity of the first stage flow model, especially within the overlap region, the flow was hard to correlate to the experimental data. This will affect the second stage spool behaviour, which will be shown in the next chapter 'Controller Design'.

The original aspect is that an analytical model of a piezoelectric ring bender controlling a spool has been developed and validated against experimental data. This includes the amplifier, ring bender with hysteresis and first stage orifice equations.

The next chapter will describe an experimental control algorithm that includes hysteresis compensation, overlap compensation and a feedforward loop. It will also show a comparison between experimental data and analytical data for the second stage.

5 CONTROLLER DESIGN

This chapter describes an experimental control algorithm developed to compensate for the first stage hysteresis and overlap as well as increase the bandwidth for the position control of the main spool.

5.1 INTRODUCTION

This chapter presents a control strategy for compensating the hysteresis of the piezoelectric ring bender, without using additional sensors (such as first stage position feedback), which add weight, cost and complexity to the valve. The first stage LVDT in the valve prototype will merely be used to monitor the performance of the piezoelectric ring bender and first stage spool and not used for control.

The influence of a reduction of first stage piezoelectric hysteresis on the second stage positioning performance was studied. The proposed control algorithm also includes compensation for the dead-band caused by the first stage spool overlap and implementation of a feed forward term to increase the second stage spool position response. The effect of each part was investigated and the complete control algorithm was compared to a control loop with only a conventional PI controller.

It has been observed the response and settling time of the second stage varies significantly at different step sizes if a conventional PI controller is used. A conventional controller can be well tuned for a certain step size, but if the step size is changed the performance of the controller would degrade. This is mainly due to the large first stage overlap and the piezoelectric hysteresis. This chapter will highlight that a conventional PI controller would perform significantly differently at different step sizes for a valve with first stage spool overlap and hysteresis. Therefore, a new non-linear controller is needed that is less sensitive to amplitude change.

5.2 CONTROLLER REQUIREMENTS

There are some requirements for the now proposed control algorithm. The new controller needs to compensate for the piezoelectric hysteresis. It also needs to compensate for the first stage dead band caused by the first stage spool overlap. The controller should also increase the bandwidth. The proposed controller should be less sensitive to amplitude change and should outperform a well tuned conventional PI controller at different amplitudes without adjusting any controller parameters.

The requirements for the proposed controller is that it should have a rise time less than 5ms and a settling time less than 20ms for all amplitudes.

5.3 CONTROLLER METHODOLOGY

5.3.1 PI Controller

The PI controllers were setup purposely to obtain the quickest response and settling time for a specific step size. The settings for K_p and K_i were obtained by measure the response and settling time at a specific step size and manually adjusted to obtain the quickest response. This was done for two different step sizes. Hence, two different PI controllers were obtained.

5.3.2 Proposed Controller

The controller parameters for the hysteresis compensation model were obtained by matching the analytical model of the hysteresis to an experimental hysteresis loop, as described in section 4.5.3.

The overlap region was obtained from examining the first stage flow curve as can be seen in Figure 4-8. The overlap was then converted into a voltage (u_+ and u_-). This was done by calculating the percentage of the spool overlap in comparison with the amount of stroke of the ring bender. The percentage equals the percentage of the maximum allowed voltage of u_2, which is ± 5 V. The O_+ and O_- was manually adjusted.

The velocity feed forward terms and the correction for asymmetry were manually adjusted for the valve. The reference model was created using the analytical model with minor adjustments when tested on the prototype valve.

The K_p and K_i values were manually adjusted to obtain a fast response and settling time at various step sizes without saturation of the controller.

5.4 CONTROLLER DESIGN

The controller platform used for this investigation was an xPC system where a Simulink model is coded in real-time to control the piezoelectric ring bender, the pilot stage spool and main stage spool. In the xPC system a control loop using a conventional PI controller, as well as the proposed control algorithm, were implemented.

A Proportional-Integral (PI) controller is a common feedback control algorithm, using Proportional, K_p, and Integral, K_i, terms as can be seen in Figure 5-1. In this case, this control loop is unlikely to be sufficient due to the non-linear relationship between input signal and first stage flow output. This is due to the non-linear piezoelectric hysteresis and the dead-band, caused by the relatively large first stage spool overlap.

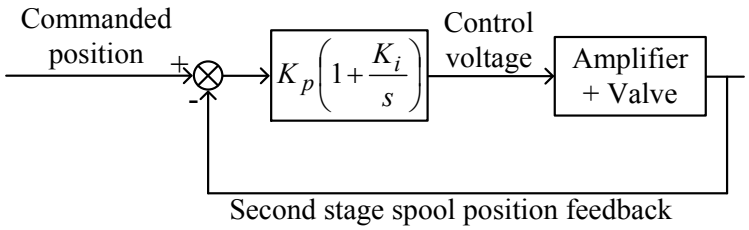

Figure 5-1. PI control loop.

The proposed control algorithm can be seen in Figure 5-2, with several sub-parts, which includes overlap compensation, hysteresis compensation and command velocity feed forward terms. It also compensates for any asymmetry due to manufacturing tolerances, as well as offset between the electrical null of the piezoelectric ring bender and the first stage hydraulic null. This implies that a voltage needs to be applied to the first stage to move the piezoelectric ring bender to bring the first stage spool to its hydraulic null position, giving no flow through the first stage.

The hysteresis and overlap compensation are intended to make the system more linear and the feed forward loop is to make the system respond faster to a position command change.

Compensation of overlap or hysteresis alone has been described previously, for example [18][87][79]. However, the combination of overlap and hysteresis compensation together is novel.

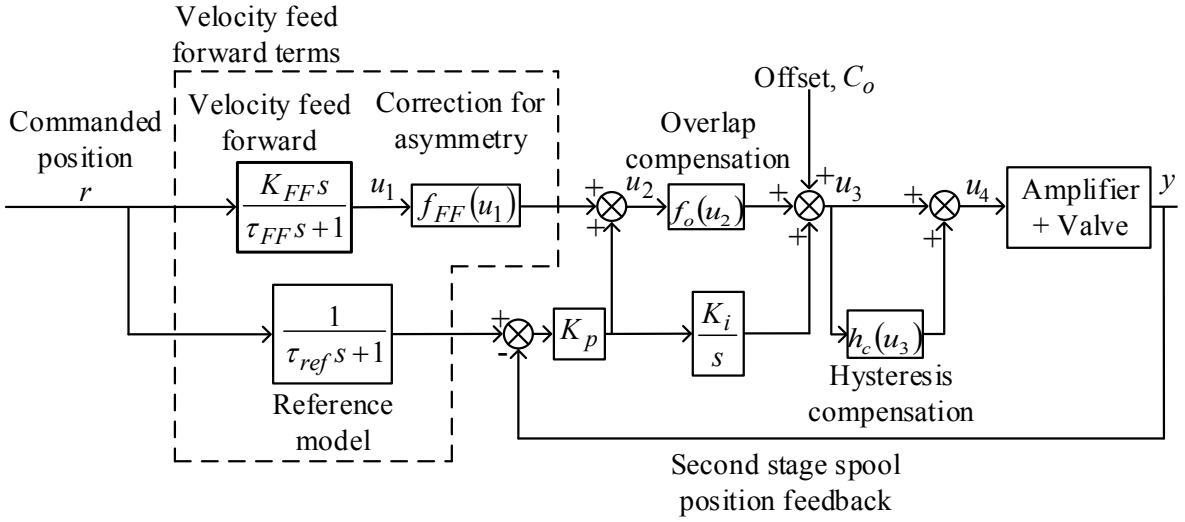

Figure 5-2. Proposed control algorithm with overlap compensation, hysteresis compensation and feed forward loop.

5.5 HYSTERESIS COMPENSATION

Previously, an inverse hysteresis model of the more complicated Prandtl-Ishinskii model has been used for hysteresis compensation of a piezoelectric ring bender [18]. The Bouc-Wen model has been used previously to compensate for the hysteresis of a rectangular piezoelectric bender [88]. However, in that work only static or low frequency (0.07Hz) responses were investigated.

The hysteresis compensation used for this proposed control algorithm is based on the Bouc-Wen hysteresis model [3], which as described earlier, is a relatively simple model and also simple to implement into the control algorithm [88]. The Bouc-Wen model has three dimensionless tuning parameters, as seen in Equation (5-1). The three tuning parameters are adjusted to obtain the desired hysteresis loop. The hysteresis term n is the deviation away from the linear response, u_3 is the demand voltage from the controller (voltage after the overlap compensation and integral gain) and α, β and γ are the three-dimensionless hysteresis tuning parameters. As shown previously, in Figure 4-7, which shows an experimental hysteresis loop and a simulated hysteresis loop where n is subtracted from the linear response, the simulated hysteresis model matches the experimental data closely. In the compensator, n times a scaling factor, is added to the control voltage, as can be seen in Equation (5-2). The scaling factor, K_h, is needed to restore the correct linear gain. Without the scaling factor the output voltage to the amplifier, u_4, would result in saturation at maximum and minimum voltage.

$$\dot{n} = \alpha\dot{u}_3 - \beta|\dot{u}_3|n - \gamma\dot{u}_3|n| \tag{5-1}$$

$$h_c(u_3) = K_h n \tag{5-2}$$

Figure 5-3 shows two experimental hysteresis loops, one with and the other without hysteresis compensation. These were both obtained by controlling the first stage in an open loop sine wave fashion at a frequency of 0.0166 Hz. As can be seen the amount of hysteresis is significantly reduced with hysteresis compensation. The three tuning parameters values used for the Bouc-Wen model can be seen in Table 5-1.

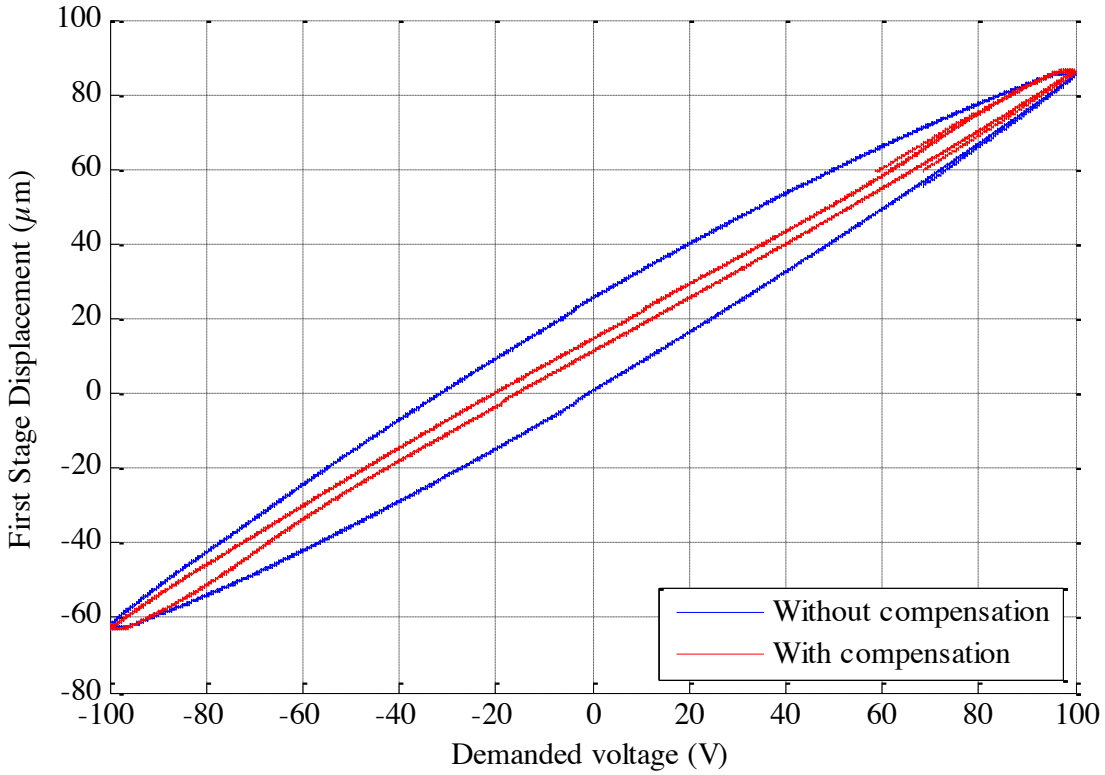

Figure 5-3. Experimental hysteresis with and without hysteresis compensation.

5.6 Overlap Compensation

To further linearize the system, the first stage spool overlap which causes a dead-band was compensated for. The principle is shown in Figure 5-4 (a). The compensator will make the spool 'jump' through the overlap region, see Figure 5-4 (b), which linearizes the relationship between the input signal and the flow output [79][87], similar what can be seen in Figure 5-4 (c).

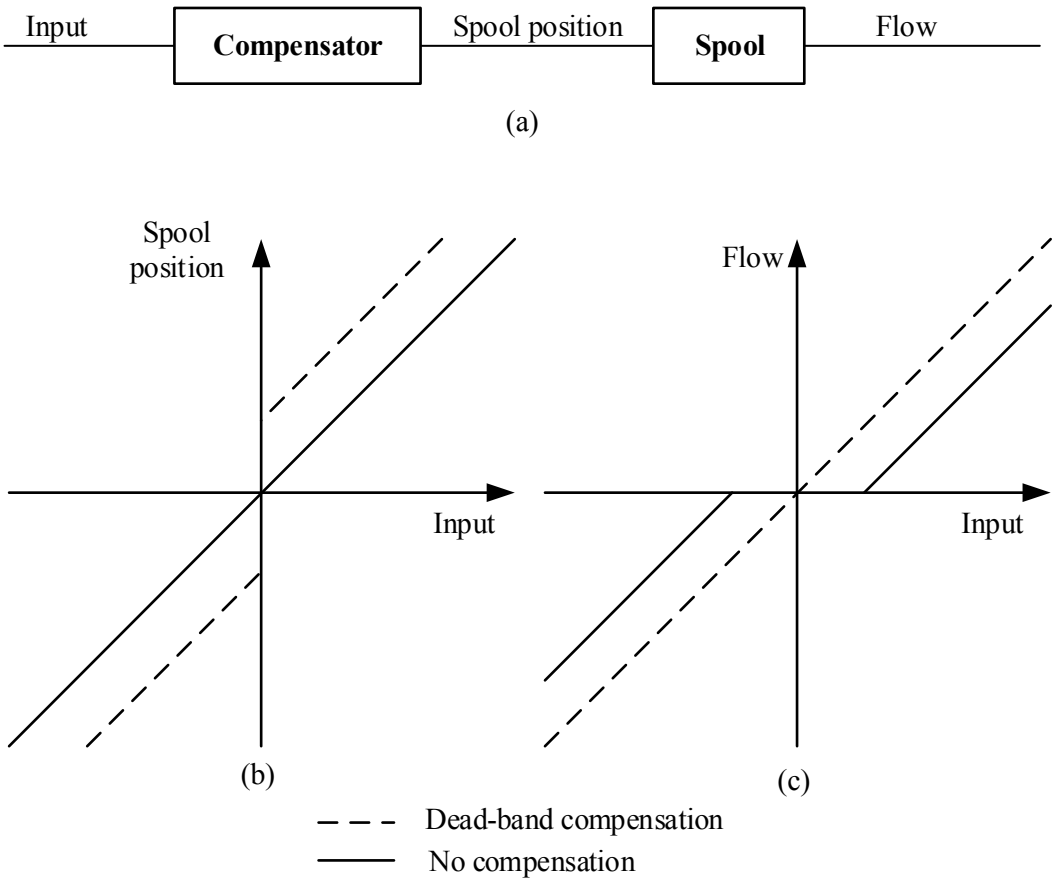

Figure 5-4. (a) Dead band compensation (b) Compensator characteristic (b) Flow output versus input with and without dead-band compensation.

In practice, the flow gain in the overlap region is not zero. Thus, the overlap compensation, within the proposed control loop was implemented as a look-up table, where a higher gain was implemented as function $f_0(u_2)$, while the first stage spool was in the overlap region, see Figure 5-5.

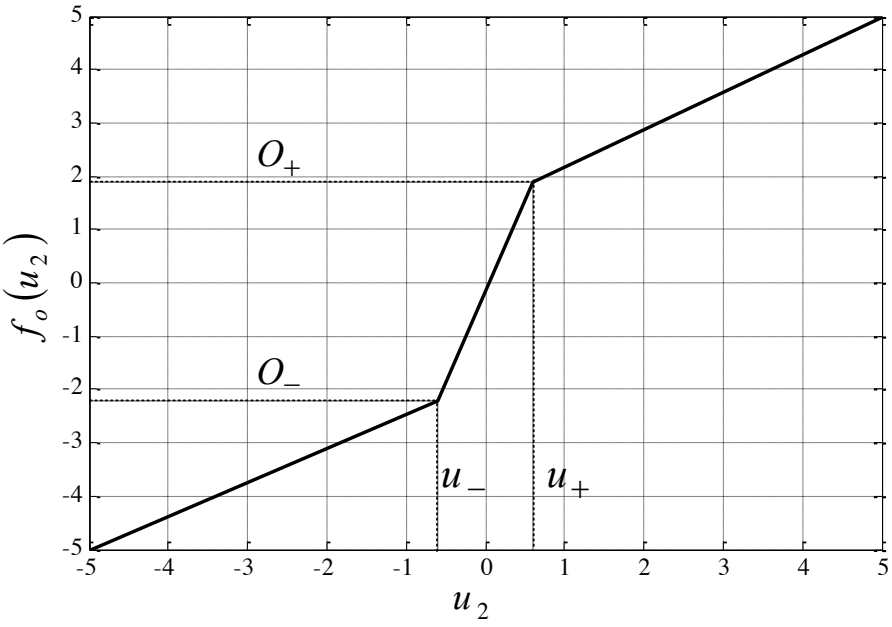

Figure 5-5. Overlap compensation function $f_0(u_2)$ showing a higher gain within the overlap region implemented into the experimental control algorithm.

5.7 COMMAND VELOCITY FEED FORWARD

The feed forward will speed up the tracking response and increase the bandwidth of the system [89][90]. The velocity feed forward consists of three parts, the velocity feed forward filter, reference model and the model to correct for asymmetry in the second stage spool behaviour. The feed forward command velocity is estimated by the differential of command position filtered by a first order lag, as can be seen in Figure 5-2.

The feedforward loop also compensates for velocity asymmetry in the system. The asymmetry is due to the null offset (offset between the electrical null of the ring bender and the hydraulic null of the spool) in the valve coupled to the non-linear stiffness of the piezoelectric ring bender mounting. The function $f_{FF}(u_1)$ term is a lookup table as shown below:

$$f_{FF}(u_1) = 1.4u_1 \text{ if } u_1 \geq 0 \tag{5-3}$$

$$f_{FF}(u_1) = u_1 \text{ if } u_1 < 0 \tag{5-4}$$

A reference model is included as a prediction of the response of the system to the feedforward path. The feedback control thus only acts on the error between the actual spool position and the predicted position. This error can also be thought of as a disturbance observer [90].

The parameters, their meaning and the values used for the control algorithm can be seen in Table 5-1.

In the next section, results for the two PI controllers are also shown, and the gains for these are also included in the table.

Table 5-1. Parameters used for the experimental control algorithm.

Parameters	Explanation	Value
α	Hysteresis tuning parameter	0.0017
β	Hysteresis tuning parameter	0.00065
γ	Hysteresis tuning parameter	0.0015
τ_{FF}	Feedforward filter time constant	0.0015 s
τ_{ref}	Reference model time constant	0.003 s
C_0	Null offset compensation	0.25 V
K_{FF}	Feedforward gain term	0.00005 $\mathrm{V/(\mu m/s)}$
K_h	Hysteresis scaling factor	0.87
K_i	Integral gain for the non-linear controller	200
K_{i1}	Integral gain for control loop PI1	1
K_{i2}	Integral gain for control loop PI2	1
K_p	Proportional gain for the non-linear controller	0.012 $\mathrm{V/\mu m}$
K_{p1}	Proportional gain for control loop PI1	0.05 $\mathrm{V/\mu m}$
K_{p2}	Proportional gain for control loop PI2	0.03 $\mathrm{V/\mu m}$
O_+	Positive overlap compensation output	1.9 V
O_-	Negative overlap compensation output	-2.2 V
u_+	Positive overlap compensation input	0.6 V
u_-	Negative overlap compensation input	-0.6 V

5.8 EXPERIMENTAL VALVE CONTROL

The valve prototype with the proposed control algorithm was tested. The effect of the different controller parts was compared. Four different controller arrangements were tested:

i. Complete controller (FF+OC+HC)
ii. Overlap compensation (OC) and hysteresis compensation (HC)
iii. Overlap compensation (OC) and feed forward (FF)
iv. Only overlap compensation (OC).

Referring to Figure 5-2, (i) is the complete system, in (ii) $K_{ff} = 0$ and the reference model is unity, in (iii) $h_c(u_3) = 0$, and in (iv) $K_{ff} = 0$, the reference model is unity, and $h_c(u_3) = 0$.

In all cases the proportional and integral gain are unchanged. Two different step responses sizes, 60µm and 120µm, were tested as well as a 30µm amplitude frequency response. The new controller is compared to a conventional PI controller at the end of this section.

All tests were performed at 207bar and at an oil temperature of 39±1.5°C.

Figure 5-6 shows the 60µm step response and Figure 5-7 shows the 120µm step response. The rise time (0-90%) and the settling time (±5%) for both amplitudes can be seen in Table 5-2 and Table 5-3.

By only compensating for the overlap the rise time is 8.2ms for a 60µm step and 7.3 for a 120µm step size. The settling time for the 120µm step was 57.6ms and for the 60µm step was not able get within ±5%. With the overlap compensation and hysteresis compensation the response is quicker, but there is more overshoot. By having the overlap compensation and a feed forward term the response was even further improved. The rise time was 10.3ms and settling time was 19.9ms for a 60µm step. For a 120µm step size rise time was 4.9ms and settling time was 5.2ms. The complete experimental controller had the overall fastest response with 4.6ms rise time and 15.7ms (although 0.8ms slower than with only overlap compensation and feed forward term) for a 60µm step and 4.3ms rise time and 4.8ms settling time for 120µm step.

The average difference between the commanded position and the actual position is 5.6µm for a 60µm step and 7.7µm for the controller without the hysteresis (OC+FF). This can be compared to the complete controller that has a difference of 4µm for 60µm step and 6.1µm for 120µm step.

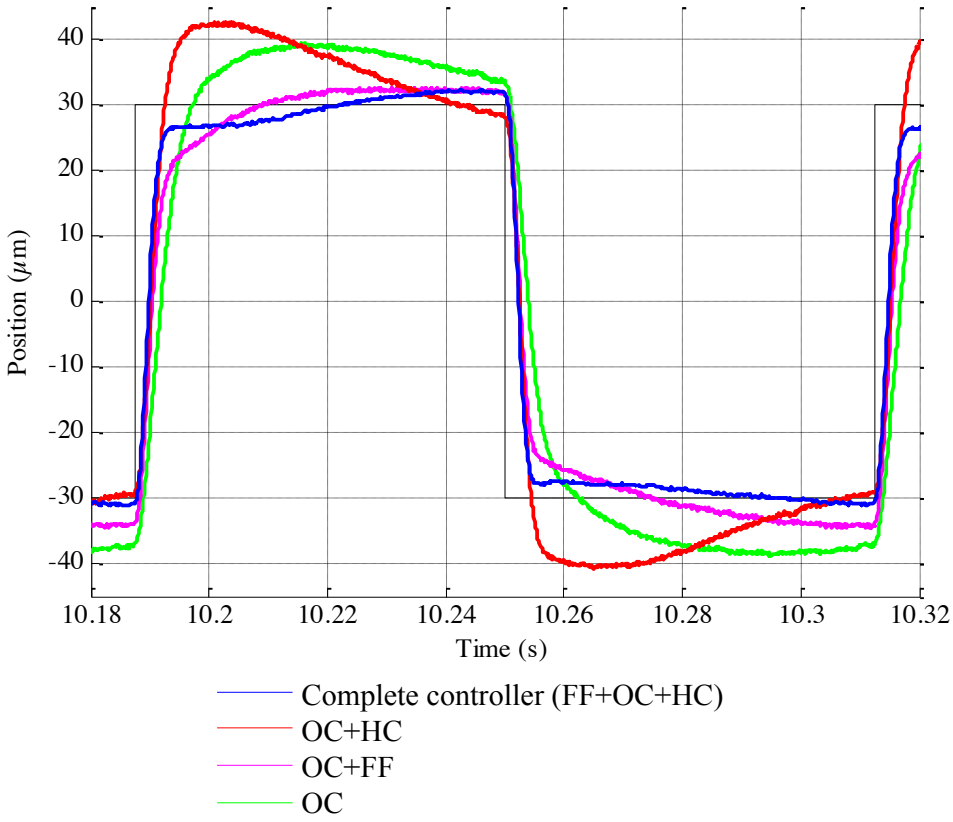

Figure 5-6. 60µm step response results comparing the four different controller scenarios.

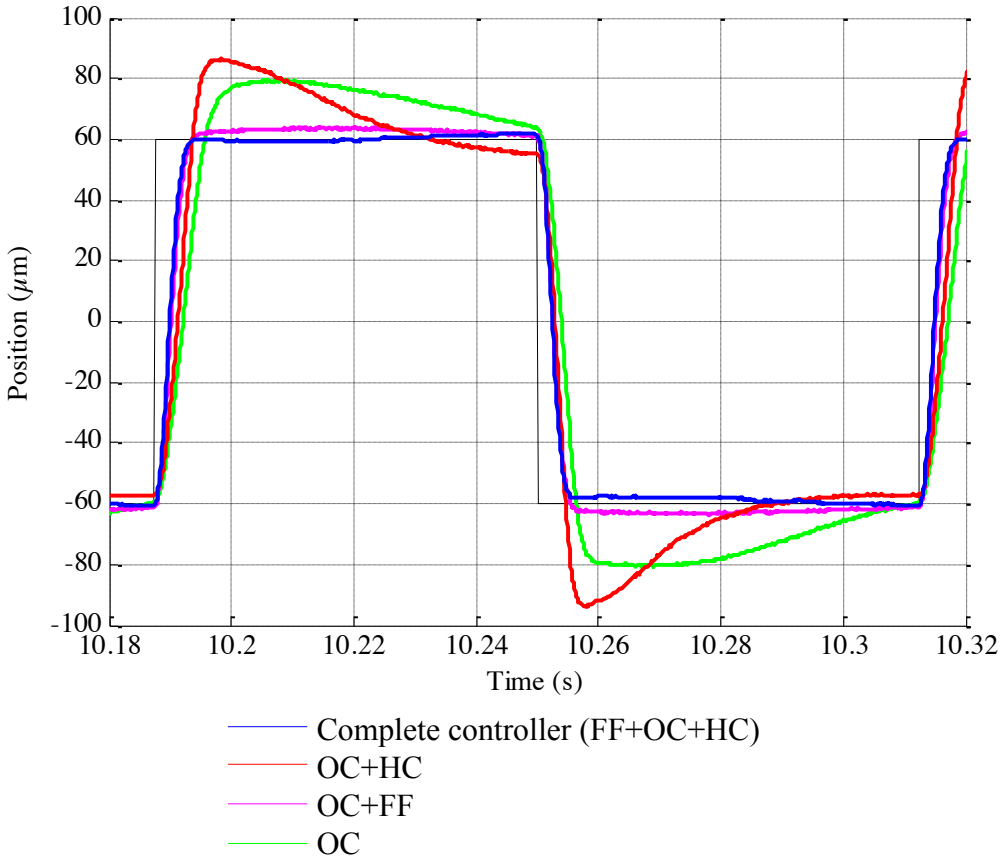

Figure 5-7. 120μm step response results comparing the four different controller scenarios.

Table 5-2. 60μm step response results with different combinations of overlap compensation (OC), feed forward (FF) and hysteresis compensation (HC).

60μm Step	**Rise time (0-90%)**	**Settling time (±5%)**
Complete controller (FF+OC+HC)	4.6ms	15.7ms
OC+HC	4.5ms	44.6ms
OC+FF	10.3ms	14.9ms
OC	8.2ms	>62.5ms

Table 5-3. 120μm step response results with different combinations of overlap compensation (OC), feed forward (FF) and hysteresis compensation (HC).

120μm Step	**Rise time (0-90%)**	**Settling time (±5%)**
Complete controller (FF+OC+HC)	4.3ms	4.8ms
OC+HC	5.7ms	35.8ms
OC+FF	4.9ms	5.2ms
OC	7.3ms	57.6ms

A frequency response test was completed, by using a chirp signal, with an amplitude of 30µm, see Figure 5-8. It can be seen that in the system where the feed forward loop is included, both the magnitude and phase lag first decreases then increases again. This is most likely due to the increase in gain within the first stage overlap region, as the control voltage starts to increase, related to the inexact overlap compensation.

It can also be seen in Figure 5-8 that the setup with overlap compensation and hysteresis compensation (without feedforward) has a better performance than the complete system until around 50 Hz for the magnitude and 30 Hz for the phase. After those frequencies the complete setup performs better than the other control algorithms.

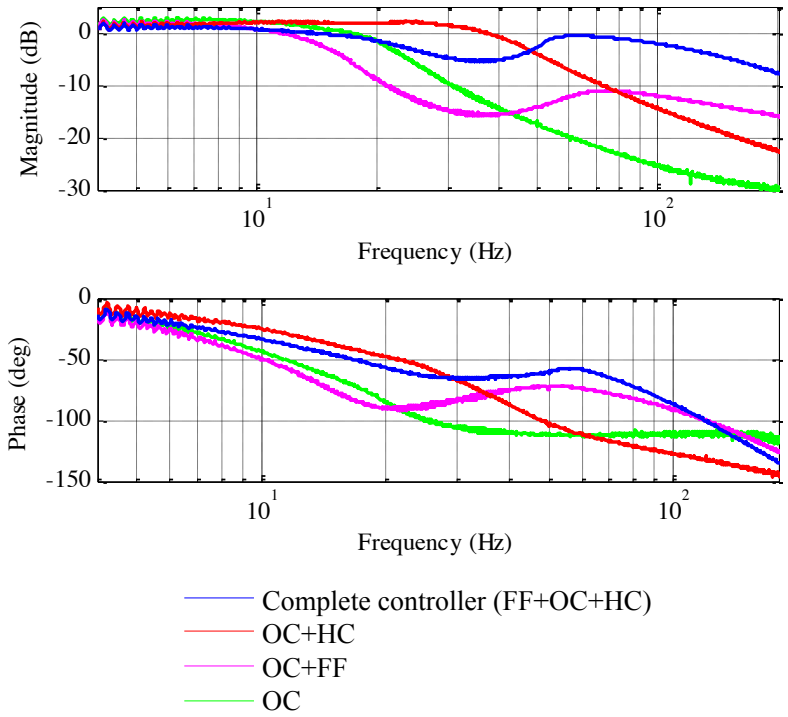

Figure 5-8. Frequency response results for a 30µm amplitude comparing the four different controller scenarios.

The complete non-linear controller was compared to a well-adjusted conventional PI controller algorithm. Responses to steps of 60µm and 120µm were measured as well as a 30µm amplitude frequency response. Two different PI setups were tested, one was tuned for a square wave amplitude of 30µm amplitude (60µm step, PI1) and the second for a 60µm amplitude (120µm step, PI2). This was done to show that for a non-linear system a conventional PI controller is sensitive to amplitude change.

It can be seen in Figure 5-9, 60µm step, and Figure 5-10, 120µm step, that for the same PI controller for the different amplitudes significantly different results are obtained. It can also be observed that the proposed non-linear control algorithm is the better controller when it comes to rise time and settling time, as can be seen in Table 5-4 and Table 5-5 as well as being less affected by the amplitude change.

The PI controller setup for a 30µm amplitude (60µm step) it did not reach within ±5% of the step within 62.5ms in either case.

Due to the large overlap of the first stage spool it is essential to obtain a control algorithm to compensate for this. It is important to be able to adjust for any nonlinearities within the system. In this system, it is also believed that the mounting of the piezoelectric ring bender creates an asymmetry in the results. This is adjusted for by having a different gain in each direction in the non-linear controller. During these tests, non of the controller reached saturation.

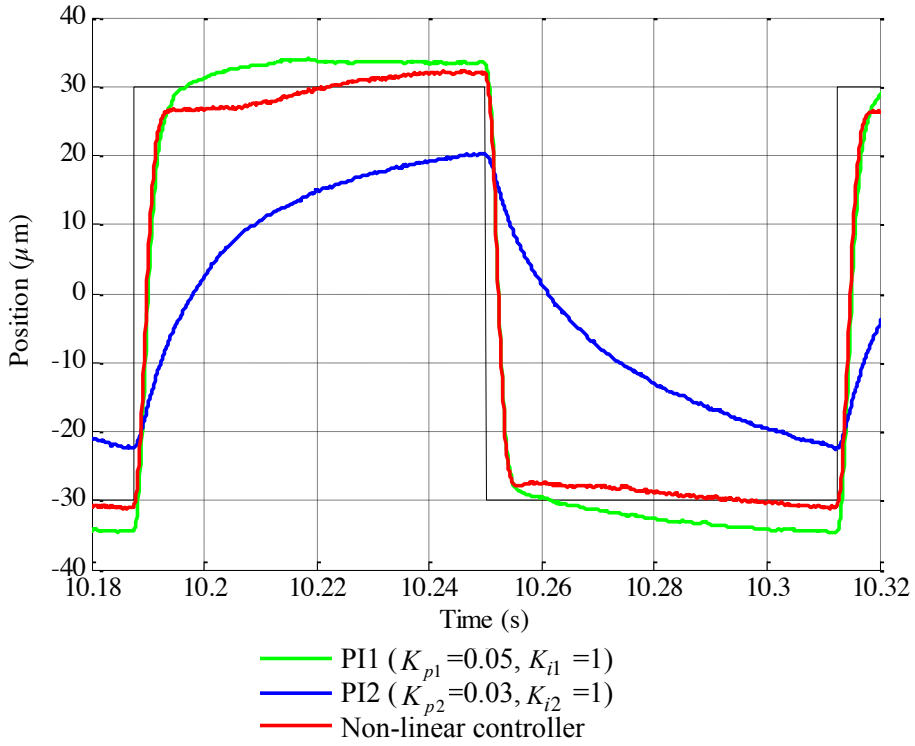

Figure 5-9. 60µm step response comparing two sets of conventional PI controller to the complete non-linear control algorithm.

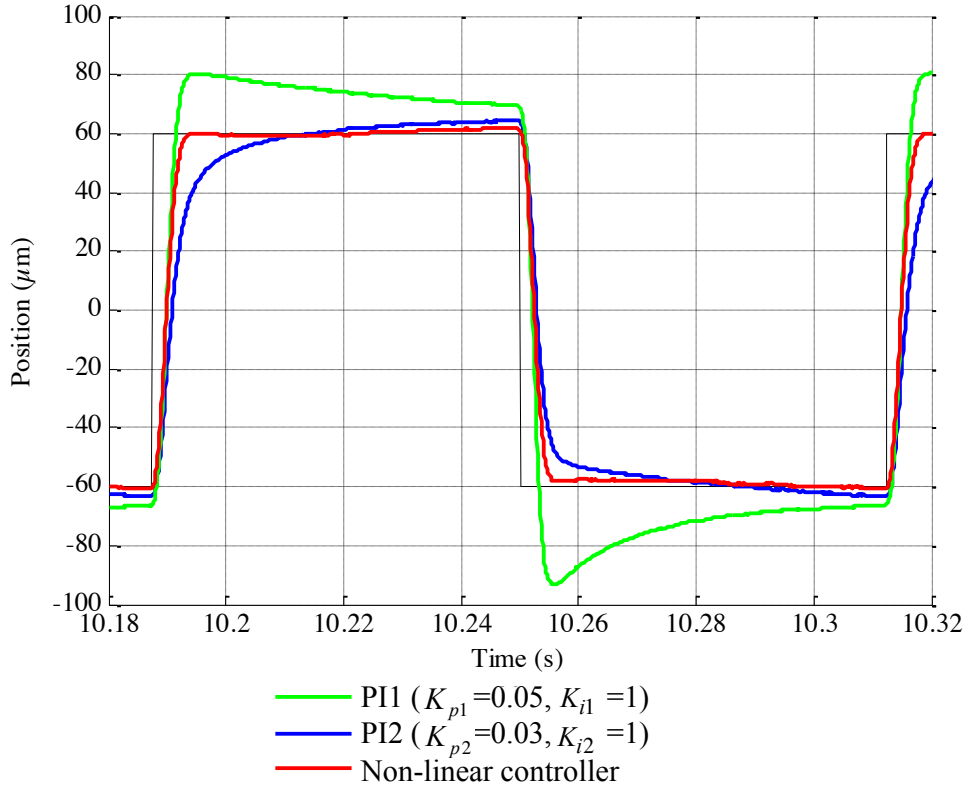

Figure 5-10. 120μm step response comparing two sets of conventional PI controller to the complete non-linear control algorithm.

Table 5-4. Rise and settling time for the two PI controllers and the non-linear controller for a 60μm step response.

60μm Step	**Rise time (0-90%)**	**Settling time (±5%)**
PI1 $(K_{p1} = 0.05, K_{i1} = 1)$	5.2ms	>62.5ms
PI2 $(K_{p2} = 0.03, K_{i2} = 1)$	>62.5ms	>62.5ms
Non-linear controller	4.6ms	15.7ms

Table 5-5. Rise and settling time for the two PI controllers and the non-linear controller for a 120μm step response.

120μm Step	**Rise time (0-90%)**	**Settling time (±5%)**
PI1 ($K_{p1} = 0.05, K_{i1} = 1$)	3.7ms	>62.5
PI2 ($K_{p2} = 0.03, K_{i2} = 1$)	9.4ms	14ms
Non-linear controller	4.3ms	4.8ms

A frequency response was completed for the two PI controllers and the non-linear controller, see Figure 5-11. It can be observed that the non-linear controller gives a better dynamic response, particularly in

terms of the magnitude throughout the frequency range. Note that the low frequency phase lag evident in the PI controller response is due to the hysteresis.

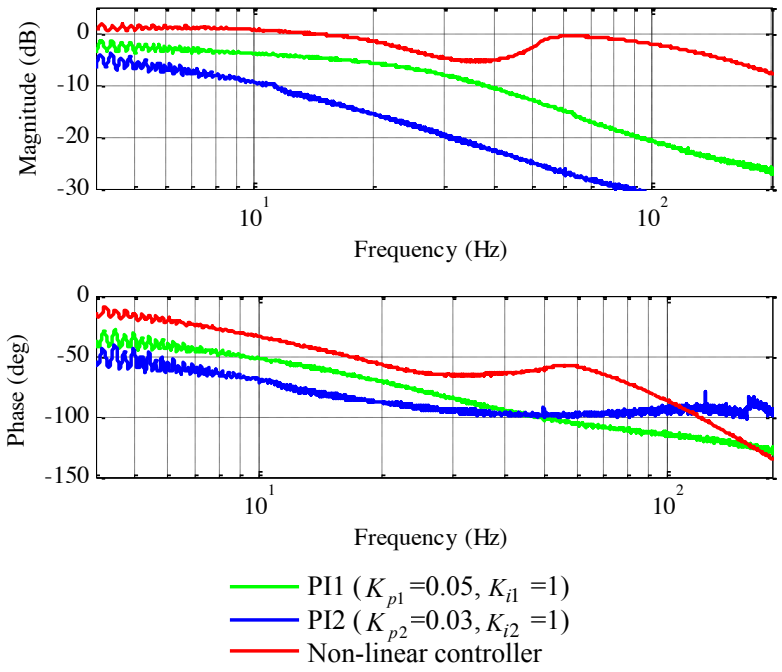

Figure 5-11. 30µm amplitude frequency response comparing the two conventional PI controller with the experimental non-linear controller.

5.9 Validation of Two Stage Valve Model

The valve dynamic experimental data was compared to the full analytical model described in Chapter 4. The second stage spool position was controlled by the complete controller described in this chapter. It is not practical to validate the full model, including second stage spool position response, before a closed loop controller is implemented. A step response with a step size of 120µm can be seen in Figure 5-12, where (a) shows positive direction and (b) negative direction. It can be observed that the analytical model correlates well with the experimental data. In the positive direction, Figure 5-12 (a), it can be seen that the analytical model predicts a small overshoot, which is likely to be due to modelling error in the first stage flow characteristics. The second stage behaviour is very sensitive the flow characteristics of the first stage spool, especially within the overlap region. Therefore, at different amplitudes the correlation will differ.

The first stage movement while controlling the second stage in a step response fashion with a step size of 120µm can be seen in Figure 5-12, (c) in positive direction and (d) in the negative direction. The analytical model matches well with the experimental data.

The amplifier behaviour for a second stage step response, as seen in Figure 5-12 (a) and (b), can be observed in Figure 5-12 (e) and (f). The analytical amplifier behaviour compares well to the

experimental data of the amplifier, it shows the same pattern, but the absolute voltage differs slightly. The difference between the analytical model and the experimental data could be due to the hysteresis of the ring bender and the starting point within the hysteresis loop.

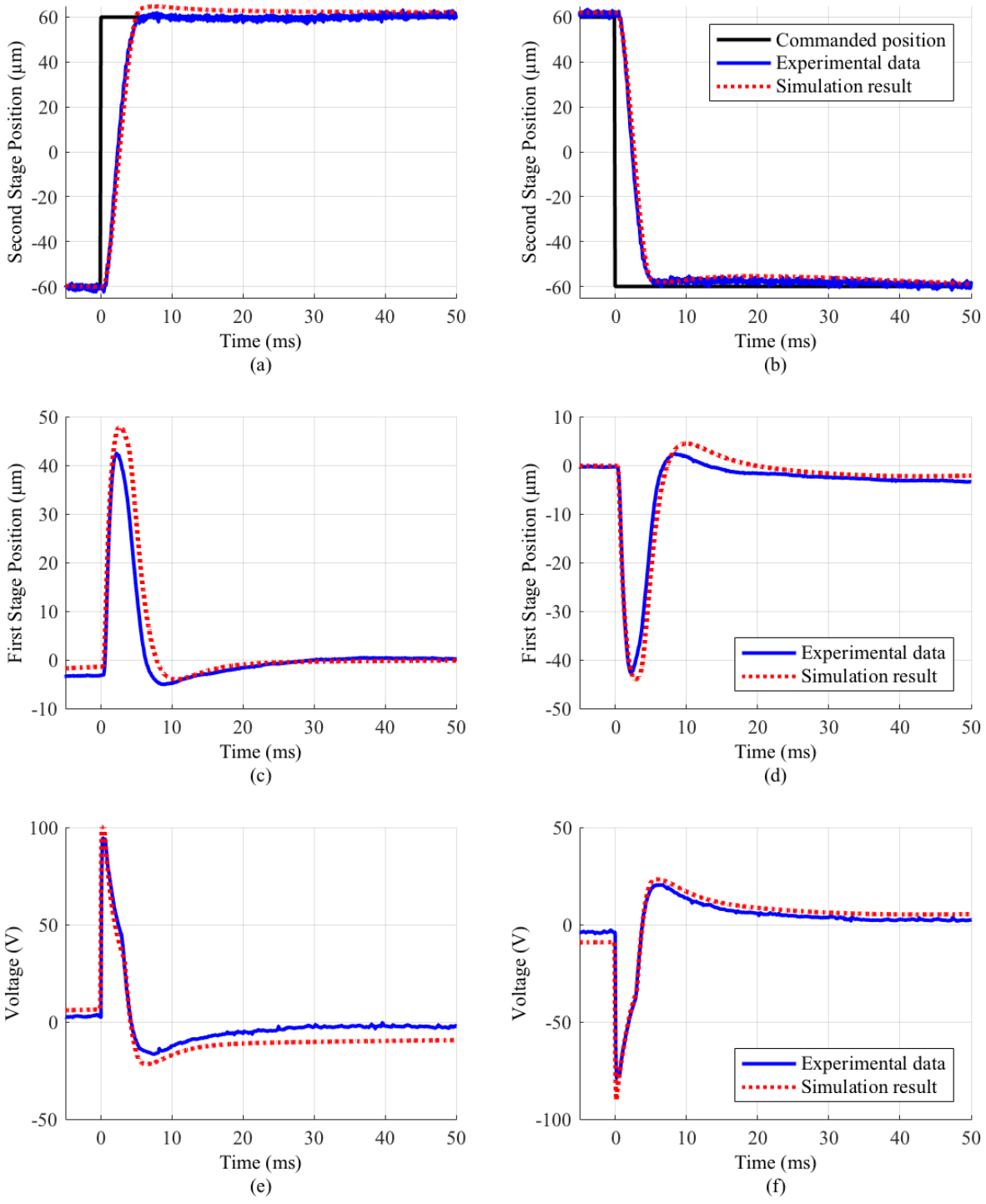

Figure 5-12. (a) Second stage step response comparison between experimental data vs analytical model with step size of 120μm positive direction (b) negative direction. (c) First stage movement for a second stage step response of 120μm comparing the experimental data and analytical model positive direction (d) negative direction. (e) Amplifier voltage for a second stage step response of 120μm comparing the experimental data and analytical model positive direction (f) negative direction.

5.10 CONCLUSION

A control algorithm for second stage spool position control was developed and tested on the piezoelectric actuated two stage servovalve. The controller integrates hysteresis compensation, overlap compensation and command velocity feed-forward into the control loop. The experimental controller was compared to a conventional PI controller with second stage position feedback.

A conventional PI controller is sensitive to amplitude changes, and therefore the performance of the controller will vary depending on the amplitude. This is due to the lack of compensation for the first stage overlap.

A higher gain in the first stage spool overlap region is essential to increase performance and be less sensitive to amplitude changes. First stage hysteresis compensation improved the response of the second stage. It allows the overlap compensation to be much more effective, due to the linearization of the piezoelectric actuator. The feed forward control has a small benefit, but does provide an improvement in the tracking response. The complete proposed control algorithm provides the fastest response. It is shown that the non-linear controller significantly outperforms two PI controllers, which span the range of plausible proportional gain values.

The simulation of a second stage step response correlates well with the experimental data. The first stage movement and the amplifier voltage also correlate well with the model while the second stage is moved in a step response fashion. However, as the second stage behaviour is sensitive to the first stage flow model, especially within the overlap region, the model fit is sensitive to amplitude changes.

Variation in the result has sometimes been observed, which is believed to be due to temperature change. The change in stiffness of the mounting with temperature may be the cause. This is not shown in the results, as only results obtained once the hydraulic system reaches a steady state temperature are present. This could be compensated for if temperature sensors are incorporated into the system.

The novel aspect is that a control algorithm has been developed that incorporates a relatively simple hysteresis compensation loop which is coupled with overlap compensation together with feed forward to increase the bandwidth. The need for effective piezoelectric hysteresis compensation before overlap compensation because viable is an important realisation. A patent has been applied for together with Moog Controls in Tewkesbury to use this control, both in a two-stage device as well as for a first stage on its own to work in open loop.

The following chapter will describe an analytical investigation of ring bender mounting optimization.

6 PIEZOELECTRIC RING BENDER MOUNTING OPTIMISATION

This chapter describes a method to find the optimized mounting arrangement for the ring bender, to obtain maximum effective work output. There are circumstances where the optimized mounting arrangement is not practically feasible, due to the small mounting overlap and thickness, but the method still provides a design guideline for the mount.

6.1 INTRODUCTION

For piezoelectric ring benders, the design of the mounting is essential to obtain as high a displacement and force as possible. The mounting can reduce displacement and force of the piezoelectric ring bender significantly if its stiffness characteristics are inappropriate.

In this investigation, different overlap, thickness and Young's modulus values for the and how these affected the maximum work output of the ring bender mounting were studied. The overlap is the length of the mount that overlaps the ring bender and the thickness is the thickness of the mount either side of the ring bender, as illustrated in Figure 6-1.

The depth behind the ring bender is not included in this investigation, and the focus is mostly on the outer edge. This is to reduce complexity of the investigation, to reduce the number of simulation runs required, and it is also believed that it does not have a major impact on the results.

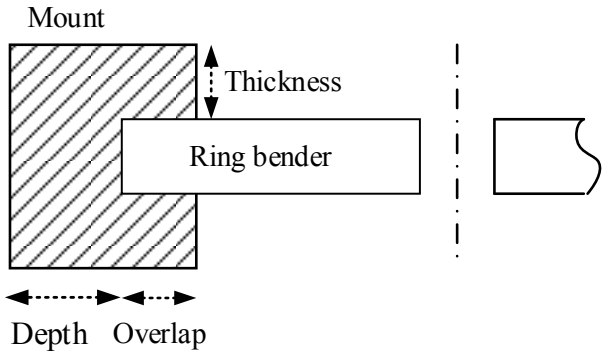

Figure 6-1. Cross section illustration of half of the ring bender and mount.

The axial stiffness and the torsional stiffness of the ring bender mount are as illustrated in Figure 6-2. The mount needs to be stiff enough to support the ring bender to provide a high axial force. If the mount is not stiff enough the mount will compress when a force is applied on the ring bender, hence less effective force output can be provided by the ring bender. At the same time the mount needs to be flexible enough to allow the outer edge of the ring bender to rotate. If the mount is not flexible enough it will limit the effective output displacement. By comparing the maximum work output of the ring

bender for different mounting arrangements an optimum trade-off between overlap and thickness is found.

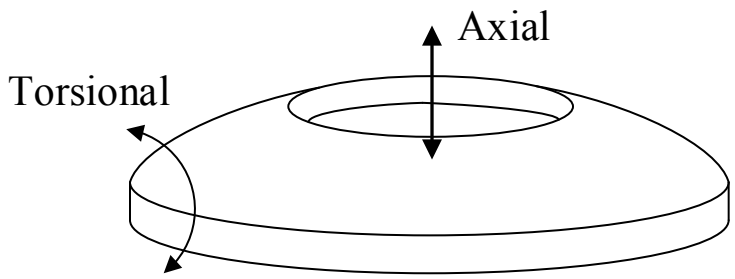

Figure 6-2. Axial and torsional stiffness acting on the mount.

6.2 METHOD OF ANALYSIS

This section describes the analysis procedure, material property assumptions, the finite element techniques used and analytical modelling. Finite Element Analysis (FEA) provides an average compression of the mount, due to applied force, in order to determine the axial stiffness. The FEA also provides an angle of rotation of the ring bender outer edge, due to an applied moment, to be able to obtain the torsional stiffness of the mount.

An analytical model of a ring bender was created based on Timoshenko plate bending equations and combined with the FEA mount axial and torsional stiffness results. From the analytical model and the FEA, the maximum work output for different mounting arrangements was calculated. The analytical model will be explained in section 6.4.

A polynomial fit to the FEA stiffness results was also used to provide a more precise optimum overlap-thickness ratio due to smaller step sizes achievable.

The approach was also used to investigate different size piezoelectric ring benders and Young's modulus of the mount.

The programs used were ANSYS 15.0 and Matlab 2012b.

6.2.1 General Analysis Procedure

For the FEA simulations a 2D axisymmetric model was created to obtain the axial stiffness and a 3D model was used for the torsional stiffness. A substitute for the piezoelectric ring bender is used in the FEA simulations which is a significantly stiffer than the mounting. Only the outer part of the piezoelectric ring bender, which is embedded in the mounting is simulated, as only the mounting behaviour is of interest. A 2D model is used for the axial stiffness to reduce simulation time and a 3D model was used for the torsional stiffness to be able to eliminate the torsional stiffness of the substitute ring bender due to is annular shape.

Multiple FEA simulations were completed, for different overlap and thickness combinations and Young's moduli, to obtain the displacement and rotation of the ring bender substitute under certain circumstances.

The procedure for the investigation is as follows:

1. Create a 2D and 3D FEA model in ANSYS workbench.
2. Create mesh.
3. Introduce constraints and loads.
4. Run FEA simulations.
5. Analyse the axial displacement or angle of the mount due to applied force or moment for multiple overlap-thickness ratios as well as different Young's moduli.
6. Fit a polynomial model to the FEA results (torsional stiffness, axial stiffness and Young's modulus) by using the least squares fit approach.
7. Create analytical ring bender model based on Timoshenko plate equations. Incorporate the torsional stiffness of the outer edge of the actuator as a boundary condition for the analytical model.
8. Combine the axial stiffness of the mount with the force output of the ring bender to obtain the effective blocking force.
9. Plot effective work output for both FEA results directly and polynomial fit from where the optimum overlap-thickness ratio can be obtained.
10. Investigate different piezoelectric ring bender sizes and different Young's moduli of the mount.

6.2.2 Material Properties

The mounting material is based on EPDM 90 (Ethylene Propylene Diene Monomer) polymer, as that material was used for the piezoelectric ring bender mount in the experimental valve. The material properties for the EPDM 90 HR can be seen in Table 6-1. These values were used for the mount in the FEA simulations.

To investigate the effect of the Young's modulus value, the Young's modulus is varied, however the Poisson's ratio remains the same. This was to investigate how the material stiffness affects the axial and torsional stiffness of the mounting.

The material for the piezoelectric ring bender substitute is structural steel. Structural steel as compared to EPDM is effectively rigid. The material of the piezoelectric ring bender substitute is not of interest in this investigation, just the stiffness of the mount itself.

Table 6-1. Material properties EPDM 90 HR.

Material Property	Value
Poisson's Ratio	0.49
Young's Modulus	10 MPa

6.3 FEA SETUP

This section will describe the FEA model, the mesh, the constraints and loads on the mount in the FEA investigation.

6.3.1 FEA Model

The model for the axial stiffness is a 2D axisymmetric surface based on the cross section of the outer edge mounting diameter for a 40mm ring bender was used, as can be seen in Figure 6-3. For the torsional stiffness, a 3D 'beam' model, with a depth (in z-direction) of 1mm was used, see Figure 6-4. A 3D beam model was used, instead of a 2D axisymmetric model, to eliminate the torsional stiffness of the ring bender itself. In both models the height of the piezoelectric ring bender substitute was 1.25mm, ther same thickness as a conventional ring bender.

The 'overlap' is the length of the mount that will overlap the piezoelectric ring bender substitute, see Figure 6-3. The 'thickness' is the amount of material above and the below the ring bender substitute, see Figure 6-3. These are the only dimensions that will be changed and investigated.

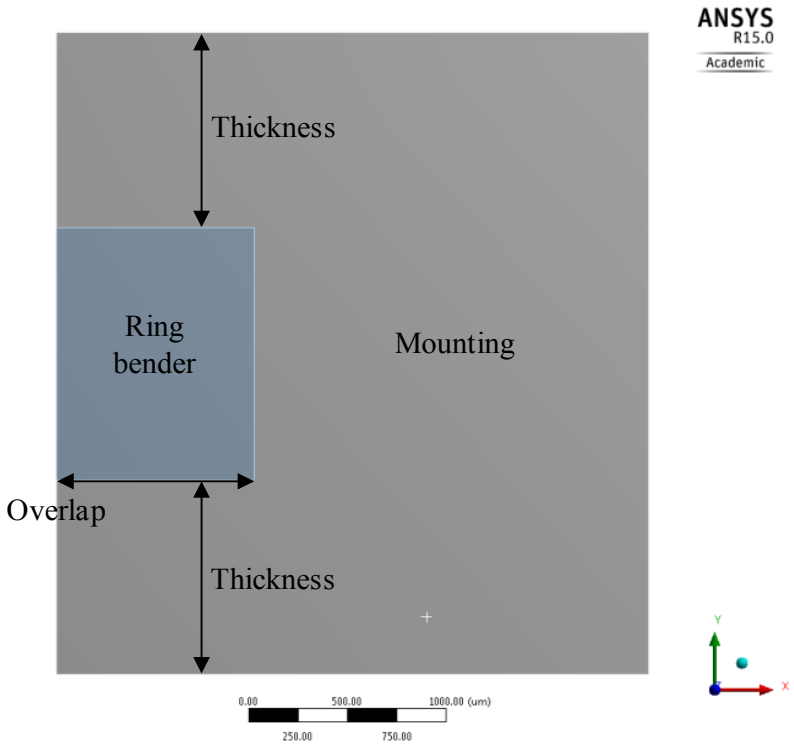

Figure 6-3. 2D axisymmetric FEA model showing the mount and the ring bender substitute and illustrating the overlap and thickness.

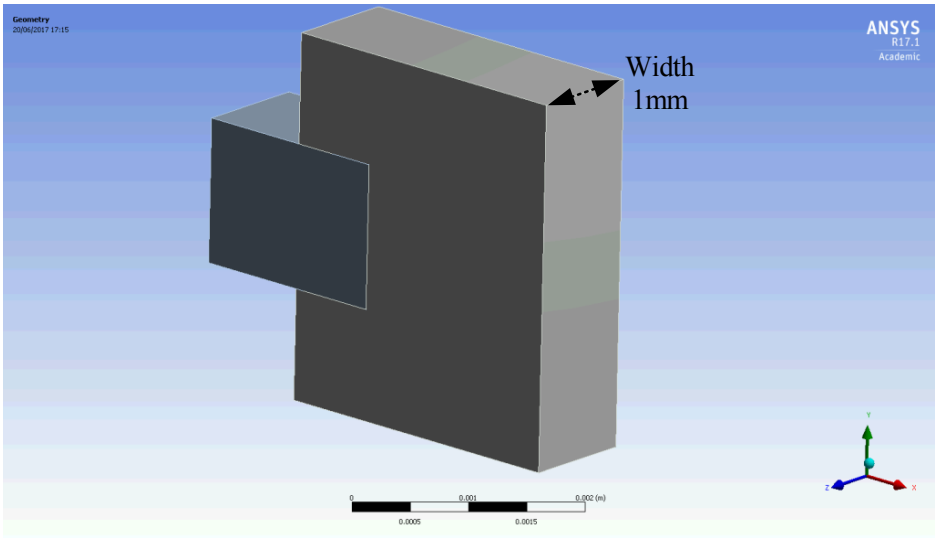

Figure 6-4. Torsional stiffness 3D model for the FEA simulations.

6.3.2 Constraints

Selected constraints and loads were implemented in the model is to attempt simulate the conditions and loads experienced on the mounting when introduced into a servovalve body.

For both the 2D and 3D simulations the three outer edges were fixed for both the force and moment simulations. To be able to investigate the axial and torsional stiffness of the mount a force and a moment were introduced. The force was applied to the upper edge of the ring bender and the moment was applied

at the inner edge of the ring bender substitute. The constraints and loads can be seen in Figure 6-5. Figure 6-5 (a) shows the load and constraints for the axial stiffness and Figure 6-5 (b) shows the load and constraints for the torsional stiffness.

The mounting and the ring bender substitute was bonded by a setting in ANSYS called “bonded”.

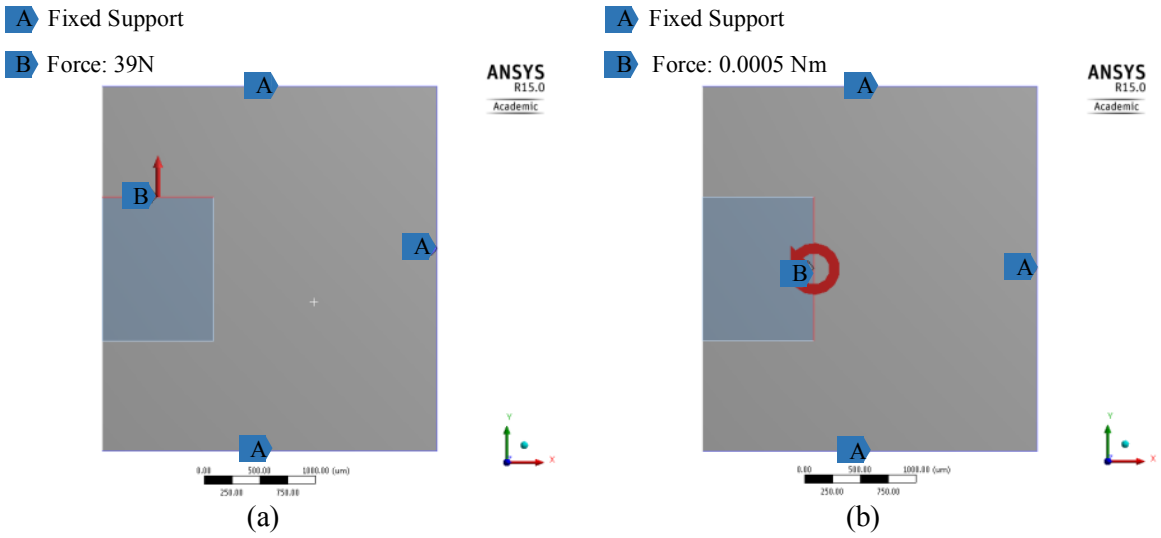

Figure 6-5. Constraints for force used to determine axial stiffness (b) Constraints for moment used to determine torsional stiffness.

6.3.3 Mesh

A mapped mesh was used, which implies that all the elements are square-shaped. An example of the mesh can be seen in Figure 6-6. To ensure that the model provides reliable results a mesh independence test was completed. This was done by reducing the element size, increasing the number of elements, and investigating how the finer mesh affects the results. At a certain point the result will not be affected by increasing the number of elements further. The lower end of the number of elements was used to reduce simulation time. The mesh independence plot can be seen in Figure 6-7, where the black circle shows the minimum number of elements that was used. A similar size mesh was used for the 3D model.

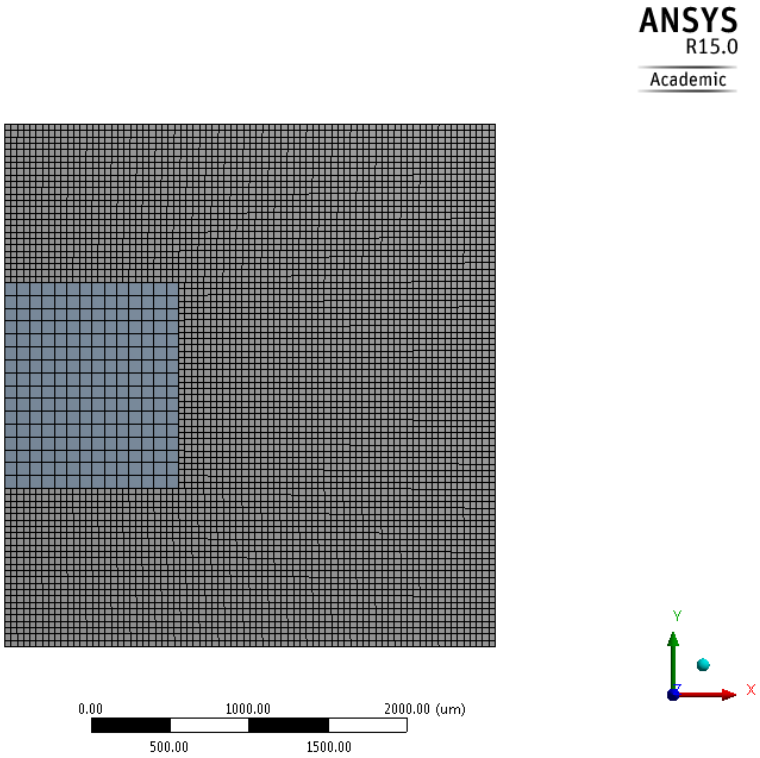

Figure 6-6. 2D mesh of the FEA model.

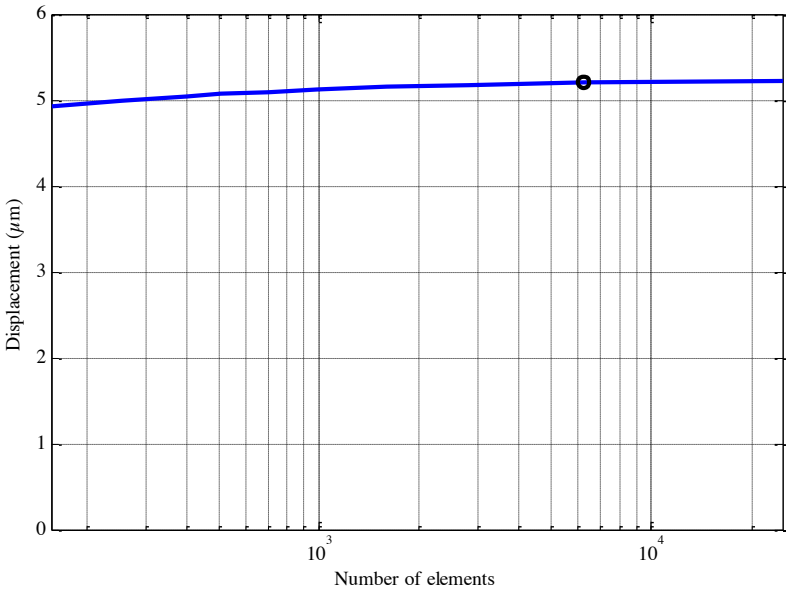

Figure 6-7. Graph showing the 2D mesh independence plot.

6.4 RING BENDER ANALYTICAL MODEL

This section presents the analytical modelling of the ring bender mounting. The analytical model was based on Timoshenko plate bending equations [61], but was rederived to introduce edge torsional

stiffness boundary conditions, and include piezoelectric deformation. From the analytical model the maximum effective ring bender force and displacement could be obtained.

For a piezoelectric bimorph bender, the external moment at any point on the curvature and the piezoelectric bending moment M_e can be related as follows [61]:

$$M_1 = D\left(\frac{1}{\rho_1} + \mu_{pr}\frac{1}{\rho_2}\right) - M_e \qquad (6\text{-}1)$$

M_1 is the external applied bending moment per unit length, $\frac{1}{\rho_1}$ is the curvature in the same plane, $\frac{1}{\rho_2}$ is the curvature out of plane and μ_{pr} is the Poisson's ratio of the piezoelectric ring bender.

D is the flexural rigidity of the plate and can be describe as show in Equation (6-2) [61].

$$D = \frac{Eh^2}{12\left(1 - {\mu_{pr}}^2\right)} \qquad (6\text{-}2)$$

where E is the Young's modulus of the piezoelectric ceramic and h is the thickness of the piezoelectric ring bender. This assumes pure bending.

The stress in a piezoelectric element in terms of electric field can be expressed as given by Equation (6-3), where d_{31} is the piezoelectric strain coefficient perpendicular to the poling direction, e is the applied electric field strength.

$$\sigma = d_{31}eE \qquad (6\text{-}3)$$

The in-plane blocking force, F_e, per unit length for one half of the piezoelectric ring bender is given by Equation (6-4). At maximum positive voltage, only half of the active layers are creating a force, at maximum negative voltage the other half will create a force.

$$F_e = d_{31}eE\frac{h_a}{2} \qquad (6\text{-}4)$$

h_a is the thickness of the active half of the piezoelectric ring bender and F_e is the force due to the piezoelectric effect. The second half of the piezoelectric ring bender will generate an equal and opposite blocking force. The two forces will be separated by a distance $\frac{h_a}{2}$. Therefore, the moment will become $\frac{F_e h_a}{2}$.

The electric field strength (e) is calculated by:

$$e = \frac{n_l V}{h_a} \qquad (6\text{-}5)$$

where n_l is the number of active layers of the piezoelectric ring bender and V is the applied voltage.

A small element of the piezoelectric ring bender and the blocking force in one half of the layers can be seen in Figure 6-8, where equal and opposite blocking force will be created by the second half. r is the radius of the piezoelectric ring bender.

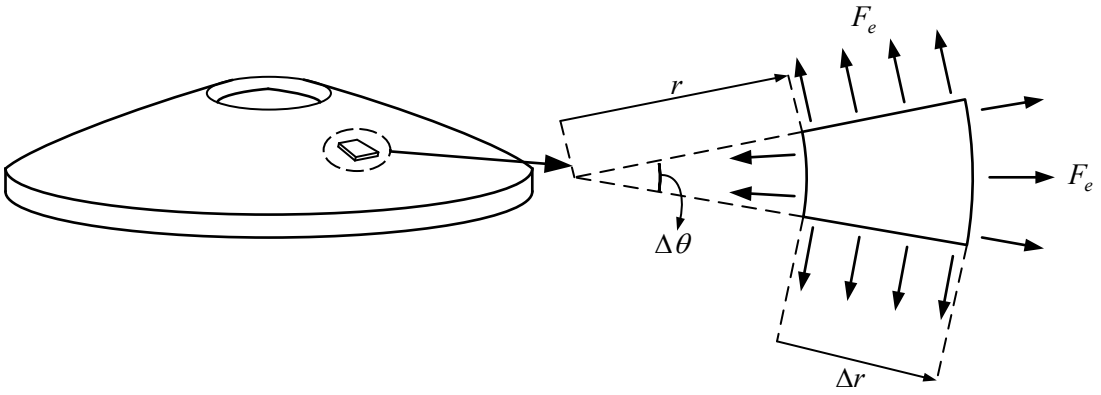

Figure 6-8. Illustration of a piezoelectric ring bender showing the effective piezoelectric forces on as small element.

By considering equal blocking moments in this two-dimensional arrangement and by taking moments in the tangential direction, the additional moment at the outer radius $(r + \Delta r)$ of the 'small element' is due to the piezoelectric force difference in the radial direction, as well as a component from the circumferential direction, which can be described as follows:

$$M_e \Delta r \Delta\theta = (F_e(r + \Delta r)\Delta\theta - F_e r \Delta\theta + F_e \Delta r \Delta\theta)\frac{h_a}{2} \tag{6-6}$$

$$M_e = \frac{F_e h_a}{2} \tag{6-7}$$

$$M_e = d_{31} e E \frac{{h_a}^2}{4} \tag{6-8}$$

For a symmetrically loaded disc the curvature of the plate or ring in the diametric section r is shown by Equation (6-9).

$$\frac{1}{\rho_1} = \frac{d\phi}{dr} \tag{6-9}$$

ϕ represents the slope (or angle) of the surface at that specific point of the section. After the deflection of the plate, the section forms a conical surface with apex A (see Figure 6-9). Then the octagonal curvature is represented by Equation (6-10).

$$\frac{1}{\rho_2} = \frac{\phi}{r} \tag{6-10}$$

Figure 6-9 shows a sectional side view of a piezoelectric ring bender and the moment and axial force per unit length that is acting on it. Figure 6-10 shows a side view of a small element, similar to the small element shown in Figure 6-8, and shows the moments and forces acting on the element.

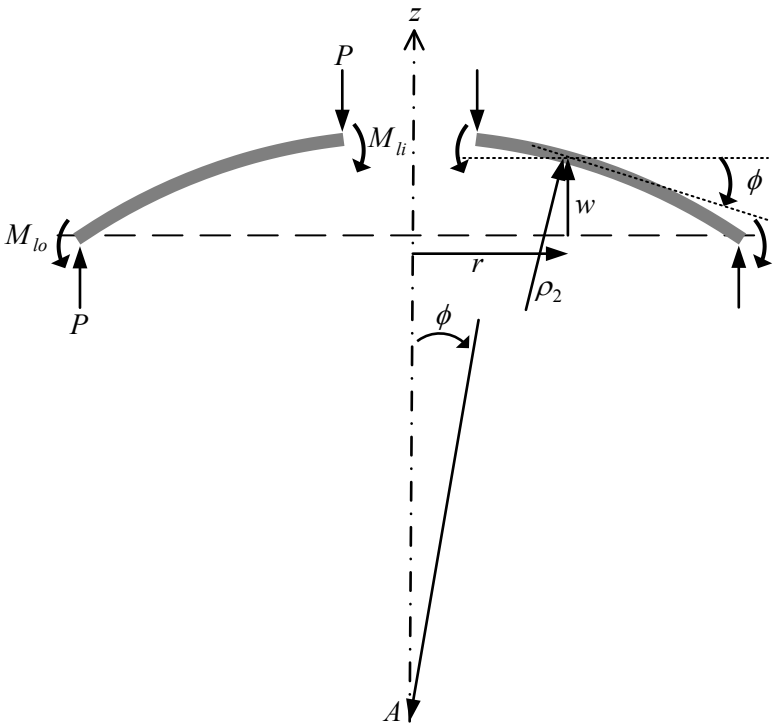

Figure 6-9. Piezoelectric ring bender cross section showing the moment and axial forces.

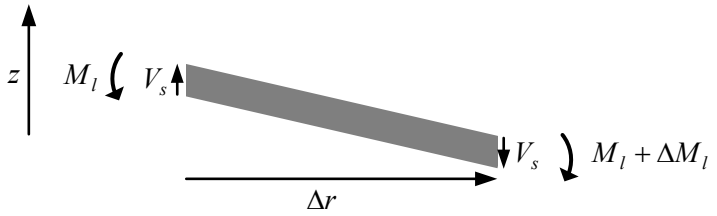

Figure 6-10. Side view of a small element within the piezoelectric ring bender.

V_s represents the shearing force per unit length acting on the sides of the small element. The effect of the shear on the bending is neglected. Thus, from Equation (6-1), Equation (6-11) and (6-12) is obtained.

In Equation (6-11) and (6-12), M_1 and M_2 represents the bending moment per unit length, where M_1 acting along the cylindrical section and M_2 is acting along the side (diametrical section) of length Δr.

$$M_1 = D\left(\frac{d\phi}{dr} + \mu_{pr}\frac{\phi}{r}\right) - M_e \qquad (6\text{-}11)$$

$$M_2 = D\left(\frac{\phi}{r} + \mu_{pr}\frac{d\phi}{dr}\right) - M_e \qquad (6\text{-}12)$$

The moment M_2 has a resultant acting in the zr plane equal to $M_2 \Delta r \Delta\theta$. By summing the moments, the equation of equilibrium gives Equation (6-13) and by neglecting smaller higher order terms Equation (6-14) is obtained.

$$(M_1 + \Delta M_1)(r + \Delta r)\Delta\theta = M_1\Delta\theta + V_s r\Delta\theta\Delta r + M_2\Delta r\Delta\theta \quad (6\text{-}13)$$

$$M_1 + \frac{dM_1}{dr}r = V_s r + M_2 \quad (6\text{-}14)$$

By substituting the values from Equations (6-11) and (6-12), Equation (6-14) becomes Equation (6-15) or Equation (6-16).

$$\frac{d^2\phi}{dr^2} + \frac{1}{r}\frac{d\phi}{dr} - \frac{\phi}{r^2} = \frac{V_s}{D} \quad (6\text{-}15)$$

$$\frac{d}{dr}\left[\frac{1}{r}\frac{d(x\phi)}{dr}\right] = \frac{V_s}{D} \quad (6\text{-}16)$$

The piezoelectric ring bender will exert a force P in the centre as shown in Figure 6-9. This results in a shear force per unit length of:

$$V_s = \frac{P}{2\pi r} \quad (6\text{-}17)$$

By substituting Equation (6-17) into Equation (6-16), Equation (6-18) is obtained.

$$\frac{d}{dr}\left[\frac{1}{r}\frac{d(r\phi)}{dr}\right] = \frac{P}{2\pi D r} \quad (6\text{-}18)$$

By integrating Equation (6-18) twice, Equation (6-19) is obtained. Where C_1 and C_2 are constants of integration, which represents the boundary conditions (mounting conditions).

$$\phi = \frac{Pr}{8\pi D}(2\ln r - 1) + \frac{C_1 r}{2} + \frac{C_2}{r} \quad (6\text{-}19)$$

$C_1$and C_2 are redefined as shown in Equation (6-20) to simplify the next derivation.

$$\phi = -\frac{1}{8\pi D}\left[-Pr\left(1 + 2\ln\frac{r}{r_o}\right) + 2C_3 r + \frac{C_4 {r_o}^2}{r}\right] \quad (6\text{-}20)$$

where r_o is the radius of the outer edge.

The deflection of the piezoelectric ring bender, w, can be obtained by integration from Equation (6-21). This will give Equation (6-22).

$$\phi = -\frac{dw}{dr} \quad (6\text{-}21)$$

$$w = \frac{{r_o}^2}{8\pi D}\left[-P\frac{r^2}{{r_o}^2}\ln\frac{r}{r_o} + C_3\frac{r^2}{r_o} + C_4\ln r\right] + C_5 \quad (6\text{-}22)$$

The inner edge displacement at a radius r_i in relation to the outer edge is given by Equation (6-23).

$$w_i = \frac{{r_o}^2}{8\pi D}\left[-P\frac{{r_i}^2}{{r_o}^2}\ln\frac{r_i}{r_o} + C_3\frac{{r_i}^2}{{r_o}^2} + C_4\ln r + P\ln 1 - C_3 - C_4\ln r_o\right] \quad (6\text{-}23)$$

By substituting the ratio of inner to outer radii by $R = \frac{r_i}{r_o}$ Equation (6-24) is obtained.

$$w_i = \frac{{r_o}^2}{8\pi D}[-PR^2 \ln R - C_3(1 - R^2) + C_4 \ln R] \tag{6-24}$$

6.5 BOUNDARY CONDITIONS

The constants from the integrations can be found from the boundary conditions.

The moment at the outer edge, M_{1o}, is given by the product of stiffness of the mounting k_o and the angle of the outer edge of the ring bender, ϕ_o.

$$M_{1o} = -k_o \phi_o \tag{6-25}$$

Substitute Equation (6-25) into Equation (6-11) and rearrange gives Equation (6-26).

$$8\pi M_e = 8\pi D \left.\frac{d\phi}{dr}\right|_o + 8\pi D \mu_o \frac{\phi_o}{r_o} \tag{6-26}$$

where:

$$\mu_o = \mu_{pr} + \frac{r_o k_o}{D} \tag{6-27}$$

Differentiating Equation (6-20) gives Equation (6-28).

$$\frac{d\phi}{dr} = -\frac{1}{8\pi D}\left[-P\left(3 + 2\ln\frac{r}{r_o}\right) + 2C_3 - \frac{C_4 {r_o}^2}{r^2}\right] \tag{6-28}$$

By substituting Equation (6-20) and (6-28) into Equation (6-26) gives Equation (6-29).

$$-8\pi M_e = (-3P + 2C_3 - C_4) + \mu_o(-P + 2C_3 + C_4) \tag{6-29}$$

Similar to the outer edge, the moment at the inner edge is given by the torsional stiffness of the mounting and the product of the angle:

$$M_{1i} = k_i \phi_i \tag{6-30}$$

where k_i is the stiffness on the inner edge.

Substitute Equation (6-30) into Equation (6-11) gives Equation (6-31).

$$8\pi M_e = 8\pi D \left.\frac{d\phi}{dr}\right|_i + 8\pi D \mu_i \frac{\phi_i}{r_i} \tag{6-31}$$

where:

$$\mu_i = \mu - \frac{r_i k_i}{D} \tag{6-32}$$

Substituting Equation (6-20) and (6-28) into Equation (6-31) gives Equation (6-33).

$$-8\pi M_e = \left[-P(3 + 2lnR) + 2C_3 - \frac{C_4}{R^2}\right] + \mu_i \left[-P(1 + 2lnR) + 2C_3 + \frac{C_4}{R^2}\right] \quad (6\text{-}33)$$

Equation (6-29) and (6-33) then be arranged to obtain the matrix shown in Equation (6-34), which can be solved for constants C_3 and C_4 for given values of M_e and P.

$$\begin{bmatrix} -8\pi M_e + P(\mu_o + 3) \\ -8\pi M_e + P\big(\mu_i + 3 + 2lnR(\mu_i + 1)\big) \end{bmatrix} = \begin{bmatrix} 2(\mu_o + 1) & (\mu_o + 1) \\ 2(\mu_i + 1) & \dfrac{1}{R^2(\mu_i - 1)} \end{bmatrix} \begin{bmatrix} C_3 \\ C_4 \end{bmatrix} \quad (6\text{-}34)$$

6.6 FREE DISPLACEMENT AND BLOCKING FORCE

The maximum displacement of a piezoelectric ring bender is achieved when the load, P, is zero. Equation (6-35) is obtained from equation (6-24) if P is zero.

$$w_{if} = \frac{{r_o}^2}{8\pi D}[-C_3(1 - R^2) + C_4 lnR] \quad (6\text{-}35)$$

Equation (6-36) is obtained from Equation (6-34), when P is zero.

$$-8\pi M_e \begin{bmatrix} 1 \\ 1 \end{bmatrix} = \begin{bmatrix} 2(\mu_o + 1) & (\mu_o - 1) \\ 2(\mu_i + 1) & \dfrac{1}{R^2}(\mu_i + 1) \end{bmatrix} \begin{bmatrix} C_3 \\ C_4 \end{bmatrix} \quad (6\text{-}36)$$

This will give the free displacement as:

$$w_{if} = \frac{M_e {r_o}^2}{D}[(1 - R^2) - \ln R] \begin{bmatrix} 2(\mu_o + 1) & (\mu_o - 1) \\ 2(\mu_i + 1) & \dfrac{1}{R^2}(\mu_i - 1) \end{bmatrix}^{-1} \begin{bmatrix} 1 \\ 1 \end{bmatrix} \quad (6\text{-}37)$$

The blocking force is the maximum force provided by the piezoelectric ring bender. The maximum force output is at maximum voltage and zero displacement, $w_{if} = 0$. From Equation (6-24), when $w_{if} = 0$, the maximum force is obtained as Equation (6-38).

$$P_b = -C_3 \frac{(1 - R^2)}{R^2 lnR} + C_4 \frac{1}{R^2} \quad (6\text{-}38)$$

By substituting P_b into Equation (6-34) Equation (6-39) is obtained.

$$-8\pi M_e\begin{bmatrix}1\\1\end{bmatrix}+\frac{1}{R^2}\begin{bmatrix}-\frac{(1-R^2)}{lnR}(\mu_o+3) & (\mu_o+3)\\ -\frac{(1-R^2)}{lnR}(\mu_i+3+2(\mu_i+1)lnR) & (\mu_i+3+2(\mu_i+1)lnR)\end{bmatrix}\begin{bmatrix}C_3\\C_4\end{bmatrix} \quad (6\text{-}39)$$
$$=\begin{bmatrix}2(\mu_o+1) & (\mu_o+1)\\ 2(\mu_i+1) & \frac{1}{R^2}(\mu_o+1)\end{bmatrix}\begin{bmatrix}C_3\\C_4\end{bmatrix}$$

Equation (6-39) can also be written as shown in Equation (6-40), from where C_3, C_4 can be obtained. P_b can then be found from Equation (6-38).

$$-8\pi R^2 M_e\begin{bmatrix}1\\1\end{bmatrix}$$
$$=\begin{bmatrix}2R^2(\mu_o+1)+\frac{(1-R^2)}{lnR}(\mu_o+3) & R^2(\mu_o-1)-(\mu_o+3)\\ 2R^2(\mu_i+1)+\frac{(1-R^2)}{lnR}(\mu_i+3+2(\mu_i+1)lnR) & -2(2+(\mu_i+1)lnR)\end{bmatrix}\begin{bmatrix}C_3\\C_4\end{bmatrix} \quad (6\text{-}40)$$

6.7 Effective Blocking Force and Free Displacement with Compliant Mounting

To obtain the effective force, P_{ef}, provided by the ring bender due to the axial stiffness of the outer edge mounting, it is modelled as two springs in series, one is the stiffness of the ring bender and the second is the mounting, from where Equation (6-41) is obtained.

$$\frac{P_{ef}}{w_{if}}=\frac{k_{rb}k_a}{k_{rb}+k_a} \quad (6\text{-}41)$$

where k_a is the mounting stiffness in the axial direction and the stiffness of the ring bender k_{rb}

The stiffness of the ring bender is $k_{rb}={}^{P_b}/_{w_{if}}$.

From Equation (6-41), Equation (6-42) is obtained and simplified to Equation (6-43)

$$\frac{P_{ef}}{w_{if}}=\frac{\frac{P_b}{w_{if}}k_a}{\frac{P_b}{w_{if}}+k_a} \quad (6\text{-}42)$$

$$P_{ef}=\frac{P_b k_a}{\frac{P_b}{w_{if}}+k_a} \quad (6\text{-}43)$$

To obtain the maximum displacement and to only investigate the effect the outer edge mounting has on the piezoelectric ring bender the inner edge stiffness k_i was set to zero and $k_o$was set to the torsional stiffness of the outer edge mounting. The $k_o$will vary and depends on the overlap and thickness, but

also the Young's modulus of the mounting. Using the results for the free displacement and blocking force in section 6.6 it can be shown that the inner edge can be high without having a negative effect on the ring bender displacement or force output.

The equations were implemented into a Matlab code to be able to calculate the maximum displacement and force output for different mounting arrangements. To be able to obtain the most efficient mounting arrangement the work output was calculated. This was done by plotting the maximum force against maximum displacement and calculating the area under the graph, as can be seen in Figure 6-11, where two example mounting arrangements can be seen. The assumed optimum mounting arrangement, overlap-thickness ratio, will be the arrangement that results in the maximum work output. The optimum arrangement will not provide the highest force or displacement possible, but it provides a good combination of force and displacement.

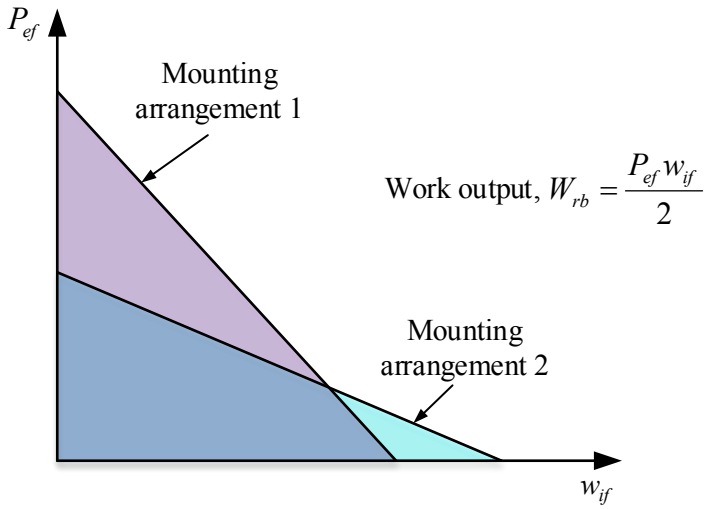

Figure 6-11. Demonstrating two different mounting arrangements and how the work output is calculated.

The parameters implemented into the analytical model for the ring bender mounting, for the 40mm ring bender, can be seen in Table 6-2.

Table 6-2. Parameters used for the mounting investigation.

Parameter	Explanation	Value CMBRO04	Value CMBR08
μ_{pr}	Poisson's ratio of the piezoelectric ring bender	0.31	0.31
d_{31}	Strain coefficient	$170 \cdot 10^{-12}$ m/V	$170 \cdot 10^{-12}$ m/V
E	Young's Modulus of the piezoelectric ring bender	$1/(17 \cdot 10^{-12})$ N/m^2	$1/(17 \cdot 10^{-12})$ N/m^2
h_a	Thickness of the piezoelectric ring bender	0.7 mm	1.25 mm
h_t	Thickness of one active ceramic layer	69.375 µm	69.375 µm
h_a	Active thickness	0.561 mm	1.11 mm
k_i	Stiffness of the mounting on the inner edge	0	0
n	Number of active layers	10	16
P	Blocking force of the piezoelectric ring bender	11 N	39 N
r_i	Inner radius of the piezoelectric ring bender	3 mm	4 mm
r_o	Outer radius of the piezoelectric ring bender	15 mm	20 mm
V	Applied voltage	100 V	100 V

6.8 FEA MOUNTING STIFFNESS RESULTS

From the FEA simulations, axial and torsional stiffnesses for a range of overlap and thicknesses were obtained. These stiffness values from the FEA simulations can be seen in the matrices in Appendix A.1. For every stiffness valve, a new FEA simulation needed to be completed, which is time consuming. Therefore, polynomials were fitted to the FEA stiffness results, by using a least square fit approach. With this approach, the step between each stiffness value can be made smaller, and more accurate, without running further FEA simulations. The polynomial equation used for the axial stiffness can be seen in Equation (6-44) and for the torsional stiffness in Equation (6-45).

$$k_a = \sum_{io=-2}^{4} \sum_{it=-6}^{6} C_{io,it}^{a} o^{io}\, t^{it} \tag{6-44}$$

$$k_t = \sum_{io=0}^{5} \sum_{it=-4}^{1} C_{io,it}^{t} o^{io}\, t^{it} \tag{6-45}$$

Figure 6-12 the FEA results for the axial stiffness and Figure 6-13 shows the torsional stiffness. The figures show the stiffness against overlap for different thickness values. It can be seen that there is a good match between the polynomial fit and the FEA results. These results are for a Young's modulus of 10MPa.

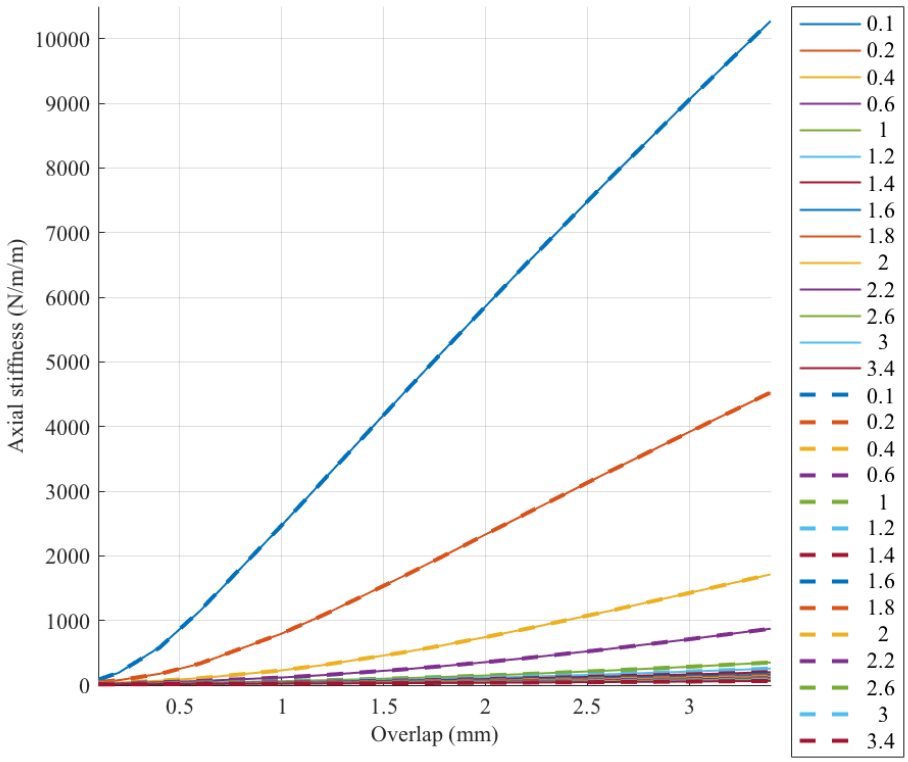

Figure 6-12. Axial stiffness mathematical model match to the FEA results. The solid lines show the original data and the dashed lines show the polynomial fit, for different thicknesses (mm).

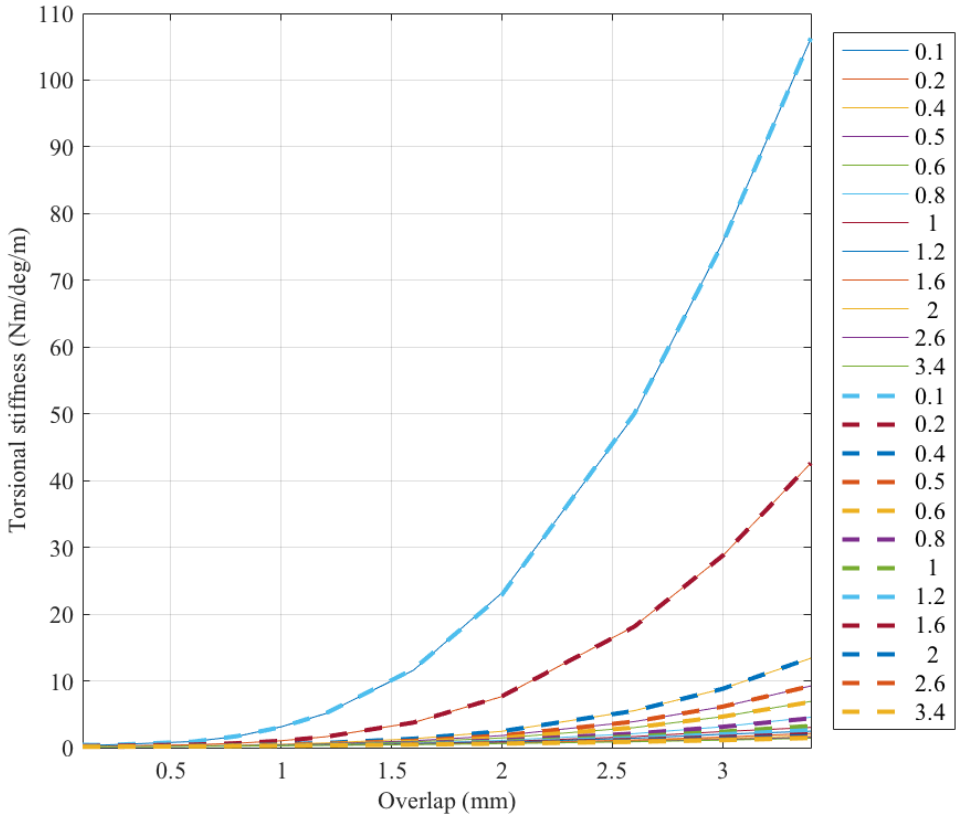

Figure 6-13. Torsional stiffness mathematical model match to the FEA results. The solid lines show the original data and the dashed lines show the polynomial fit, for different thicknesses (mm).

6.9 YOUNG'S MODULUS

The Young's modulus of the material will affect the stiffness of the mounting. FEA simulations were completed for different Young's modulus and overlap values. The thickness was set to 1mm for all Young's modulus simulations since only the effect of the Young's modulus was important.

It can be seen in both Figure 6-14 that shows the axial stiffness and Figure 6-15 that shows the torsional stiffness that the Young's modulus changes the stiffness of the mount. The Young's modulus simply acts as a scaling factor for the mounting stiffness.

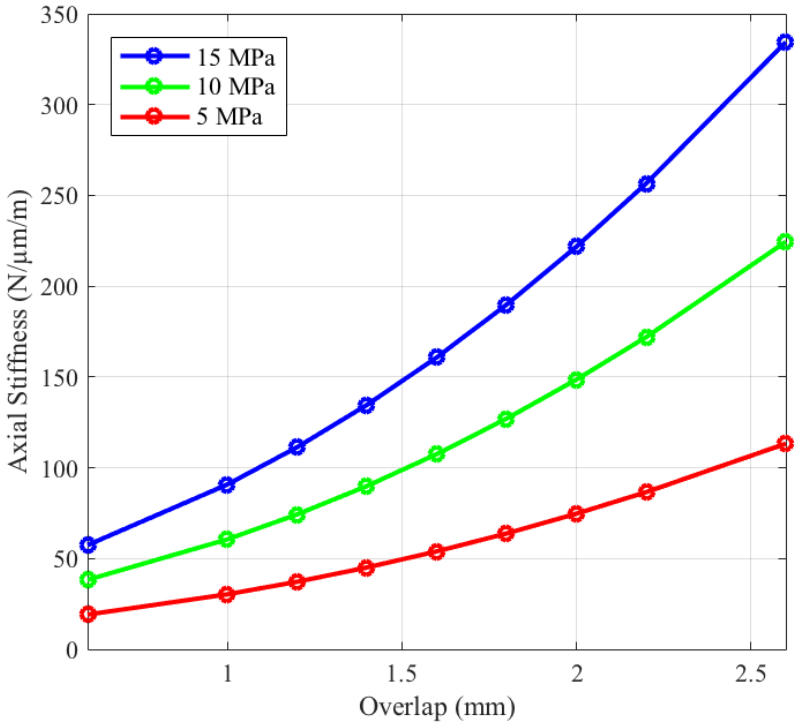

Figure 6-14. Effect of Young's moduli on axial stiffness for a 1 mm thickness.

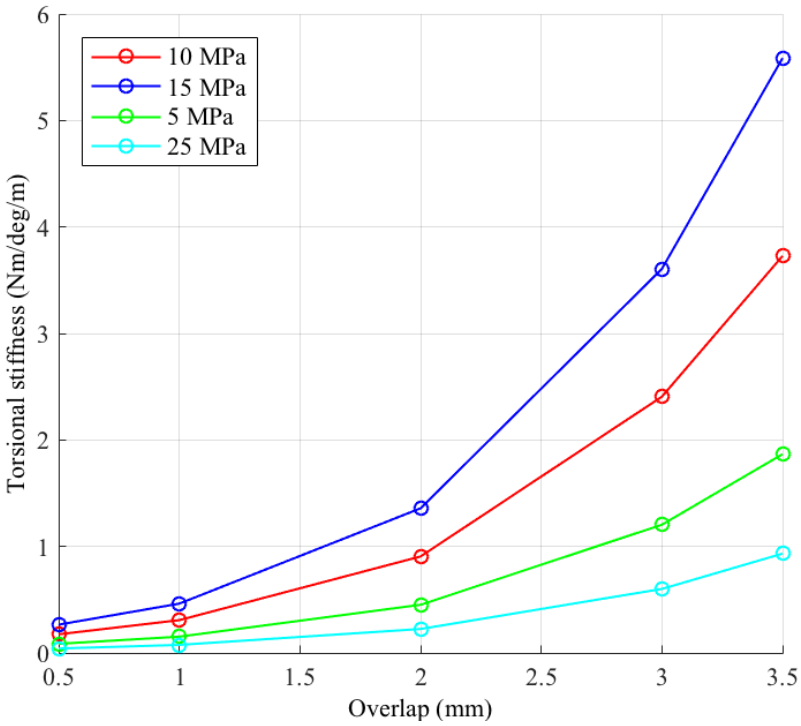

Figure 6-15. Effect of Young's moduli on torsional stiffness for a 1 mm thickness.

6.10 Results: Mounting Optimisation

The most desirable results for the axial stiffness would be as high stiffness as possible to reduce the displacement of the mount when the ring bender exerts a force. On the other hand, the torsional stiffness

needs to be as low as possible so as not to prevent the ring bender from bending, which would reduce the ring bender maximum displacement [58]. To acquire the optimal thickness and overlap, the work output was calculated, as can be seen in Figure 6-11. Examples of some of the force-displacement curves from the analytical model can be seen in Figure 6-16. The work output was calculated by calculating the area under the line that connects the maximum displacement and maximum force for each overlap-thickness combination. The 'optimum', overlap-thickness combination, gives the maximum work output. These results are obtained for the Noliac CMBR08 ring bender as used in the valve prototype. Parameter values for this ring bender are given in Table 6-2. Values for a 30mm ring bender are also shown, the results for which given in Appendix A.2.

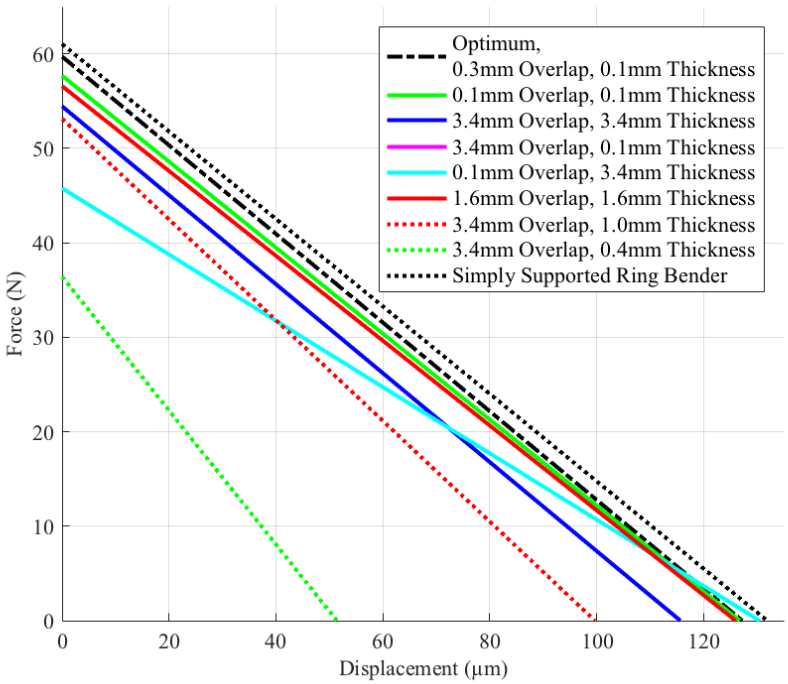

Figure 6-16. Different overlap-thickness ratio examples showing the maximum force output and maximum displacement for a mount with a Young's modulus 10MPa.

A contour plot of the work output (mJ) using the raw FEA results, can be seen in Figure 6-17 (a). Figure 6-17 (b) shows a contour plot of the work output using the stiffness polynomials. These results are for 10MPa Young's modulus. The point of highest work output is represented by a blue circle.

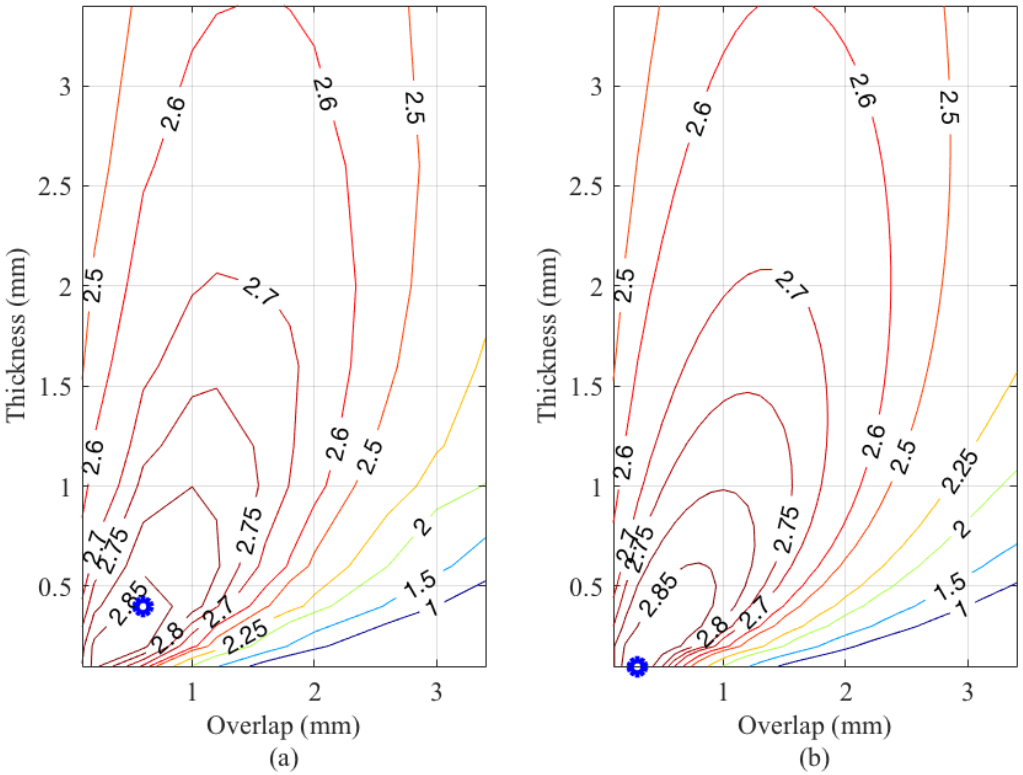

Figure 6-17. Work output for 40 mm piezoelectric ring bender in mJ (a) raw FEA results (b) polynomial fit results (10MPa Young's modulus).

From the raw FEA results it was found that the optimum overlap-thickness combination was an overlap of 0.7 mm and a thickness of 0.4 mm, see blue circle in Figure 6-17 (a). Using the fitted polynomials, it was found that the optimum overlap-thickness combination was an overlap of 0.3 mm and a thickness of 0.1 mm, see blue circle in Figure 6-17 (b). The difference is due to the smaller step size in the polynomial fit.

6.11 Optimization and Design Guide

Given that the optimum mounting might not be realistic, this section will provide guidelines of how to obtain a good sub optimal overlap-thickness combination. To obtain the maximum work output and the optimum overlap-thickness combination for a certain design, it is necessary to know the minimum overlap and/or thickness set by other design constraints.

The total work output for a 40mm ring bender and a mounting with a Young's modulus of 10MPa is plotted in Figure 6-18. It can be seen that, for a certain thickness the same amount of work output can be achieved with two different overlap values. Similarly, for one overlap the same work output can be

achieved at two different thickness values. The optimum thickness-overlap combination is marked with a blue circle, as can be seen in Figure 6-18. The further from this optimum, the lower the work output and less force and/or displacement will be obtained from the piezoelectric ring bender.

Depending on the design constraints (requirements), a certain thickness or overlap might be required. In Figure 6-18a line called 'Thickness' can be seen. This line represents the maximum output work for a specific thickness, allowing the corresponding overlap to be read off. As an example, (the dashed line in Figure 6-18), if a thickness of 1.5 mm is required this gives an overlap of about 1.2 mm to achieve the maximum work output.

Also in Figure 6-18a line called 'Overlap' can be seen. This line represents the maximum work output for a specific overlap. If a certain overlap is required, in this example 1.5 mm (see dotted line in Figure 6-18), the maximum work output for this overlap occurs at thickness of about 1.0 mm.

In Appendix A.2 the results and graphs that can be used as design guides can be found for the two sizes of piezoelectric ring benders, 40mm and 30mm as well as the results for different Young's modulus.

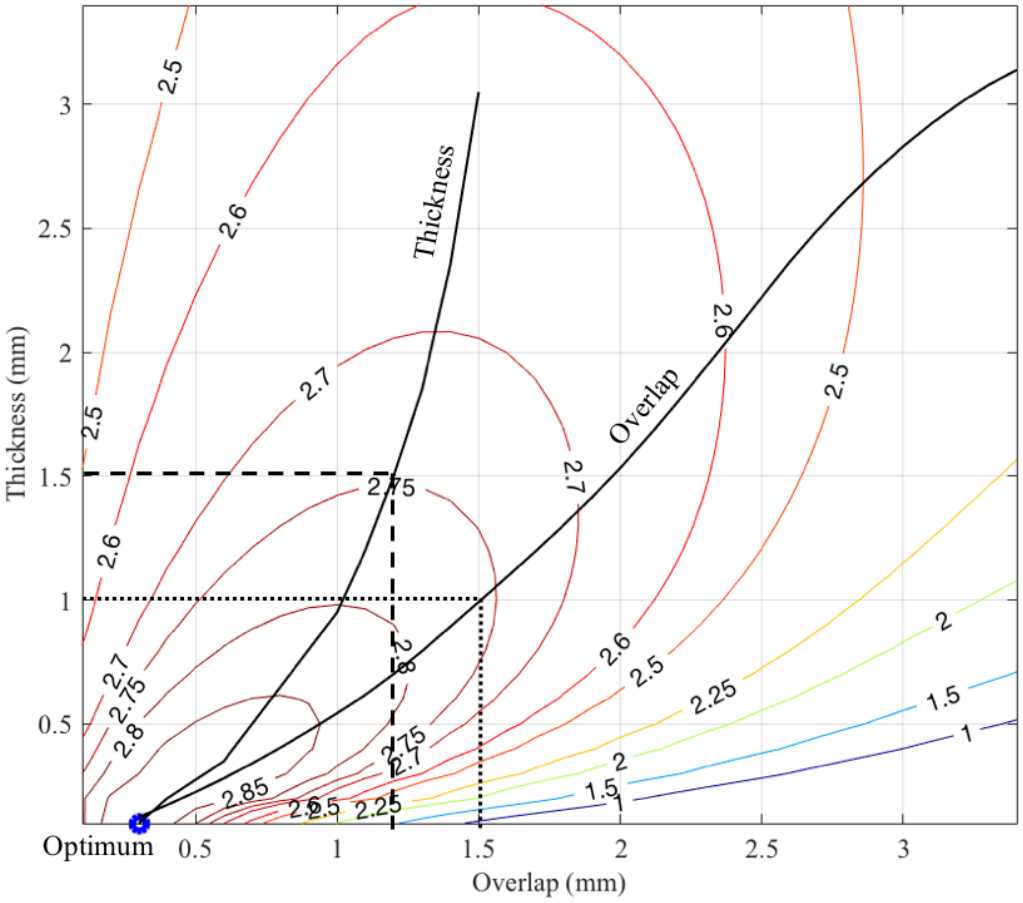

Figure 6-18. Example of a piezoelectric ring bender work output, showing the maximum work output for a certain overlap and for a certain thickness.

6.12 VALIDATION OF THE ANALYTICAL RING BENDER MOUNT MODEL

A short experimental investigation was carried out into the effect of mounting. This section provides a comparison between the analytical model of the mounted ring bender and experimental data.

6.12.1 Experimental Test Hardware

A test arrangement was designed and manufactured to test the force and displacement of the mounted ring bender. An illustration of the test arrangement can be seen in Figure 6-19 and a photograph can be seen in Figure 6-20. The mounting was made of two rectangular cross section ring seals that sandwiched the ring bender. The mount was manufactured out of EPDM90HR and the dimension specification of the mount can be seen in Table 6-3.

Table 6-3. Dimensions of the ring bender mount.

Parameter	**Value**
Outer diameter	43 mm
Inner diameter	37 mm
Thickness	2 mm

An Instron machine was used to obtain the force. To eliminate any backlash in the Instron machine or movement in the test arrangement an independent laser displacement sensor was used to measure the ring bender displacement and it was placed in a square shape metal frame. The ring bender and the mount was attached to the same frame. If there is any movement in the test arrangement this should therefore not affect the displacement measurements.

To be able to move and place the laser displacement sensor into the correct position it was held between two plastic spacers by a pair of bolts. The mounts where held in place by two plastic rings, which also have a certain thickness to control the squeeze. The plastic disc on top of the ring bender has no significant weight and is used to protect the ring bender from possible cracking or distortion due to the force applied by the measuring probe.

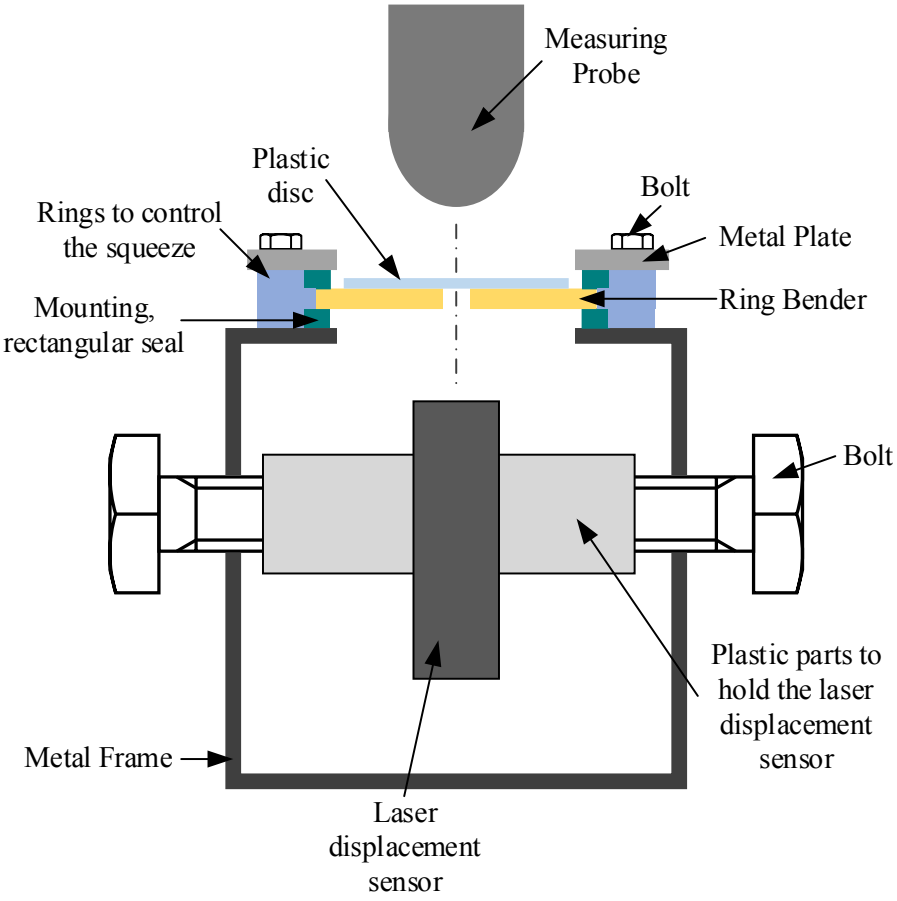

Figure 6-19. Illustration of the ring bender mounting experimental arrangement.

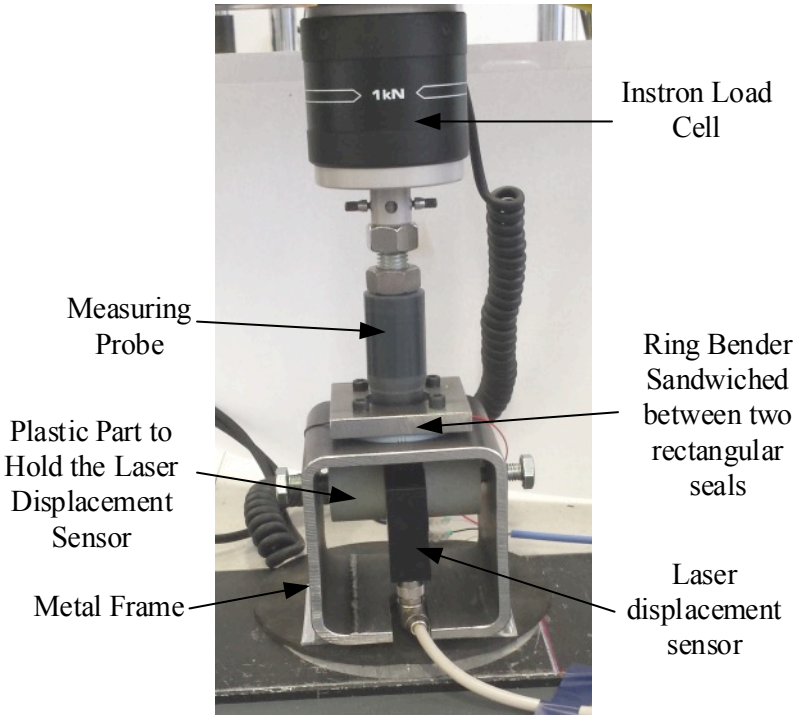

Figure 6-20. Photograph of the ring bender mounting arrangement using the Instron machine.

6.12.2 Mounting Young's Modulus Measurement

An additional test arrangement was used to estimate the Young's modulus of the mount material. This was achieved by inserting the ring seal between two flat surfaces in the Instron machine and compressing the mount while recording the amount of compression and the force applied. By obtaining the gradient of the line, see Figure 6-21, and using Equation (6-46) the Young's modulus of the mount was calculated for 10% (0.2mm compression) and 30% (0.6mm compression) squeeze level. It can be seen in Figure 6-21 that the gradient of the lines varies for different squeeze levels, hence the Young's modulus changes. The average Young's modulus for 10% squeeze can calculated as 13.7MPa and 17.5MPa for the 30% squeeze, as can be seen in Table 6-4.

$$E_m = \frac{F_m t_m}{\delta A_m} \tag{6-46}$$

where E_m is the Young's modulus of the mount, F_m is the force applied, δ is the amount of compression, t_m is the original thickness of the mount and A_m is the area of the mount.

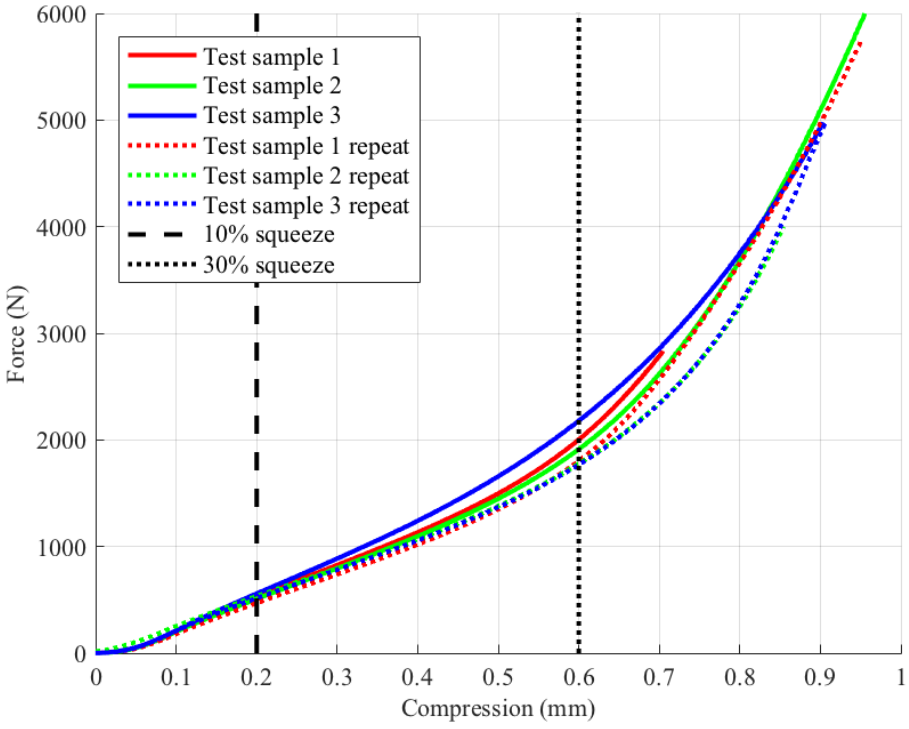

Figure 6-21. Graph for different ring seals comparing compression versus force.

Table 6-4. The squeeze levels, thickness and calculated average Young's modulus of the mounting.

Squeeze level	Compression	Final Thickness	Young's modulus
10%	0.2 mm	1.8 mm	13.7 MPa
30%	0.6 mm	1.4 mm	17.5 MPa

6.12.3 Measured Force-Displacement Characteristics for Mounted Ring Bender

The experimental maximum force-displacement curve was obtained by using the test arrangement described in section 6.12.1. Three tests were completed to obtain the force versus displacement for each of the two squeeze levels, and three separate tests were carried out for each squeeze level to obtain the maximum displacement (with zero force). Figure 6-22 shows the experimental data and a comparison with the analytical model. It can be seen that the experimental data does not show a completely linear relationship between force and displacement. This non-linear relationship has been found for other piezoelectric actuators [91]. The analytical maximum force and displacement output correlates well with the experimental data. It can be seen that both the analytical model and experimental data for the 30% squeeze (Young's modulus of 17.5MPa) shows a higher force and lower displacement than the 10% squeeze (Young' modulus of 13.7MPa).

In the Noliac data sheet provided for the ring benders the parameters have a tolerance between $\pm 15\%$ to $\pm 20\%$. Therefore, the Young's modulus and the strain coefficient of the piezoelectric ceramic (d_{31}) was adjusted from the manufacturer's data to match the experimental data, as shown in Table 6-5. By increasing the ring bender strain (d_{31}) both the force and displacement will increase, but the gradient of the line will remain the same, essentially a scaling factor. By reducing the Young's modulus of the ring bender, the force output and displacement was increased, but the force will increase more in relation to the displacement (gradient of the line will change).

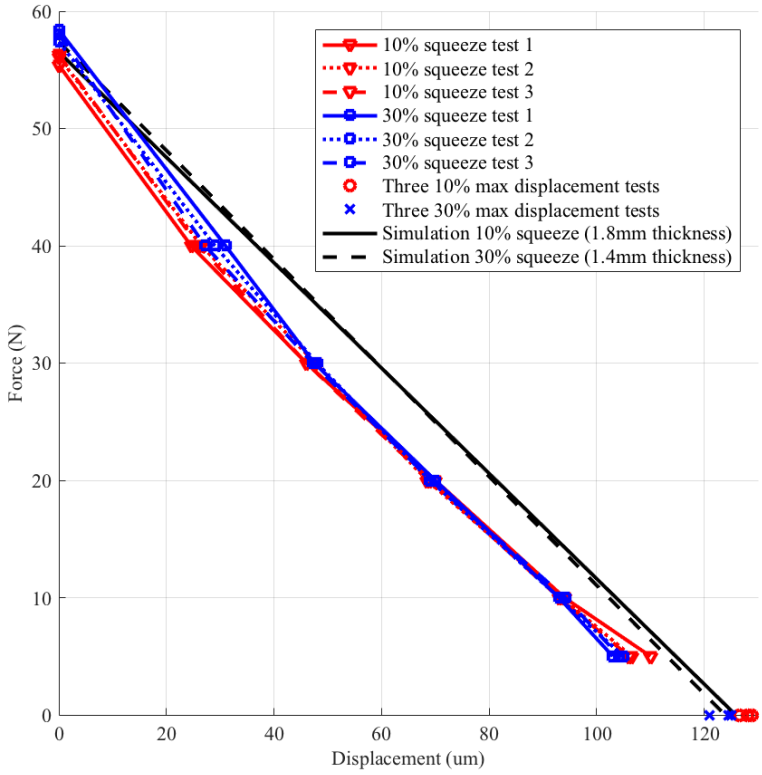

Figure 6-22. Graph comparing the analytical model to experimental data.

Table 6-5. Data sheet value and the model values for the ring bender.

Parameter	**Symbol**	**Data sheet value**	**Model value**	**Difference**
Young's modulus	E	$1/(17 \cdot 10^{-12})$ Pa	$1/(15 \cdot 10^{-12})$ Pa	-13.3%
Strain coefficient	d_{31}	$170 \cdot 10^{-12}$ m/V	$182.5 \cdot 10^{-12}$ m/V	$+7.4\%$

As shown in Figure 6-22 there is not much difference in output between the two squeeze levels and Young's moduli. This is also shown in the contour plots in Figure 6-23, (a) shows the 10% squeeze and 13.7MPa Young's modulus and (b) shows the 30% squeeze and 17.5MPa Young's modulus. The thickness and overlap in both cases is shown by a blue cross and it can be observed that both provide similar work output and are in the area where the change in either overlap or thickness does not have a significant effect on the work output.

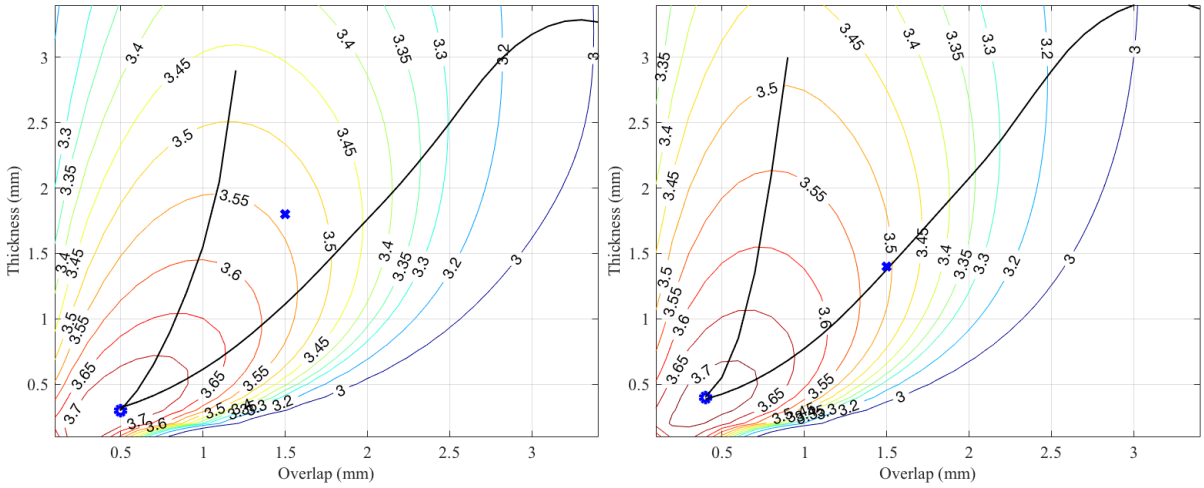

Figure 6-23. Contour plot of the work output, the blue circle shows the optimum overlap-thickness combination and the blue cross shows the overlap-thickness combination used (a) 10% squeezed, Young's modulus of 13.7MPa (b) 30% squeezed, Young's modulus of 17.5MPa.

The following section provides the optimized overlap-thickness combination for different Young's modulus values.

6.13 Optimisation: Overlap-Thickness combination

The adjusted Young's modulus and strain of the ring bender was implemented into the analytical model to obtain the optimized overlap-thickness combination of the mount. As the Young's modulus changes the optimum overlap-thickness combination changes as well. In Table 6-6 the mathematical optimum overlap and thickness for different Young's moduli can be seen. It can be seen that there is an increase in thickness while the Young's modulus increases. The optimum overlap seems to vary between 0.3 to 0.5 mm without a clear relationship, which is probably due to the maximum work being fairly insensitive to the overlap within this range.

Table 6-6. Mathematical optimum overlap and thickness for a 40mm piezoelectric ring bender for different Young's modulus (polynomial fit).

Young's modulus (MPa)	Optimum overlap (mm)	Optimum thickness (mm)
5	0.4	0.1
10	0.3	0.1
13.7	0.5	0.3
15	0.5	0.4
17.5	0.4	0.4
20	0.4	0.4

The optimum overlap-thickness combination seems to tend to very small values for each, which is a 'knife edge' with a very small thickness. As the stiffness and Young's modulus increases the thickness of the knife edge increases.

Due to the small optimum overlap and thickness values, this is in reality, most likely not practical. However, it can depend on the design and purpose of the mounting. For this research, the mount is also used as a seal to ensure no fluid reaches the wire attachments of the piezoelectric ring bender and therefore need to have a certain overlap.

The next section provides a conclusion of the ring bender mount investigation.

6.14 CONCLUSION

From the investigation of the ring bender mounting an optimum overlap-thickness combination can be found. However, the optimum solution is dependent on the Young's modulus of the mounting. The analytical model was validated against experimental data. The optimum solution also implies that the overlap and thickness tend to zero. Small overlap and thickness will allow the ring bender edge to rotate while being axially stiff to provide maximum force. This thin, optimum, solution might not be feasible in certain applications, for example when the mount is used as a seal as in this research project. There is an area where a good overlap-thickness combination can be found for a specified overlap or thickness. The Young's modulus works as a scaling factor of the stiffness of the mount, and interacts with the ring bender in such a way as to change the optimum mount dimensions.

The following chapter describes durability and encapsulation of a ring bender submerged into a phosphate ester based aerospace hydraulic fluid.

7 FLUID COMPATIBILITY, DURABILITY AND ENCAPSULATION OF PIEZOELECTRIC RING BENDERS

7.1 INTRODUCTION

Applications where piezoelectric actuators are used in harsh conditions and in more critical components are increasing. Examples where piezoelectric actuators are present include satellites, aircraft engines, medical surgery instruments, sonar, laser systems, nano and micro positioning [29]. Therefore, the durability of the piezoelectric actuators, especially in harsh environments, needs to be ensured. To ensure that piezoelectric actuators are durable and will not fail or degrade during operation they may need to be encapsulated to protect them from a potentially harmful environment.

As described in Chapter 3, Valve Design, in this investigation a piezoelectric ring bender actuates a two stage servovalve that could potentially be introduced in next generation aircrafts. When the piezoelectric ring bender will be in service it will be submerged in aircraft hydraulic fluid. It is therefore essential to guarantee that the piezoelectric ring bender will not degrade when submerged in the hydraulic fluid. Hyjet is the fluid to be used in this study which is a tradename for the phosphate-ester fluid used in civil aerospace.

The aim of this chapter is to determine if and why piezoelectric ring benders degrade or fail when in contact with Hyjet while in operation, and if encapsulation methods are needed. In addition, possible methods for encapsulation have been tested and evaluated.

Due to the limited amount of published work on durability and reliability of piezoelectric actuators in phosphate ester based fluid, the testing in this thesis is of an ad-hoc fashion. However, the results provide a future researcher the possibility to design a more rigorous testing program. It provides an understanding of the failure modes and difficulties with testing piezoelectric actuators in hydraulic fluid.

This is an extensive section presenting the results from numerous tests.

7.1.1 Fault Tree

During initial testing it was discovered that there were failures of the ring benders operating in Hyjet, and a number of possible mechanisms were identified. These possible causes are captured in a ‘fault tree’ that can be seen in Figure 7-1. The fault tree describes possible failure modes that need to be investigated. This will be discussed again later in the section 7.7.

The fault tree is divided into two paths, the first one is an electro-chemical attack (1.) and the second is mechanical fatigue (2.). Mechanical fatigue could be due to simple mechanical fatigue (2.1) when in operation (without hydraulic fluid present), essentially the ring bender (piezoelectric material, solder

material or electrode material) breaking down due to fatigue. It could also be that the piezoelectric ceramic, the solder or the electrodes are weakened by the hydraulic fluid (without electric field applied, 2.2).

The electro-chemical failure (1.) is a failure that involves the hydraulic fluid and an applied electric field. This is split up into two paths. One is a migration of metal ions from the external electrical connections into the hydraulic fluid (1.1). This could be done by fluid reaching the electrical connections. The second (1.2) is that the fluid penetrates the ring bender ceramic and reaches the internal connections. Or, there could be a combination of these (1.3), that the fluid needs to reach the electrical connections and at the same time penetrate the ceramic and create an electrical circuit with the internal electrodes. The Hyjet forms an electro-chemical cell between the external electrical connections and the internal electrodes, where metal is removed from the solder and potassium is applied to the internal electrodes. The hydraulic fluid could reach the external electrical connections by leaking past the seal (1.1.1), this could be due to poor seal squeeze, poor seal due to surface roughness or due to surface porosity or cracks. It could potentially also penetrate the edges of the ring bender (1.1.2). The Hyjet could penetrate the piezoelectric ceramic (1.2.1) through the bulk porosity or cracks.

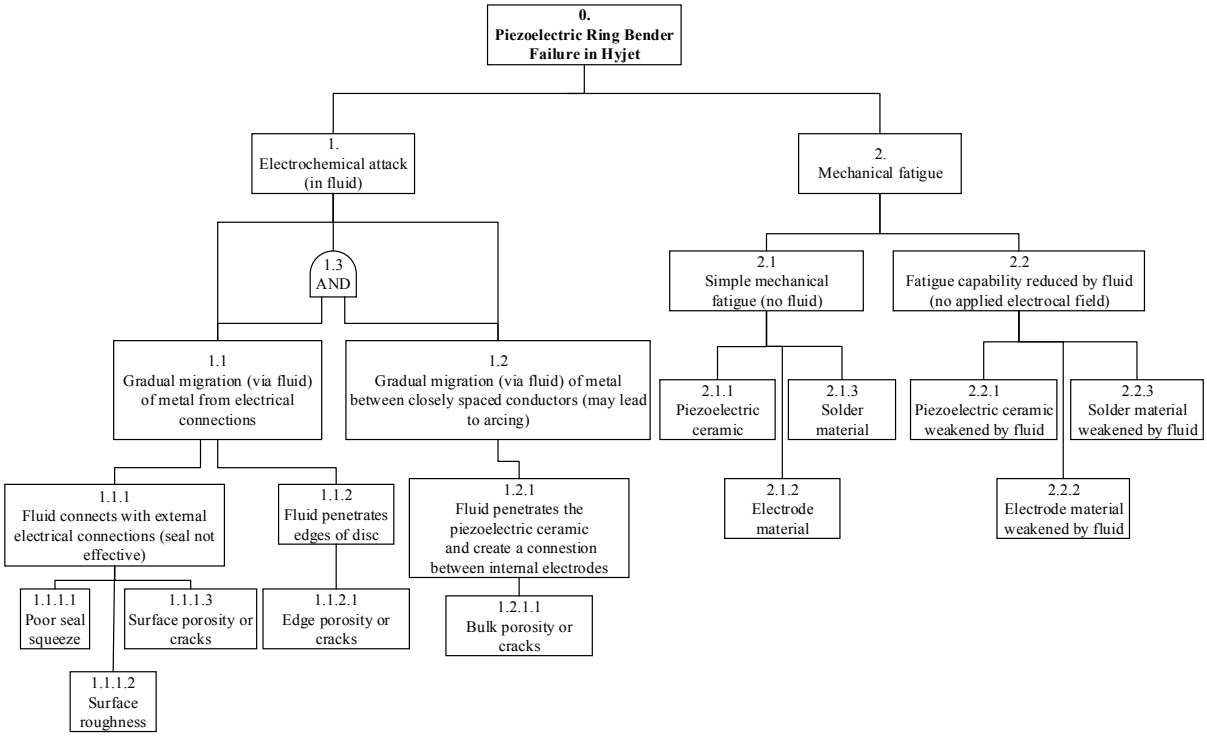

Figure 7-1. Piezoelectric ring bender in Hyjet fault tree [92].

The valve prototype was tested in mineral oil therefore no failure occurred during testing of the valve.

7.1.2 Hyjet

The hydraulic fluid that is used in this investigation is a fire-resistant phosphate ester-based aviation hydraulic fluid called Hyjet V+, which is designed for commercial aircraft hydraulics. The Hyjet

includes a potassium compound, which is present to provide protection against corrosion. The potassium picks up unwanted water molecules that are mixed in with the Hyjet and also attaches to negative charged areas for corrosion protection [93]. Hyjet is an aggressive fluid that will attack many plastic and rubber materials. Therefore, it is essential to have Hyjet resistant material when working with Hyjet.

Hyjet V+ was used for all the tests in this chapter, unless stated otherwise.

7.2 RING BENDER TESTING IN FLUID

This section describes the testing conducted to understand the durability of the piezoelectric ring bender operating in Hyjet.

7.2.1 Ring Bender in Hyjet, Initial Testing

The first tests were to investigate how the Hyjet would affect the piezoelectric ceramic, solder, electrodes and wires while no potential difference is applied to the electrode. A ring bender, with its wires attached, was submerged into the Hyjet without voltage applied, as well as different disconnected wires with their insulation. The Hyjet does not affect the piezoelectric ceramic, the solder or the electrodes, since no damage was detected. Some wire insulation did swell up, but the insulation used on the piezoelectric ring bender was not affected by the Hyjet.

Since no degradation is observed on the ring bender when no voltage is applied, tests are necessary to investigate the ring benders with applied voltage when submerged into hydraulic fluid.

The first test conducted with an electric field was undertaken by submerging a ring bender and its electrical connections, as received from the manufacturer, into the hydraulic fluid. An electric field was applied to the piezoelectric ring bender as can be seen in Figure 7-2, where the red wire was held at +200V, the blue at 0V and the black at 0V. The colours represent the colour of the wire attached to the ring bender. In this case, as shown in Figure 7-2, the top half of the ring bender exhibits an electrical field, due to the potential difference between the electrodes. This applied electric field is the maximum rated electric field (3kV/mm). The background colour is to show the electric field applied, green represents existence of an electric field and white no electric field applied. Each ceramic layer is 67μm.

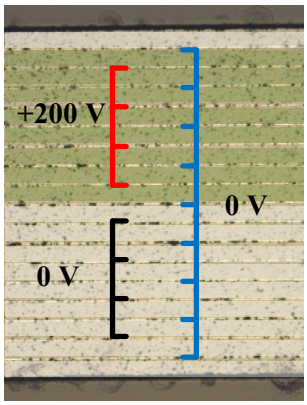

Figure 7-2. Illustration of the applied voltage for the initial tests for the ring bender test in Hyjet.

After 40 hours of being submerged in the Hyjet, as can be observed in Figure 7-3, the red wire attached to the ring bender failed. An electrochemical reaction had taken place between the ring bender and the hydraulic fluid. Around the blue wire connection, a black area can be seen, see Figure 7-3 (a). In the test, the red wire corroded to the extent that it detached from the ring bender, see Figure 7-3 (b). A cross section of the ring bender, across the black spot, reveals that several of the internal electrodes were damaged and have separated from the piezoelectric ceramic, as can be seen in Figure 7-4 (a) and (b). Three tests were conducted with similar results.

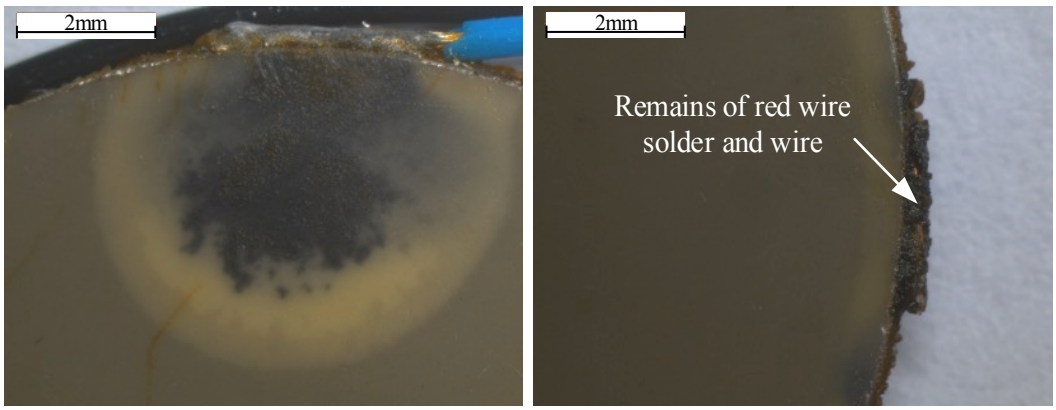

Figure 7-3. (a) Black spot around the blue wire (b) Red wire remains.

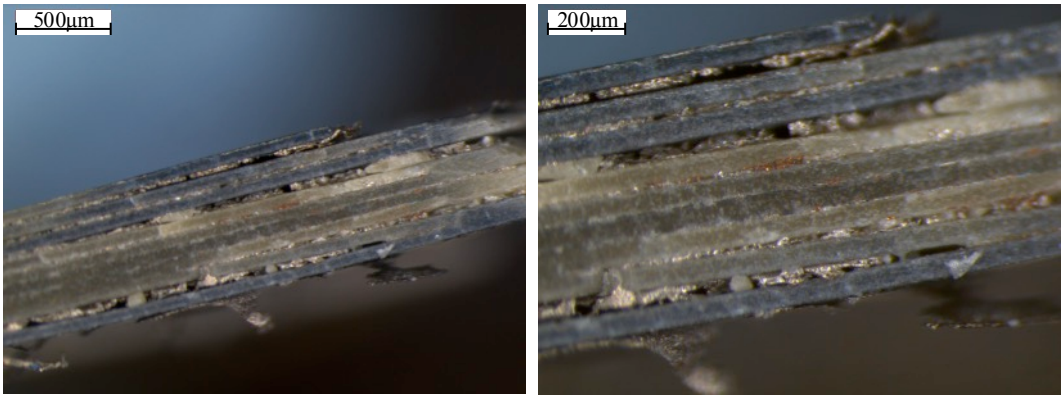

(a) (b)

Figure 7-4. (a) Cross section of the piezoelectric ring bender across the black spot (b) zoomed in on the damaged electrodes.

A Scanning Electron Microscope (SEM) investigation was conducted on the tested piezoelectric ring bender. The weight percentage of the elements present in the black spot present around the negative charge wire (blue wire, seen in Figure 7-3 (a)), can be seen in Figure 7-5. It can be seen that there is a significant amount of potassium and oxygen present, which indicate the presence of a potassium compound. This suggests that the potassium present in the Hyjet is doing what it was intended to do, attach to a negatively charged surface to prevent corrosion. The black potassium compound is only found on the negative charge side.

It is believed that the ion displacement occurs as between the positive and negative charged electrical connections, as illustrated in Figure 7-6. The positive charged silver and copper ions will enter the Hyjet and the positively charged sodium, potassium and calcium will attach to the negatively charged area (in this case the blue wire), creating an electro-chemical reaction. The electrical wires used for the ring benders are silver plated with a copper core and the solder is a silver based solder [94][33].

This is similar results to Beck et al. who found in their experiment that corrosion could be produced via an electrochemical reaction in a phosphate based hydraulic fluid. They found that a film of deposited sodium carbonate was formed at the cathode and corrosion occurred at the anode [95].

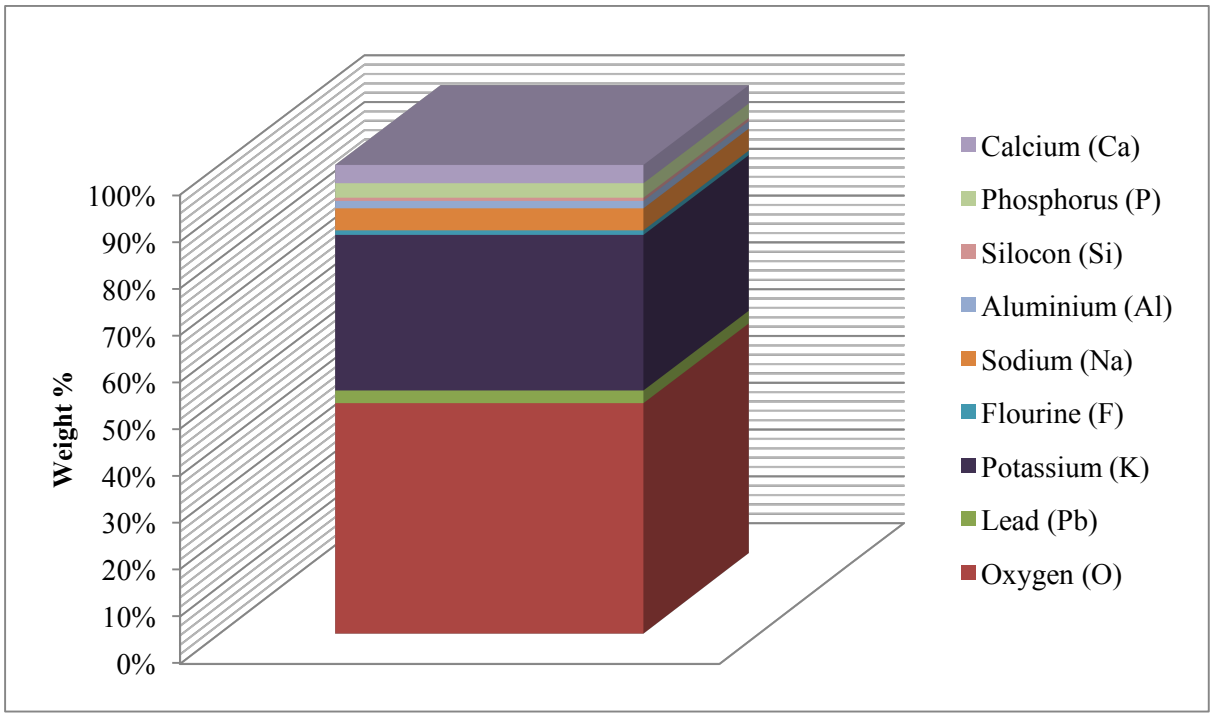

Figure 7-5. Weight percentage of the elements present at the black spot obtained by the SEM.

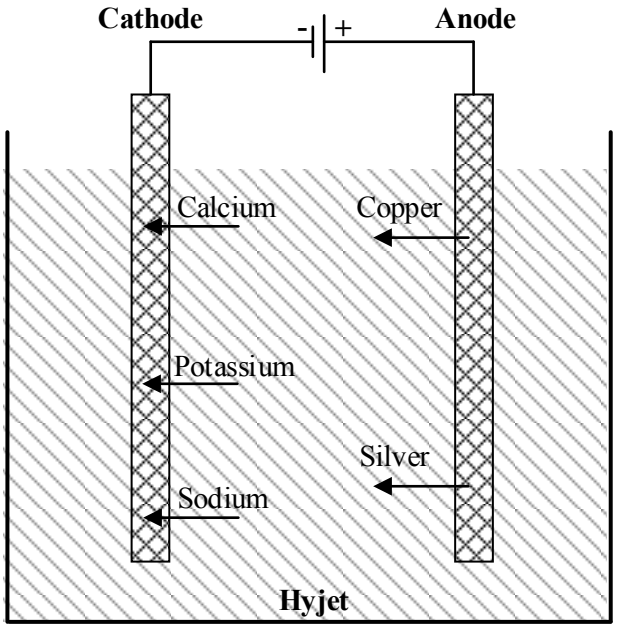

Figure 7-6. Chemical reaction between the anode and cathode submerged in Hyjet.

7.2.2 Wire Testing

A test was conducted where two wires were inserted into the hydraulic fluid to investigate the electrochemical reaction. The two wires acted as an anode (+200V) and cathode (0V), as can be seen in Figure 7-7 where a schematic diagram of the electrical circuit can be seen. Figure 7-8 (a) shows the positive charged wire and it can be observed that the silver coating has been stripped away and the copper core is exposed, as can be seen by the orange colour on the left half of the wire. Figure 7-8 (b)

shows the negative charged wire that is coated with a chemical component, most likely the same potassium compound seen in previous tests. This shows a similar result as hypothesised in Figure 7-6.

From these first tests, it is clear that to successfully test the piezoelectric ceramic itself under an applied electric field the wires and the electrical connections needs to be isolated away from the Hyjet.

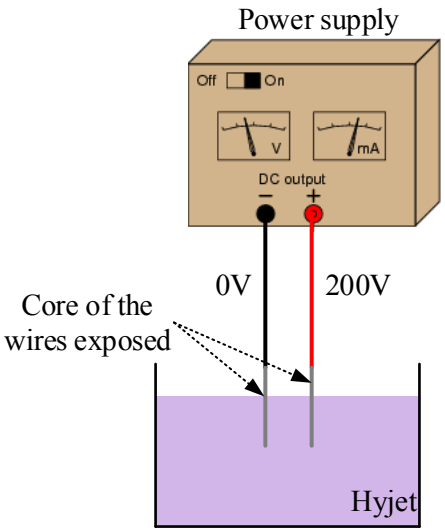

Figure 7-7. Schematic diagram of the wire test in Hyjet, where two wires are inserted into the Hyjet with a potential difference of 200V.

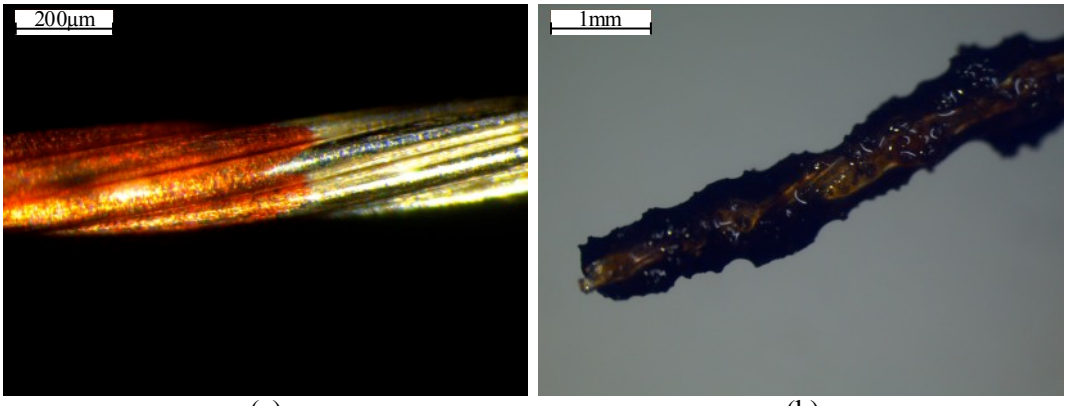

Figure 7-8. Microscopic photographs of the two wires tested in Hyjet (a) positive charged, +200V, red wire (b) grounded, 0V, blue wire.

7.2.3 Ceramic Testing

These initial tests indicated that to be able to test the piezoelectric ceramic itself and to investigate if encapsulation is needed, the electrical connections need to be isolated from the hydraulic fluid. Therefore, new test hardware was designed to achieve this. Both static and dynamic tests were completed.

7.2.3.1 Damage Rating

The piezoelectric ring benders will be rated depending on the damage from the testing, 1 is the least amount of damage and 5 is the most amount of damage, as can be seen in Figure 7-9 and as follows:

0. No damage observable.
1. No visible damage with the naked eye. Possible minor damage can be seen under a microscope.
2. Discoloration on the electrical connections.
3. Cracks visible and discoloration of the electrical connections.
4. Significant visible damage and discoloration on the electrical connections.
5. Black spots visible and damage to at least one ceramic layer.

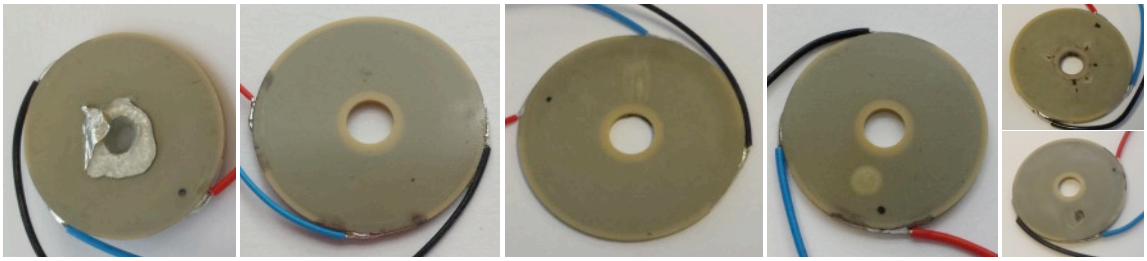

1. 2. 3. 4. 5.

Figure 7-9. Photographs of the ring benders rating the damage on the piezoelectric ring bender after testing in Hyjet.

7.2.3.2 Test Hardware

Test hardware was designed to isolate the electrical connections from the hydraulic fluid, thus the hydraulic fluid was only in contact with the piezoelectric ceramic. The parts used for the tests can be seen in Figure 7-10.

The piezoelectric ring bender was ‘sandwiched’ between two O-rings and held in place by two acrylic plates, see Figure 7-11 (a), which shows the test setup from the side and Figure 7-11 (b) from the top. The void between the two acrylic plates was filled with Hyjet, as can be seen in Figure 7-12 and Figure 7-13. This arrangement will allow the hydraulic fluid to be in contact with the piezoelectric ceramic, but not reaching the wires or electrical connections. A third acrylic plate was added to ensure no leaking can occur while handling the sample and to ‘protect’ the test sample and Hyjet from being contaminated.

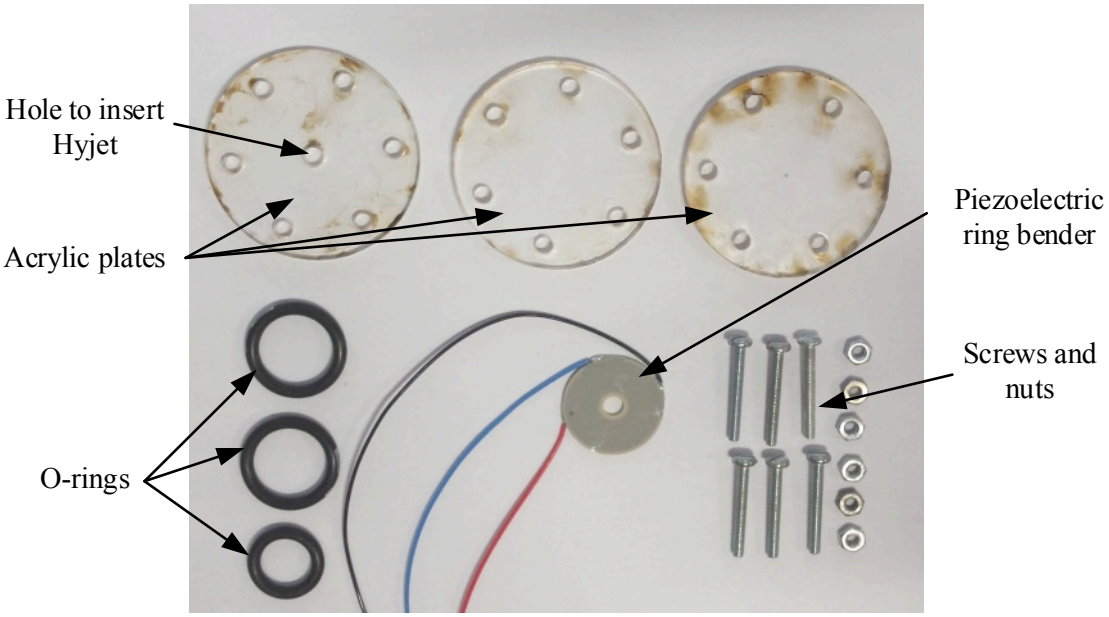

Figure 7-10. Parts used for the test harware for the ring bender in Hyjet testing.

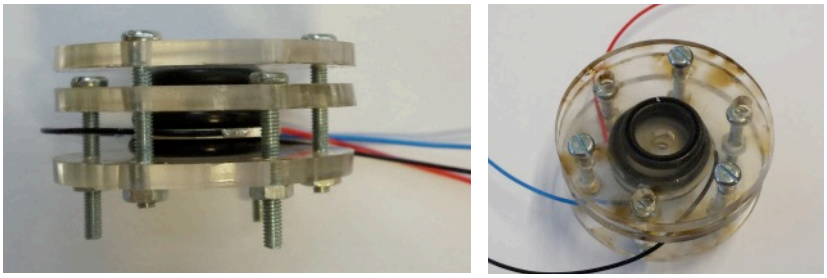

Figure 7-11. (a) Side view of the test hardware with the piezoelectric ring bender sandwiched between the seals (b) top view of the test setup.

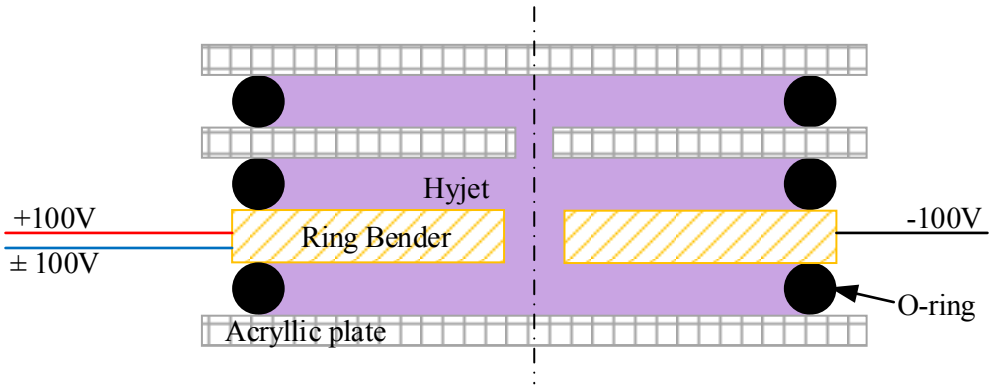

Figure 7-12. Cross section illustration of the hardware design showing the piezoelectric ring bender sandwiched between two O-rings and with the void filled with Hyjet.

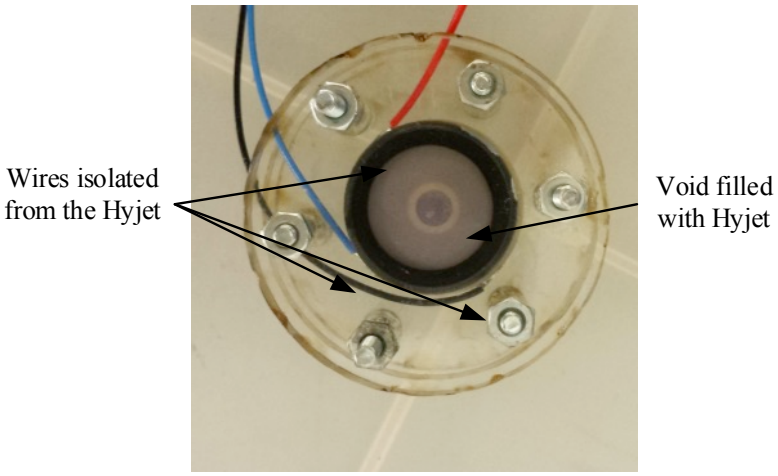

Figure 7-13. Photograph of the Hyjet test sample where the void surrounding the ring bender is filled with Hyjet.

7.2.3.3 Electric Field Test Scenarios

The test of Section 7.2.1 was a static test (denoted with an "S") where 200 volts was applied to the red wire and the blue and black wire were at zero volts as can be seen in Figure 7-14 (a), designated Test S1. Test S1 is one option to obtain the maximum rated electrical field (3kV/mm) between the electrodes in the top half of the ring bender. In addition to Test S1 three more static tests were conducted with the new test setup to replicate the range of polarities during normal operation.

Test S2, see Figure 7-14 (b), gives zero displacement of the piezoelectric ring bender due to the equal applied electric field on the two halves of the ring bender; the red wire was held at +100 V, the black wire at -100 V and the blue wire was held at 0 V. Test S3 and Test S4, Figure 7-14(c) and (d), gives the maximum positive and negative displacement of the ring bender. In Test S3 the red wire is held at + 100 V, black wire at -100 and the blue at -100 V. In Test S4 the red wire is held at +100 V, black wire at -100 and the blue at +100 V.

The background colour is to show the electric field applied: green represents an electric field in the top half, white no electric field and red electric field in the lower part.

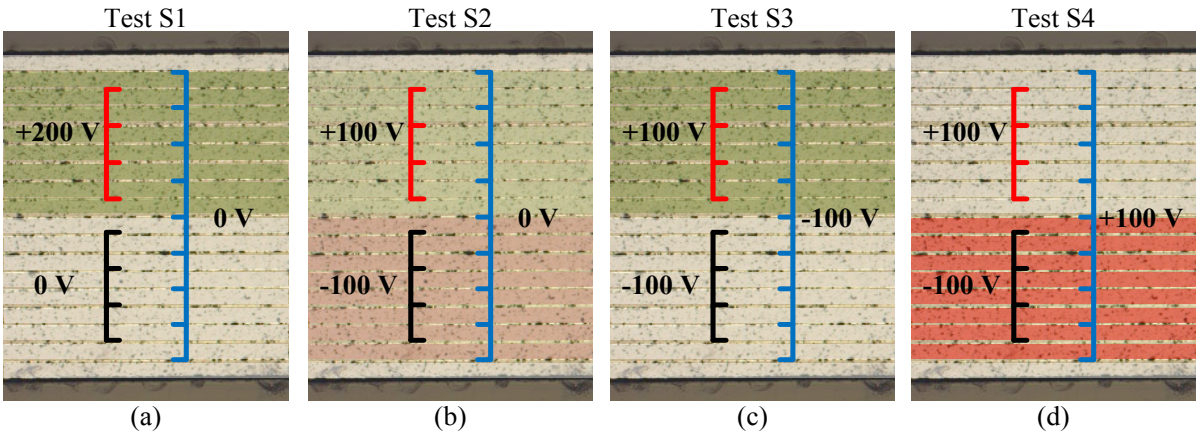

Figure 7-14. Test scenarios showing the different voltages applied to the three wires (a) the voltages for Test S1 (b) the voltages for Test S2 (c) the voltages for Test S3 (d) the voltages for Test S4.

In addition to static tests, the actuator was subjected to AC voltages (dynamic), denoted by "D". Test D5 was varying the voltage to the blue wire from -100 V to +100 V using a sine wave at either 3Hz or 30Hz, the red wire held at constant +100 V and black wire at constant -100 V. The tests were conducted while the ring bender was submerged in Hyjet. These tests were conducted to investigate if the movement of the ring bender or the switching of the electric field could have an impact. The movement could potentially initiate crack growth in the ceramic, which could create a path for the Hyjet to reach the electrodes.

Due to a limited number of ring benders, some of the ring benders were subjected to several different test scenarios. This was only conducted in case no significant damage was observed.

7.2.4 Testing in Air

Before testing the piezoelectric ring benders in Hyjet one test was conducted in air. A ring bender identified as Disc 1 was tested in air to investigate if there is a possibility that it will start to degrade without the presence of Hyjet. The ring bender was tested for 21 days with no signs of any damage or discoloration on the electrical connections, see Table 7-1. The damage was rated to 0.

Table 7-1. Results from testing Disc 1.

Disc 1	
Test:	Test 1
Test procedure:	D5, Dynamic
Duration:	21 days
Observation:	No visible damage or discoloration on the electrical connections.
Damage:	0

7.2.5 Testing in Water

The test with Disc 2 was conducted using water instead of Hyjet for a duration of 86 days. Water was investigated since several papers refer to moisture, humidity and water attacking the piezoelectric actuators [96][47][42][43]. When the test was stopped, no visible damage could be observed and the damage was rated as 0. There could be two reasons why no damage was present. First, the water could still be leaking out past the seals (as is suspected for the Hyjet tests described next), but compared to the Hyjet the water will evaporate and not stay to form an electric circuit. The second reason could be that the Hyjet might be more prone to form an electrical circuit via the first internal electrode, by finding a path through the outer most ceramic layer. The test results from Disc 2 can be seen in Table 7-2

Table 7-2. Results from testing Disc 2.

Disc 2	
Test:	Test 1
Test procedure:	D5, dynamic test, submerged in water
Duration:	86 days
Observation:	No observed damage or discoloration on the electrical connections.
Damage:	0

7.2.6 Testing in Hyjet

Five piezoelectric ring benders (Disc 3, Disc 4, Disc 5, Disc 6 and Disc 7) were tested in Hyjet under the Test S1 testing conditions. The piezoelectric ring benders were tested for approximately 6 months without any sign of significant degradation or failure visible. There was a small amount of discoloration visible on the wires and electrical connections

Due to the long tests without any sign of degradation additional tests were conducted on the five piezoelectric ring benders.

Disc 3 was tested for 191 days under test condition Test S1. There was no significant amount of degradation visible. However, there was some small discoloration on the positive (red) and negative (blue) connection. The second test was a dynamic Test D5, which was tested for 9 days where again only a small amount of discoloration on the red and blue wire was visible. The amount of damage was rated to 2. The test and results can be observed in Table 7-3.

Table 7-3. Results from testing Disc 3.

Disc 3		
Test:	Test 1	Test 2
Test procedure:	S1, Static test	D5, Dynamic 30Hz.
Duration:	191 days	9 days
Observation:	Very small amount of discoloration around the wires, no other visible damage on the ceramic.	Very small amount of discoloration around the wires, no other visible damage on the ceramic.
Damage:	2	2

Disc 4 was tested for three different scenarios, Table 7-4 shows the tests and results. The first one was the Test S1 which was tested for about 6 months. Only a small amount of discoloration on the electrical connections was found. The second test was Test S3 which was tested for about four days. Again, only a small amount of discoloration on the electrical connections was found. The third test was the dynamic test Test D5, which was tested for about 20 days or about 52 million cycles, only a small amount of discoloration on the electrical connections was found. The damage was rated to 2 in all circumstances.

Table 7-4. Results from testing Disc 4.

Disc 4			
Test:	Test 1	Test 2	Test 3
Test procedure:	S1, Static test	S3, Static test	D5, Dynamic 30 Hz
Duration:	187 days	4 days	20 days, ~ 52 million cycles
Observation:	Small amount of discoloration around the wires, no other visible damage on the ceramic.	Small amount of discoloration around the wires, no other visible damage on the ceramic.	Small amount of discoloration around the wires, no other visible damage on the ceramic.
Damage:	2	2	2

Table 7-5 shows the tests and results of Disc 5. Similar to Disc 3 and Disc 4, Disc 5 was tested for approximately 6 months under Test S1 conditions and only a small amount of discoloration on the red wire connection and no other visible damage could be observed.

The second test that was done on Disc 5 was the Test S4. The test was stopped after 91 hours due to signs of degradation where a lighter coloured area can be seen, see Figure 7-15. The lighter coloured

area is most likely due to failure of the internal electrodes. When the internal electrodes start to degrade, it becomes detached from the piezoelectric ceramic, similar to what can be seen in Figure 7-4, which causes the difference in colour. It is also anticipated that Hyjet has reached the electrodes. On a closer examination of the lighter coloured area, see Figure 7-16 (a) and with higher magnification in (b). In Figure 7-16 a pin hole in the middle of the lighter coloured area can be seen. This is most likely the point where the Hyjet penetrates the ceramic.

Table 7-5. Results from testing Disc 5.

Disc 5		
Test:	Test 1	Test 2
Test procedure:	S1	S4
Duration:	187 days	91 hours (3.8 days)
Observation:	Small amount of discoloration around the wires, no other visible damage on the ceramic.	Visible lighter spot with a pin hole in the middle was visible.
Damage:	2	4

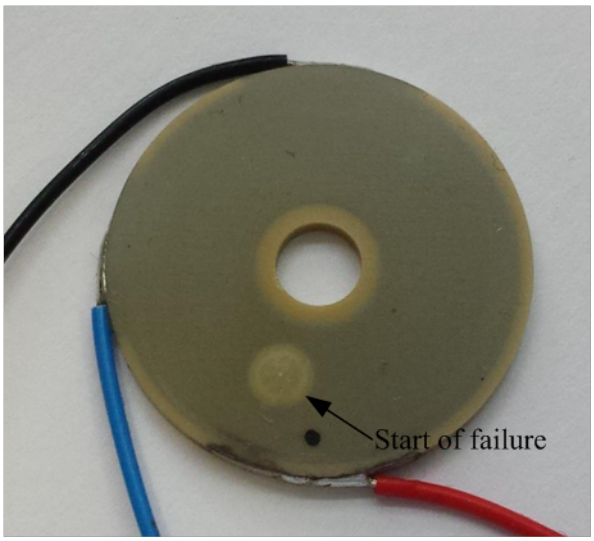

Figure 7-15. Disc 5 shows sign of degradation where a lighter spot is visible.

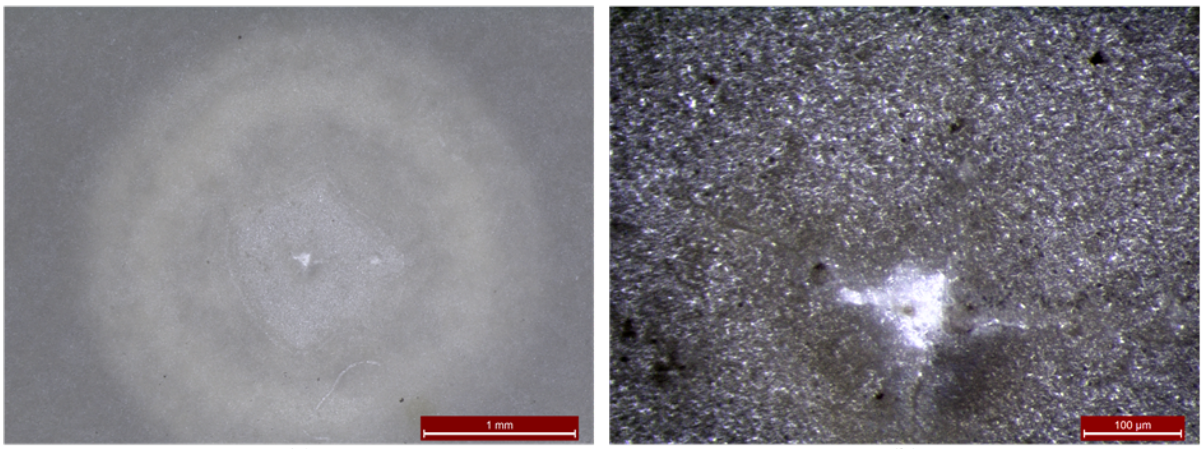

Figure 7-16. Microscopic photographs of Disc 5 (a) lighter coloured area (b) pin hole in the middle of the lighter coloured area.

Disc 6 underwent three different test scenarios, two static and one dynamic. The first was tested under the Test S1 conditions for 176 days. Only a small amount of discoloration was found around the electrical connections. Rated damage was 2. The second test was the static Test S2, which was tested for 13 days. There was a small amount of discoloration was found around the electrical connections, but no more than for Test S1 and rated damage was 2. The third test was the dynamic Test D5, which was tested for 51 days. Even after this test there was only a small amount of discoloration found around the electrical connections and no other visible damage, and the damage was rated to 2. The test results from Disc 6 can be seen in Table 7-6.

Table 7-6. Results from testing Disc 6.

Disc 6			
Test:	Test 1	Test 2	Test 3
Test procedure:	S1, Static test	S2, Static test	Test D5, Dynamic test sine wave 30Hz
Duration:	176 days	13 days	51 days, ~132 million cycles
Observation:	Small amount of discoloration around the wires. No other visible damage on the ceramic.	Small amount of discoloration around the wires. No other visible damage on the ceramic.	Small amount of discoloration around the wires. No other visible damage on the ceramic.
Damage:	2	2	2

The tests and results for Disc 7 can be seen in Table 7-7. Disc 7 underwent two tests; the first test was the static S1 test tested for 161 days. There were only small signs of discoloration on the wires and the damage was rated to 2. The second test was the dynamic D5 tested at 30 Hz. After approximately 4 days (~10 million cycles) the test was stopped since significant damage on the ceramic was detected. The Disc 7 and the failure can be seen in Figure 7-17 (a).

Before any tests were conducted, photos were taken with a microscope to examine if any possible failure point or defects could be detected, where a failure could be initiated. No obvious signs of defects could be found, which can be seen in Figure 7-17 (b), which shows the area where the failure occurred.

A high magnification image of the damage can be seen in Figure 7-18 (a), where the damaged area is zoomed in and is encircled in red in Figure 7-17 (a). While the dynamic test was running, sparks could be seen coming from the area where the failure was observed. This spark can be seen in Figure 7-18 (b). Every time the spark was visible a 'clicking' sounds could be heard. Figure 7-19 (a) shows a 'pin hole' through the ceramic and internal electrodes and what's is metal which has melted and solidified around the pin hole. Figure 7-19 (b) shows the red wire connection where some discolouration can be seen. It is likely that some Hyjet has leaked past the seal, reached the positive electrical connection, and penetrated through the first layer of ceramic, which finally damaged the outer layer. The spark is most likely due to sparking between two internal electrodes, which has melted them. This is probably a short circuit bridge between two internal electrodes. Both the failures on Disc 7 and Disc 5 have occurred on the side where a 'black mark' is applied on the piezoelectric ring bender. This black mark is indicator for the positive electrode side [33].

Table 7-7. Results from testing Disc 7.

Disc 7		
Test:	Test 1	Test 2
Test procedure:	S1, static test	D5, 30 Hz sine wave
Duration:	161 days	4 days, ~10.3 million cycles
Observation:	Small amount of discoloration around the red and blue wires, no other visible damage on the ceramic.	Large damage and sparks visible while voltage was applied.
Damage:	2	5

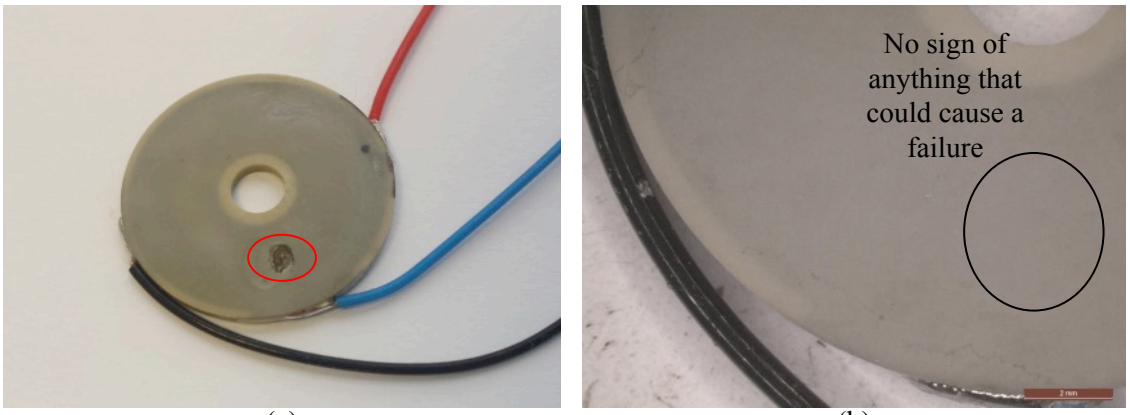

Figure 7-17. Disc 7 (a) photograph of the ring bender after test A5 showing damage (b) photograph of the area where the damage was found that was taken before any tests were conducted and not showing of anything that could initiate failure.

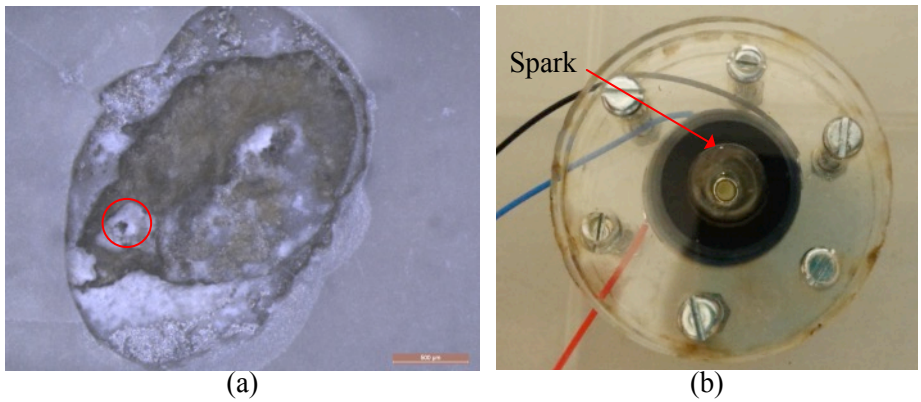

Figure 7-18. Disc 7 (a) microscopic photograph of the damaged piezoelectric ceramic and electrodes (b) photograph of a visible spark during the test.

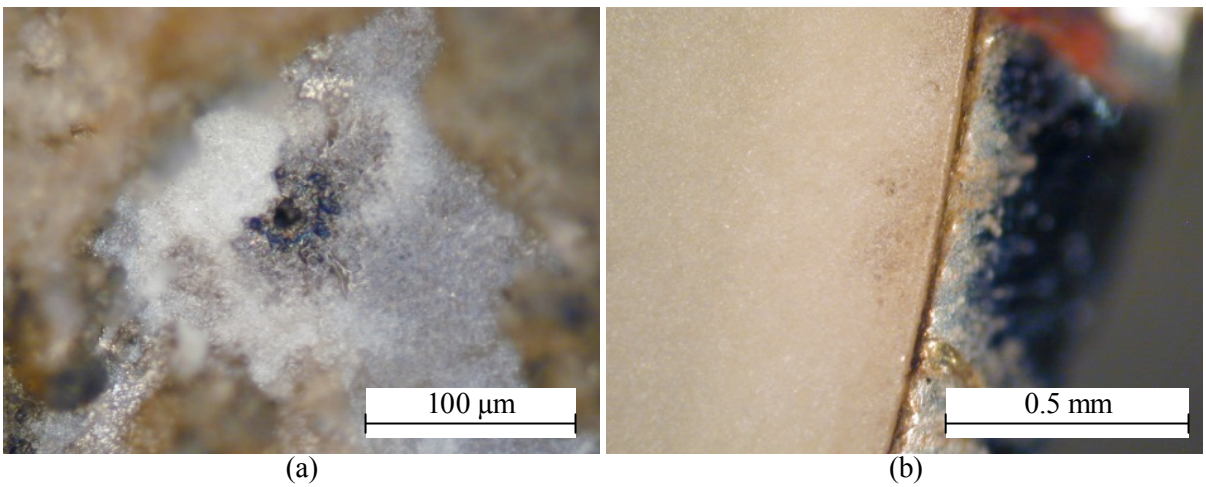

Figure 7-19. Disc 7 (a) microscopic photograph of the pin hole in the ceramic and electrodes (b) microscopic photograph of the red wire connection.

Disc 8 was tested under Test S2 conditions, which meant that the red wire was held at +100 V, the black at -100 V and the blue wire at 0 V. It can be seen on both the red and blue, see Figure 7-20 (a) and (b) that there is discoloration around the positive (red) and negative (blue) electrical connection.

Table 7-8. Results from testing Disc 8.

Disc 8	
Test:	Test 1
Test procedure:	S4, static test
Duration:	21 days
Observation:	Discoloration around the red and blue wires. No other visible damage on the ceramic.
Damage:	2

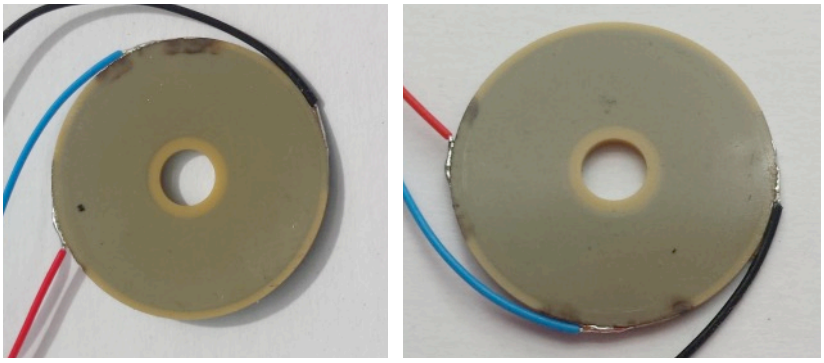

(a) (b)

Figure 7-20. Photograph of Disc 8 after testing (a) the top side of Disc 8 (b) the bottom side of Disc 8.

After these first tests is was observed that many of the tested piezoelectric ring benders had some amount of discoloration around their electrical connections, mainly on the red wire (positive wire). The reason for this is most likely that a small amount of Hyjet has been able to leak past the O-rings and reached the electrical connections, which resulted in an electrical circuit, between the electrical connection and the internal electrode. In some of the tests, a thin layer of Hyjet could be observed around the outside of the O-ring. However, this layer was difficult to detect. There is also the assumption that the Hyjet can penetrate the first layer of piezoelectric ceramic via cracks or pores.

There are a few hypotheses why the Hyjet was able to leak out:

I. Surface roughness, the seal will not seal properly.
II. Higher pressure inside the test setup that will force the Hyjet past the seal. The higher pressure can be due to:

a. The compression on the whole test setup when the last acrylic plate is added. No air is able leak out and equalise the pressure.
b. Temperature increase related to piezoelectric ring bender movement (mechanical losses) and electrical losses.

III. While handling and inspection of the test samples.

7.2.7 Testing in Hyjet with Extra Anode

To test the hypothesis that the Hyjet is leaking past the seals and reaching the electrical connections several tests were set up where the red wire (positive wire) was inserted back into the fluid to simulate this condition. This was done by connecting a second wire to the red wire and this second wire was inserted into the fluid as can be seen in the illustration in Figure 7-21 and photograph Figure 7-22.

The blue wire was not reinserted since it is connected to the outer internal electrode, which is the first electrode that the will be reached by the Hyjet. Therefore, no electrical circuit would be created. The red wire was chosen since it is the wire connection where most discoloration (electrochemical corrosion) could be seen.

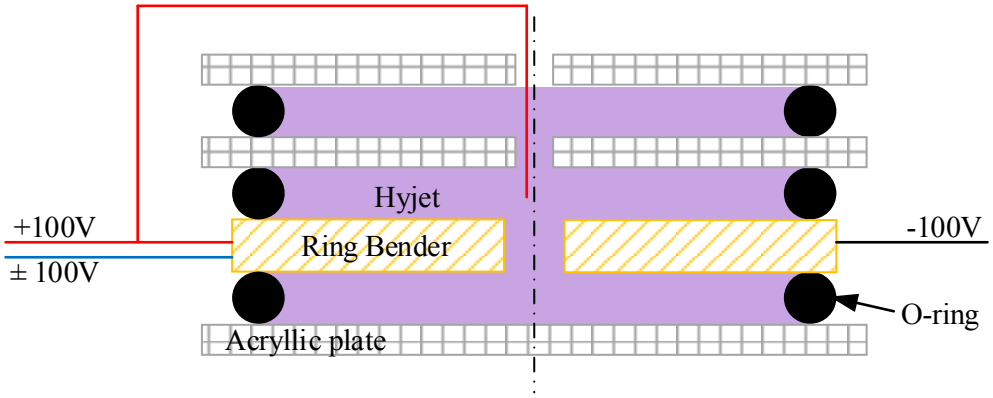

Figure 7-21. Schematic cross section diagram illustrating the test scenario where the red wire inserted into the Hyjet.

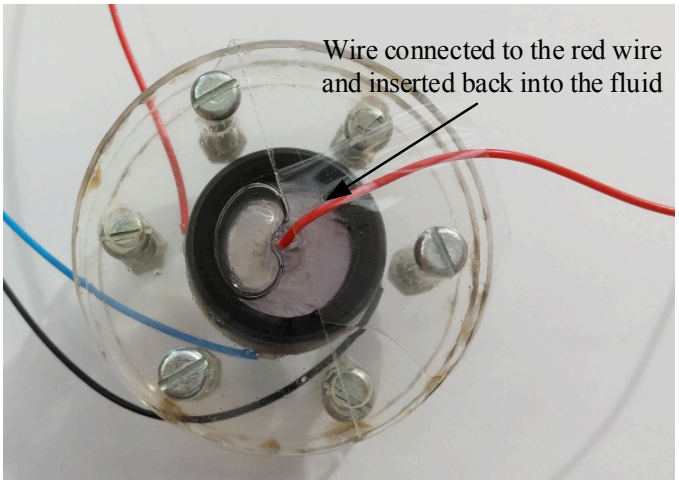

Figure 7-22. Photograph of the test hardware when ted wire is feed back into the fluid.

Table 7-9 shows the test information, observation and amount of damage for Disc 9 which was tested under these conditions. The test of Disc 9 was stopped after 17 hours as a crack was visible, as can be seen in Figure 7-23. 17 hours is significantly shorter time for damage to occur than for previous tests. This indicates that if the Hyjet reaches the positive connection and an electrical circuit is created it will significantly shorten the life of the piezoelectric ring bender.

Table 7-9. Results from testing Disc 9.

Disc 9	
Test:	Test 1
Test procedure:	D5, 3 Hz sine wave, Anode in the Hyjet.
Duration:	17 hours
Observation:	A crack started to be visible
Damage:	3

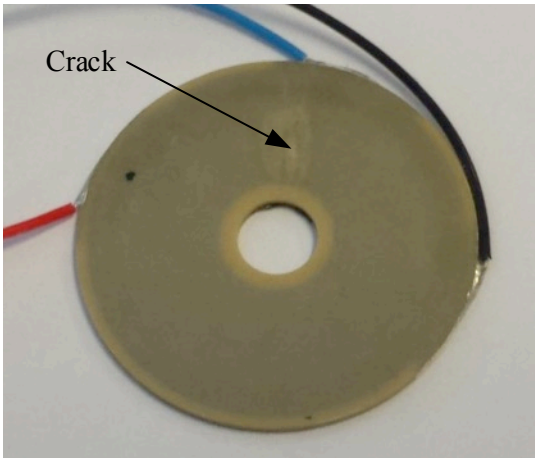

Figure 7-23. Photograph of Disc 12 showing a visible crack.

Disc 10 was tested in the same fashion as Disc 9, and the results can be seen in Table 7-10. This test was stopped after 16 hours of testing since a significant amount of damage was visible. Several black spots and cracks were evident, which can be seen in Figure 7-24. Figure 7-25 shows two of the black spots on Disc 10. It can be seen that there are small holes and cracks through (at least) the first outer inactive ceramic layer.

Table 7-10. Results from testing Disc 10.

Disc 10	
Test:	Test 1
Test procedure:	D5, 3 Hz, Anode back in the Hyjet.
Duration:	16 hours
Observation:	Several black sports are visible
Damage:	5

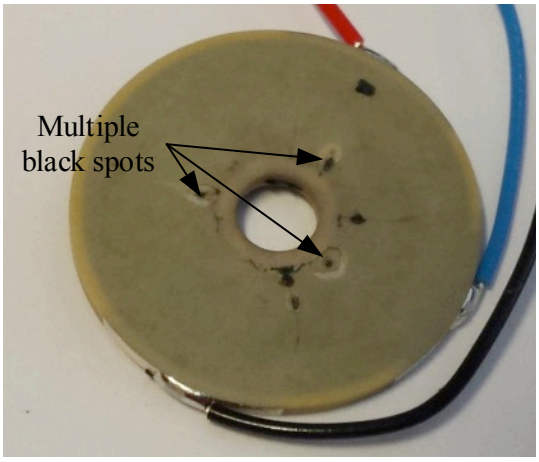

Figure 7-24. Photograph of the damage show by the black spots on Disc 13.

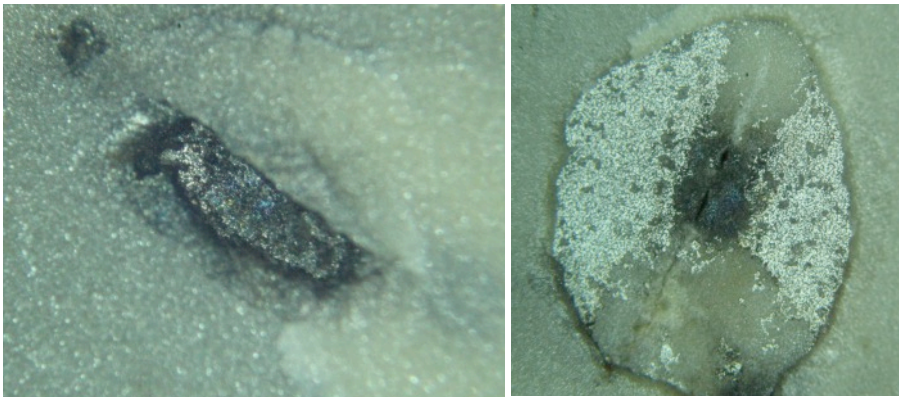

(a) (b)

Figure 7-25. Microscopic photograph showing two of the black spots on Disc 13.

Disc 11 was tested, similar to Disc 9 and Disc 10, but with the static Test S3 condition, and with the red wire feed back into the Hyjet. The results of the test can be seen in Table 7-11. After 10 hours, the test was stopped. As can be seen in Figure 7-26 (a) a significant number of small cracks had started to develop. On the opposite side, see Figure 7-26, a black layer has formed. This suggests that there is no

significant difference if there is a constant voltage or a dynamic voltage is applied, in both circumstances failure will occur relatively fast. The damage was rated to 4.

Table 7-11. Results from testing Disc 11.

Disc 11	
Test:	Test 1
Test procedure:	S3, Static test, Anode back in the Hyjet.
Duration:	10 hours
Observation:	A lot of small cracks and discoloration on the surface.
Damage:	4

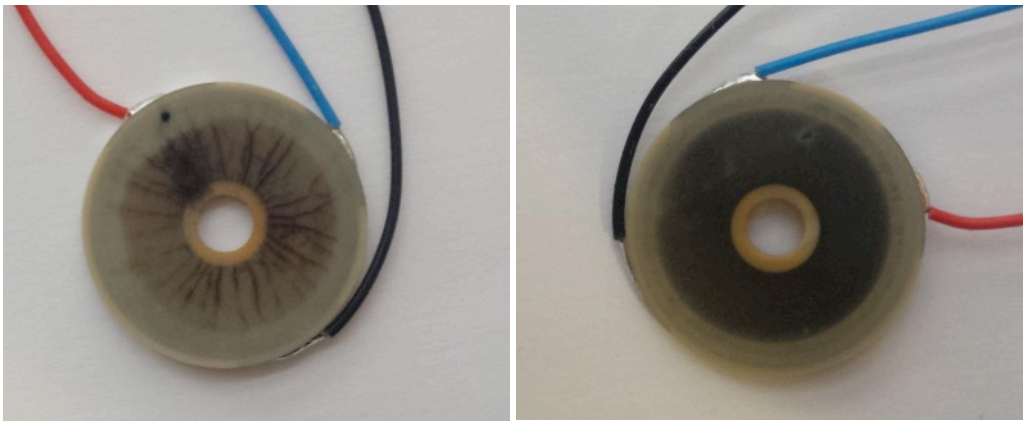

(a) (b)

Figure 7-26. Photographs of Disc 11 after testing where both cracks and discoloration can be seen (a) top side of Disc 11 (b) bottom side of Disc 11.

7.3 ENCAPSULATION

From the tests with Disc 9, Disc 10 and Disc 11 it can be observed that the piezoelectric ring bender will be damaged in a short amount of time if the Hyjet reaches the electrical connections. A hypothesis is that the Hyjet penetrates the outer layer of ceramic to form an electrical circuit. A test was set up to investigate possible encapsulation of the piezoelectric ring bender. Most literature and patents suggest using a metallic layer for protection, since a polymer protection would not be completely impermeable [48].

Three types of epoxy were tested to be used for encapsulation of the ring bender, since it would be relatively easy to apply, cheap and it would not affect the stiffness of the ring bender to a great extent. Different types of Epoxy were submerged into Hyjet. It was found that the epoxy tested would not be suitable for encapsulation of the piezoelectric ring bender. All the epoxy tested would eventually soften in Hyjet. The epoxy tested can be seen in Table 7-12. One electrical insulation varnishes, RS Insulation

Varnish 199-1480 [97], was tested as well with a similar outcome to the epoxy. The varnish was tested since it is easy to apply. The tests varied between 2 weeks up to 8 months.

Table 7-12. Epoxy specifications [98][99][100].

Manufacturer	**Name**	**Features**
Loctite	EA0151	- 2 part epoxy - Clear colour
RS	851-044	- 2 part epoxy - Black colour
Struers	SpeciFix20	- 2 parts epoxy - Clear colour

An aluminium metallic foil, with a thickness of 80µm, was applied to the surface of a ring bender, see Figure 7-27, to stop the Hyjet penetrating the ceramic. To investigate if this encapsulation was sufficient even if the Hyjet breaches the seals and reaches the electrical connectors the red wire was fed back into the Hyjet in a similar way as for Disc 9-10. Epoxy was added to the middle of the disc to ensure that the fluid would not penetrate through the middle, and force its way underneath the foil, although this is unlikely to give a permanent protection. The outer edge will be outside the seal; therefore, no fluid would be able to penetrate underneath the outer edge. It is assumed that the O-ring would be able to create a better seal on a metallic foil than on the ring bender ceramic. The foil is a metallic material, there are no subsurface cracks and the surface roughness is believed to be better, therefore it is believed that the better seal would be made. The foil was applied so that it would not be in contact with the electrical connections to ensure no short circuiting.

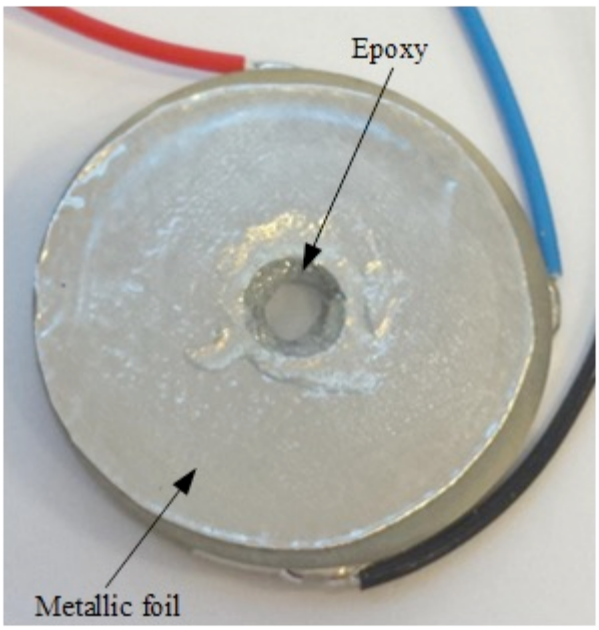

Figure 7-27. Photograph of Disc 12 with the metallic foil attached to protect the piezoelectric ceramic with epoxy applied on the inner edge to prevent Hyjet to find a pathway underneath the seal through the inner diameter.

In Table 7-13 the results from the test with Disc 12 can be seen. The test was a dynamic test and was stopped after 250 hours and the metallic foil was taken off the piezoelectric ring bender and investigated. A small amount of possible damage could be found, this damage could only be seen under a light microscope. This was some discoloration on the surface or the ceramic and small, approximately 10 µm pin holes, as can be seen in Figure 7-28. This was found in the area where the O-ring was pressing down against the metal foil. It is possible that small holes were already present, caused during the handling of the foil or were made in the metallic foil due to the force from the O-ring and the surface roughness of the piezoelectric ring bender. It is possible that a small amount of Hyjet had managed to get in contact with the ceramic and cause this relatively small damage. The damage was rated to 1-2.

At the end of the test epoxy used in the middle of the piezoelectric ring bender had turned rubbery. This confirms that this epoxy is not suitable for use in Hyjet.

Table 7-13. Results from testing Disc 12.

Disc 12	
Test:	Test 1
Test procedure:	D5, Dynamic test, sine wave 3 Hz, Anode back in the Hyjet. The ceramic is covered by a metal foil.
Duration:	250 hours
Observation:	No discoloration of the Hyjet, no sign of Hyjet leakage, No sign of discoloration on any of the wires, epoxy turned rubbery. There were small pin holes on the ceramic when investigated under a microscope.
Damage:	1-2

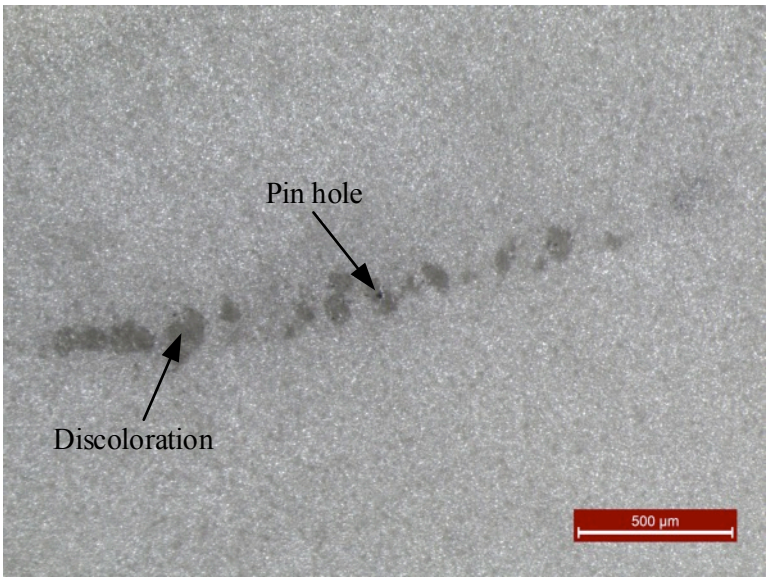

Figure 7-28. Microscopic photograph of the small pin holes found on Disc 12 after 250 hours of testing.

Disc 13 was tested in the same way as Disc 12, dynamic D5 test, the metallic foil was applied to the surface of the piezoelectric ring bender and the red wire feed back into the Hyjet. The results from this test can be seen in Table 7-14. The test was running for 500 hours (~21 days), there were no visible signs of degradation either on the electrical connections nor the surface of the piezoelectric ring bender ceramic and the damage was rated to 1.

Table 7-14. Results from testing Disc 13.

Disc 13	
Test:	Test 1
Test procedure:	Test D5, Dynamic test, sine wave 3 Hz, Anode back in the Hyjet. The ceramic is covered by a metal foil.
Duration:	500 hours
Observation:	No sign of discoloration on the wire and no visible defects on the ceramic as the foil is taken off.
Damage:	1

7.4 SEM INVESTIGATION

If flaws or pores were present in the piezoelectric ceramic, this would most likely not be seen under a normal light microscope. To investigate possible failure points in the piezoelectric ceramic, a Scanning Electron Microscope (SEM) investigation was conducted. The top surface of a piezoelectric ring bender was scanned to investigate the surface and possibilities of pores or potential flaws. A cross section of a piezoelectric ring bender was examined to analyse the bulk material, surface roughness and possible interconnected pores or cracks.

7.4.1 Surface

The surface of a piezoelectric ring can be seen in Figure 7-29 (a) and (b). The surface is made up of small grains of piezoelectric ceramic. In Figure 7-29 (a), magnification x250, darker areas can be seen, this is most likely contamination attached to the surface. In Figure 7-29 (b) the grains of the piezoelectric ceramic can be seen, magnification of x950. It can also be seen that there are voids between grains.

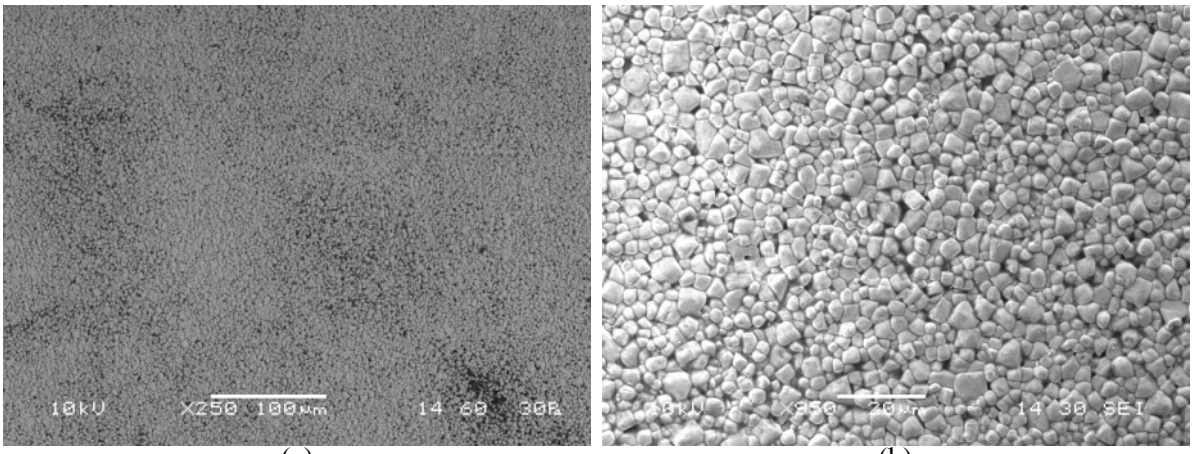

(a) (b)

Figure 7-29. SEM image of the piezoelectric ceramic surface showing the piezoelectric grains (a) magnifications of x250 (b) magnification of x950.

The images in Figure 7-30, (a) x2000, (b) x5500, (c) x3300 and (d) x5000, shows a higher magnified image of the piezoelectric ceramic surface, where it can be seen that the grains are of mixed sizes and shapes. The size of the grains are between 1-10µm across with irregular shapes. In between some of the grains, voids can be seen (darker or black areas). The size of these voids are approximately the same size as the piezoelectric ceramic grains. These 'normal' voids are due to the shapes, size and the packing of the ceramic. From the pictures in Figure 7-30 it cannot be known if the voids form a connected path going all the way down to the first electrode or just a missing surface grain. If these voids create a path to the first electrode it could be possible that the Hyjet is reaching the electrode through these voids and channels. On the surface of the piezoelectric ring bender that was scanned no significant or obvious defects, other than the 'normal' voids, were found.

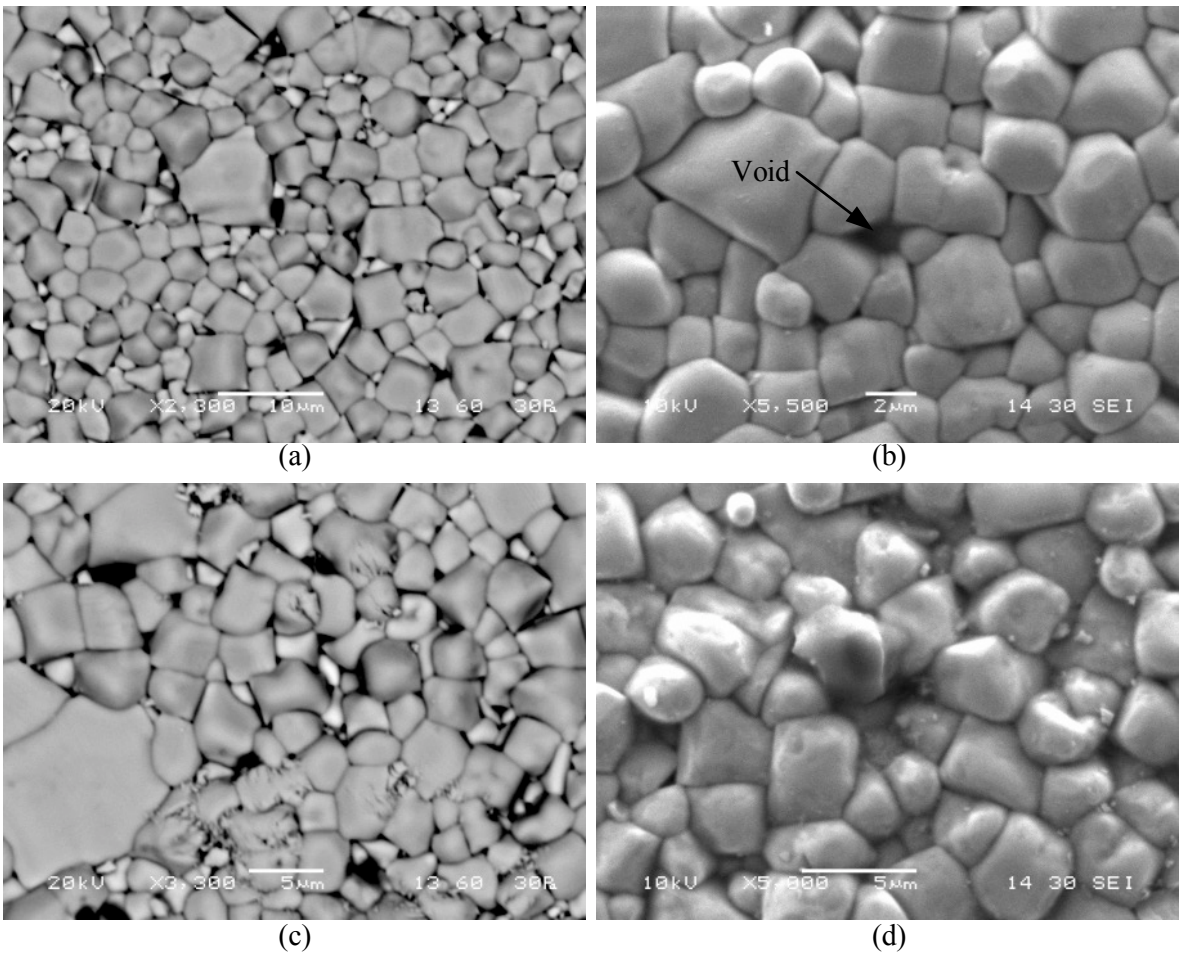

Figure 7-30. Example SEM images of the piezoelectric ceramic surface showing the piezoelectric grains (a) magnification of x2300 (b) magnification of x5500 (c) magnification of x3300 (d) magnification of x5000.

7.4.2 Cross Section

Disc 5 was cut in half and set in resin to investigate the internal structure of the piezoelectric ring bender. All SEM cross section images were taken off Disc 5. Figure 7-31 shows a cross section of a piezoelectric ring bender. In Figure 7-31 (a), the magnification is x170, where six layers of piezoelectric ceramic with its electrodes in between the ceramic layers can be observed. Additionally, a significant number

of possible pores can be observed (black spots). In Figure 7-31 (b) a further zoomed in picture, magnification of x350, the electrodes and pores can be seen.

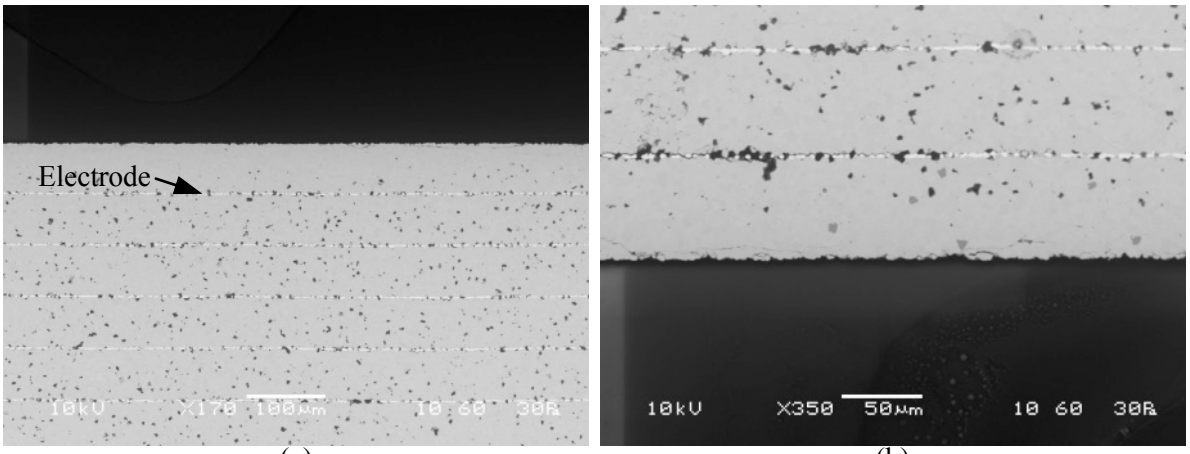

(a) (b)

Figure 7-31. SEM images of a cross section of the ring bender (a) six piezoelectric ceramic layers with the electrodes, magnification of x170 (b) piezoelectric ceramic and the electrodes, magnification x350.

Figure 7-32 (a) and (b) shows two outer inactive ceramic layers, where both cracks and pores can be observed. The cross section that can be seen has previously been submerged and tested in Hyjet (Disc 5). In both Figure 7-32 (a) and (b) cracks going from the surface towards the first electrode and pores can be observed. The cracks do not reach the electrode, which is most likely why no visible failure can be observed on the surface in these specific places. The cracks could be a feature of the manufacturing or the cutting and inspection process. However, they are more likely to be a result of testing. Several papers indicate that cracks have been created during dynamic testing and is a reason for failure [96][42]. During the inspection, cutting and polishing process of the sample it is more likely that the piezoelectric grains are chipped of or pulled out, creating pores, than that cracks are being created.

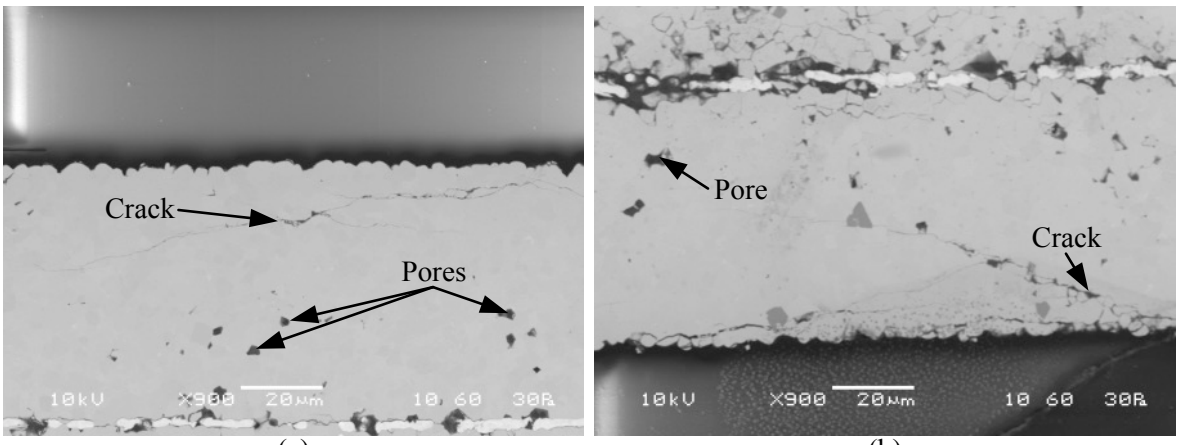

(a) (b)

Figure 7-32. SEM images of a cross section of Disc 5 (a) outer inactive layer showing both pores and cracks, magnification x900 (b) outer inactive layer showing both pores and cracks, magnification x900.

As can be seen in Figure 7-15 Disc 5 has a lighter coloured area, which is believed to be a start of a failure. A cross section of this area was investigated and can be seen in Figure 7-33 (a), red circle, that the lighter colour area indicated that the electrodes are damaged and that the piezoelectric ceramic layers are delaminated from each other and the electrodes. It can also be observed in Figure 7-33 (b) and (c) that there is a relatively large crack starting from the outer surface moving through the ceramic towards the first electrode. There is a possibility that the Hyjet could have reached the electrode through these cracks, which would connect a circuit and damage the electrodes. If a circuit was connected this probably means that the Hyjet is in contact with the positive (red) wire. Figure 7-33 (d) shows the damaged electrode and the surrounding piezoelectric ceramic. It can be observed that the ceramic grains are starting to separate from each other.

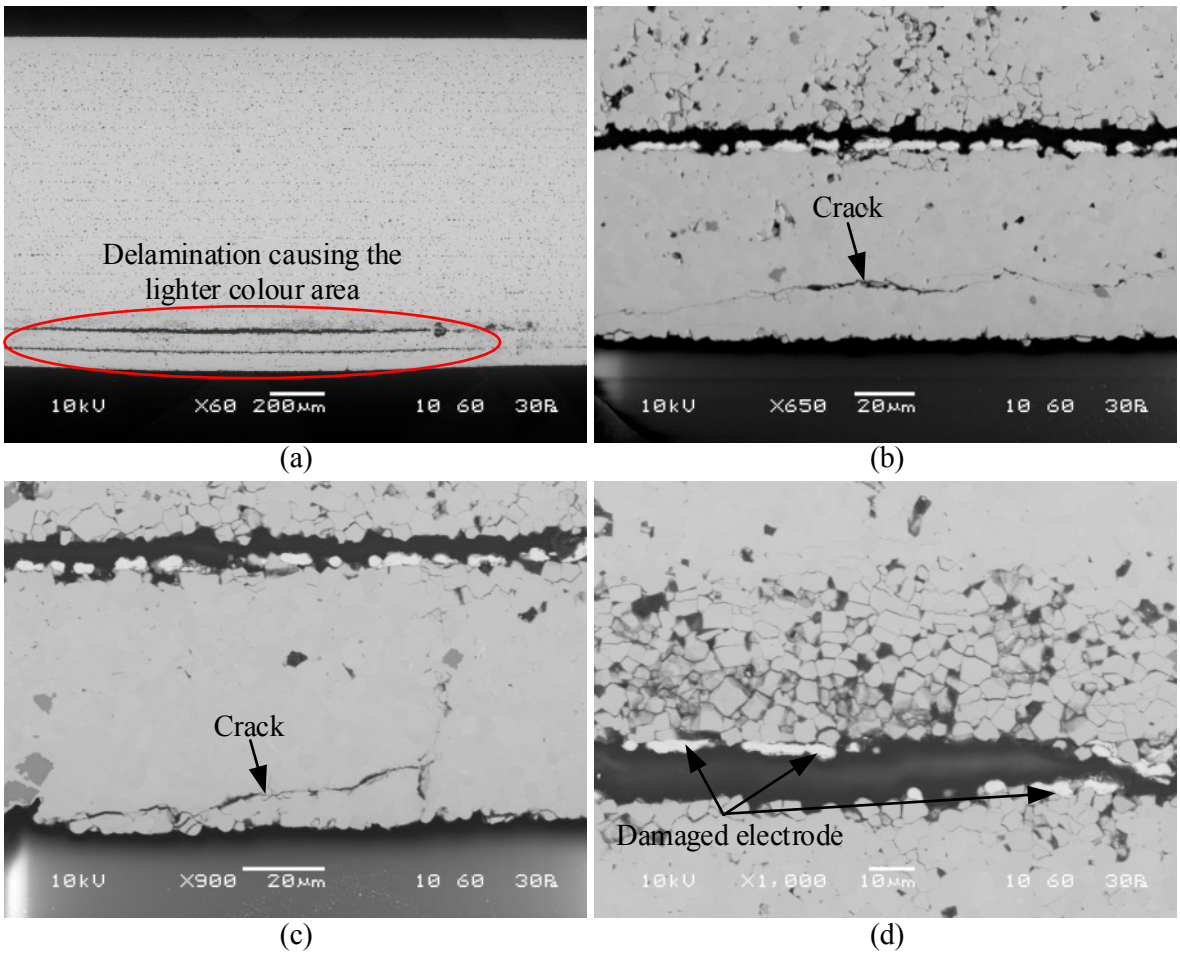

Figure 7-33. SEM cross section images of Disc 5 (a) delamination of piezoelectric ceramic layers, lighter coloured area (b) crack in the piezoelectric ceramic (c) crack in the piezoelectric ceramic starting from the surface moving towards the first electrode (d) damaged electrode and the surrounding piezoelectric ceramic.

7.4.3 Surface Roughness

By examining a cross section of a piezoelectric ring bender, the surface roughness can be investigated. The surface roughness was investigated to examine if the surface of a piezoelectric ring bender is smooth enough to create an effective seal under the O-ring.

Cross section images, with different magnifications, of the top surface of a piezoelectric ring bender can be seen in Figure 7-34 (a), (b), (c) and (d). It can be seen that some piezoelectric ceramic grains are 'sticking out' from the surface and do not seem to be well attached. These areas are probably areas where voids can be seen when the top of the surface is inspected. It also appears to be these areas where cracks are originating from. In Figure 7-34 (a), (c) and (d) several cracks are visible. These could potentially create a pathway for the hydraulic fluid to leak past the seal and reach the electrical connections.

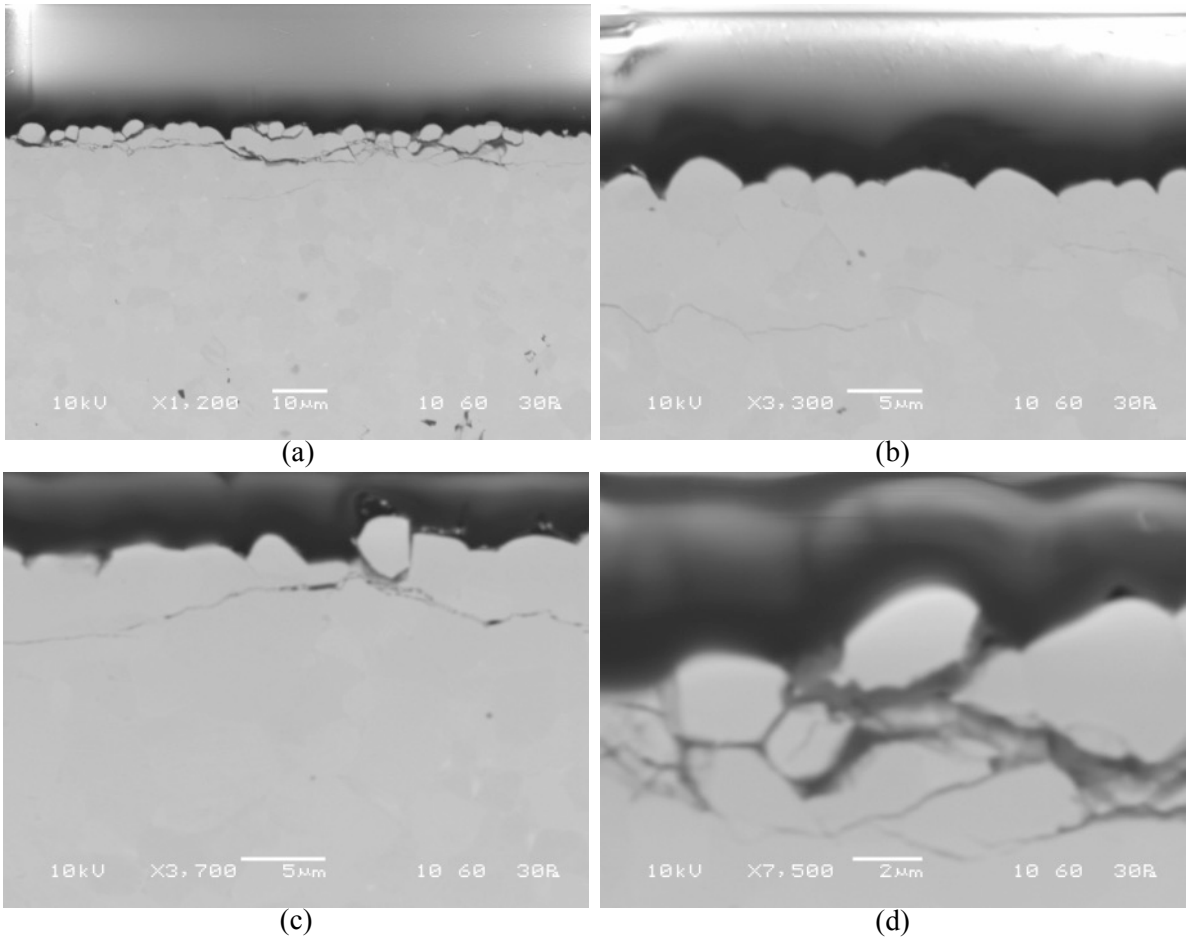

Figure 7-34. SEM cross section images of Disc 5 showing the surface roughness (a) top layer, magnification x1200 (b) top layer, magnification x3300 (c) top layer, magnification x3700 (d) top layer, magnification x7500.

To obtain a surface roughness measurement a laser profilometer was used. The ISO Rz is the average peak to trough roughness. It is based on a one peak and one valley per sample length, five sample lengths are then averaged [101]. By using a profilometer to measure the surface roughness it was found that the average ISO Rz is about 4-5 µm. An example of the surface roughness from the profilometer measurements can be seen in Figure 7-35. It was also observed that there are several relatively high peaks and low troughs. This causes issues when trying to seal on the surface. These peaks and troughs could potentially create paths for the hydraulic fluid to get past the seal.

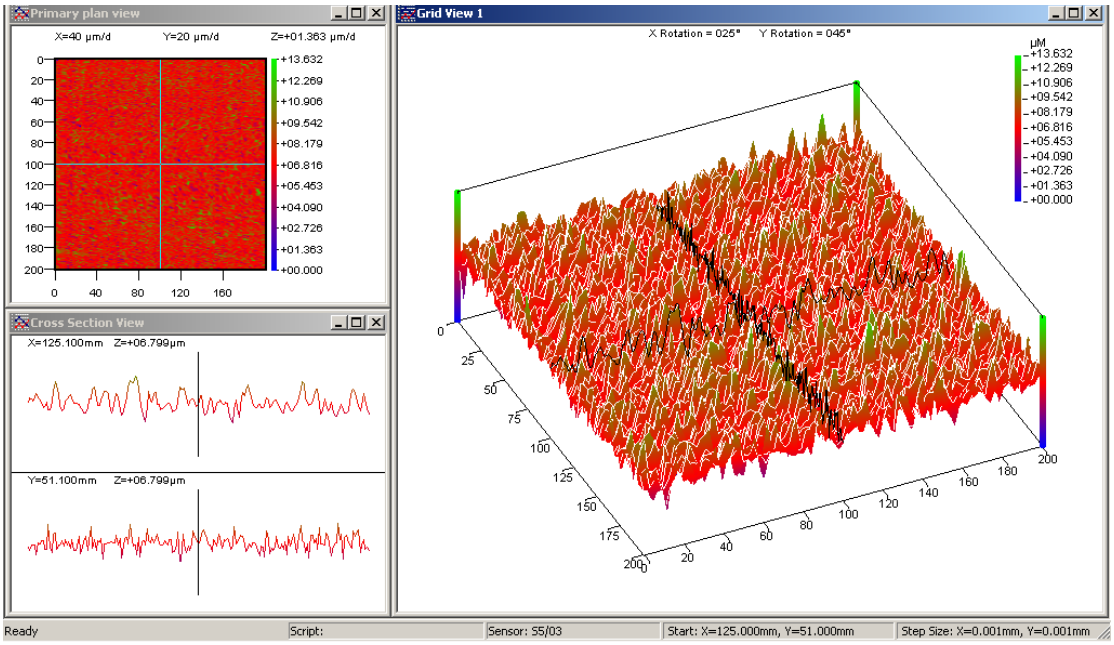

Figure 7-35. Example of the profilometer surface roughness measurements.

7.5 POROSITY

The porosity of the piezoelectric ring bender was measured to discover if fluid could penetrate the ceramic. The porosity of the piezoelectric ceramic was measured by using a mercury method. Due to the non-wetting properties of mercury, an external force is needed to force the mercury into the pores. Relatively low pressure is required for large pores, whilst higher pressure is required for smaller pores. The volume of mercury that intrudes into the test sample is measured at each pressure change. The volume corresponds to a certain size of pore [102].

The porosity was measured to be 3-4%. However, the pore size of the porosity in the piezoelectric ceramic was 5-60 nm, which can be seen by the peak in Figure 7-36. There is also another peak at around 100 µm, this is most likely due to surface or near-surface effects. These surface or near-surface effects are most likely due to cracks or voids similar to what can be seen in Figure 7-34 (a), (c) and (d) or even surface roughness. This implies that the piezoelectric ceramic is dense, the small porosity, sub 60 nm could possibly due to the mercury being force between the piezoelectric grains.

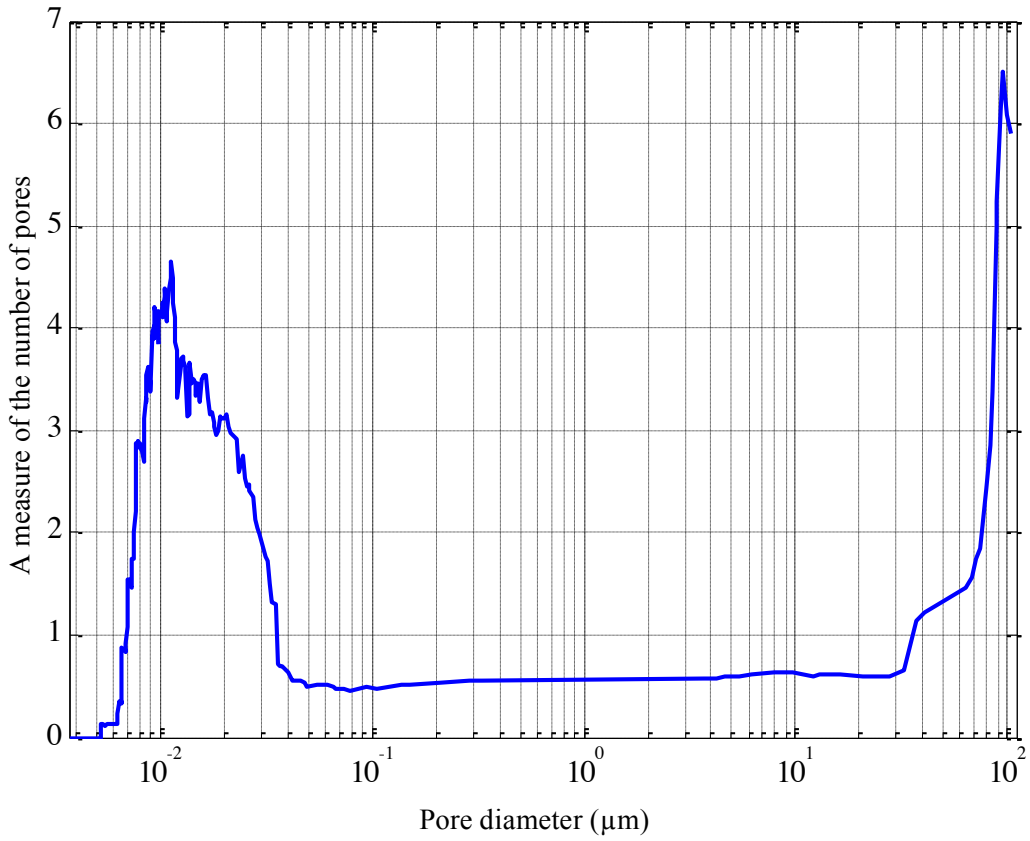

Figure 7-36. Graph showing the pore size measured through mercury testing, where a peak at around 5-60nm can be observed.

It appears that the two outer inactive layers are denser or have less grains pulled out than the 'bulk', active piezoelectric ceramic layers. This can be seen in Figure 7-37, where the outer inactive layer is highlighted by a red circle, that there is an absence of pores (black spots) in the inactive layer. In the 'bulk' (active ceramic layers) a significant number of pores or missing grains can be seen and the pores are about the same size as the piezoelectric ceramic grains, around 5 µm. It is not unusual to see a denser outer ceramic layer, which is most likely due to the manufacturing process, as the electrodes prevent the removal of atmospheric gases trapped between the ceramic grains. In the outer ceramic layer there is no electrode to prevent the gases from escaping. Similar results, with a denser outer layer, have been observed by Noliac, the piezoelectric actuator manufacturer [103]. However, some of the pores visible in the bulk material will be grains missing due to being pulled out or chipped off during the cutting or polishing process.

The pores created by the polishing method are expected to have irregular shaped, like the piezoelectric ceramic grains, whereas the pores formed during manufacture are rounder with no sharp corners. In Figure 7-33 (b) and (d), which shows the damaged electrode and ceramic, the individual grains can be

seen. It can also be observed that some grains are missing, which is probably due to the polishing process.

By using a reflecting microscope, triple point pores could be observed, see Figure 7-38. Triple point pores are small voids (compared to the pores where a gain has been pulled out) that are formed as a result of the shapes and packing of the piezoelectric ceramic grains. The shapes are irregular and might leave a void between grains. It is possible that these are the pores that show up in the mercury test, 5-60nm size.

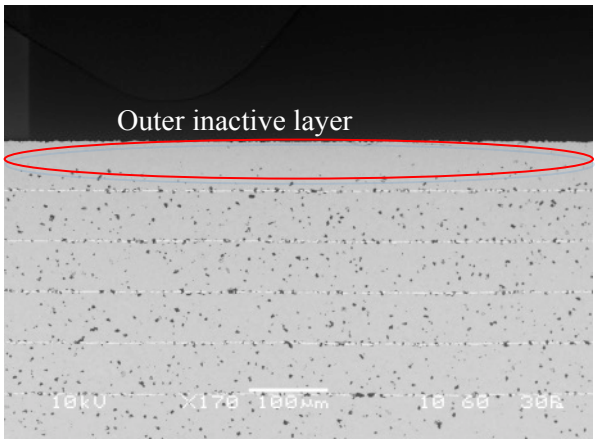

Figure 7-37. SEM cross section image showing the outer inactive layer more dense than the 'bulk' active piezoelectric ceramic.

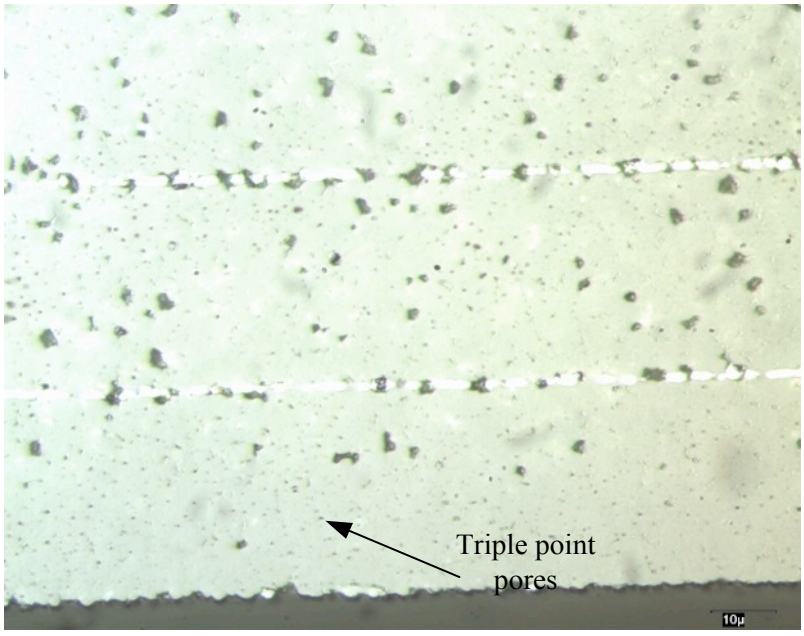

Figure 7-38. Reflecting microscope cross section photograph of the piezoelectric ring bender cross showing pores and triple point pores.

7.6 HELIUM TEST

To investigate the possibility that the O-ring cannot create a sufficient seal on the piezoelectric ring bender surface, a helium test was conducted. A Pfeiffer helium leak detector was used to detect and quantify the helium leakage, see Figure 7-39. The Pfeiffer helium leak detector can detect and quantify a very low amount of helium present in the chamber. A metallic disc was tested to have a base line for how much a good seal would leak. This was compared against the amount of leakage when tested on a piezoelectric ring bender.

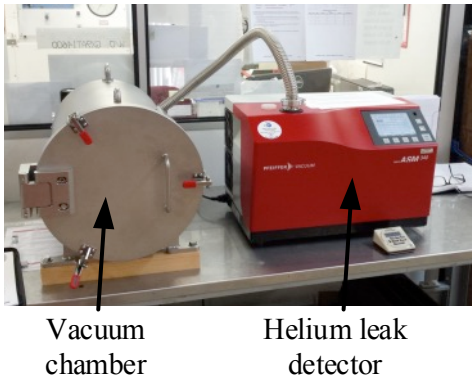

Figure 7-39. Photograph of the Pfeiffer helium sniffing machine used to investigate the helium leakage.

The Piezoelectric ring bender or the metallic disc was 'sandwiched' between two O-rings. The squeeze on the O-rings was controlled by two plastic rings, as can be seen in Figure 7-40 where a CAD drawing cross section of the test hardware can be seen. Figure 7-41 shows the hardware; the pipe was added increase the helium volume. The extra volume was added to ensure a relatively constant pressure even if leakage occurred. The helium was filled up by the use of the check valve.

The three different squeeze percentages of the O-ring that was tested were:

- 8 %
- 13 %
- 20 %

13 % squeeze is the amount that is normally used. The reason for testing different squeeze percentages is to investigate how this will affect the seal. The helium pressure was 6.9bar, which is the maximum return pressure of the hydraulic system. Due to the design of the valve the ring bender will be operating in return pressure.

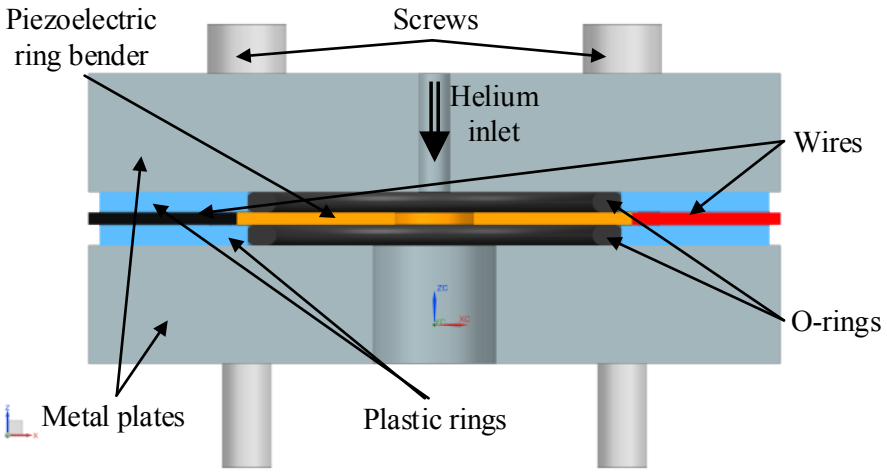

Figure 7-40. Cross section CAD illustration of the helium testing test hardware showing how the piezoelectric ring bender is sandwiched between two O-rings.

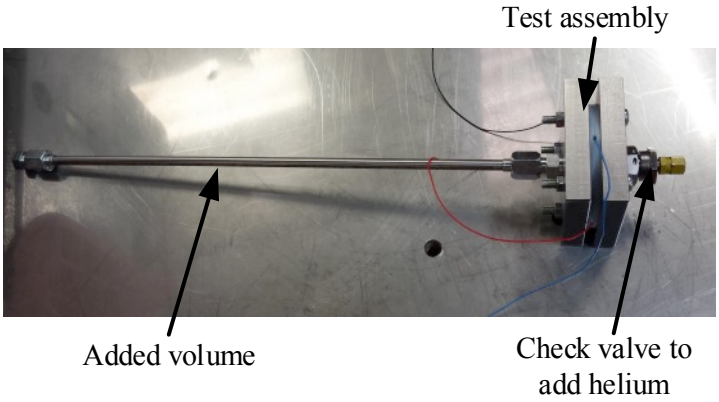

Figure 7-41. Photograph of the helium test hardware showing the test assembly, check valve and the added volume.

The leakage results from the helium test can be seen in Figure 7-42, where it can be observed that if the squeeze on the piezoelectric ring bender is not sufficient, the leakage will be significantly greater than for a metal disc. However, at a squeeze of 13% there is no significant difference between the piezoelectric ring bender and the metal disc. At 20% it is difficult to make a clear conclusion since there is a large spread in the results for the ring bender. However, it is clear that it is essential to closely control the squeeze when sealing on piezoelectric ceramic. The results in Figure 7-42 are the average leakage from three tests at each squeeze level.

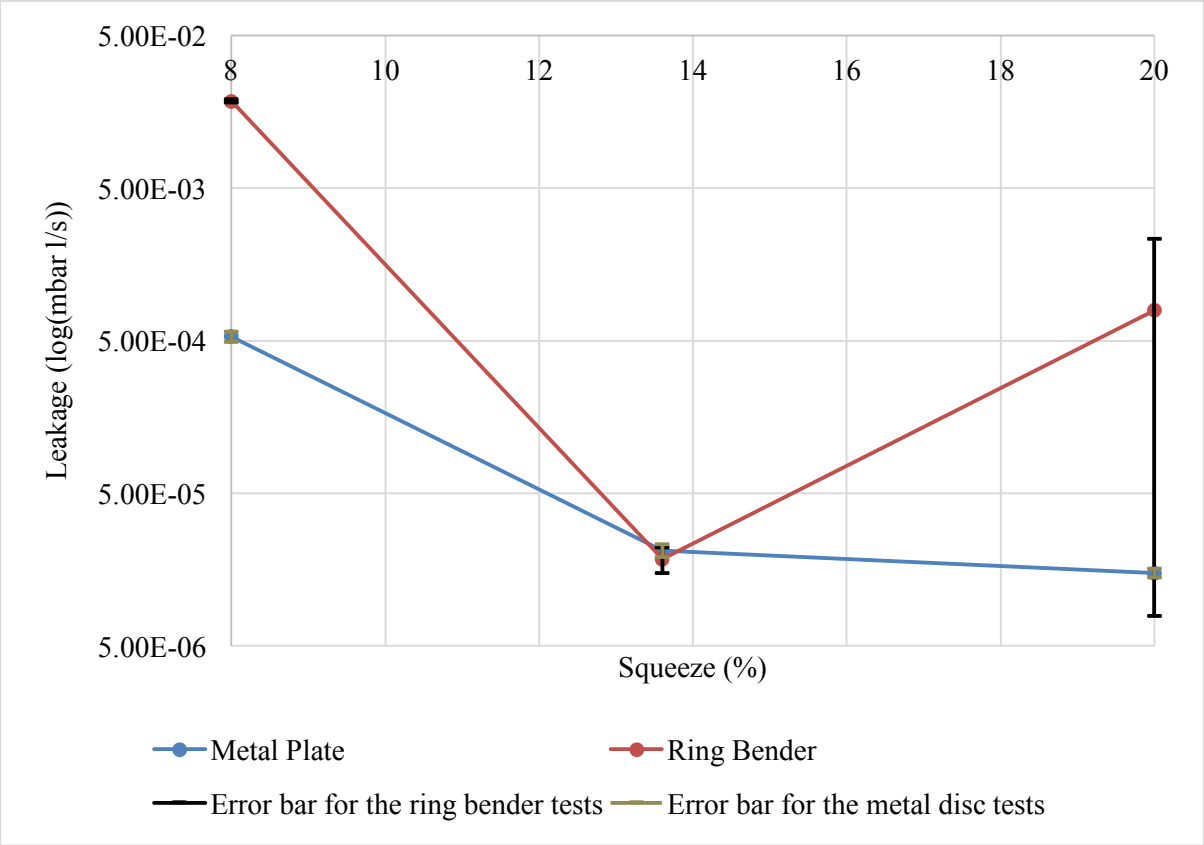

Figure 7-42. Graph showing the average results and error bars from the Helium test for different squeeze levels.

Due to the vacuum chamber, dynamic tests of the piezoelectric ring bender could not be conducted. It is important that the O-ring provides a good seal even when the piezoelectric ring bender is moving. Usually O-rings do not have to seal on a moving part. When a ring bender is moving, this could potentially make it harder to create a sufficient seal to ensure no leakage.

7.7 Discussion

From the tests conducted it is likely that the reason for failure is due to Hyjet leakage past the seal and reaching the electrical connections. This is supported by the observation that the wires and electrical connections have traces of an electrochemical reaction. Additionally, when the positive wire (red wire) is fed back into the Hyjet, failure occurs significantly faster than without it being fed back into the Hyjet. A thin film was visible around the seal and the electrical connection in some of the tests, which is likely to be hydraulic fluid leaking past the seal. If the Hyjet leaked past the seal and reached the wires, an electrical circuit could be created as a result. This could also explain the discoloration around, mainly, the red wire and the red wire solder. As an example, there was a small amount of Hyjet that had leaked out when testing Disc 9. However, this was not obvious and would not have been seen if not inspected carefully. Hypothetically therefore, the Hyjet might have leaked out in previous tests and reached the wires, without being observed. A Hyjet leakage in previous tests as well could potentially

explain some of the failures. The tests where the red wire is inserted into the Hyjet support the theory that failure occurs when an electrical circuit is made, as both of these tests showed signs of degradation and failure within a very short time.

For an electrical circuit to be created, the Hyjet also needs to be able to reach the internal electrodes. Any flaws in the outer layer of piezoelectric ceramic would most likely not be seen under a microscope beforehand. The defects might be subsurface cracks that cannot be seen. Another uncertainty is that it is unknown how large defects, voids or cracks need to be to create a path for the fluid to reach the electrodes and cause a failure. One question is whether the point where a failure starts already has a defect. There are gaps between the piezoelectric ceramic grains, but if these gaps alone are big enough for fluid to reach the electrode is unknown. The hypothesis is that somehow a circuit needs to be closed through the outer layer of ceramic to be able to have a failure.

There have been several additional tests (not reported earlier) done to investigate how the Hyjet affects the piezoelectric ceramic when no voltage is applied, by submerging a ring bender in Hyjet. Several different electrical wires, different epoxy and varnish compounds and the metallic foil were submerged in Hyjet to investigate the effect. The piezoelectric ceramic or its electrodes will not degrade when submerged in Hyjet when no voltage is applied. Different electrical wires have been submerged into Hyjet, some wire insulation will swell up, but the PTFE insulation used for the piezoelectric ring bender is not effected by the Hyjet. The metallic foil itself is not affected by the Hyjet, but the adhesive used to apply the foil will degrade if in contact with the Hyjet. However, if the foil is not letting any Hyjet through this is not of any concern.

The epoxy or varnish has been considered as a potential encapsulation for the piezoelectric ring bender. However, all the epoxy and varnish tested will eventually soften. The time for this to occur is different, it can take a few days or even months until degradation can be observed.

There are failure causes that are more likely than others, as can be seen in the fault tree in Figure 7-43. It is not likely that the failure is due to an electro-mechanical failure by simply degrading due to fatigue without Hyjet present.

The ceramic, wires or the solder do not degrade when no electrical field is applied. It is likely that there is a combination the Hyjet getting in contact with the electrical connections and the Hyjet is finding a path, through the ceramic, to the first internal electrode. The reason for the Hyjet leaking past the seal could be poor squeeze on the O-ring in combination with the surface roughness or possible subsurface cracks. The movement of the ring bender could create a pumping effect which promotes leakage.

It is likely that if the piezoelectric ceramic is protected to ensure no fluid penetrates to the electrodes or that no fluid reached the electrical connections no failure will occur. The reason the positive connection (red wire) needs to be protected is that it works as an anode and the control connections (blue) as a

cathode. The control connection (blue) could be both positively and negatively charged, due to the desired movement of the ring bender. The Hyjet contains potassium ions which are positively charged, which will be drawn to the negatively charged areas. As the Hyjet gets in contact with the Hyjet an electrical circuit can be made. The metallic ions from the positive (red) wire and solder will dissolve into the Hyjet, hence the corrosion. Since the first internal electrode is connected to the control (blue) wire the Hyjet could be 'drawn' into the piezoelectric ceramic and reach the electrode and damage it. As shown by the tests when an electrical circuit is made the ring bender starts to degrade quickly.

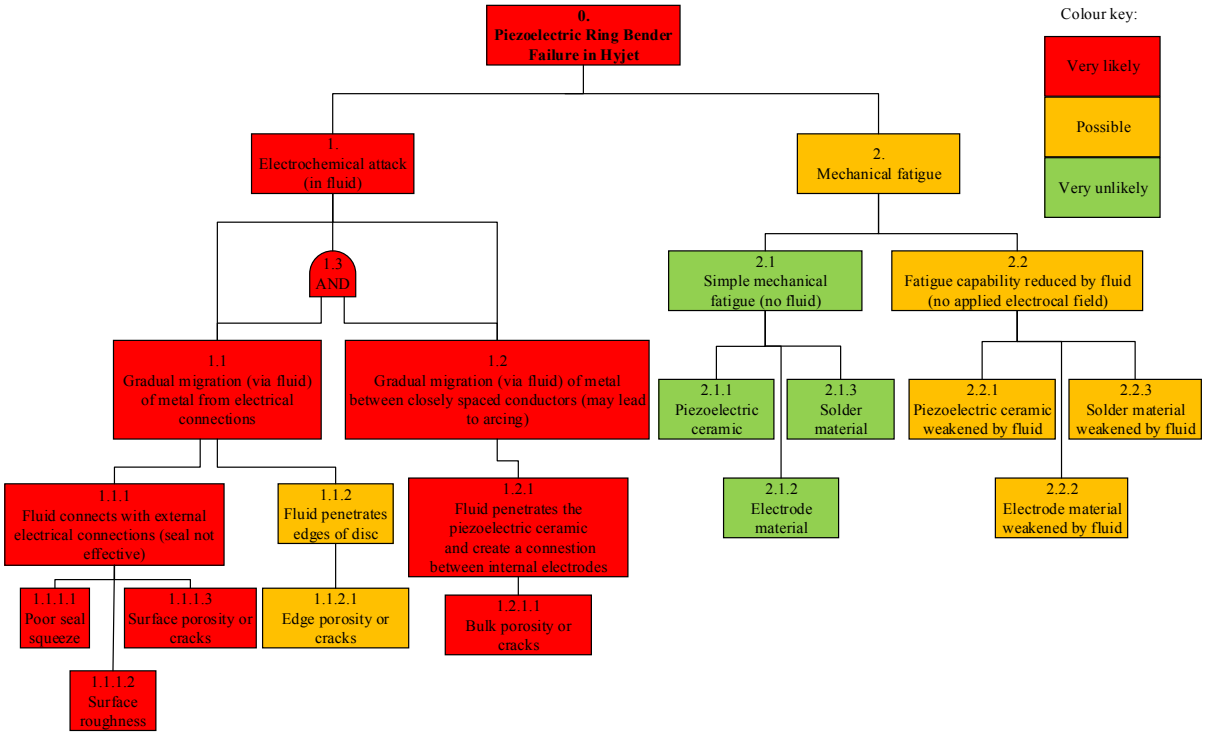

Figure 7-43. Final fault tree illustrating the likely scenarios that could break down a piezoelectric ring bender submerged in Hyjet.

7.8 CONCLUSION

From the tests and investigations completed in this chapter several conclusions can be drawn.

When no electrical field is applied the piezoelectric ceramic, the internal electrodes or the electric connections will not degrade.

When a cycling electric field is applied to the piezoelectric ring bender it will not degrade significantly in air nor in water. Most literature about degradation of piezoelectric actuators talk about water or moisture to be of concern. However, in this investigation this is not the case.

When the piezoelectric ring bender is in operation with an electric field and submerged in Hyjet if the Hyjet reaches the electrical connections, especially the positive wire, a failure will occur within hours. An electro-chemical reaction is taking place between the positive charge connection, the Hyjet and the

variable voltage which is connected to the internal electrode closest to the surface. However, if the ceramic is protected so that it is impermeable or the Hyjet does not reach the electrical connections no failure will occur.

By applying a metallic foil on the surface of the piezoelectric ring bender, to prevent Hyjet from penetrating the ceramic, this will significantly improve the life of the piezoelectric ring bender. The metal layer for a piezoelectric ring bender needs to be flexible to allow the piezoelectric ring bender to bend. Most literature and patents state that a metal layer needs to be applied to protect the piezoelectric actuator, since most polymers are permeable.

The piezoelectric ceramic surface seems to be more prone to leak at lower O-ring seal squeeze than using a metallic surface. The dynamic movement of the piezoelectric ring bender could have an impact on the amount of leakage.

The SEM investigation shows signs of cracks that start from the surface going towards the first electrode and also shows a large number of pores. These pores are a combination of piezoelectric grains being pulled out of during the polishing process and, isolated pores which are manufacturing defects.

The surface roughness of the piezoelectric ring bender surface is about ISO Rz 4-5 µm. The helium test shows that the seal squeeze on the piezoelectric ring bender surface needs to be sufficient, in this case at least 13%, otherwise there could be leakage.

The final recommendation for the encapsulation would be to apply a two layer protection, where the first layer would be an insulated polymer layer and the second a metallic layer. The first polymer layer could be applied by dipping and would work as a secondary protection as well as insulating the electrical connections. It would protect the connections from possible leakage and protect from short circuit in case the metallic layer would get in contact with the connections. The metallic layer would work as an impermeable layer and could also give a better sealing for an O-ring or similar elestomeric seal.

The ring bender used in the valve prototype was submerged in mineral oil, therefore no failure occurred during testing of the valve.

The next chapter will present the conclusions from the research project and present some possible future work.

8 CONCLUSION AND FUTURE WORK

8.1 CONCLUSIONS

Significant progress has been made in developing a new approach to servo-mechanism design which makes use of novel first-stage actuation in combination with an AM valve body. The results of the study demonstrate the clear potential of the technology for replacing conventional designs. If the future development of such servo-valves is done thoroughly, it is anticipated that this would support the drive towards a lighter, cheaper and more efficient valve technology.

8.1.1 Valve Design

It is the first time a piezoelectric ring bender has been used to control a small first stage spool in a two stage servovalve. The first stage spool had significant overlap and electrical second stage position feedback was used. The valve was successfully tested and the ring bender shows potential to be used for future aerospace hydraulic servovalves and to make the valves both lighter and less complex. By using a small first stage spool with significant overlap the internal leakage was reduced by 80% in comparison to a conventional first stage. It was possible to develop an additive manufactured valve body and this manufacturing method shows great potential to be used for manufacturing of aerospace valve bodies. To the authors knowledge the valve tested in this research was the first AM valve tested.

8.1.2 Analytical Model

A dynamic analytical model of the novel two-stage piezoelectric actuated valve with a first stage small spool has been developed. The sub-models in the analytical model include the amplifier for the piezoelectric ring bender, the ring bender including hysteresis, the first stage spool, the flow from the first stage to the second stage and the second stage spool. The dynamic model was developed to obtain further understanding of the complete system. The analytical model was also used for controller development.

The analytical model of a dynamic second stage step response correlates well with the experimental data. The first stage movement and the amplifier also compares well while the second stage is moved in a step response fashion. The analytical model shows that the valve behaviour was largely as expected. However, the second stage behaviour is sensitive to the first stage flow model, especially within the overlap region. It is hard to create a flow curve that matches consistently a range of amplitudes.

8.1.3 Controller Design

Due to the large first stage spool overlap a conventional Proportional-Integral controller for second stage spool position control is sensitive to amplitude changes, and therefore the performance of the controller will vary depending on the amplitude. An alternative control algorithm was developed and

tested to obtain a more consistent response. The experimental controller integrates hysteresis compensation, overlap compensation and feed-forward into the control loop.

To compensate for the first stage overlap a higher gain was implemented within the overlap region to increase performance and be less sensitive to amplitude changes. Ring bender hysteresis compensation improved the response and accuracy of the second stage performance. It also makes the overlap compensation perform more accurately, due to the linearization of the ring bender. The feed forward path increases the bandwidth of the second stage tracking response. The complete experimental control algorithm provides the quicker response compared to a conventional PI controller. This is the first time a controller has been developed to compensate both for spool overlap and piezoelectric hysteresis together and a patent has been applied for.

8.1.4 Ring Bender Mounting

From the investigation of the ring bender mounting an optimum overlap-thickness combination can be found. However, the optimum solution is dependent on the Young's modulus of the mounting. The optimum solution also implies that the overlap and thickness would be very small. Small overlap and thickness will allow the ring bender to rotate at its outer edge while being stiff axially to provide maximum force. This thin, optimum, solution might not be feasible in certain applications, for example when the mount is used as a seal as in this research project. However, the model can still be used to find a suitable thickness when the overlap is specified beforehand, and vice versa. The Young's modulus works as a scaling factor of the stiffness of the mount and will increase or decrease the stiffness.

8.1.5 Durability and Encapsulation

When the piezoelectric ring bender was tested in Hyjet (a very common civil aerospace hydraulic fluid) and no voltage is applied the piezoelectric ceramic will not degrade. Nor will the solder or the wires used for the ring bender. The insulation on some wires can swell when submerged in Hyjet.

This research shows that the piezoelectric ring bender is unlikely to degrade in air or water when an electric field is applied.

A significant finding in this research is that when an electric field is applied to the piezoelectric ring and submerged in Hyjet, and the Hyjet reaches the electrical connections, especially the positive connection, a failure will occur within hours. This is due to an electro-chemical reaction between the positive charge connection, the Hyjet and the negative internal electrode. However, if the ceramic is protected or the Hyjet does not reach the electrical connections this failure is significantly delayed. A metallic foil applied on the surface of the ring bender can protect the ceramic from being penetrated by the Hyjet and will significantly improve the life of the piezoelectric ring bender.

An elastomeric seal pressed against piezoelectric ceramic surface seems to be more prone to leak at lower seal squeeze than using a metallic surface. The dynamic movement of the piezoelectric ring bender could have an impact on the amount of leakage.

From SEM images, there are signs of cracks that start from the surface going towards the electrode that could possibly help the Hyjet penetrate the ceramic and reach the first internal electrode. Multiple pores are also observed.

The surface roughness of the piezoelectric ring bender surface is about ISO Rz 4-5 µm. A helium test shows that the seal squeeze on the piezoelectric ring bender surface needs to be sufficient, in this case at least 13%, otherwise the seal would be less effective than using the seal against a metal surface.

This is the first time an extensive investigation has been done to research the failure modes of ring benders in a phosphate ester based fluid.

8.1.6 Overall Conclusion

A two stage piezoelectric actuated Additive Manufactured (AM) servovalve for aerospace use, was designed, manufactured and successfully tested. This research could potentially change the design of future servovalves. It is reasonable to believe that AM will be used in the future to manufacture valve bodies. When the material characteristics are better understood, the valves could be designed to minimize weight and electronics could also be incorporated in to the valve design. AM is already in use for valves for robotics and it is just a question of time when the first AM valve will be introduced in aerospace.

Using electrical second stage spool position feedback means that the conventional feedback wire, which has fine manufacturing tolerances, is no longer needed. This could make the valve less complex, more accurate, lighter and smaller since the second stage spool can be made shorter. In this research, an LVDT was used, but this could be replaced by a digital encoder, by doing this the noise can be reduced and no analogue to digital converter is needed. By using an electrical second stage spool position feedback there is more flexibility in controller design.

The internal leakage was considerably reduced by using a small first stage spool with significant overlap. Since there is a need to make valves more efficient, this solution could be used with other actuation methods other than a ring bender, for example a linear force motor. Therefore, it is possible that a first stage small spool with large overlap could be used in future valves where low leakage is essential, however an appropriate non-linear controller needs to be used.

The controller designed in this research, with overlap compensation, hysteresis compensation and a feed forward path, considerably outperforms a conventional PI controller and could also be adjusted and used for other actuation methods which exhibits hysteresis. This non-linear compensation could

potentially also be used in an open loop fashion, if the first stage was to be used on its own in other applications, as a direct drive valve.

The concept of the prototype shown in this research and shows potential; however, it is yet to be proven that the complete valve can be made lighter and hopefully also cheaper.

It was found that the ring bender will fail in Hyjet if the Hyjet makes contact with the electrical connections. To prevent this, an encapsulation method and a good hydraulic seal is essential. It could be possible that the encapsulation could be incorporated during the manufacturing process of the ring bender. The ring bender could potentially be used, without encapsulation, in industrial or military applications where a form of mineral oil is used, but it still needs to be tested more rigorously. If a ring bender is used as valve actuation method, a large number of ring benders will be needed. This would significantly reduce the price of ring benders, which could potentially make the valves cheaper.

An optimized mounting arrangement can be found and this tends to be a thin knife edge. If the ring bender were to be used in a mineral oil, as the prototype valve in this research, the ring bender could be fully submerged and an optimum mounting can be used as it does not have to act as a seal. The mounting optimization method developed in this research could be used as a guideline for mounting a ring bender for other applications as well.

8.2 FUTURE WORK

From this research project, there are still areas that could be considered for further investigation.

There are several short-term challenges:

i. The valve prototype tested could be optimized for weight. This includes several areas:
    a. Shorten the second stage spool.
    b. Replace second stage LVDT with a digital encoder.
    c. Incorporate the first stage into the AM valve design.
    d. Remove the first stage LVDT.
    e. Optimise valve body for weight.
    f. Integration of electronics.
    g. Investigate if a smaller ring bender have enough force and displacement to control a first stage spool.
ii. The limitations and possibilities with using a charge amplifier instead of a voltage drive amplifier to drive a ring bender need to be further understood.
iii. A better nulling arrangement for the first stage spool and ring bender, to be made easier and more precise.

Long-term challenges are:

i. Further understanding of different encapsulation methods and material, and how they can be applied to the ring bender. Investigate if this could be incorporated into the manufacturing process of the ring bender. A more structured test program is needed.
ii. More material properties for the additive manufacturing needs to be understood.
iii. Making a safety assessment investigation of electrical spool position feedback for civil aerospace.
iv. Testing piezoelectric ring benders in other hydraulic fluids.

REFERENCES

[1] Moog Controls, "Servovalve Leakage Fuel Costs," Internal Report, Moog Controls, Tewkesbury, 2012.

[2] J. Persson, A. Plummer, C. Bowen, and P. Elliott, "Non-linear Control of a Piezoelectric Two Stage Servovalve," *15th Scand. Int. Conf. Fluid Power, SICFP'17, June 7-9, 2017, Linköping, Sweden*, 2017.

[3] D. K. Sangiah, "Fluid Metering Using Active Materials," PhD Thesis, University of Bath, 2011.

[4] D. McCloy and H. . R. Martin, *Control of Fluid Power: Analysis and Design*, 2nd ed. Chichester, UK: Ellis Horwood Limited, 1980.

[5] O. Olsson and K.-E. Rydberg, *Kompendium i Hydraulik*. Linkoping: Bokakademin, 1993.

[6] Moog Inc., "Electrohydraulic Valves... A Technical Look," Technical brochure, Moog Inc., 2002.

[7] Moog Inc., "Type 26 Single Inlet Flow Control Servovalves," Technical brochure, Moog Inc.

[8] R. W. Park, "Contamination Control - A Hydraulic OEM Perspective," Moog Australia, Monash University, 1997.

[9] H. E. Merritt, *Hydraulic Control Systems*. John Wiley & Sons Inc., 1967.

[10] Moog Inc, "Sub Miniature Servo Valves Pilot Operated Flow and Pressure Control E024 B & LB Series P, Q and S," Technical brochure, Moog Inc., 2015.

[11] R. H. Maskrey and W. J. Thayer, "A Brief History of Electrohydraulic Servomechanisms," *J. Dyn. Syst. Meas. Control*, vol. 100, no. 2, p. 110, 1978.

[12] J. Sparow, "Hydraulic Schematic Trubleshooting," 2010. [Online]. Available: http://www.hydraulicstatic.com/20100514_torque-motor.html. [Accessed: 20-Nov-2015].

[13] A. Fouad, "Experimental and Theoretical Investigation for Electro-hydraulic Servovalve Systems Control," PhD Thesis, University of Technology Bagdad, 2014.

[14] Moog Inc., "62 Series Installation and Operation Instruction Electrohydraulic Servovalve," Technical brochure, Moog Inc., East Aurora, 2009.

[15] L. J. Persson, A. R. Plummer, C. R. Bowen, and I. Brooks, "Design and Modelling of a Novel Servovalve Actuated by a Piezoelectric Ring Bender," in *ASME/BATH 2015 Symposium on Fluid Power and Motion Control, FPMC 2015*, 2015.

[16] J. Persson, C. R. Bowen, A. R. Plummer, and P. L. Elliott, “FPNI2016-1538 Dynamic Modelling and Performance of a Two Stage Piezoelectric Servovalve,” pp. 1–10, 2016.

[17] J. Tong, C. Bowen, J. Persson, and A. Plummer, “Mechanical Properties of titanium-based Ti – 6Al – 4V Alloys Manufactured by Powder Bed Additive Manufacture,” *Mater. Sci. Technol.*, no. March, 2016.

[18] F. Stefanski, B. Minorowicz, J. Persson, A. Plummer, and C. Bowen, “Non-linear control of a hydraulic piezo-valve using a generalised Prandtl – Ishlinskii hysteresis model,” *Mech. Syst. Signal Process.*, vol. 82, pp. 412–431, 2017.

[19] J. Persson, A. Plummer, C. Bowen, and I. Brooks, “A Lightweight , Low Leakage Piezoelectric Servovalve,” 2017. [Online]. Available: http://www.gfpsweb.org/?q=content/lightweight-low-leakage-piezoelectric-servovalve-7. [Accessed: 02-Nov-2017].

[20] J. Persson, A. Plummer, C. Bowen, and I. Brooks, “A Lightweight , Low Leakage Piezoelectric Servovalve,” in *Recent Advances in Aerospace Actuation Systems and Components*, 2016.

[21] B. Jeffe, W. R. Cook, and H. Jeffe, *Piezoelectric Ceramic*. Academic Press Inc, 1971.

[22] J. Van Randeraat, *Piezoelectric Ceramic*. London: Mullard Limited, 1968.

[23] S. Choi and Y. Han, *Piezoelectric Actuators: Control Applications of Smart Materials*. United states: CRC Press Taylor & Francis Group, 2010.

[24] D. R. Askeland and P. P. Phulé, *The Science and Engineering of Materials*. United States: Nelson, 2006.

[25] Physik-Instrumente, “Piezo Technology - Applications and Markets.” [Online]. Available: https://www.piceramic.com/en/applications/. [Accessed: 28-Nov-2015].

[26] Noliac, “Materials - Tutorial.” [Online]. Available: http://www.noliac.com/fileadmin/user_upload/documents/Tutorials/Tutorials_Materials.pdf. [Accessed: 17-Feb-2017].

[27] M. Bazghaleh *et al.*, “A digital charge amplifier for hysteresis elimination in piezoelectric actuators,” *Smart Mater. Struct.*, vol. 22, no. 7, p. 75016, 2013.

[28] M. J. F. Bertin, C. R. Bowen, A. R. Plummer, and D. N. Johnston, “An Investigation of Piezoelectric Ring Benders and Their Potential for Actuating Servo Valves,” in *Proceedings of the Bath/ASME Symposium on Fluid Power and Motion Control*, 2014, p. 6.

[29] Noliac, “Noliac Applications,” 2017. [Online]. Available: http://www.noliac.com/card/list/applications/. [Accessed: 20-Sep-2016].

[30] S. Ouchouche, C. Goueffon, and B. Andersen, “Application-Specific Piezoelectric Components : High Displacement in a Small Component Size,” Noliac, Kvistgaard, Denmark.

[31] Noliac, “Products/Actuators/Ring Stacks/NAC2125-HXX.” [Online]. Available: http://www.noliac.com/products/actuators/ring-stacks/show/nac2125-hxx/. [Accessed: 17-Feb-2017].

[32] Noliac, “Products/Actuators/Plate Benders/CMBP08.” [Online]. Available: http://www.noliac.com/products/actuators/plate-benders/show/cmbp08/. [Accessed: 17-Feb-2017].

[33] Noliac, “Products/Actuators/Ring Benders/CMBR08.” [Online]. Available: http://www.noliac.com/products/actuators/ring-benders/show/cmbr08/. [Accessed: 01-Jan-2017].

[34] L. Zhu, E. Shiju, X. Zhu, and C. Gao, “Development of Hydroelectric Servo-Valve Based on Piezoelectric Elements,” *2010 Int. Conf. Mech. Autom. Control Eng. MACE2010*, pp. 3330–3333, 2010.

[35] J. Jeon, Q. Nguyen, Y. Han, and S. Choi, “Design and Evaluation of a Direct Drive Valve Actuated by Piezostack Actuator,” *Adv. Mech. Eng.*, p. 12, 2013.

[36] J. Jeon, C. Han, Y.-M. Han, and S.-B. Choi, “A new type of a direct-drive valve system driven by a piezostack actuator and sliding spool,” *Smart Mater. Struct.*, vol. 23, no. 7, p. 75002, 2014.

[37] D. T. Branson, F. C. Wang, D. N. Johnston, D. G. Tilley, C. R. Bowen, and P. S. Keogh, “Piezoelectrically actuated hydraulic valve design for high bandwidth and flow performance,” *Proc. Inst. Mech. Eng. Part I J. Syst. Control Eng.*, vol. 225, no. 3, pp. 345–359, 2011.

[38] J.-P. Lecerf, C. Favey, and P. Meurice, “Electrofluidic Transducer of Nozzle/Plate and Hydraulic Servo-Valve Equipped with such Trnsducer,” United States, Patent US4705059, 1987.

[39] M. Bertin, “Piezoelectric Actuation of an Aero Engine Fuel Metering Valve,” PhD Thesis, University of Bath, 2017.

[40] K. Wu, “Design, Fabrication and Characterization of a Piezo-electric Micro Control Valve,” Master Thesis, University of Twente, 2014.

[41] C. Mangeot, “Maturity of Piezoelectric Actuator Applications in the Aerospace Industry,” in *IMeche Derby, Smart Actuation Applications*, 2014.

[42] J. Thongrueng, T. Tsuchiya, and K. Nagata, “Lifetime and degradation mechanism of multilayer ceramic actuator,” *Japanese J. Appl. Physics, Part 1 Regul. Pap. Short Notes Rev. Pap.*, vol. 37,

no. 9 PART B, pp. 5306–5310, 1998.

[43] D. A. Van Den Ende, B. Bos, W. A. Groen, and L. M. J. G. Dortmans, "Lifetime of piezoceramic multilayer actuators: Interplay of material properties and actuator design," *J. Electroceramics*, vol. 22, no. 1–3, pp. 163–170, 2009.

[44] H. C. Ling and a M. Jackson, "Correlation of Silver Migration With Temperature-Humidity-Bias(THB) Failures in Multilayer Ceramic Capacitors," *IEEE Trans. Components, Hybrids, Manuf. Technol.*, vol. 12, pp. 130–137, 1989.

[45] P. Pertsch, S. Richter, D. Kopsch, N. Kramer, J. Pogodzik, and E. Hennig, "Reliability of Piezoelectric Multilayer Actuators," in *Contribution to Actuator 2006 conference, Bremen*, 2006.

[46] P. M. Weaver, M. G. Cain, M. Stewart, A. Anson, and J. Franks, "The Effects of Porosity, Electrode and Barrier Materials on the Conductivity of Piezoelectric Ceramics in High Humidity and DC Electric Field," *Smart Mater. Struct.*, vol. 21, no. 4, p. 9, 2012.

[47] B. Andersen, F. Jensen, and S. Ouchouche, "Reliability of Piezoelectric Actuators at Extreme Operating Conditions," Noliac, Kvistgaard, Denmark.

[48] J.-F. Berlemont, "Method of Encapsulating an Actuator Having a Piezoelectric Actuator Stack," Patent EP2343746A1, 2011.

[49] R. H. Bosch and J.-F. Berlemont, "Encapsulating Arrangement For an Electrical Component," Patent US 20090294556A1, 2009.

[50] H. Bayer *et al.*, "Piezoelectric Actuator With Encapsulation Layer Having a Thickness-Varying Property Gradient," Patent US8198783B2, 2012.

[51] M. Cook, "Gas Pressurised Encapsulation for an Actuator," Patent EP2079113A1, 2008.

[52] G. A. Ricci-Ottati and R. H. Bosch, "Hydraulic Intensifier Assembly for a Piezoelectric Actuated Fuel Injector," Patent US6520423B1, 2003.

[53] "Marine Engineering," 2011. [Online]. Available: http://zaclongmanrotar.blogspot.co.uk/2011/06/diesel.html. [Accessed: 30-Mar-2017].

[54] P. Automation and H. Janocha, "Modeling , Identification and Compensation A modified Prandtl-Ishlinskii Approach of Complex Hysteretic Nonlinearities," *Eur. J. Control*, vol. 9, no. 4, pp. 407–418, 2003.

[55] A. J. Fleming and S. O. R. Moheimani, "Improved Current and Charge Amplifiers for Driving Piezoelectric Loads, and Issues in Signal Processing Design for Synthesis of Shunt Damping

Circuits," *J. Intell. Mater. Syst. Struct.*, vol. 15, no. 2, pp. 77–92, 2004.

[56] V. Hassani, T. Tjahjowidodo, and T. N. Do, "A survey on hysteresis modeling, identification and control," *Mech. Syst. Signal Process.*, vol. 49, no. 1–2, pp. 209–233, 2014.

[57] F. Stefański, B. Minorowicz, and A. Nowak, "Hysteresis Modelling of a Piezoelectric Tube Actuator," *Adv. Intell. Syst. Comput.*, vol. 351, 2015.

[58] "Technical Note PD410 Circular PICMA Bender Piezo Actuators," Technical Note, PI Ceramics GmbH, Lederhose, 2014.

[59] Noliac, "Mounting and Connect." [Online]. Available: http://www.noliac.com/products/actuators/ring-benders/show/cmbr08/. [Accessed: 17-Feb-2017].

[60] R. J. Roark, *Formulas for Stress and Strain*, Third Edit. McGraw-Hill Book Company Inc, 1954.

[61] S. Timoschenko, *Strength of Materials, Part 2 Advanced Theory and Problems*, Third Edit. CBS Publisher, 2002.

[62] "Standard Practice/Guide for Design for Additive Manufacturing," ASTM 52910.2, 2013.

[63] D. L. D. Bourell, J. J. Beaman, M. C. Leu, and D. W. Rosen, "A brief history of additive manufacturing and the 2009 roadmap for additive manufacturing: looking back and looking ahead," *US-Turkey Work. Rapid Technol.*, 2009.

[64] W. E. Frazier, "Metal Additive Manufacturing: A Review," *J. Mater. Eng. Perform.*, vol. 23(6), p. 12, 2014.

[65] Subcon, "Tipping Point for Additive Manufacturing." [Online]. Available: http://www.subconshow.co.uk/visiting/show-news/2017/05/24/tipping-point-for-additive-manufacturing. [Accessed: 24-Jul-2017].

[66] G. Paul, Z. Timothy, G. Eric, and B. Chris, "Additive Manufacturing for Next Generation Actuation," in *Recent Advances in Aerospace Actuation Systems and Components*, 2016, p. 6.

[67] B. Dutta and S. Froes, "The additive manufacturing (AM) of titanium alloys," *Met. Powder Rep.*, vol. 72, no. Number 2, 2017.

[68] Eos, "Aerospace: Vectoflow - Additive Manufacturing of probes for measuring speed and temperature in turbo engines." [Online]. Available: https://www.eos.info/aerospace-vectoflow-additive-manufacturing-of-probes-for-measuring-speed-and-temperature-in-turbo-engines-ea0691d8a20ee1eb. [Accessed: 11-Aug-2017].

[69] Eos, "Aerospace: RUAG - Additive Manufacturing of Satellite Components." [Online].

Available: https://www.eos.info/case_studies/additive-manufacturing-of-antenna-bracket-for-satellite. [Accessed: 11-Aug-2017].

[70] G. Small, "A New Way of looking at Metal Additive Manufacturing Processes." [Online]. Available: http://www.moog.com/news/blog-new/GeorgeSmallVeripart_1.html. [Accessed: 24-Jul-2017].

[71] Renishaw, "Hydraulic Block Manifold Redesign for Additive Manufacturing." [Online]. Available: http://www.renishaw.com/en/hydraulic-block-manifold-redesign-for-additive-manufacturing--38949. [Accessed: 24-Jul-2017].

[72] Eos, "Industrial 3D printing of high-tech aerospace components." [Online]. Available: https://www.eos.info/aerospace. [Accessed: 11-Aug-2017].

[73] A. J. Collins, "Method for producing servo valve manifolds and manifold with curvilinear flow gallery of single piece construction," Patent WO2014199158A1, 2014.

[74] W. P. Taylor, "Fluid manifold," Patent US20160298662A1, 2016.

[75] S. A. Weickel and B. J. Atkin, "A combination manifold and valve housing for a manifold bank made by an additive manufacturing method," Patent WO2017058237A1, 2017.

[76] D. K. Sangiah, A. R. Plummer, C. R. Bowen, and P. Guerrier, "A novel piezohydraulic aerospace servovalve. Part 1: design and modelling," *Proc. Inst. Mech. Eng. Part I J. Syst. Control Eng.*, vol. 227, no. 4, pp. 371–389, 2013.

[77] C. Mangeot, B. Anderssen, and R. Hilditch, "New Actuators for Aerospace," Noliac, Kvistgaard, Denmark, 2008.

[78] G. V. Caliri, "Introduction to Analytical Modeling," Waltham, BMC Software, Inc.

[79] A. C. J. Elrod, R. C. Heagey, D. C. Muths, L. L. Nichols, and C. E. Cobb, "Electrohydraulic Servovalve with Flow Gain Compensation," Patent US5285715A, 1994.

[80] J. C. Jones, "Development in Design of Electrohydraulic Control Valves From Their Initial Design Concept to Present Day Design and Applications," in *Workshop on Proportional and Servovales, Monash University*, 1997, p. 19.

[81] M. Yeomans and P. Elliott, "Personal Contact at Moog Controls." Tewkesbury, 2017.

[82] MathWorks, "xPC Target For use with Real-Time Workshop," Selecting Hardware Guide, The MathWorks Inc., 2007.

[83] M. Ismail, F. Ikhouane, and J. Rodellar, "The Hysteresis Bouc-Wen Model , a Survey," *Arch Comput Methods Eng*, pp. 161–188, 2009.

[84] A. P. Plummer, “Servohydraulic Simulink Model,” University of Bath, 2003.

[85] A. A. El-Sayed, M. H. Gobran, M. Galal Rabie, and M. R. Shalaan, “Investigation of Characteristics of an Electrohydraulic Servoactuator Incorporating Jet Pipe Amplifier.”

[86] DesignAerospace, “Servovalve, Hydraulic - Description.” [Online]. Available: http://www.daerospace.com/HydraulicSystems/ServovalveDesc.php. [Accessed: 30-Mar-2017].

[87] Vickers, “Proportional Valves: Adjustment Procedure.” Vickers, 1993.

[88] M. Rakotondrabe, “Bouc – Wen Modeling and Inverse Multiplicative Structure Actuators to Compensate Hysteresis Nonlinearity in Piezoelectric Actuators,” *IEEE Trans. Autom. Sci. Eng.*, vol. 8, no. 2, pp. 428–431, 2011.

[89] Parker Hannifin - Electromechanical Automation Div., “Fundamentals of Servo Motion Control.” [Online]. Available: http://www.compumotor.com/whitepages/ServoFundamentals.pdf. [Accessed: 20-Jan-2017].

[90] A. R. Plummer, “Model-based Motion Control for Culti-Axis Servohydraulic Shaking Tables,” *Control Eng. Pract.*, vol. 53, pp. 109–122, 2016.

[91] M. Cain and M. Stewart, “The measurement of blocking force,” NPL Report MATC(a)48, National Physical Laboratory, Teddington, UK, 2001.

[92] P. Elliott, “Failure Tree (Personal comunication).” Moog Controls, Tewkesbury, 2016.

[93] Exxon Mobil, “Exxon HyJey V.” [Online]. Available: https://www.exxonmobil.com/english-US/Aviation/pds/GLXXHyJet-V. [Accessed: 15-May-2017].

[94] Weico, “Hook-Up Wire MIL-W-16878/4.” [Online]. Available: http://www.weicowire.com/image/pdf/hookupwire/Type E spec Sheet.pdf. [Accessed: 11-Sep-2017].

[95] T. R. Beck, D. W. Mahaffey, and J. H. Olsen, “Pitting and Deposits with an Organic Fluid by Electrolysis and by Fluid Flow,” *J. Electrochem. Soc.*, vol. 119, no. 2, p. 155, 1972.

[96] D. Zheng, J. Swingler, and P. Weaver, “Current leakage and transients in ferroelectric ceramics under high humidity conditions,” *Sensors and Actuators*, vol. 158, pp. 106–111, 2010.

[97] RS, “Polyurethane coating,” 2003. [Online]. Available: http://docs-europe.electrocomponents.com/webdocs/007a/0900766b8007a359.pdf. [Accessed: 10-Sep-2017].

[98] Loctite, “Product Description Sheet Loctite EA 0151,” 2015. [Online]. Available:

https://tds.us.henkel.com/NA/UT/HNAUTTDS.nsf/web/E1BE61E77076ECDA882571870000DB10/$File/EA 0151-EN.pdf. [Accessed: 11-Sep-2017].

[99] RS, "Datasheet RS Pro 50 ml Black Epoxy Dual Cartridge Potting Compound," *RS*. [Online]. Available: http://docs-europe.electrocomponents.com/webdocs/1512/0900766b81512b87.pdf. [Accessed: 11-Sep-2017].

[100] Struers, "Selection of Resin." [Online]. Available: http://www.struers.com/en-GB/Knowledge/Mounting/Cold-mounting#cold-mounting-how-to. [Accessed: 11-Sep-2017].

[101] Zygo, "Zygo Surface Texture," 2013. [Online]. Available: file:///C:/Users/ljp46/Downloads/ZYGO-SurfText.pdf. [Accessed: 06-Oct-2016].

[102] M. I. Corporation, "Mercury Intrusion Porosimetry Theory," 2010. [Online]. Available: http://www.micromeritics.com/Repository/Files/Mercury_Porosemitry_Theory_poster_.pdf. [Accessed: 10-Sep-2017].

[103] "Personal meeting with Noliac." Tewkesbury, 2016.

APPENDIX

A.1 MOUNTING STIFFNESS MATRIX

Table A - 1. Axial mounting stiffness matrix from the FEA investigation.

Axial	Unit:	N/mm/m	Young's Modulus:	1.00E+07									
Thickness (mm)	Overlap (mm)												
0.1	**0.1**	**0.2**	**0.4**	**0.6**	**1**	**1.2**	**1.6**	**1.8**	**2**	**2.2**	**2.6**	**3**	**3.4**
0.1	84.69731579	191.0976506	584.1097998	1148.877929	2470.563122	3155.155514	4518.28761	5190.789934	5855.921721	6512.956347	7802.007099	9055.823856	10272.64914
0.2	45.7638521	75.75939251	174.8068826	332.6478624	796.387322	1077.686434	1689.726898	2008.036876	2329.18413	2650.894425	3289.458008	3916.041203	4526.725153
0.4	28.74429373	39.35532271	67.36095748	107.2695076	228.2840304	309.2851058	506.9539512	620.6856582	742.3449168	870.5407761	1141.567099	1424.973665	1714.037166
0.6	22.83932291	29.21511243	44.17824048	63.44204489	118.0450114	153.9788839	243.6236277	296.8399833	355.2098103	418.3235355	557.0651554	709.5871673	872.5109344
1	17.94824853	21.65448921	29.41029513	38.27751027	60.55297044	74.30202767	107.4998751	127.0347064	148.5329342	171.978355	224.510536	284.1870387	350.3498274
1.2	16.68963671	19.83080763	26.19558045	33.22525674	50.1838752	60.35220072	84.41740273	98.39017829	113.6758564	130.279632	167.3824337	209.4992165	256.3675438
1.4	15.7379381	18.49756463	23.95709131	29.83438014	43.58970194	51.64917403	70.38979812	81.12933011	92.80171619	105.4113645	133.4302712	165.1028804	200.3435152
1.6	14.95745045	17.43845251	22.25544205	27.34139189	38.973784	45.66923538	61.01906931	69.71777008	79.11495345	89.21241215	111.5271366	136.6196991	164.3857832
1.8	14.28581276	16.54902495	20.87944964	25.37941198	35.49071877	41.23267228	54.25404728	61.56864343	69.43311544	77.85664025	96.35572026	117.0190749	139.7762242
2	13.69543001	15.77954746	19.71992244	23.76083447	32.71444648	37.74448484	49.05899992	55.3794792	62.14935756	69.37103567	85.1609745	102.7077934	121.9482266
2.2	13.17395956	15.10596931	18.72241664	22.39112149	30.41922464	34.88964778	44.8900919	50.44612686	56.38204351	62.69803521	76.46683981	91.71298021	108.3764215
2.6	12.31092007	13.99716493	17.10258945	20.19272842	26.8157549	30.45355111	38.50236203	42.94342596	47.67167512	52.69047035	63.59674987	75.63476699	88.75318559
3	11.65510513	13.15385858	15.87357182	18.53789322	24.13970672	27.17143577	33.82400298	37.47241228	41.34775835	45.45485879	54.37048044	64.21056604	74.94165756
3.4	11.16535255	12.52050991	14.94520559	17.28451669	22.11587967	24.69580165	30.30190777	33.35703001	36.5929514	40.01652218	47.44031052	55.63810664	64.59546459

Table A - 2. Torsional mounting stiffness matrix from the FEA investigation.

Torsional	Unit:	Nm/m/deg	Young' Modulus:	1.00E+07							
	Overlap (mm)										
Thickness (mm)	0.1	0.2	0.6	0.8	1	1.2	1.6	2	2.6	3	3.4
0.1	0.399119561	0.38941943	0.912147291	1.681791737	3.121337324	5.07948621	11.61336508	23.17403419	49.75719333	75.67987374	106.2434105
0.2	0.231402751	0.228666146	0.42891463	0.656100971	1.030957771	1.623931939	3.757938761	7.64723688	18.18167784	28.69537494	42.62220717
0.4	0.157745026	0.159826855	0.27006508	0.363603761	0.496783305	0.688768727	1.324316428	2.444810189	5.532079501	8.808268117	13.39354901
0.5	0.14454151	0.147104451	0.2438118	0.319797808	0.424314664	0.568599966	1.024602648	1.801809145	3.89635618	6.121812209	9.242599488
0.6	0.136382501	0.138975365	0.227170945	0.293252391	0.381176129	0.498770689	0.857224863	1.448048758	2.998605483	4.635665926	6.920576918
0.8	0.1275483	0.129775515	0.207592535	0.262990691	0.333281736	0.42308012	0.681587537	1.084596142	2.091615223	3.127527215	4.553495875
1	0.123198518	0.125230117	0.196917877	0.24685634	0.308146625	0.38403412	0.593400941	0.906109218	1.657745348	2.40674788	3.020641786
1.2	0.120330265	0.122552932	0.190665885	0.237317459	0.293397882	0.361167101	0.541983258	0.803172992	1.408038663	2.00011215	2.461070535
1.6	0.119116047	0.12090006	0.185414108	0.228652655	0.279269793	0.338598378	0.489290127	0.695553748	1.148406232	1.574744044	2.128413807
2	0.117842191	0.11989168	0.183405014	0.225372876	0.273687818	0.3921708	0.465549062	0.644274755	1.020161487	1.362847736	1.796023059
2.6	0.117581078	0.119413822	0.182330835	0.22385416	0.271152336	0.324612915	0.451880964	0.611217327	0.928201032	1.20542725	1.547891055
3.4	0.117048127	0.118898314	0.181420063	0.222760483	0.269835321	0.322771263	0.446804478	0.597285133	0.882013299	1.12001959	1.40547342

A.2 MOUNTING Graphs

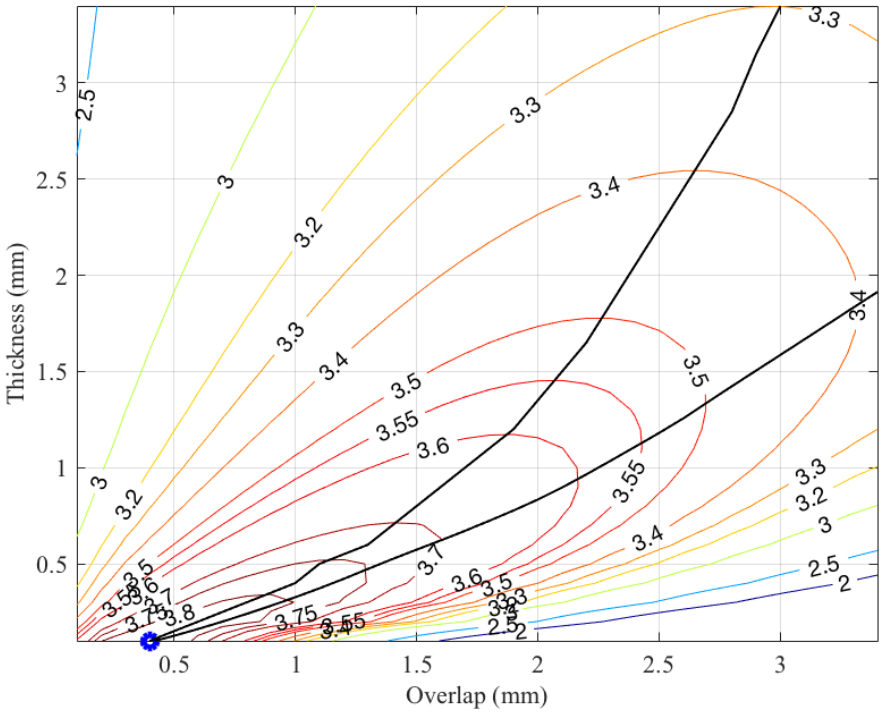

Figure A - 1. Work output for Young's modulus of 5MPa for a 40mm ring bender.

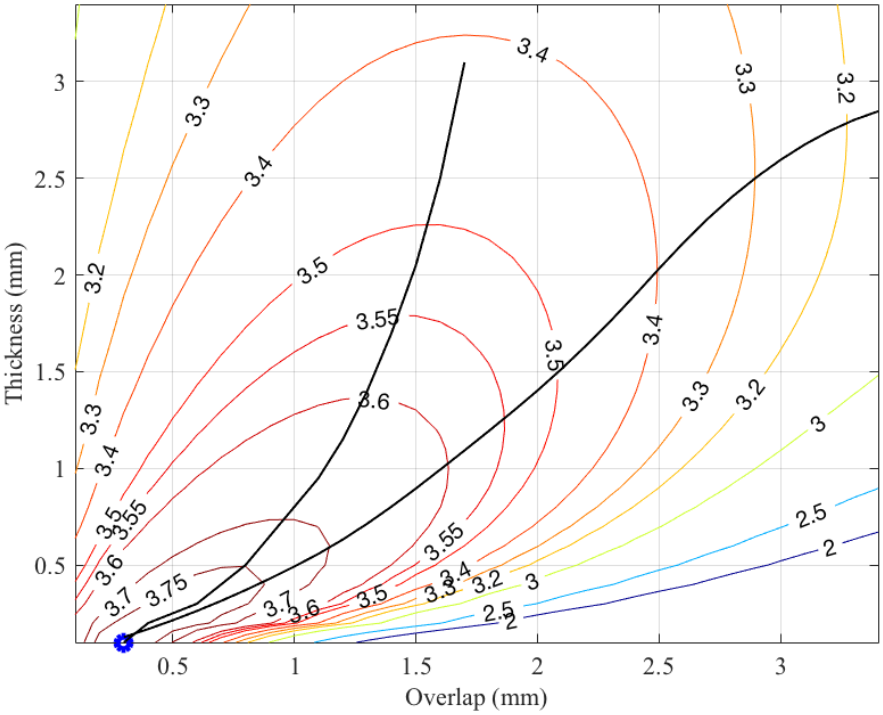

Figure A - 2. Work output for Young's modulus of 10MPa for a 40mm ring bender.

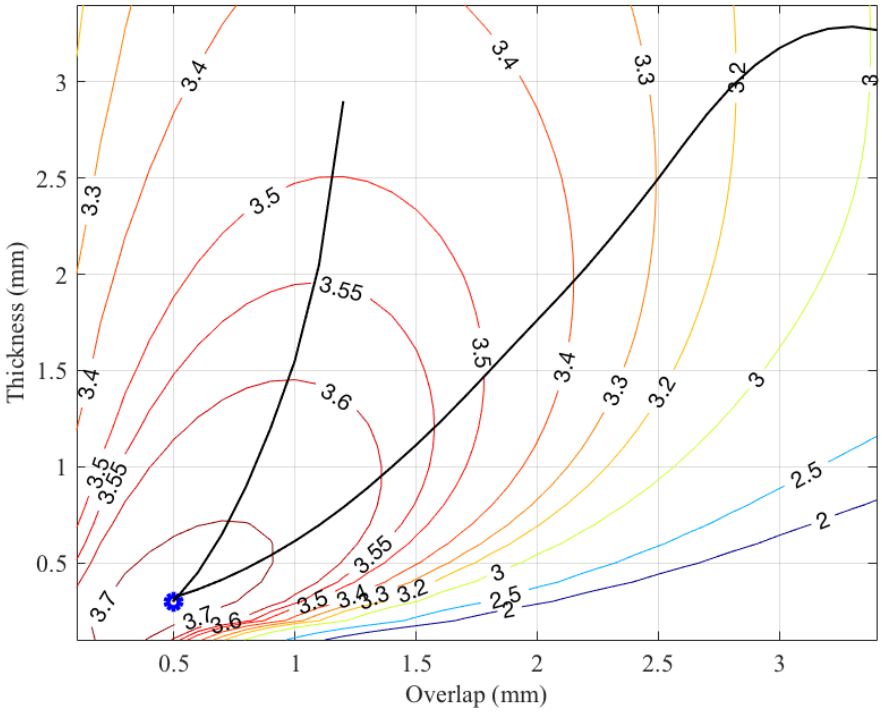

Figure A - 3. Work output for Young's modulus of 13.7MPa for a 40mm ring bender.

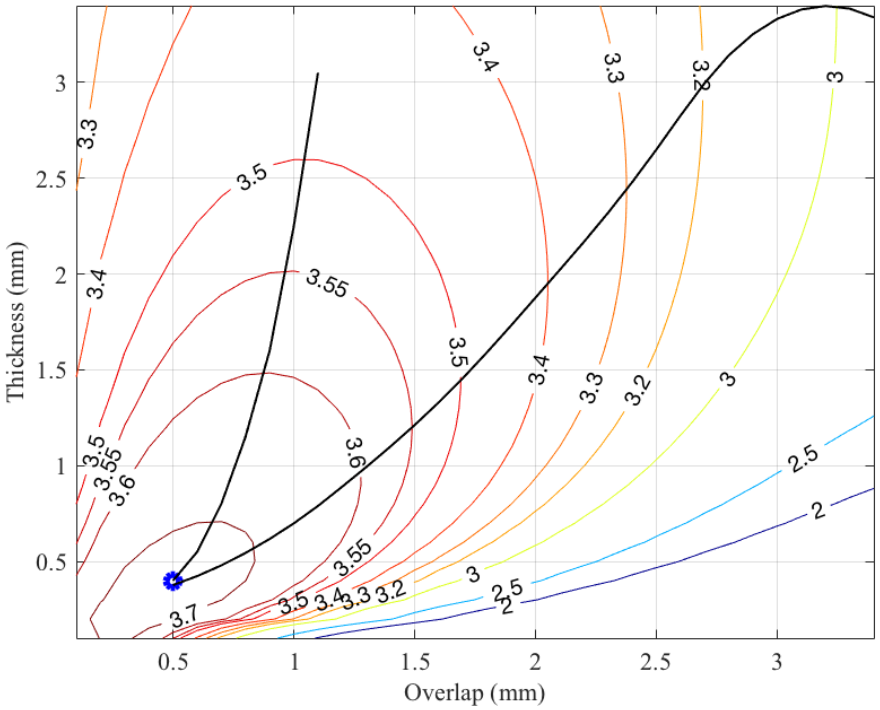

Figure A - 4. Work output for Young's modulus of 15MPa for a 40mm ring bender.

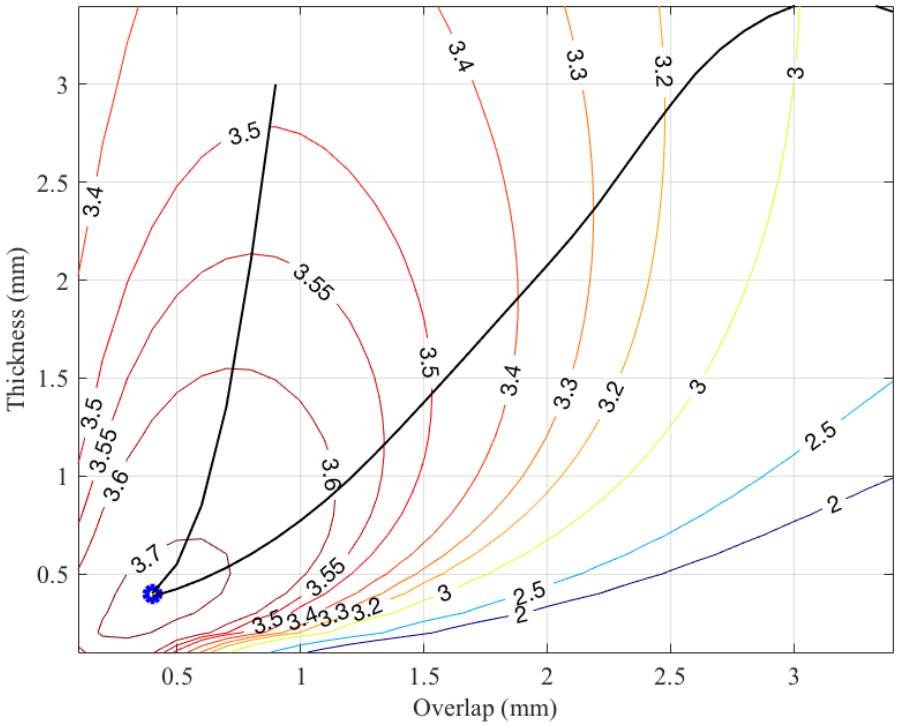

Figure A - 5. Work output for Young's modulus of 17.5MPa for a 40mm ring bender.

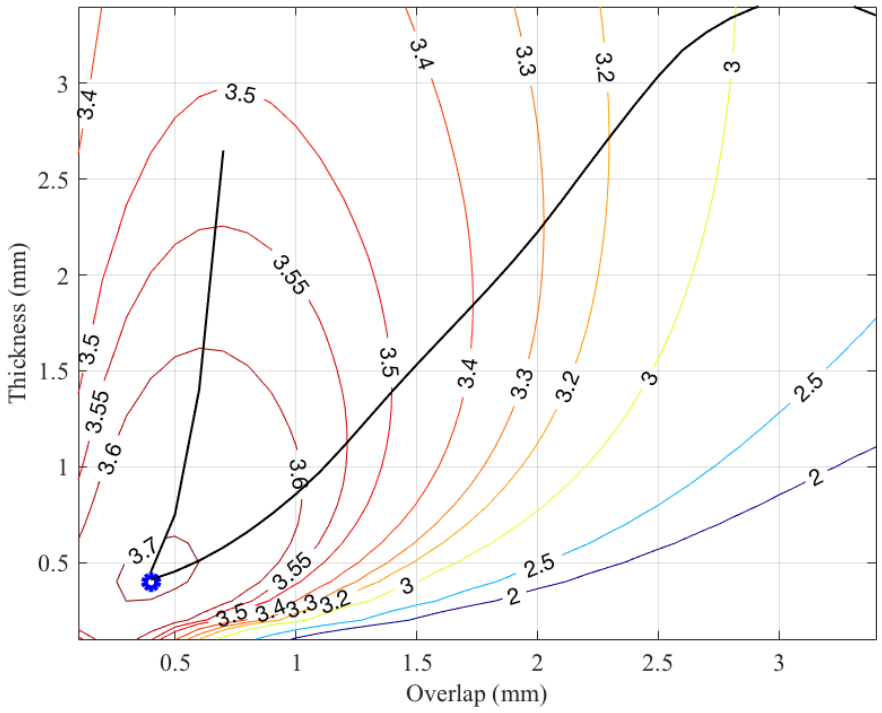

Figure A - 6. Work output for Young's modulus of 20MPa for a 40mm ring bender.

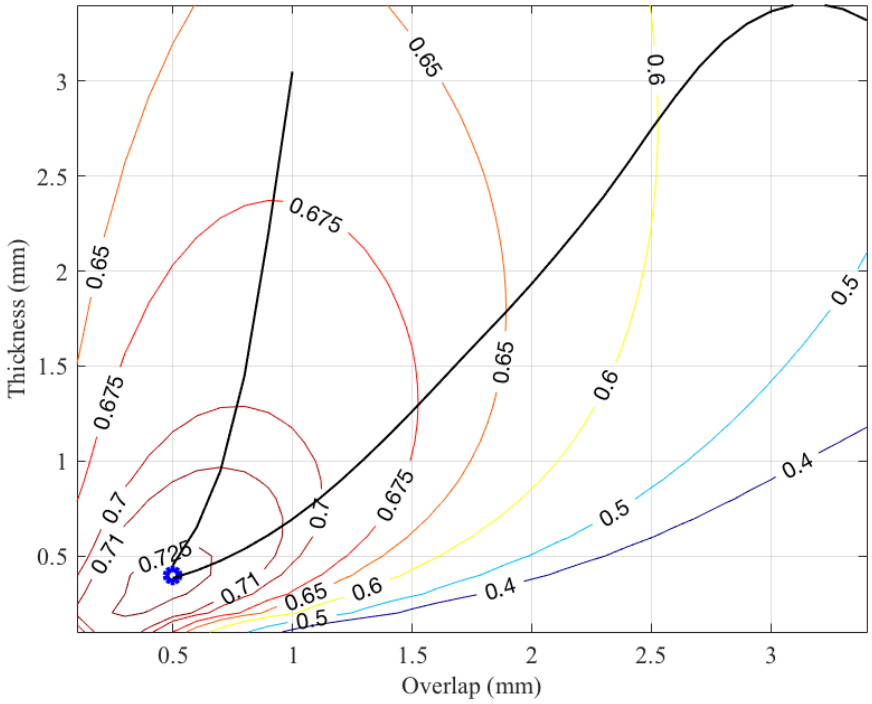

Figure A - 7. Work output for Young's modulus of 5MPa for a 30mm ring bender.

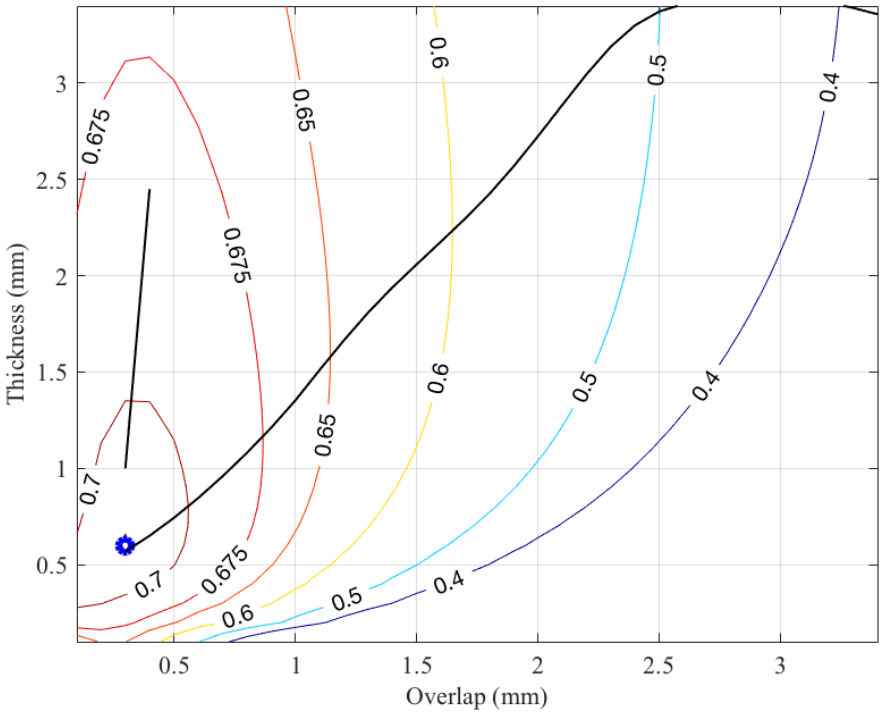

Figure A - 8. Work output for Young's modulus of 10MPa for a 30mm ring bender.

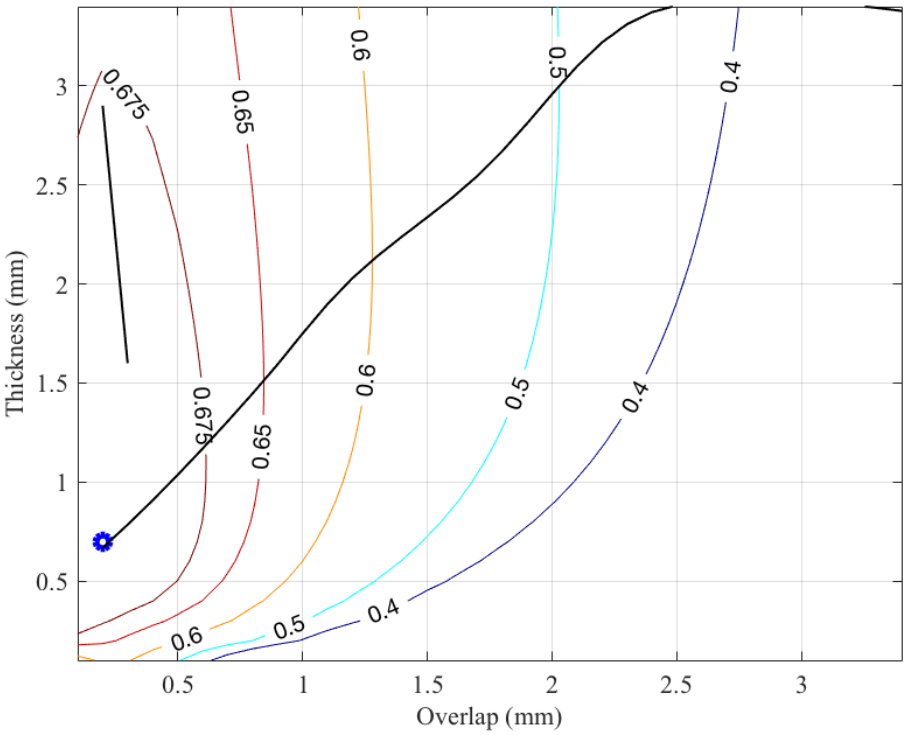

Figure A - 9. Work output for Young's modulus of 13.5MPa for a 30mm ring bender.

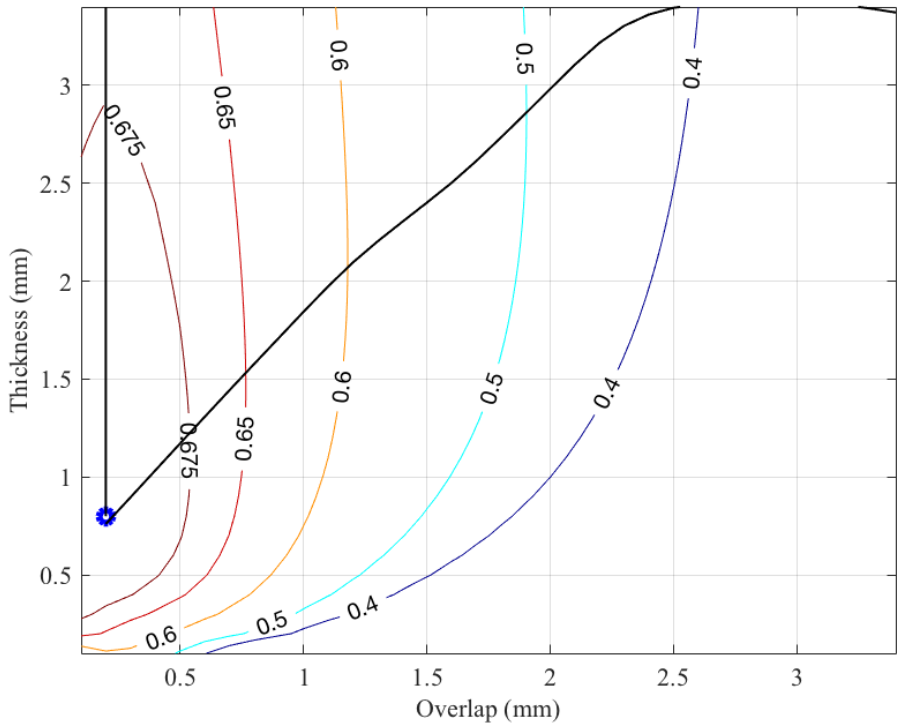

Figure A - 10. Work output for Young's modulus of 15MPa for a 30mm ring bender.

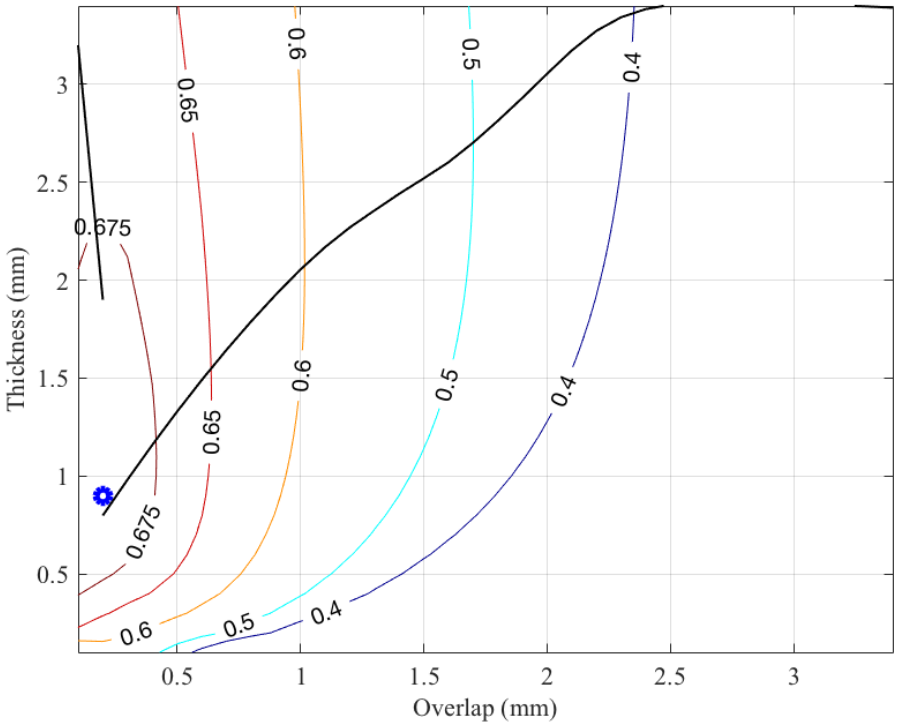

Figure A - 11. Work output for Young's modulus of 17.5MPa for a 30mm ring bender.

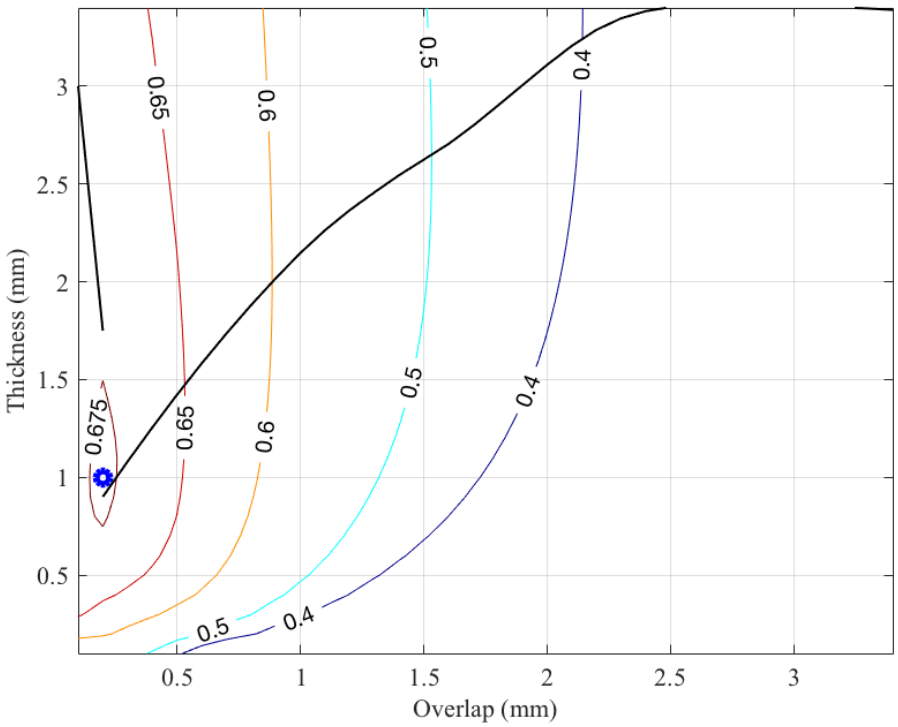

Figure A - 12. Work output for Young's modulus of 20MPa for a 30mm ring bender.